Dipl. Ing. Martin Neumann

Investigation of the Behavior of Shock-Absorbing Structural Parts of Transport Casks Holding Radioactive Substances in Terms of Design Testing and Risk Analysis

BAM-Dissertation Series, Volume 45
Berlin, 2009

This study was created by BAM Bundesanstalt für Materialforschung und- prüfung [Federal Institute of Materials Research and Testing] in cooperation with Bergische Universität Wuppertal.

The author would like to thank US NRC (United States Nuclear Regulatory Commission) for providing the english translation of the PhD-thesis.

Printer's Imprint

**Investigation of the Behavior of
Shock-Absorbing Structural Parts of
Transport Casks Holding Radioactive Substances
in Terms of Design Testing and Risk Analysis**

2009

Publisher
BAM Bundesanstalt für Materialforschung und- prüfung
Unter den Eichen 87
12205 Berlin
Telephone:+49 30 8104-0
Telefax: +49 30 8112029
E-mail: info@bam.de
Internet: www.bam.de

Layout: BAM-Arbeitsgruppe Z.64
ISSN: 1613-4249
ISBN: 978-3-9812354-8-7

Investigation of the Behavior of Shock-Absorbing Structural Parts of Transport Casks Holding Radioactive Substances in Terms of Design Testing and Risk Analysis

Submitted by
Dipl.-Ing. Martin Neumann
From Eisenhüttenstadt

Dissertation Accepted

by the Department of Safety Engineering of Technical Division D
of Bergische Universität Wuppertal
to earn the Degree of

Doctor of Engineering Sciences
(Dr.-Ing.)

Examination Commission:

Chairman:	Prof. Dr. René Treibert
1st Expert Examiner:	Prof. Dr. Sylvius Hartwig
2nd Expert Examiner:	Prof. Dr. Detlef Filges
Member:	Prof. Dr. Uli Barth

Date of Verbal Examination: May 28, 2009

Berlin, 2009

"Discovery must precede practical use."
Max Planck (1858-1947)

Acknowledgement

This work was created from July 2004 to August 2007 at the Federal Institute for Material Research and Testing (BAM) in Berlin within the "Transport Cask Safety" team.

I want to thank Prof. Dr. Sylvius Hartwig, my doctoral studies advisor, for shepherding my work, for his constant readiness to discuss issues and for his very much on-target comments. I want to thank Prof. Dr. Detlef Filges for taking care of the second expert report. I also want to thank Prof. Dr. René Treibert for being the chairman and for Prof. Dr. Uli Barth for his readiness to officiate with the examining commission.

I especially want to thank Director and Professor Dr. Bernhard Droste, the leader of the "Transport Cask Safety" team of BAM, for his tremendous support, his very valuable suggestions, comments and references.

I also want to thank the Federal Ministry of Education and Research for the financial support it provided for these investigations under Promotion Task 02S8274, as well as BAM, represented by Vice President Prof. Dr. Thomas Böllinghaus, for all the help and support given as part of the BAM Doctoral Degree Application Program.

I want to thank the members of the "Transport Cask Safety" team of BAM, especially Dr. Frank Wille, Dr. Linan Qiao, Dr. Viktor Ballheimer and Dr. Steffen Komann for their steadfast participation in discussions and the fruitful exchange of scientific thoughts. I want to thank the staff members of the "Experimental Cask Investigations" team and especially Dr. André Musolff and Dipl. Ing. Thomas Quercetti for arranging the technical experiments and providing the appropriate measurement results in connection with drop tests involving experimental objects.

I want to thank the members of the "Experimental Supporting Framework Safety" team of BAM and especially Dipl. Ing. Jürgen Herter for the tremendous help they gave me in arranging the technical experiments connected with the shock tests on wood samples. I want to thank the "Measurement and Testing Technology, Sensory Analysis" team, especially Dipl. Phys. Klaus-Peter Gründer for comprehensive assistance and support connected with shock-absorber measurement using the strip projection method. I want to thank Prof. Dr. Dietmar Klingbell, the leader of the "Operational Stability and Parts Safety" team for his readiness to engage in discussion, especially in conjunction with model design.

I want to thank the Gesellschaft für Nuklear-Systeme mbH [Society for Nuclear Systems] (GNS), represented by Dr. Heinz Geiser, for agreeing to the use of experimental results in the context of shock-absorber testing. I want to thank Mitsubishi Heavy Industries (MHI) for agreeing to use drop test results based on the MSF69BG testing pattern.

I want to thank Dipl. Ing. Sebastian Festag for his constant readiness to discuss questions relating to safety engineering with me.

Particularly heartfelt thanks go to my wife Anett and my entire Neumann/Lehmann/John/Klaus family, all of whom contributed to the success of this endeavor in their own way.

Abstract

Transport casks for radioactive materials with a Type-B package certificate have to ensure even under severe accident scenarios the radioactive content remains safely enclosed, in an undercritical arrangement and that ionising radiation is sufficiently shielded. The impact limiter absorbs in an accident scenario the major part of the impact energy and reduces the maximum force applied on the cask body. Therefore the simulation of the behavior of impact limiting devices of transport casks for nuclear material is of great interest for the design assessment in the package approval as well as for risk analysis in the field of transport of radioactive materials The behaviour of the impact limiter is influenced by a number of parameters like impact limiter construction, material properties and loading conditions. Uncertainties exist for the application of simplified numerical tools for calculations of impact limiting devices.

Uncertainties exist when applying simplified numerical tools. A model describing the compression of wood in axial direction of wood under large deformations for simulation with complex numerical procedures like dynamic Finite Element Methods has not been developed yet. Therefore this thesis concentrates on deriving a physical model for the behaviour of wood and analysing the applicability of different modeling techniques.

A model describing the compression of wood in axial direction under large deformations was developed on the basis of an analysis of impact limiter of prototypes of casks for radioactive materials after a 9-m-drop-test and impact tests with wooden specimens. The model describes the softening, which wood under large deformation exhibits, as a function of the lateral strain constraint. The larger the lateral strain restriction, the more energy wood can absorb. The energy absorbtion capacity of impact limiter depends therefore on the ability of the outer steel sheet structure to prevent wood from evading the main absorption zone. This consistutes a model for the compression of impact limiters.

In order to absorb significant energy, wood must be stabalized by stiff cask or impact-limiter structures. An elastic recovery has to be added to after the drop test measure deformations. The Projected Fringe Method for the 3-dimensional surface digitalisation was applied successfully for the first time. The method allows us to determine and chart the surface of the impact limiter in advance and after the test. Therefore, it is suitable for a damage and deformation documentation of impact limiting devices subjected to a drop test.

A simplified numerical tool for the calculation of rigid body decelerations and impact limiter deformations was developed. This tool can be applied puposefully in the design assessment of transport casks for radioactive materials under certain limitations. For a risk anaysis different accident scenarios, for instance, the impact in on real targets can be evaluated and compared to the regulatory impact in a simple and cost-efficient way.

A full scale model of the CONSTOR V/TC was subjected to a 9-m-drop-test. The rigid-body-deceleration as an evaluation scheme, which is widely used up to now is not suited for an assessment of the loading of the package under accident conditions for casks like the CONSTOR V/TC with large, relative to each other movable masses. The cask can not be treated as a rigid body.

A substitute model on the basis of conclusions from impact limiter analysis and wooden specimen impact tests was developed for the axial compression of wood. The substitute model takes the lateral strain constraint as triaxiality of the stress field into account. The applicability of different material formualtions for the substitute model as well as further modeling techniques were analysed. Of the proposed combinations, none could simulate the behaviou of wood under large deformations in an acceptable manner.

Different modeling strategies for impact limiter of radioactive materials transport packages analysed and evaluated. The Finte Element Method can be applied purposefully in type assessment and risk analysis. Prerequisite is an extensive verification with experimental methods, where the boundary conditions of the simulation have to be adjusted to the conditions in the impact limiter concerning lateral strain restriction.

Table of Contents

List of Illustrations

List of Tables

List of Symbols

List of Illustrations

List of Tables

List of Symbols

Latin Script

A	Surface	m^2
a	Acceleration	$m \cdot s^{-2}$
a_j	Eigenvectors	m
A_O	Surface	m^2
B	Continuum, body	-
b	Width	m
C_{ijkl}	Material tensor/elasticity tensor	$N \cdot mm^{-2}$
D	Effective dose	mSv
d	Diameter	m
D_i	Moment of momentum	$kg \cdot m^2 \cdot s^{-1}$
d_{kj}	Deformation velocity tensor	s^{-1}
e^{ij}	Distortion deviator	-
E_{pl}	Plastic tangent module	$N \cdot mm^{-2}$
F	Force	N
f	Stability, strength	$N \cdot mm^{-2}$
f	Filter frequency	Hz, s^{-1}
f_i	Volume-related force	$N \cdot m^{-3}$
f_{SD}	Depth of shock absorber force	m
t_i	Surface-related force	$N \cdot m^{-2}$
H	Isotropic stabilization curve	$N \cdot mm^{-2}$
h	Height	m
H_{ij}	Anisotropic stabilization curve	$N \cdot mm^{-2}$
I	Impulse	$kg \cdot m \cdot s^{-1}$
I_1	1st invariant of the stress tensor	$N \cdot mm^{-2}$
I_2	2nd invariant of the stress tensor	$N^2 \cdot mm^{-4}$
I_3	3rd invariant of the stress tensor	$N^4 \cdot mm^{-6}$
J_1	1st invariant of the stress deviator	$N \cdot mm^{-2}$
J_2	2nd invariant of the stress deviator	$N^2 \cdot mm^{-4}$
J_3	3rd invariant of the stress deviator	$N^4 \cdot mm^{-6}$
k	Proportionality constant	
M	Torque	Nm
m	Mass	kg
$n(x)$	Random sampling scope	-
H	Plastic potential	$N \cdot mm^{-2}$
Q_i	Heat flow	$J \cdot s^{-1}$
q_i	Temperature gradient	$K \cdot m^{-1}$
r	Radius	m
S	Specific entropy	$J \cdot kg^{-1} \cdot K^{-1}$
s	Path	m
s^{ij}	Stress deviator	$N \cdot mm^{-2}$
S_d	Dynamic factor	-
s_u	Variability quantity	-

s_{ij}	Poisson constants	-
Δt	Time difference	s
T	Temperature	K, ºC
t	Time	s
T_{ki}	PIOLA KIRCHOFF'S stress tensor	$N \cdot mm^{-2}$
Δu	Virtual displacement	m
U	Internal energy	J
u	Moisture content	%
u	Displacement	m
V	Volume	m^3
v	Velocity	$m \cdot s^{-1}$
$v(x, y)$	Deformation at point x, y	m
W	Work	Nm, J
x	Coordinate, path	m
Y	Isotropic floor boundary	$N \cdot mm^{-2}$
y	Coordinate, path	m
Y_{ij}	Anisotropic flow boundary	$N \cdot mm^{-2}$
z	Coordinate, path	m

Greek Script

α	Slap Down angle	º
β	Angle of shock-absorber edge	º
δ	Deformation	m
δ_{ij}	KRONECKER symbol	-
$\sigma_{dB\parallel}$	Crush strength parallel to fiber direction	$N \cdot mm^{-2}$
$\sigma_{dB\mid}$	Crush strength orthogonal to fiber direction	$N \cdot mm^{-2}$
ε	Expansion	-
ε^{D}_{ij}	Distortion ball tensor	-
ε_m	Mean expansion	-
ε_{ijk}	LEVI-CEVITA permutation tensor	-
ε_{ij}	Distortion tensor	-
∇	Nabla operator	-
v	Poisson's ratio	-
ω	Angular velocity, circle frequency	s^{-1}
Φ	Specific free energy	$J \cdot kg^{-1}$
φ	Load-fiber angle	º
ρ	Density	$kg \cdot m^{-3}$
$\overline{\sigma}$	Stress function of shock absorber	$N \cdot mm^{-2}$
$\overset{0}{\sigma ij}$	Stress ball tensor	$N \cdot mm^{-2}$
σ_λ	Eigenvalues, Main stresses	$N \cdot mm^{-2}$
σ_m	Mean stress	$N \cdot mm^{-2}$
σ_v	von MISES comparison stress	$N \cdot mm^{-2}$
$\sigma_{50/50}$	Stress at 50% axial and 50% radial load	$N \cdot mm^{-2}$
σ_{ij}	Stress tensor	$N \cdot mm^{-2}$

Θ	Absolute temperature	K

Indices

0	Initial value
a	Axial direction
c	Pressure (compression)
d	Dynamic
dtr	Oven-dried wood
e	Element related
el	Elastic
I	Index
j	Index
max	Maximum value
min	Minimum value
pl	Plastic
r	Radial direction
s	Static
SD	Shock absorber
t	Tangential direction
t	Traction (tension)
u	Moist wood

1 Introduction and Objective

Transport of radioactive substances in various forms are required in the context of the nuclear fuel cycle for the purpose of generating power in nuclear power plants. Attention is focused here not only on the transport of uranium hexafluoride (UF6) due to the high radioactivity potential and the high heat output, but also on the transport of spent fuel elements and highly radioactive waste from reprocessing.

Fuel elements and waste transport casks, equipped with screwed or welded locking systems, are provided with shock-absorbing parts. In case of a possible accident, the shock-absorbing parts reduce the mechanical stress on the other transport cask components in that a large part of the kinetic energy is absorbed by the shock absorber, which, compared to the cask and the impact body, is more "resilient." In Germany, these shock-absorbing parts frequently consist of internal steel structures upon which large-volume steel plate capsules are attached. The cavities are filled with wood of various types and fiber orientations.

In the process of licensing the transport cask for radioactive substances, we perform a design test that is done by an appropriate authority for the purpose of testing the evidence as to the type enclosure of the radioactive content, the subcriticality, the screening and the safe heat evacuation. A big challenge here is represented by providing evidence of mechanical resistance against serious accident events, which mostly defines the marginal conditions for all of the abovementioned specific test data.

Risk analyses are performed with the objective of determining the magnitude of threats that could spring from a technical system in connection with the evaluation of threats arising during the transport of radioactive substances. The real task behavior is considered only to a minor extent due to uncertainties tied to the determination of stress and stressability.

Determining the risk connected with the transport of radioactive substances is a very complex and voluminous process. This is why this study deals with risk reduction connected with the transport of radioactive substances, the shock-absorbing parts that have a stress-reducing effect on the tightness of the enclosure. Figure 1.1 shows an excerpt from the safety engineering action chain in mechanical accident situations during the transport of radioactive substances as well as the abstraction of this accident situation during design testing. In this study, we will focus on the safety behavior of the transport cask and here again exclusively on the behavior of the shock-absorbing parts. This study does not describe the behavior, for example, of the cask body or the sealing system.

So far, no physical model has been created for the purpose of describing compression behavior of axially stressed wood in conjunction with large deformations. No comprehensive numerical simulation of the shipping item behavior has been done because there has been no model for the behavior of the wood so far.

The objective of this study therefore is to derive a model for the behavior of wood-filled shock-absorbing parts. In conjunction with design testing and risk studies, we want to derive and evaluate the possibilities of modeling shock-absorbing parts using mathematical methods.

1 Introduction and Objective

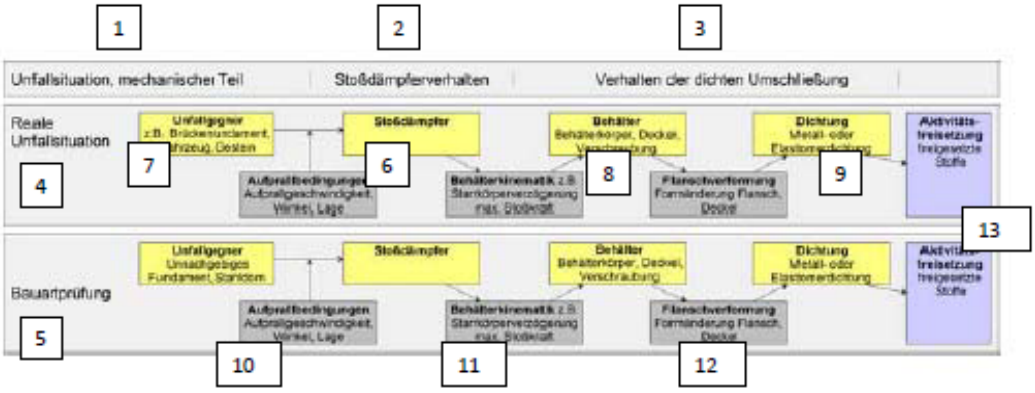

Figure 1.1: Illustration of the Safety Engineering Action Chain Connected with the Release of Radioactive Substances

[Key: 1) Accident situation, mechanical part; 2) Shock-absorber behavior; 3) Behavior of sealed enclosure; 4) Real accident situation; 5) Design testing; 6) Accident target, for example, bridge pillar, vehicle, [illegible]; 7) Shock absorber; 8) Cask [illegible] lid, contamination; 9) Seal, metal or elastomer seal; 10) Accident object, nonresilient [illegible]; 11) Shock absorber; 12) [Illegible]; 13) Seal, metal or [illegible] seal].

For this purpose, we first of all want to engage in some basic considerations in regard to the exact place of this study in the group of topics constituting the design testing of transport casks for radioactive substances and risk analysis connected with transports in these casks. We describe the motivation for a more in-depth approach to the energy absorption mechanisms taking place in the shock absorber and their modeling with the help of numerical methods. Then we present the shock-absorbing parts of transport casks. For wood used as main energy absorption material, we perform a bibliography study regarding the parameters that influence the energy absorption.

Experimental investigations will be described in the next chapter. The behavior of shock-absorbing parts is analyzed with cask drop tests. On the basis of these analysis results and the bibliography search, we will perform experimental investigations on the behavior of wood in response to large deformations resulting from pressure stresses in conjunction with the variation of the parameters called multiaxiality and stress velocity. With the help of these results, we derive a physical model for the compression behavior of axially stressed wood in response to large deformations.

The results of the experiments with wood samples and the results from the cask drop tests will be used as verification base for the subsequently described mathematical investigations. First, we will present the development of a separate simplified numerical method for estimating the impact delay and the shock-absorber deformation, and this will be verified with the help of experimental results and conclusions will be drawn. Then the shock tests on wood and a drop test of a cask substitute mass with shock-absorbing parts are simulated and evaluated with the Finite Elements Method (FEM). The results are compiled, discussed, and further prospects are outlined.

The results of this work are intended to bring about a better understanding and a better modeling of the behavior of shock-absorbing parts. In that way, this study can serve as a foundation for the optimization of designs of shock-absorbing structural parts as well as for improved determination of risks connected with the transport of radioactive substances.

2 Fundamental Considerations

In this chapter, we describe the marginal conditions for this study. To begin with, we underscore the significance of the transport of radioactive substances in the nuclear fuel cycle in order to emphasize the substantial significance of transports when it comes to the operation of nuclear power plants (KKW). For this purpose, we will describe the transports necessary in conjunction with nuclear power plant supply and waste disposal. Design testing, as part of the licensing procedure for transport casks, follows. Risk analysis is described as a method for determining the magnitude of risks connected with the transport of radioactive substances. When it comes to design testing and risk analysis, we developed the reason for an in-depth analysis of the mechanisms involved in energy absorption and for an investigation of the possibilities of modeling connected with the simulation of shock-absorbing parts.

2.1 Nuclear Fuel Cycle

Since the start of its use for civilian purposes in 1954[1], nuclear energy has developed into an important part of worldwide power supply. Since then, the net output has been increasing continually. In 1965, the worldwide net output came to about 5 gigawatts, and ten years later, it already was 75 gigawatts, while in the middle of the Eighties, it had climbed to 250 gigawatts. Today, 444 nuclear power plants with a total net output of about 375 gigawatts are operated in 31 countries; they supply about 16% of the worldwide power requirements [SVA08]. Figure 2.1 shows the worldwide distribution of the number of these blocks. The largest operator of nuclear power plants is the USA with about 100 gigawatts, followed by France with about 63 gigawatts and Japan with about 48 gigawatts.

Figure 2.1: Worldwide Distribution of Nuclear Power Plants According to [SVA07]

The last nuclear power plant was built in Germany in 1989, and according to current legislation, the last reactor (Neckarwestheim II) is to be shut down in 2021; nevertheless, the

[1] The first nuclear power plant with a thermal output of about 30 MW went into operation in Obninsk, Soviet Union, in 1954 according to KOTCHETKOV [Kot04].

peaceful use of nuclear energy will also continue to be extremely important in the future. Currently, 34 nuclear power plants are under construction in 14 countries with a total output of about 28 gigawatts and 83 nuclear power plants are in the planning phase with a total output of 92 gigawatts [SVA08].

Regardless of the fact that Germany dropped out of the nuclear energy field, there is a continuing need for addressing the subject of nuclear engineering safety. Germany directly adjoins five countries that have nuclear power plants (The Netherlands, Belgium, France, Switzerland and Czechia), and it is also located in the area of operations of another 11 countries (Great Britain, Spain, Slovenia, Sweden, Lithuania, Slovakia, Hungary, Romania, Bulgaria, Russia and the Ukraine). Some of these countries are today operating reactors whose safety systems are not up to the current state of the art in Germany.

The most widely used reactor types are the boiling water reactor and the pressurized water reactor. In both cases, energy generation is based on the fission of atomic nuclei by neutrons. When a neutron with a certain energy impacts a fissile atomic nucleus, then the latter can break up into two or more smaller parts, releasing energy. In the process, additional neutrons are released from the atomic nucleus, and they can trigger more fission. If this process is self-perpetuating, then it is called a chain reactor. Other reactor types are the fast breeder reactor and the thorium high-temperature reactor[2]. Nuclear fuel primarily consists of the uranium isotope U-235, which is present to the extent of about 0.7% in the worldwide uranium deposits. As for the remaining uranium isotopes, uranium U-238 is present to the extent of 99.3% and uranium U-234 is present only in traces. Among the natural uranium isotopes, only uranium U-235 can generate a self-perpetuating chain reaction in the reactor. Uranium is a slightly radioactive heavy metal that is found almost everywhere in the world. The biggest uranium mining countries are Canada, Australia, Namibia, Niger and South Africa. The deposits offer different concentrations of uranium in the rock. One can find up to 150 t of uranium per 1,000 t of stone (uranium ore). A high concentration of uranium was also found in the former bismuth mine of the German Democratic Republic that at its peak supplied 75 to 80% of the Soviet uranium consumption according to GEIPEL [Gei99], today still holding third place worldwide with respect to the total quantity extracted nowadays (total extraction volume 220,000 t of uranium). MURRAY [Mur03] offers a comprehensive overview of the many aspects connected with the use of nuclear energy.

2.1.1 Uranium Dressing

According to VOLKMER [Vol03], the uranium contained in uranium ore is separated from other substances by physical and chemical methods. For this purpose, the ore is ground up and is dissolved with acid or lye. Using an oxidation agent (for example, Na_2ClO_4 or MnO_2), the uranium is converted from the quadrivalent, poorly soluble form into the hexavalent form (uranyl sulfate).

$$2UO_2 + 2H_2SO_4 + O_2 \longrightarrow 2UO_2(SO_4) + 2H_2O \qquad (2.1)$$

[2] Both reactor types are based on the fact that nonfissile radioactive substances (as in this case uranium 238 and thorium 232) are converted into fissile substances (in this case, plutonium 239 and uranium 233).

Ammonium diuranate ($(NH_4)_2U_2O_7$), also called "yellow cake," with a technical purity of about 70-80%, is separated from the liquid uranyl sulfate, adding MnO, NaOH or NH_3. To get a purer uranium that is more enriched with uranium U-235, "yellow cake" is converted into the gaseous compound uranium hexafluoride (UF_6), which is then filtered and which is enriched to a U-235 portion of about 3-4% via the diffusion, thermal diffusion nozzle, or centrifugation method. The transformation of uranium hexafluoride is called conversion. Uranium hexafluoride is converted into ammonium uranyl carbonate to make the basic fuel element substance uranium dioxide.

$$UF_6 + 2H_2O \longrightarrow UO_2F_2 + 4HF \tag{2.2}$$

$$UO_2F_2 + 6NH_3 + 3CO_2 + 3H_2O \longrightarrow (NH_4)_4[UO_2(CO_3)_3] + 2NH_4F \tag{2.3}$$

The yellow ammonium uranyl carbonate can be separated and can be broken down by heat supply into its component parts, that is, ammonium, carbon dioxide, hydrogen fluoride and uranium trioxide (UO_3). Uranium trioxide is reduced in a hydrogen atmosphere at high temperatures to uranium dioxide (UO_2), which is the actual nuclear fuel. Uranium dioxide (a gray powder) can be pressed and sintered to form UO_2 pellets and can be charged into tubes consisting of Zirkaloy[3]. These tubes are lined up to form a fuel element.

2.1.2 Operation and Waste Disposal

During the fuel element's dwell time in the reactor amounting to a few years, the share of uranium U-235 in the fuel element drops to less than 1% again, assuming an average specific energy conversion of 45 MWd/kg of uranium[4]. In the fuel rod, there is an accumulation along with plutonium Pu-239 that is formed from uranium U-238 by neutron capture also of the fission products of uranium U-235 and plutonium Pu-239 as well as residual quantities of uranium U-236, neptunium, americium and curium.

$$U_{92}^{238} + n_0^1 + 2e_{-1}^0 \longrightarrow Pu_{94}^{239} \tag{2.4}$$

After an average dwell time of 3-5 years, the fuel elements are taken out of the reactor and are put up for intermediate storage in the fading tank. The dwell time in the fading tank is determined by the burnup[5] of the fuel elements. There are two possibilities for further treatment of the spent fuel elements after brief intermediate storage in the fading tank. The spent fuel elements are transloaded into containers and are put up for intermediate storage in many countries[6]. The final storage of these fuel elements is planned but does not take place as yet due

---

[3] An alloy consisting of zirconium and small quantities of tin, iron, nickel and chrome.

[4] 1 MWd = 1 megawatt day $\hat{=}$ 24,000 kWh.

[5] The term "burnup" is used to refer to the decline of the portion of uranium 235 and the enrichment with radioactive fission products.

[6] For example, USA, Sweden, Finland, Germany.

to the fact that the final storage facilities are not yet present. Transports of spent fuel elements for reprocessing have been outlawed in Germany since July 1, 2005 [AtG08]; in the Federal Republic of Germany, all fuel elements in transport casks (TB) for spent fuel elements are currently stored in intermediate storage facilities near the power plant site [BFS03]. In the future, they are to be transported to a packaging plant and then to a suitable final waste dump, they are to be transloaded into final dump casks and are to be stored there.

The fissile material remaining in the fuel elements can continue to be used for economic purposes by reprocessing. This strategy was adopted, for example, by Great Britain, France, Switzerland and Japan. For this purpose, the fission products have to be removed and the portion of uranium U-235 has to be enriched again. The fuel elements are packed in transport casks (TB) and are shipped to one of the reprocessing plants[7]. Here, the fuel elements are first of all sawed in order then to be broken down into boiling nitric acid (HNO_3) into their components uranium, plutonium and fission products. This process is referred to as the PUREX[8] process.

$$2UO_2 + 6HNO_3 \longrightarrow 2UO_2(NO_3)_2 + NO_2 + NO + 3H_2O \tag{2.5}$$

Adding extraction agent tri-n-butyl phosphate ($(C_4H_9O)_3PO$, TBP30), we get uranyl nitrate ($UO_2(NO_3)_2$), plutonium-IV-nitrate ($Pu(NO_3)_4$) and nitrates of the fission products. For the case of uranium, the process is given in equation 2.5. The uranium is again converted into uranium dioxide (UO_2) and, together with the plutonium dioxide (PuO_2), it is processed into mixed-oxide fuel elements (MOX).

The remaining highly radioactive waste (HAW[9]) must be treated and must be prepared for intermediate and final storage[10]. The packaging is done during a fading phase in cooled high-grade steel tanks lasting about 5 years. Waste with negligible heat generation is packaged in metal, bitumen or concrete casings. Highly heat-generating waste is mixed with liquid gas and is poured into chills [ingot molds][11]. Glass is used because it best meets the requirements for immobilization and final storage of radioactive residual substances (good mechanical strength, high resistance to leaching, good heat stability and heat conductivity and high resistance to ionizing radiation) according to VOLKMER [Vol03].

2.1.3 Transport

The transport of radioactive substances is of fundamental significance in terms of the supply and waste disposal of nuclear power plants. Different types of radioactive substances with varying radioactivity must be transported in conjunction with the operation of nuclear power plants. Basically, we differentiate between the supply and the waste disposal of nuclear power plants. Supply can be subdivided into the following areas:

---

[7] La Hague in France or Sellafield in Great Britain.
[8] Plutonium-Uranium-Recovery by Extraction.
[9] High-Active-Waste.
[10] Also called conditioning.
[11] For example, high-grade steel flasks with about 400 kg each of vitrified waste.

- transport of uranium or for uranium ore dressing;
- transport of the uranium concentrate "yellow" cake to the conversion plant;
- transport of uranium hexafluoride (UF_6) for fuel element production;
- transport of the fresh fuel elements to the nuclear power plants;
- transport of the recovery of uranium to the conversion plant.

Uranium ore is shipped for uranium ore dressing usually in open trucks because the uranium ore dressing plants usually are located in the direct vicinity of the deposit. The "yellow cake" uranium ore concentrate is shipped in commercially available steel casks with a capacity of 200 l to the conversion plant. After conversion into uranium hexafluoride (UF_6), the UF_6, which is solid under standard conditions, must be shipped in special UF_6 pressure casks due to the low sublimation temperature of only 56º. After production, the "fresh" fuel elements are packaged in fuel element transport casks and are shipped to the nuclear power plant. Ensuring adequate radiation screening is no problem due to the low specific radioactivity of the uranium, although subcritical arrangement of the fuel elements must be guaranteed.

Transport involved in waste disposal for nuclear power plants or reprocessing plants can be subdivided as follows:

- transport of the spent fuel elements for intermediate storage or to the reprocessing plant;
- transport of the fuel elements from the intermediate storage facility to the packaging plant;
- transport of highly radioactive waste for intermediate storage;
- transport of highly radioactive waste/fuel elements from the intermediate storage facility or the packaging plant to the final waste dump.

Spent fuel elements or the highly radioactive waste from the reprocessing plants have very high radioactivity due to the fission products and thus involve a very high heat output. Due to this high radioactivity, transport casks for spent fuel elements and HAW casks must also guarantee a tightly sealed enclosure and screening of the radioactive content in serious accident scenarios.

2.2 Design Testing of Transport Casks for Radioactive Substances

Design testing is the basis of the procedure for licensing transport casks for radioactive substances. In this connection, we test data that must ensure that the casks are suitable for attaining the defined protection targets. Typical cask designs, testing conditions and data acquisition concepts are described following an overview of the fundamental regulatory provisions.

Fuel elements and HAW transport and intermediate storage casks, along with packages for infectious substances, are the only hazardous goods packages by means of which one can basically make the substances "accident proof." This means that even in case of serious accident scenarios, it must be sufficiently probable to maintain the protection targets. Here are the protection targets that dominate the basic principles of cask design:

- preventing release of radioactivity;
- ensuring subcriticality;
- ensuring shielding.

The currently applicable regulatory provisions to attain these protection targets as well as the concepts used are presented in the following chapters.

2.2.1 Explanation of Concepts

The following explanation of concepts are taken from ADR [ADR07] and are to be used in the field of radioactive substance transport.

A **shipping item** is the package with radioactive content, such as it is ready for transportation.

Packaging consists of all of the parts necessary for the complete enclosure of the radioactive content.

Content is made up of the radioactive substances with all of the contaminated or activated solid substances, liquid substances or gases within the package.

2.2.2 Regulatory Documents

The guidelines, laws and decrees described here regulate the requirements for the shipping items as a function of the radioactive content. According to [TSR08], we distinguish among the following:

- released shipping items;
- industrial shipping items (IP-1, IP-2 and IP-3);
- Type A shipping items;
- Type B shipping items;
- Type C shipping items.

Released shipping items are packages that contain only very small quantities of radioactive substances. Certain requirements apply, so, for example, when they are open, it must be possible to recognize which substances is contained therein.

Industrial shipping items contain radioactive substances with low radioactivity - LSA (Low Specific Activity) or SCO (Surface Contaminated Object). There are additional requirements, such as marking on the surface or recording in the shipping papers.

Type A shipping items should remain undamaged also during possible "routine" incidents in the course of transportation. That includes, for example, falling down from certain heights, being subjected to action of spray water, and stacking of packages.

Type B packages are used to transport radioactive material with a great damaging potential, such as, for example, spent fuel elements or highly radioactive waste from reprocessing. The high degree of damage potential resulting from the content in the case of Type B shipping items results in the requirement for making the packages basically "accident proof." The protection targets of the package must be met even in the most serious accident scenarios that might be assumed. These requirements apply according to ADR [ADR07], along with the Type B shipping items, also to shipping items with contents of Hazardous Goods Class 6.2 (infectious substances).

Requirements for Type C shipping items are even higher because, in contrast to the Type B shipping items, they are licensed for air shipment. The detailed illustration of the model assumptions and the hazard potential of the content of a package derived therefrom is described in the "Q System" of the International Atomic Energy Agency (IAEA) [TSR08].

The requirements for the licensing of transport casks for radioactive substances are based on the recommendations of the IAEA. The basic requirements for radioactive protection are spelled out in the following:

- International Basic Safety Standards for Protection Against Ionizing Radiation and for the Safety of Radiation Sources [IAE03]

These requirements are translated into conditions that must be complied with during shipment by the following:

- "Regulations for the Safe Transport of Radioactive Materials" (TS-R-1) [TSR08], whose application is supported by:

- "Advisory Material for the IAEA Regulations for the Safe Transport of Radioactive Material" (TS-G-1.1) (TSG08a).

Further light is cast on additional aspects in:

- Compliance Assurance for the Safe Transport of Radioactive Material [IAE94a];

- Quality Assurance for the Safe Transport of Radioactive Material [IAE94b];

- Radiation Protection and the Safety of Radiation Sources [IAE96];

- Planning and Preparing for Emergency Response to Transport Accidents Involving Radioactive Material (TS-G-1.2) [TSG08b].

The IAEA Standards represent recommendations without any legal obligation for the national states and in the UN Model Regulations are converted into instructions specifically designed for the particular carriers:

- ADR - European Agreement on the International Transport of Hazardous Goods by Road [ADR07];

- RID - Order on the International Railroad Transport of Hazardous Goods [RID06];

- I - European Agreement on the Transport of Hazardous Goods on Inland Waterways in Conjunction with ADNR - Decree on the Transport of Hazardous Goods on the Rhine (and Mosel) [I07] [I06];

- IMDG - International Maritime Dangerous Goods Code [IMD06] in conjunction with INF - International Code for the Safe Carriage of Packaged Irradiation Nuclear Fuel, Plutonium and High-Level Radioactive Wastes On-Board Ships [INF06];

- ICAO-TI - International Civil Aviation Organization - Technical Instructions [ICA07] and IATA-DGR - International Air Transport Association - Dangerous Goods Regulations [IAT08].

For use in Germany, these rules for the conveyance of hazardous goods become obligatory via the legal decrees:

- GGBefG - Law on the Conveyance of Hazardous Goods [GGB06].

for the highway, railway, maritime and inland navigation as well as air traffic carriers, which are subject to:

- GGVSE - Decree on the Domestic and Border-Crossing Transport of Hazardous Goods by Roads and by Rail [GGV06];

- GGVSee - Decree on the Transport of Hazardous Goods Via Naval Vessels [GGV07a];

- GGVBinSch - Decree on the Transport of Hazardous Goods on Inland Waterways [GGV07b];

- Air Transport Licensing Order [LVZ08].

These decrees spell out the authority for implementation of the responsibility areas contained in the rules. When radioactive substances above a defined hazard degree A_2[12] are transported, then specially licensed packaging must be used for this purpose. This licensing is done by the Federal Bureau for Radiation Protection (BfS) on the basis of information supplied by the Federal Institute for Materials Research and Testing (BAM). The division of labor between these two institutions as well as the procedure involved in the filing and processing of applications are defined on the basis of GGBefG §3, Paragraph 1 [GGB06] and the decrees [GGV06], [GGV07a], [GGV07b], [LVZ08] issued by the Federal Ministry of Transportation, Construction and Urban Development (BMVBS) in the following guideline:

- R003 - Guideline for the Process in Design Licensing of Shipping Items for the Transportation of Radioactive Substances, of Radioactive Substances in Special Form, or Slightly Dispergatable Radioactive Substances [BMV04].

The mentioned laws, decrees and guidelines constitute the body of regulatory documents applicable to the safe transport of radioactive substances on all permanent transportation routes. A clear survey can be found in [BAM08].

2.2.3 Testing Conditions

A distinction is made between the following transportation conditions in the described regulatory work regarding the definition of the stresses that the package must withstand. The transportation conditions include the proper and expert handling for both serious and routine accident scenarios:

- routine transportation conditions (no incidents);
- normal transportation conditions (minor incidents);
- transportation accident conditions (accidents).

Uneventful shipment is considered to take place under routine transportation conditions. The cask components are stressed only, for example, by bumps resulting from rough spots on the road surface or planned handling, such as, for example, during transloading. Normal transportation conditions include minor incidents, such as, for example, rough deposit during transloading. Transportation accident conditions are treated by a serious transportation accident. This covers combinations of different stresses such as impact and fire.

[TSR08] prescribes consecutive processing of the following tests:

1. mechanical tests;
2. thermal tests;

[12] A_2 is the radioactivity boundary value derived in [TSR08] for all radioactive substances or contained in tables. The maximum quantities of radioactive substances to be transported are given as a multiple of A_2.

3. water immersion test.

The data supporting the accident safety of transport casks holding radioactive substances comprise the following tests, specifically [TSR08]:

1. Mechanical tests

    a) 9-m drop on an nonresilient foundation;

    b) 1-m spike drop;

    c) crush test for light and specifically light packages.

2. Thermal tests

    a) enveloping fire at 800ºC for 30 minutes.

3. Water immersion test

    a) a water depth of 15 m for at least 8 hours;

    b) with more than 10^5 A_2 content, a water depth of 200 m for at least 1 hour.

In addition to the mentioned tests, the package must undergo further testing under routine and normal transport conditions. In this study, we will not consider tests under routine and normal transport conditions because tests under accident transport conditions for the most part have coincident characteristics in terms of the mechanical stresses of the shipping items.

The sequence of mechanical tests must be so chosen that *"upon completion of the mechanical test, the test object will have suffered such damage that the maximum possible damage will occur during the next following heating test."* For example, depending on the construction principle in one case, a 9-m drop with subsequent 1-m spike drop can be most damaging, whereas in another case, the 1-m spike drop before the 9-m drop will cause the greatest damage. From the area of mechanical testing, we will in this study only consider the 9-m drop upon the unyielding foundation because the shock-absorbing parts above all are responsible for protecting the shipping item in case of 9-m drops.

There is no special protection philosophy for the package against terrorist attacks.

So far, we have pointed out only the requirements that must be established for transport casks holding radioactive substances in terms of design testing. Now we will describe the typical constructions that meet these requirements.

2.2.4 Principles of Construction

Many different container models are used worldwide. This study deals with the container designs for spent fuel elements and highly radioactive wastes such as they are mainly used in Germany at this time and in the foreseeable future. These designs generally, as shown in Figure 2.2, consist of the cask body, the lid, the shock-absorbing parts, the impact devices and the shielding devices against α-β-γ and neutron radiation.

The cask body, as a rule, consists of forged steel or ductile cast iron and, depending on the shielding and mechanical requirements, has wall thicknesses of between 250 mm and 450 mm. Other components of the shipping item are attached to the cask body with the help of screwing elements. To ensure the tightly sealed enclosure of the contents and at the same time the loadability and unloadability, the frequently monolithically executed cask bodies are closed with a lid sealing system. The lid system on casks made in Germany usually consist of two mutually independent lids, each of which can separately ensure the enclosure of the contents. The metal sealing rings or also

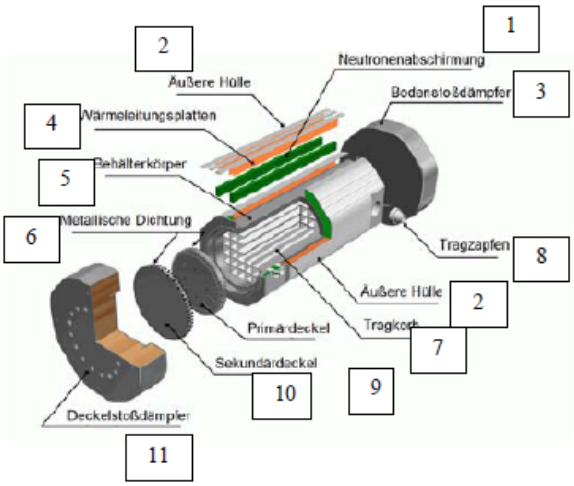

Figure 2.2: Profile Through an MHI (Mitsubishi Heavy Industries) Transport Cask

[Key: 1) Neutron shielding; 2) Outer shell; 3) Bottom shock absorber; 4) Heat conduction plates; 5) Cask body; 6) Metallic seal; 7) Carrying peg; 8) Carrying basket; 9) Primary lid; 10) Secondary lid; 11) Lid shock absorber].

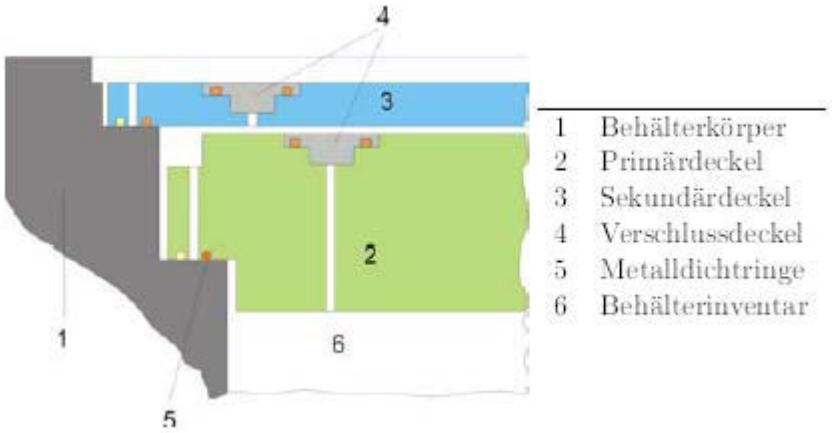

Figure 2.3: Simplified Lid System

[Key: 1) Cask body; 2) Primary lid; 3) Secondary lid; 4) Closing lid; 5) Metal sealing ring; 6) Cask inventory].

Figure 2.4: Metal Sealing Ring, Type Helicoflex® HN200, with Internal and External Sheathing Cut Open

the elastomer sealing rings are used as a seal shown in Figure 2.4. The sealing rings are in a groove between the cask body and the lid. Figure 2.3 shows the lid system variant developed in Germany with the primary and secondary lids for long-term intermediate storage in transport and storage casks holding radioactive substances. Uniform pressing of the seal is ensured by a large number of screwing elements and the stiff construction of the cask flange and the lid. [13]Carrying pegs are attached to the cask body so that the container can be handled. The *α-, β- and γ-* radiation of the contents as well as the effects of fires are adequately shielded by the cask body material (forged steel or ductile cast iron). The neutron radiation is shielded by hydrogen-containing moderator materials. UHMW polyethylenes or resins are usually employed. A carrying basket is provided inside the cask to hold the radioactive content. The carrying bask ensures subcritical arrangement of the radioactive inventory.

Figure 2.5: Round, Wood-Filled Shock Absorbers on the GNS (Gesellschaft für Nuklearsysteme mbH) POLLUX® Cask After 9-m Horizontal Drop

[13] Ultra High Molecular Weight.

Figure 2.6: Filling of Shock Absorbers Attached to the Cask Ends (left: MHi shock absorber, right: GNS CONSTOR® shock absorber)

Shock-absorbing parts are usually attached in order to reduce the stresses on the cask components in connection with various accident scenarios. Many different constructions have been used in the past. In the case of currently used cask designs, the wood-filled shock absorbers (Figure 2.5) attached to the cask bottom and lid are most widely employed. Other designs, for example, are aluminum rings positioned around the cask (usually referred to as jacket shock absorbers). This study concentrates on the wood shock absorbers attached to the cask ends because they are most widely used in Germany. These shock-absorbing parts consist of steel plate constructions whose cavities are filled with woods of various types and orientations (Figure 2.6). In case of a shock, the shock-absorbing parts reduce the stresses on the components of the tightly sealed enclosure and of the radioactive content in that the kinetic energy is absorbed by the shock absorber, which is rather resilient when compared to the cask body. The intensity of the shock against the cask body, against the lids, the lid screw elements and the carrying basket with radioactive content are thus significantly reduced to tolerable stresses.

2.2.5 Drop Positions for the 9-m Drop

In this section, we described the requirements for the drop tests that are governed by the provisions of TS-R-1 of IAEA [TSR08], Paragraph 727(a):

> *For the I drop test, the test objects must so fall upon the impact foundation that it will suffer the greatest possible damage and the drop height, measured from the lowest part of the test object all the way to the surface of the impact foundation, must be 9 m.*

The requirements for the impact foundation are given in [TSR08], Paragraph 717:

> *The impact foundation for the drop tests according to Nos. 705, 722, 725(a), 727 and 735 must have a level, horizontal surface that must be so constituted that any increase in its resistance to shifting or deformation during the impact of the test object would not lead to any significantly greater damage to the test object.*

Due to the differing test specimen constructions[14], the drop position, where the test object or the various safety-relevant components suffer the greatest damage, is not clear. Necessarily, in a different drop position, the cask body is exposed to the greatest stress than, for example, the lid-screwing device. This is why the test object in general is subjected to several drop tests with different drop orientations. Experiences gathered by the BAM over the next year showed that for many test objects, the following drop orientations turn out to be the most damaging[15]:

1. vertical drop (perpendicularly upon the lid/bottom);

2. horizontal drop (upon the jacket line);

3. edge drop on the lid area (center of gravity over the impact spot);

4. slap down with secondary impact on lid side (slightly inclined horizontal drop).

The damaging drop positions are frequently identified with the help of advance calculations using the FEM. Various drop positions must be modeled and the stresses of the components of the tight enclosure must be compared. When it comes to the maximum stress upon the lid and the screw elements, we find that the vertical drop (see Figure 2.7, left) and the edge drop (see Figure 2.8, left) are frequently decisive as a result of the stress coming from the mass force of the content. Regarding the cask body, the greatest stress is often supplied by the horizontal drop (see Figure 2.7, right) and, depending on the geometric conditions, also the slap down drop position (see Figure 2.8, right). The combination of the 9-m drop test with the 1-m spike drop cannot be considered here for reasons of scope.

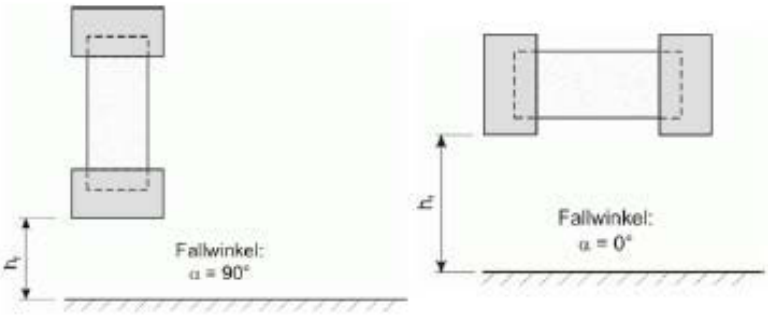

Figure 2.7: Vertical Drop (left) and Horizontal Drop (right)

[Key: Fallwinkel = Drop angle].

[14] Geometry, material, etc.
[15] Listing not complete, depending on model.

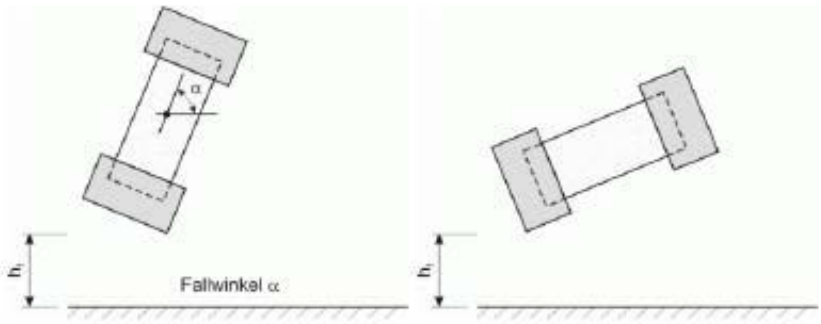

Figure 2.8: Edge Drop (left) and Slap Down (right).

[Key: Fallwinkel = Drop angle].

2.2.6 Data Recording Concepts

At this point, we want to discuss the possible concepts with whose help we can provide data in support of the matter of safety. Providing evidence as to the attainment of the protection targets in various ways is permitted according to the regulatory work. Information on possible data and position methods can be found in [TSR08] in Paragraphs §701 - §702. But *"evidence as to compliance with the design criteria required according to Section VI must be provided by one or several of the methods listed below."*

- *performance of tests with (...) prototypes or serial specimens of the package.*
- *reference to earlier satisfactory and adequately similar evidence.*
- *performance of tests with models of a suitable scale (...) to the extent that technical experience showed that the results of such tests are suitable for design purposes.*
- *calculation or justified consideration when the calculation methods are recognized as generally stressable and conservative.*

In Germany, according to the current status of design testing, evidence is provided with the help of a combination of drop tests and computations. On the one hand, mathematical methods require a verification by comparisons with suitable experimental results due to a plurality of partly not definitely known parameters as well as general modeling uncertainties, among other things in conjunction with the simulation of the shock-absorbing parts. On the other hand, drop tests alone are frequently not enough to document all aspects connected with the evaluation of safety.

Mathematical Evidence

Computations are of fundamental significance in model testing already today. Here, above all, we use analytical and FE methods. A model verification is performed according to the current state of science and technology with the help of experimental results. Dynamic FEM methods are frequently employed because shock-like processes are to be simulated. For this

purpose, the shock-absorbing parts must be modeled in detail. In order to image the shock-like stress using static FEM methods, the maximum rigid body delay of the cask body was determined in the past with the help of simplified numerical methods, such as the precursors of the *"ImpactCalc"* program (Chapter 5). This rigid body delay is transferred with the help of a gravitation field into a static calculation for the components of the tightly sealing enclosure. This form of simulation is referred to as *"quasistatic"* analysis. In that way, the shock-like stress is simulated with the help of a permanently acting gravitation field. With the help of this method, there is no need for any detailed modeling of the shock-absorbing part in the context of FEM. The usefulness of quasistatic analyses for stress determination on the cask body will not be further discussed in the context of this study.

Guideline BAM GGR 008 [GGR03] describes basic requirements for mathematical evidence to be used by operating personnel in conjunction with conservativity, validation and verification, quality assurance and result illustrations.

Mathematical methods for instrumentation planning are used to provide data through drop tests. Application sites for expansion and acceleration sensors as well as the most damaging drop positions are identified by advance calculations. In highly stressed areas, for example, notches, it is impossible to use expansion measurement strips, and on the basis of the results of nearby expansion measurement strips, stresses on the most highly stressed points are determined mathematically. The influence deriving from various parameters on the stress are estimated and marginal conditions can be changed with the help of follow-up computations. For example, the effects of a change in the material properties at higher or lower temperatures (according to IAEA [TSR08], temperatures of -40ºC up to a maximum operating temperature, but at least 70ºC, must be considered) upon the stress on the container can be investigated.

The container stress, which is achieved during experiments, cannot be exactly controlled. Even small changes in the drop position can cause big changes in the mechanical stress upon the test objects. Follow-up computations are used to identify and evaluate minor deviations from the desired marginal conditions of the experiment.

Drop tests with test objects that completely correspond to the design that is to be licensed are often not possible. An example would be ruling out the use of real fuel elements as an inventory in drop tests. The evaluation of the differences between the model that is to be licensed and the test object in general is done mathematically. Worldwide, there are so far only two drop test stands on which drop tests can be performed with currently used large casks in accordance with the IAEA[16], and for cost reasons, drop tests are often performed with models on suitable scales. Evidence as to the transposability of the investigation results should preferably be mathematically provided.

Mathematical computations make an important contribution to evidencing the accident safety of transport containers for radioactive substances together with instrumentation planning, stress determination, parameter studies, transposability considerations and as support for

[16] That includes the drop test stand of the BAM in Horstwalde near Berlin with a maximum cask mass of 200 t, and according to GUSKOV et al. [G+ 01], the drop test stand in Saint Petersburg with a maximum cask mass of 140 t.

experimental investigations. Errors in modeling the stress on the components of the tightly sealed enclosure, which essentially is characterized by the quality of the simulation of the behavior of the shock-absorbing parts, have an effect on all of the computational investigation results. The quality of the computational simulation of the behavior of the shock-absorbing parts under accident stresses therefore is essential for many parts of the safety data record.

2.3 Development of the Safety Data Record Concept in Conjunction with Design Testing

In the following subchapter, we will describe the history of the safety data record concept for transport casks in order to explain the origin of requirements for transport casks holding radioactive substances (9-m drop upon an nonresilient foundation, 1-m spike drop, water immersion test and fire for 30 minutes at 800ºC flame temperature). The subchapter then goes on to the risk analysis, which was used for the first time in 1975 to evaluate a technology. This method was not yet used for the creation of the IAEA regulatory documentation and thus cannot be the basis of any data record concept according to IAEA. POPE [Pop04] published a more extensive description of the history of the safety data record concept in conjunction with design testing.

2.3.1 History

According to POPE [Pop04} when the IAEA was founded in 1957[17], there were no international recommendations and regulations for the safe transport of radioactive substances. The Preparatory Commission of the IAEA (Preparatory Commission of the International Atomic Energy Agency) [UN57] thereupon in 1957 recommended the founding of an advisory panel, which later on was to be converted into a Standing Committee. A resolution of the United Nations Economic and Social Council (ECOSOC) [UN59] recommends the continuation of the "Committee of Experts on the Transport of Dangerous Goods" with the suggestion that the IAEA be charged with formulating and disseminating recommendations regarding the transport of radioactive substances. The foundation of the first publication (IAEA Transport Regulations 1961 [IAE61]), among other things, included the recommendations of the United States Interstate Commerce Commission (USICC), which was charged with drafting and implementing rules for the shipment of hazardous goods by the U.S. Congress.

At that point in time, the rules were very general, above all, the term "maximum credible accident" (assumption for the most serious accident that the package would have to withstand) up to that time was not used in any of the regulations governing the transport of hazardous goods. As MESSENGER & FAIRBAIRN [MF63] 1963 found, it is impossible to build a package that would withstand any and all external actions. *"If there were such a thing, it would no longer be transportable."* In the view of MESSENGER & FAIRBAIRN [MF63}, shock and fire were the most dangerous events, and they recommended the following procedure:

1. *Frontal impact at 30 mph (13.41 m/sec) (or equivalent drop from 30 ft. (9.14 m) high) upon a rigid structure, followed by*

[17] In the form of the "Atoms for Peace" Organization.

2. *a 30-minute enveloping liquid fire of medium flame temperature amounting to $T \geq 800°C$ without cooling and*

3. *immersion in water if the penetration of water were to constitute a hazard.*

The foundations of these recommendations are described in the following subsections and can be found partly more in-depth in POPE [Pop04] or in the mentioned sources.

Mechanical Tests

Using the data available at that time regarding possible drop heights, probabilities and frequencies of crane handling (in particular, during crane handling operations in ports above very hard foundations), of collisions with other vehicles and other accidents (derailings, aircraft crashes, impacts against rigid structures), MESSENGER & FAIRBAIRN [MF63] drafted the recommendations entitled *"9-m Drop Upon the Nonresilient Foundation."* They considered the fact that, for example, heavy transports must maintain speed limits and that a part of the impact energy is absorbed by the deformation of the vehicle or by the impact object. In the case of bridges, for example, drop heights of more than 9 m are possible, although that probability is very minor (MESSENGER & FAIRBAIRN [MF63]). In addition, there must be no shortfall when it comes to currently existing test criteria. The USA required an impact from a height of 15 ft. (4.57 m) upon a nonresilient foundation, whereas Great Britain demanded an impact from a height of 40 ft. (12.2 m) upon a steel plate on 50 cm of concrete. Fireproof safes were subjected to an impact from a height of 30 ft. (9 m) upon consolidated rubber. At that time, an impact from a height of 30 ft. upon a nonresilient foundation was recommended.

APPLETON & SERVANT [AS65] in 1965 stated that a push stress caused by impact upon a protruding object, such as a pole, could be simulated by an impact from a lesser height upon a suitable object. Following upon the discussion of this topic, the regulations were expanded by the addition of the spike test from a height of 1 m (originally 3 ft.). According to [TSG08a] §727.3, drop height and spike geometry are more likely the result of engineering considerations rather than derivations from accident analyses. Impact upon the spike was defined in the regulatory documents of 1964 [IAE64] as *"impact from a height of 3 ft. upon the end of a 6-inch-thick steel spike consisting of unalloyed steel."*

The definition of the nonresilient foundation was derived by FAIRBAIRN & GEORGE [FG66]: *"A concrete block with at least ten times the mass of the part to be tested, covered with a steel plate having a minimum thickness of 1.25 cm with large-surface contact."* The works of DROSTE et al. [D+98], BLYTHE et al. [B+83] and McCLURE et al. [M+80] confirmed that an impact from a height of 9 m upon a nonresilient foundation corresponds to definitely higher impact velocities against real obstacles.

According to CLARKE et al. [C+76], the stress resulting from the 9-m drop of course covers vast ranges of mechanical resistance, but in the case of the packages with ever-smaller deadweight, one can observe a rising probability for a crush stress. The relevance of this stress was described by investigations, among other things, in the BAM, published by WIESER

[Wie82]. The dynamic "crush test" was added for light[18] and specifically light[19] shipping items in the 1985 regulatory work [TSR85]. Further discussions concerning the "crush test" were entertained by McCLURE [McC77], COLTON & ROMANDER [CR80], HÜBNER & MASSLOWSKI [HM83], CHEVALIER et al. [C$^+$83] and DIGGS et al. [D$^+$83].

Thermal Tests

MESSENGER & FAIRBAIRN [MF63] investigated a plurality of factors influencing fires in conjunction with serious accidents. That included the type and volume of the fuel, possible fire temperatures influenced by the wind, etc., and the duration of the fire. Effective mean flame temperatures were estimated on the basis of melting points of various materials and alloys. A hot environment with a temperature of at least 800ºC for a duration of 30 minutes without any artificial cooling was considered as recommendation. According to BADER [Bad63][20], the temperatures in open pool fires amount to as much as 1010ºC; nevertheless, FAIRBAIRN & GEORGE [FG66] proposed a temperature of 800ºC and a duration of 30 minutes because the peak temperatures could be reached only very locally and because serious transport fires rarely lasted more than half an hour. Supported by confirming investigations in the United States conducted by POPE et al. [P$^+$80] and JEFFERSON & McCLURE [JM83], a test with the marginal conditions described in Table 2.1 was introduced.

Table 2.1: Thermal Tests According to [TSR08]

Enveloping Fire at		
Flame temperature (average)	800ºC	
Duration of tests		30 min
Minimum radiation coefficient of fire	0.9	
Surface absorption coefficient	0.8	

Water Immersion Test

Initially, according to [IAE64], the water immersion test consisted of immersion in 3 ft. (0.914 m) of deep water for a duration of 24 hours. The shallow immersion depth resulted from the realization that water penetration is prevented by the tightly sealed enclosure and that water penetration in most cases did not yet signify a hazard. Later editions [IAE64] demanded an immersion depth of 15 m for a period of at least 8 hours. For transport items with certain shapes containing irradiated fuel elements in the edition of 1985 [TSR85], the stepped-up water immersion test was supplemented by an immersion depth of 200 m for a period of 1 hr. The reason was that the penetration of water in this case would result in an increase in the criticality due to neutron moderation. In the TS-R-1 of 1996 [TSR96], this test was expanded for all shipping items with a content of more than 10^5 A_2.

[18] $m \leq 500$ kg.
[19] $p \leq 1000$ kg/m^3.
[20] His report was used, among other things, as a basis for the determination of a mean temperature in open pool fires.

2.3.2 Design-Exceeding Experiments

The history of the data record concept for Type B shipping items was explained in greater detail in Section 2.3.1. A series of experiments exceeding design figures was carried out above all in Germany, Great Britain and the USA in order to confirm the concept according to the particular current state of the art. Just how great the safety reserves of the casks are in comparison to the 9-m drop or the 30-minute fire or what stress the 9-m drop upon the nonresilient foundation would represent in comparison to real accidents was examined under the most serious accident situations. A detailed description of the following facts can also be gleaned from DROSTE [Dro01] and SCHULZ-FORBERG & HÜBNER [SFH00].

Mechanical Experiments

Crash tests with transport casks for radioactive substances were performed by the Sandia National Laboratories in 1978 by direction of the U.S. Department of Energy (USDOE). YOSHIMURA [Yos78] described the experiments. The accident scenarios included the following:

- impact of a fuel element transport cask mounted on a highway vehicle upon a massive reinforced steel structure at 60 mph (about 100 km/hr) and 80 mph (130 km/hr);

- impact of a locomotive against a transport cask mounted on a highway vehicle at 80 mph (130 km/hr);

- impact of a transport cask mounted on a rail vehicle upon a massive reinforced steel structure at 80 mph (130 km/hr), followed by an enveloping fire.

In the first case, the cask weighed 20.5 t and was filled with an exactly replicated model of a fuel unit of the Savannah type. There were plastic deformations on a fuel element assembly, but there was no fracture of the fuel element pellet-clad jacket. In the second experiment, the cask weighed 22.9 t and was only slightly damaged except for a 26-mm-deep impression at the impact site. Minor leaks were found. In the third case, the cask weighed 61.8 t and was stressed purely elastically during the accident.

In a comprehensive investigation[21] of the MAGNOX cask system in Great Britain, a locomotive with three freight cars and a total mass of 250 mg at a speed of 160 km/hr hit a 48 mg MAGNOX fuel element transport cask of the original scale [MAG85]. The investigation comprised calculations, original and model experiments, in which the results of experiments with casks on the original scale and the model scale were compared.

The tightly sealed enclosure remained intact and the measured stresses were less than in the case of the 9-m drop on the nonresilient foundation.

[21] The investigation comprised calculations, original and model experiments, in which we also compared the results of tests with casks on the original scale and the model scale.

In a drop test conducted by the German GNS Company, MOSAIK casks were dropped from a height of 800 m out of a helicopter upon a concrete runway (JANBERG [Jan91] and ANDERSEN et al. [A+78]).

An aircraft crash was simulated (GLASER [Gla80] and DROSTE et al. [DVWQ02]) by gunfire in Germany using casks of Type CASTOR® Ia[22], CASTOR® Iia[23] and TN1300. The engine, the hardest part of an aircraft, was modeled by a projectile. The projectiles consisted of 5-m-long hollow cylinders with a diameter of 600 mm and a wall thickness of 5 mm. On the inside, 1.64 m from the tip, there was a pipe that replicated the engine shaft. The mass, 1,000 kg, which was too small by a factor of 1.7, was compensated by a higher impact velocity. The speed of the projectile was between 292 m/sec and 306 m/sec. The casks were fired upon a total of three times.

- CASTOR® Ia bottom piece - Impact laterally upon cask.
- CASTOR® Iia - Impact on the seal area with cask inclined.
- CASTOR® Iia - Central impact upon lid.

Particularly relevant in terms of density was the perpendicular impact upon the lid system of the CASTOR® Iia, where the cask integrity and adequate tightness were preserved. The TN1300 withstood similar experiments without integrity loss or major plastic deformations of the cask wall.

In a drop test conducted by BAM with an original cask of Type CASTOR® Ic from a height of 19.5 m upon a heavy load foundation, WIESER et al. [WJH83] showed that the maximum impact deceleration was only half as much as in case of a drop from 9 m upon the nonresilient foundation. DROSTE et al. [D+95] conducted a 14-m drop test of a CASTOR® VHLW® CASK WITH A 120-mm-deep flaw in the 260 mm-thick wall upon a steel roller bearing (Figure 2.9) without any loss of cask integrity.

[22] Bottom piece.
[23] Reduced length.

Figure 2.9: CASTOR® VHLW® Cask with a 120-mm-Deep Flaw in the 260-mm-Thick Wall, Impact Upon a Steel Roller Bearing

Drops of heavy Type B casks from a height of 200 m were performed along with a series of drop tests from a height of 200 m with light containers for α-emitters. According to SCHULZ-FORBERG & HÜBNER [SFH00], a 1:2 model cask of a TN 8/9 (mass of model 4 mg) fell several times upon different foundations. Because the cask upon the first drop missed the 20-x-80-m concrete surface, it hit forest ground and was found only after a protracted search. There was no damage except for minor deformations. A repeat of the experiment was successful; this time, a larger impact surface was hit (structure: 40-cm-thick reinforced concrete). Tightness[24] and container integrity were preserved.

Even extreme but potentially conceivable terrorist actions were examined by means of hollow charge firing tests. PRETZSCH & LANGE [PL94] show that the radiological consequences remain minor after the object has been fired upon. Assuming routine weather, the radiation dose, already at a range of 150 m, would be smaller than the value of the natural average annual exposure in Germany.

Currently, work is underway in the USA to prepare the "Package Performance Study" (NUREG-1768) in connection with which casks of originals size were to be subjected to mechanical and thermal accident scenarios. This series of experiments was triggered by a number of technical problems relating to the tolerability of accident stresses on fuel element transport casks raised by NUREG-CR-6672 SPRUNG et al. ([S+00]).

Thermal Experiments

The resistance of a railroad tank car filled with propane was examined in 1999 on the experimental grounds of BAM in Horstwalde, and the results were published by DROSTE et al. [DPH99], [DP01], [DVWQ02]. One CASTOR® THTR/AVR® was placed (Figure 2.10) directly next to the railroad tank car in the fire. During the explosion of the railroad tank car, which generated a fireball with a diameter of 150 m, the CASTOR® THTR/AVR® was hit directly, it

[24] Tested by a bubble test.

flip-flopped and landed about 7 m from its original position (Figure 2.11). The cask remained completely intact except for some minor deformations.

Figure 2.10: Fire Test with a Railroad Tank Car and a CASTOR® THTR/AVR® according to [DPH99] Before (left) and After the Experiment (right).

Mathematical Investigations

Many investigations were performed by mathematical means in the course of the further development of hardware and software. WIESER et al. [W+04] numerically investigated the tightness of a cask standing in the depot in response to a stress resulting from an aircraft crash. A method for the calculation of at least conservative leakage rates was presented in spite of the restrictions connected with the transposability of seal gaps on leakage rates.

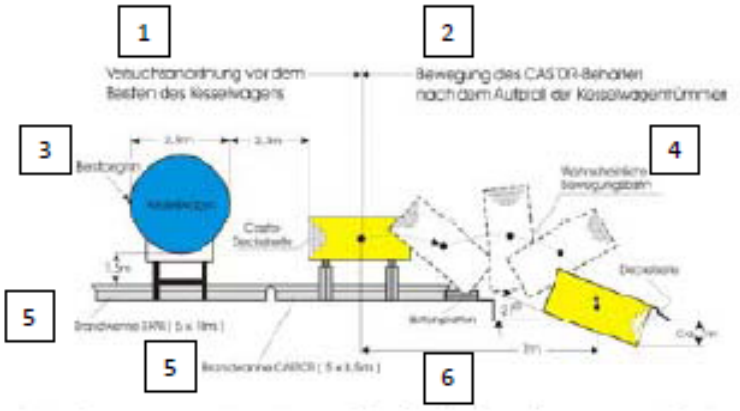

Figure 2.11: Fire Test with a Railroad Tank Car and a CASTOR® THTR/AVR® - Diagram

[Key: 1) Experimental arrangement prior to the bursting of the tank car; 2) Movement of the CASTOR cask after impact of the tank car wreckage; 3) Start of burn [illegible]; 4) Probable movement path; 5) Fire well; 6) Concrete plates; [Other entries illegible]].

According to RID [RID06], one cannot rule out the possibility that shipping items holding radioactive substances are transported in composite trains also carrying other hazardous goods. The effects of an explosion in the immediate vicinity of the shipping items were

investigated mathematically by BALLHEIMER et al. [B+04]. Compared to the stresses resulting from the IAEA testing conditions, the stresses this time were minor.

A TN-1300 cask was mathematically exposed to four hours of fire at 800ºC to determine the safety reserves (SCHNEIDER & JOBST [SJ85]). In spite of the fact that the fire lasted eight times as long when compared to the required testing time, the temperature calculated in the endangered lid area was 315ºC, something that was definitely below the failure temperatures of the seals, amounting to about 380-400ºC, as determined by BAM by BREHM et al. [B+86].

2.3.3 Conclusions

In this subchapter, we described a series of experiments that went beyond the original design figures and that proved in a publicly effective manner that the 9-m drop test, which at first sight is relatively unspectacular, nevertheless definitely matches graver accident situations. Nevertheless, one can conceive of accident situations where an at least partial release of the radioactive content would be possible in spite of the fact that the transport cask model was licensed. The development of the risk analysis made it possible also to quantify or at least to estimate the residual risk underlying the data-recording concept, something that was also done several times on the past for transports in Germany.

2.4 Risk Analysis as Safety Engineering Instrument

In the past, safety frequently resulted from partly very longstanding experience with the uncertainty of situations further in the past. A safety that was generated in this way naturally was very expensive in connection with these accidents (trial-and-error procedure). It is quite obvious that this procedure is all the less suitable the greater and more catastrophic are the anticipated consequences arising from the failure of a technology. Subsequently, safety was considered with the help of deterministic methods. In this connection, deterministic means that by using certain safety devices, one can rule out any failure of the system based according to "just plain horse sense." We did a definition as to what threshold developments are still credible and as to when they can be ruled out. This differentiation naturally contains an implied estimation of the occurrence probabilities. If nevertheless there were catastrophic trouble developments, then we spoke of unforeseeable factors or "force majeure." In this case, there was a paradigm change upon the publication of the RASMUSSEN report on the risk to the general public deriving from nuclear power plants in the USA [R+75] [WAS75], who investigated and quantified the risk to the general public with probabilistic and partly deterministic methods (see also HARTWIG [Har99]). Since then, it has been increasingly realized that no technology is completely safe, that there will always be a residual risk, although it may be small, and that unsafe circumstances may occur. The existence of this residual risk introduces the question as to its magnitude and quantifiability but also as to its acceptability.

2.4.1 Safety

The ISO [ISO04] describes safety as *"safety: freedom from unacceptable risk of harm."* DIN 31000, Part 2 [DIN87] clearly states in the foreword: "*Because in technology, as everywhere in daily life, there cannot be any absolute safety in terms of freedom from any kind of*

risk, the task is to reduce the risk to a justifiable measure." The requirement for an assessment decision on the justifiability of a risk here underscores the very simple basic principle: absolute safety cannot be achieved. The basis of the risk decision thus is the comparison of the risk R, which is to be determined, with a suitable boundary risk R_v, which is to be determined. Here, the boundary risk according to DIN 31000 [DIN87] is defined as the greatest still-justifiable risk from a technical procedure or condition that is to be evaluated. Safety exists when $R < R_v$ and hazard exists when $R > R_v$.

2.4.2 Risk

According to HARTWIG [Har99], risk is defined as stochastic products from damage and the probability of damage occurrence. DIN 31000 [DIN87] defines damage as *"disadvantage arising from the injuring of choses in action."*

HARTWIG [GS00b] describes risk with the help of four risk indices. The absolute frequency describes, for example, the number of accidents per year. The relative frequency weights the absolute frequency in relation to the number of exposed persons. The accident frequency rate no longer ties the relative frequency in with a fixed time frame (for example, one year), but with the time the exposed persons are endangered. To determine the accident seriousness number, we multiply the accident frequency rate with the number of accident days per accident. This means that from the absolute frequency all the way to the accident seriousness number, we observe a further precisization of the results, but also a more laborious and expensive determination.

2.4.3 Justifiability of Risks

The question as to the quantification of the residual risk deriving from a technology raises another important question: What kind of residual risk can we accept for the population at large? This is the place where, in the past, it was proposed to perform a risk comparison, that is to say, to perform the assessment decision concerning the justifiability of a risk on the basis of a comparison with technologies already in use (see SCHÖN [Sch93]). In the past, this procedure proved only to be of limited use because it did not sufficiently consider the risk perception, in other words, the perception of a risk among the population at large. This can be made clear by way of example, comparing the procedure of energy with the help of coal and nuclear power. Although in the past a large number of people died when energy was obtained from coal[25], this form of energy procurement is perceived by the population at large to be relatively low risk, whereas nuclear power so far has claimed only a comparatively small number of victims[26], which, however is perceived among the population as a high-risk technology. Along with the functional dependence of the risk perception on socialization, we encounter here the effect that identical risks (for example, number of dead per period of time) were

[25] According to [NI007], in the USA alone during the last century, 11,639 individuals perished as a result of accidents with more than 5 fatalities in connection with coal mining.

[26] According to the IAEA [IAE06] Report, 31 individuals died as a direct consequence of the only accident that in the International Nuclear Event Scale (INES of the IAEA [INE01]) was placed in the most serious category 7, in other words, the Chernobyl accident. During the period from 1992-2002, about 4,000 deaths were determined, conservatively speaking, from cancer resulting from radiation exposure.

perceived in different ways depending on whether it involved an accident with 1,000 dead or 1,000 accidents with one dead each. It becomes clear that when it comes to the information derived from justifiability, one must consider other factors, such as the local and temporal distribution of damage types and volumes as well as the distribution of the victims, those threatened and those damaged. Here we must touch on the psychological effects (see also CLARENBURG in HARTWIG [Cla83]) when it comes to the acceptance of risks. Determining a uniform boundary risk is not justifiable due to the gradient connected with risk perception.

Basically, the desired advantages should be weighed against the disadvantages acquired, among other things, by risks, using as basis a description of the objective of an undertaking, which is to be evaluated. Here one must also adequately take into consideration the risks arising from substitute undertakings connected with the rejection of a technology so as not to increase the risk overall.

2.4.4 Probabilistic Analyses in the Nuclear Engineering Area

The safety of technical systems is customarily evaluated in two different ways. Safety design in the conventional sense is referred to as *deterministic*. In contrast to that, working with the probabilistic procedure (probabilistic risk analysis or risk study), we quantitatively determine the risks deriving from a system failure by way of the determination of occurrence probabilities of series of events that are not covered by the design. The essential procedure for the risk study comprises the following:

- identification of triggering events;
- determination of the course of events;
- quantification of the occurrence probability of various courses of events by means of reliability analysis.

Risk study result magnitudes, for example, are the overall frequency of accident-related radioactivity releases or the frequency of accident-related damages or exposures. Because the risk study definitely goes beyond the scope of deterministic analyses, the resultant discovery can be used for different applications. BERG [Ber95] includes in this also the quantification of safety margins.

Probabilistic Reliability Analyses. Probabilistic reliability analyses determine the probability of a system failure. One procedure that is customary in this connection involves the method of fault tree analysis. In the fault tree, we assemble the individual probabilities of the failures of individual components to make up a larger tree. For example, on the basis of the component failures, we can conclude as to what kind of probability and under what marginal conditions we can expect a system failure [GRS98]. As an alternative, we can estimate the unavailability of safety functions by the frequency of the failure of a triggering event. Figure 2.12 presents a graphic illustration. Here, the fault tree illustration is presented for the main types of releases from chlorine tank cars according to HARTWIG [Har99]. The probabilities of releases based on various types of enclosure failures are described in an illustrative fashion.

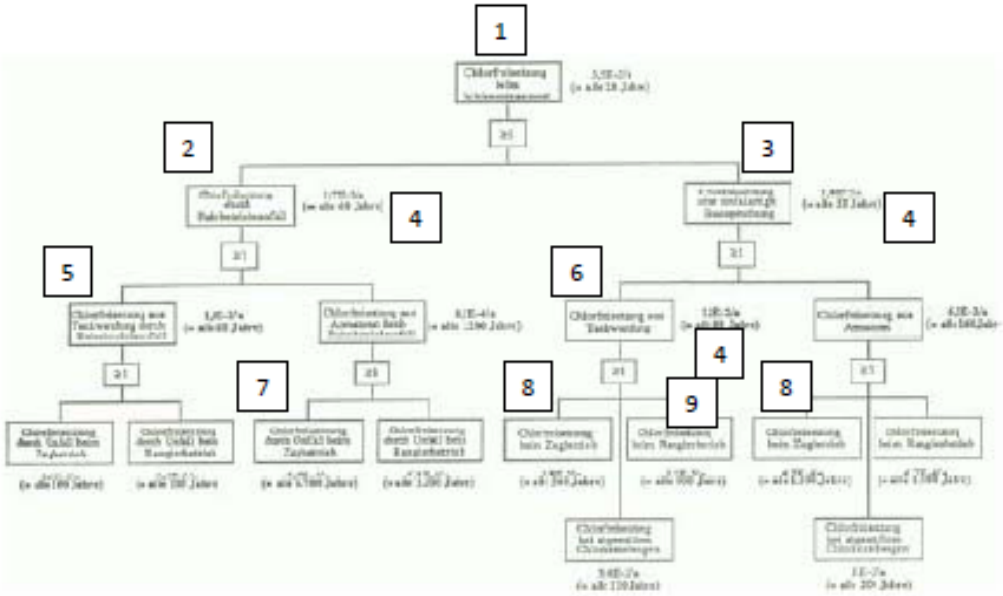

Figure 2.12: Main Types of Radiation Release from Chlorine Tank Cars During West German Rail Transport Based on Fault Tree Illustration for the Reference Year 1990 and Their Occurrence Probabilities According to HARTWIG [Har99]

[Key: 1) Chlorine release during rail transportation; 2) Chlorine release due to railroad operation failure; 3) Chlorine release due to [illegible] stress; 4) Year; 5) Chlorine release from tank car as a result of rail operations accident; 6) Chlorine release from tank car; 7) Chlorine release due to train operation accident; 8) Chlorine release during train operation; 9) Chlorine release during train switching operation].

Probabilistic Risk Analysis. Building on the reliability analysis, the risk analysis or risk study determines not only the probability of a system failure but also tries to estimate the consequences of that system failure. The fault tree method, used for the reliability analysis, is now enhanced by the event tree analysis or the event force analysis (see also FARMER in HARTWIG [Far83]). The event tree shows what developments could materialize from a trouble event with what probability, depending on whether the required systems to control the trouble work or fail as planned. The occurrence probability of the different developments can then be calculated from the combinations of both procedures.

A study by DENNIS [Den78] discusses the accident situations involving fire, impact, crush, immersion and spike impacts. The seriousness of the accident and its occurrence probability were determined for each of these situations. Among other things, the study determines that the expected speed change in 99.4% of all impact accidents was less than 50 km/hr[27] for casks with a mass of more than 36 t. The maximum shock force acting on the cask is greater during impact upon a nonresilient foundation because of the very short shock time than in

[27] Equivalent drop height h = 9.83 m.

case of an impact against a real foundation. An updating of the study by LAHS [Lah87] shows that 99.94% of all conceivable mechanical accident events are covered by the IAEA testing conditions. CLARKE et al. [C+76] confirmed that 99.95% of all highway transport accidents are covered by the spike test.

Continual risk analyses on RAM transports were performed in the USA. In 1977, the United States Nuclear Regulatory Commission (USNRC) published a study entitled: *"Final Environmental Statement on the Transportation of Radioactive Material by Air and Other Modes."* NUREG-0170 [NUR77]. This study investigated the transport of all radioactive substances used in the USA on all carriers (highway, rail, air and water). Based on the study results, the USNRC, 1981, stated that: *"... the current regulatory work to protect the population against inappropriate risks due to the transport of radioactive substances is adequate"* (46 FR 21629, April 13, 1981). The first damage model used (called Model I) assumed that when the test stress is exceeded, the complete content would immediately be released. This model was entirely too unrealistic; therefore, a second model (Model II) was developed. When testing conditions are exceeded, this model assumed a gradual increase in the release rate (as a function of the seriousness of the accident).

NUREG-0170 did not focus directly on the transport of spent fuel elements; therefore, additional mathematical investigations were conducted with the generic steel-lead-steel casks. The results were published by FISCHER [fis87] (NUREG-CR-4829) or also "Model Study"). A comparison of this investigation with NUREG-0170 showed that the stresses *"... are at least 3 times less than determined in NUREG-0170"* [NUR77].

In 1996, the USNRC decided that the risk connected with the transport of spent fuel elements must be tested again. The basis for initiating the renewed study consisted of the following:

1. increase in the anticipated number of shipments;

2. transport on lines and with casks that were not considered earlier;

3. availability of newer statistical data and improved analysis methods.

The results of this NUREG-CR-6672 study, including a comparison with NUREG-0170 ([NUREG77]) and NUREG-CR-4829 (FISCHER [Fis87]) were published by SPRUNG et al. [S+00].

Investigations were conducted in Germany several times on radiation exposure under "normal transportation conditions" and probabilistic transport accident risk analyses focusing on individual transport casks and certain lines. The procedure, customary according to the current state of the art and technology, is described by LANGE et al. [L+07]. For instance, FETT et al. [F+97] investigated the return of vitrified and bituminized waste from La Hague, France, to Gorleben in CASTOR® HAW 20/28, TS 28 V and VII cast container casks. LANGE, GRÜNDLER & SCHWARZ [L+91] considered the transport of medium-radioactive and slightly radioactive waste with the help of the I-II concrete casks, the I-III cast casks, and the Type I-VII

cask containers to the Konrad final waste dump. Figure 2.13 shows the anticipated frequency of effective doses > D above the effective D as a result of the investigations conducted by LANGE, GRÜNDLER & SCHWARZ [L+91]. The essential findings were summarized as follows:

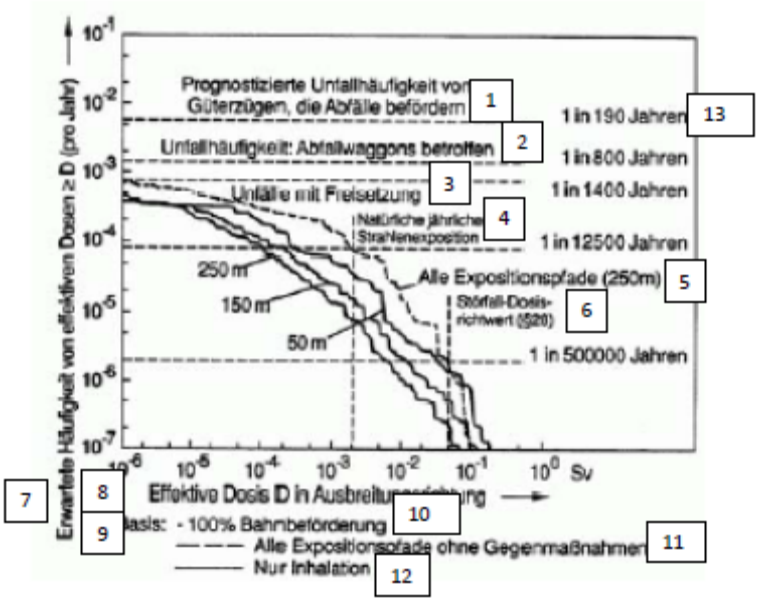

Figure 2.13: Frequency Distribution of the Effective Lifetime Dose Based on Waste Transport Accidents in the Final Dump Region (perimeter 25 km) According to LANGE et al. [L+91] (Farmer Diagram)

[Key: 1) Prognosticated accident frequency of freight trains carrying weight; 2) Accident frequency: involving waste freight cars; 3) Accidents involving release; 4) Natural annual radiation exposure; 5) All exposure paths; 6) Trouble dose value; 7) Anticipated frequency of effective doses per year; 8) Effective dose D in the direction of propagation; 9) Basis; 10) Rail transport; 11) All exposure paths without countermeasures; 12) Inhalation only; 13) Year].

- One transport accident involving release is sufficiently unlikely during a 40-year transport phase to the final waste dump.

- The risk connected with rail transport is less than with highway transport.

- As the distance to the accident site increases, the radiation exposure or contamination would decline considerably (with a factor of 10 whereas the distance is multiplied by a factor of five).

- At a distance of 250 m, an effective dose of ≥ 50 mSv[28] would occur on the average only every 400,000 years.

FETT et al. [F+93] worked on the transport of medium-radioactive and slightly radioactive waste from different nuclear power plants as well as research and experimental

[28] Maximum annual dose for persons professionally exposed to radiation.

reactors using barrel containers, primary containers and big containers to Morsleben. In the context of the project entitled "Safety Studies for Waste Disposal" (PSE), safety analyses were made on transports of radioactive materials for highways by TULLY et al. (T^+85] and for rail by SCHNEIDER & JOBST [SJ85]. All of the mentioned studies confirm that the risk is to be estimated as more than very slight. For normal transport conditions, the maximum anticipated radiation exposure is < 0.02 mSv/year for the population at large and < 2 mSv/year for more exposed cargo-handling personnel. In the case of transport accidents according to FETT et al. [F^+97], we must expect a release of minimum quantities with an occurrence possibility of 1/1,000, and for radiologically relevant quantities, we must figure on 1/25,000 for all transports together. Radiologically relevant here means that the radiation dose[29] would not exceed the value of the natural radiation dose during one year following a real accident at a distance of 250 m from the accident site. Accidents with higher release figures can be expected with an occurrence probability of 10^{-7}/year.

There are many other investigations covering special aspects involved in the transport risk; here we might mention, for example, BALLHEIMER et al. [BPD00], DROSTE et al. [D^+98], McCLURE et al. [M^+80] and BLYTHE et al. [B^+83]; they covered especially the influence exerted by the subsoil. Other studies were performed by McCLURE et al. [McC77], McSWEENEY et al. [M^+75], HALL et al. [H^+77b], McSWEENEY & JOHNSON [MJ77] and HAEBERLIN et al. [H^+77a]. All studies estimate the risk to the population from the shipment of radioactive substances as acceptable when compared to other technical risks. The topic of this study does not include a comprehensive risk analysis, such as it was done, for example, by HARTWIG [Har99] for heavy gases using the example of the chlorine substance cycles.

Cask Behavior in RAM Risk Studies

The first risk studies assumed a complete release of the complete radioactive content of a cask in case of an accident involving drop heights of more than 9 m. The procedure is conservative but not realistic because, even if the drop height of 9 m is definitely exceeded, the stresses on the cask, assuming realistic accident bodies, are less than in the case of the drop on the nonresilient foundation. Realistic foundations are definitely softer when compared to nonresilient foundations (BALLHEIMER et al. [BPD00]. The risk study done by LANGE, GRÜNDLER & SCHWARZ [L^+91] devotes relatively little space to the topic of cask failure and subsequent release behavior. The possible accident situations are subdivided into stress classes. Release portions for certain radionuclides are matched up with the stress classes without any sources being given. Greater details were provided on this subject only in FETT et al. [F^+97]. A general global failure of the cask is ruled out. Releases are estimated on the basis of experiments involving the following upon a CASTOR® Iia (GLASER [Gla80] and BAM [BAM82]). The leakage rate, determined during the firing action, was applied with a safety factor of 10 for the stress class of more than 80 km/hr.

The procedure is probably conservative, although it does not fully consider the design features of currently used casks. The cask types currently used for waste disposal at German power plants differ significantly from the cask models of the 1st generation, such as the CASTOR® Ia, CASTOR® Ic, and CASTOR® Iia. Extraregulatory tests, such as the firing tests,

[29] 50-year sequence, population dose.

are very laborious in experimental terms and cost a lot of money. The further development of computerized methods provided new alternatives on that score. For example, an aircraft crash upon a German intermediate storage dump was examined mathematically by WIESER & QIAO [WQ06].

In the course of the further development of computation methods, it is now possible to support the risk analyses by means of the quantification of the cask behavior in response to accident stresses using mathematical methods. Two important areas must be considered regarding the tightly sealed enclosure of the radioactive contents during transport as part of the risk analysis by way of a first approximation: The load injection coming from the accident situation and going into the cask as well as the resultant behavior of the sealing system generally is the weakest spot in the tightly sealed enclosure. Many approaches have been tried to tackle the behavior of the sealing system, such as, for example, the calculations done by BALLHEIMER et al. [BPD00] and WIESER & QIAO [WQ06]. The behavior of the sealing system in response to accident stress, however, cannot be a topic of this study for reasons of scope.

The behavior of the shock-absorbing parts is of decisive significance with regard to the stress on the lid-flange system. They decide on the safety reserves that are present as a result of the licensing-related impact upon the nonresilient foundation from a height of 9 m when compared to stresses occurring in realistic accidents. So far, the risk studies did not consider the influence deriving from the behavior of the shock-absorbing parts. A precise analysis of the processes involving shock-absorbing parts and the resultant improved simulation possibilities using numerical methods would help in this case in order further to improve the precision of the quantification of risks involved in the transport of radioactive substances by improving the description of the cask stress involved in accident situations.

2.5 Difficulties Connected with the Modeling of Shock-Absorbing Parts

In the earlier subchapters, we derived the need for a modeling of shock-absorbing parts using numerical methods. First of all, manifold investigations are necessary for model design testing and they can be performed only mathematically. For this purpose, the simulation of the behavior of shock-absorbing parts constitutes the basis for many numerically determined stresses on the components of the transport items. The numerical simulation of the behavior of the shock absorber is a prerequisite for risk analysis if a realistic cask stress is to be achieved. In the following, we will describe the difficulties connected with the mathematical simulation of the behavior of shock-absorbing parts according to the current state of technology and science.

Experimental results are to be transferred frequently to altered marginal conditions with the help of computations. In model design testing, that can be the case with the evaluation of the influence of an operating temperature above the experimental temperature or when it comes to evaluating a geometry change or in connection with an investigation of the influence of the material parameter variations in a risk analysis that can, for example, mean the investigation of the impact on certain accident bodies or a minor change in the impact angle. That requires a computation model that will commensurately describe the behavior of the shock-absorbing part in a robust manner and with physically justifiable parameters. Such a model is so far not available. Here is why:

Basically, the mechanical properties of wood are not sufficiently known. Little has been published about the behavior of wood in response to major deformations; the behavior is described in phenomenological terms only to a limited extent. To the extent that they are available, flow curves for wood as well as general material law parameters are frequently not directly applicable.

The results of experiments with wood samples must be transferred to the wood in the shock absorber. During this transfer, the material parameters must be adapted to the drop test results. The complex possibilities connected with parameter adaptations will lead to uncertainties as to the form in which the adaptation may be performed.

Unclear also are the factors that can influence the mechanical properties of wood and thus also the energy-absorption behavior of shock-absorbing parts. Examples are the temperature and the moisture content of the wood. It is also unclear as to the extent to which these dependences must be considered in model testing.

Drop tests as part of model licensing are performed partly with scale models; therefore, when it comes to transfer to the models that are to be licensed, one must also evaluate the influence of the expansion ring. When scale models with identical material properties are used, one can observe higher expansion rates than in experiments with prototypes of the original magnitudes (NEUMANN et al. [NWD07]).

The interaction between wood as shock-absorber filling and the surrounding sheet-metal pieces has not yet been investigated adequately so far. It is, of course, known that the sheet-metal pieces perform supporting function for the wood, but the attendant mechanisms have not been clarified and quantified in scientific terms.

2.6. Summary

The precise analysis of the behavior of shock-absorbing parts of transport casks for radioactive substances is of fundamental significance for the determination of the failure criteria as part of the risk analysis, on the one hand, and for model testing for the determination of cask stress, on the other hand.

In model testing, the shock-absorbing parts decide on the height of the stress on components of the shipping items during the 9-m drop upon the nonresilient foundation. They considerably diminish the intensity of the impact due to energy conversion. It would be very interesting to improve our understanding of the behavior of the shock-absorbing parts as well as of the quality of simulation when it comes to the safety of transport casks for radioactive substances

So far, the real cask behavior in accident situations has been considered in risk analyses only to a small extent. Here, modeling the behavior of shock-absorbing parts can help improve the analysis quality in connection with the determination of the magnitude of risks and can thus make a contribution to the more precise description of the magnitude of safety.

3 Shock-Absorbing Parts of Transport Casks

Following a presentation of current BE/HAW transport casks and intermediate storage dump casks, we will concentrate in this chapter especially on the construction of the shock-absorbing parts. The lead sheathing in WILKINS & GUINAN [WG73], which was used primarily for shielding, must be considered as one of the first forms of shock-absorbing materials for the casks used to hold radioactive substances. Thereafter, many investigations were performed with the most varied shock-absorber concepts and shock-absorbing materials. After a description of the most frequently used deign principles and a brief overview of the possible shock-absorber materials, this study concentrates on the wood-filled shock absorber because the shipping items used in Germany for radioactive substances to a great extent contain wood-filled shock absorbers.

3.1. Principle of Shock Absorption in Transport Casks

3.1.1 Function

Figure 3.1: Prototypes of Fuel Element Transport Casks TN900 (left) and CASTOR® Ic (right) Before or After a 9-m Drop Test

Energy-absorbing parts are used in order to convert as much kinetic energy as possible in case of an impact over a longer period of time and path in a cask that is unprotected when compared to the shock into plastic form change energy. By increasing the shock time and the shock path, one can convert the same kinetic energy into heat, assuming there is a significant reduction in the maximum shock force.

$$W = \int_0^{s_{max}} F(s)\,ds \tag{3.1}$$

W	-	Geleistete Arbeit
$F(s)$	-	Kraftfunktion
s	-	Weg

W - Work done
F(s) - Force function
s - Path

The performance capacity of a shock-absorber concept consists of the ability in accident situations to minimize the maximum stress on the object that is to be protected. The less is the maximum force that acts upon the object to be protected, the greater will be the ability to withstand the impact or bump. It was, above all, steel structures and sheet-metal structures that were used as shock-absorbing parts at the beginning of transport with spent fuel elements. The transport casks, as we can see looking at the models TN900 and CASTOR® Ic visible in Figure 3.1, are the casks that are equipped with "hard," "integrated" shock absorbers, such as, for example, cooling ribs. Minor deformation paths of shock-absorbing parts resulted in heavy stresses on the cask body.

Figure 3.2: 9-m Drop Test with a CONSTOR® V/TC Experimental Cask on the Original Scale at the Drop Test Facility of the BAM

Figure 3.3: 1:2 Model CASTOR® HAW TB2 Before a Slap Down Drop Test at the Drop Test Facility of the BAM

Today, however, we mostly use shock absorbers with screwed-on, relatively "soft" steel plate constructions filled with wood, as we can see in Figure 3.2, in order to be able to achieve

the necessary shock absorber with the help of the currently available masses and dimensions. Large volumes with fillings of relatively "soft" wood types, such as balsawood, fir, pine and red cedar, result in a definite reduction of the stress during impact. The shock absorbers shown in Figure 3.2 have the following dimensions: 3510 x 3510 x 1800 mm.

In contrast to that, models such as the CASTOR® HAW 28M (Figure 3.3 as 1:2 test specimen CASTOR® HAW TB2) have a combination of wood-filled shock-absorbers at the cask ends and rings made of aluminum. The aluminum rings are intended to protect the transport cask, especially in case of a horizontal drop or in case of a Slap Down (see 2.2.5) against heavy stresses. This design principle is used for the acceptance conditions (diameter limitation) for shipping items holding radioactive substances from the reprocessing plant at La Hague.

3.1.2 Shock-Absorber Materials

The many materials that are used frequently according to ALGHAMDI [Alg01] in the field of radioactive substance transport for shock absorbers include various foams, aluminum honeycombs and woods of the most varied types. Bonded mixtures (chipboard, MDF) and steel or sheet metal structures are used less frequently. The materials that are currently used for the most part can be subdivided into the group of the cellular[1] solid bodies.

The shock-absorber materials according to HENRY et al. [H$^+$01] are generally selected in terms of costs, performance, availability, fire resistance and familiarity with the material. The last point plays an important role. Certain materials are preferred in the various countries, depending upon the fundamental cask concept and transport strategy. For example, German, French and Japanese cask makers generally use wood-filled shock absorbers; according to McMURTRY & HOHNSTREITER [MH95][2] and GLASS et al. [GDM92], Great Britain and the USA above all use aluminum honeycomb, steel structures or sheet metal structures and PU foams. HENRY et al. [H$^+$01] have warned us that an estimation of the performance capacity of a shock-absorbing part based only on the materials used would be misleading. It is not so much the material but rather more the shock-absorber concepts in combination with the safety engineering design concepts of the casks that will decide the performance capacity.

Next we will briefly describe widely used shock-absorber materials, followed by a more detailed consideration on the subject of wood as a shock-absorber material.

Synthetic Foams

Closed-pore polyurethane foams (PU foams) have proved effective in the case of the synthetic foams, for example, as against phenolic foams, because in the case of the open-pore foams, there were problems with water infiltration due to their high hygroscopicity[3] according to HENRY et al. [H$^+$01]. Advantages can also be described from the basically isotope material behavior (where, according to LI et al. [LMB00], it must, upon closer examination, be

[1] Cell or cellular are derived from the Latin "cella - chamber, small, enclosed space" and "cellarium" - "accumulation of cells."

[2] Here we compare aluminum foams, PU foams, honeycombs and sinter materials.

[3] Ability to react to the moisture content of the surrounding air with water vapor absorption or release.

considered as anisotropic), the favorable production costs as well as the possibly very good thermal protection in case of fire due to the formation of a surface protection layer. Disadvantages derive from the poor specific energy absorption capacity, as determined, for example, by MOURÃO & NETO [MaN03].

Aluminum

Aluminum is used, above all, in the form of aluminum foams, honeycombs or aluminum ring shock absorbers (see Figure 3.3). According to HANSSEN et al. [H$^+$02], aluminum foams do not have any pronounced constant plateau but rather display a continual rise in the stress along with expansion. According to McMURTRY & HOHNSTREITER [MH95], the material likewise cannot be considered as ideally isotropic. According to HANSSEN et al. [H$^+$02], it is especially the high production costs that so far prevented broad use.

The term "honeycombs" refers to a family of cellular materials with two-dimensional periodic structures. Aluminum honeycombs are used on a large scale in the USA (for example, SINGH et al. [SSB04] or SPRUNG et al. [S$^+$00]. According to HENRY [H$^+$01], a positive effect can also be derived from a pronounced, ideal-constant plateau, a high degree of deformability and, according to GLASS et al. [GDM92], a negligible expansion rate dependence of the mechanical properties. The high anisotropy determined by MAJI et al. [MSD92], the great stress rise as of consolidation, the high thermal conductivity in case of fire, and the high price constitute disadvantageous effects.

Many attempts have already been made to describe the material in constitutive terms on the basis of the vast employment spectrum for aluminum honeycombs. HANSSEN et al. [H$^+$02] examine and discuss usual constitutive models for honeycombs in terms of their usability for aluminum honeycombs. MOHR & DOYOYO [MD04] propose an expanded constitutive model.

3.2 Detailed Consideration Regarding Wood as Shock-Absorber Material

According to GIBSON & ASHBY [GA97], wood is the oldest material used most frequently by man. The term "material" is derived from the Latin "materies, material," meaning tree trunk. A resting place for old Paleolithic wild horse hunters was discovered in Schöningen, Lower Saxony, in 1994. The seven completely preserved spears consisting of wood were dated at an age of more than 400,000 years according to THIEME [Thi99]. In 1990, near the city of Erkelenze - North Rhine-Westphalia - a well box construction made of oak wood was discovered and dated to the year 5090 B.C. (KOSCHICK [Kos98]). The beams, expertly worked with stone axes, are notched bilaterally and are connected with each other by way of a block structure. Around about 2500 B.C., the Egyptians already made wooden furniture, sculptures, coffins and death masks. The Greeks used wood to build beds and sitting furniture around 700 B.C.

During the 16th century, so much wood was used in Europe due to the great demand that structural wood had to be imported from the "New World." This is why, according to [DFW05], a permanent forestry industry was launched in Germany already at the start of the 18th century[4], according to which each harvested surface had to be reforested. Present-day

[4] First mention in 1713 by VON CALROWITZ.

annual wood output according to NIEMZ [Nie93b] comes to about 10^9 mg and thus roughly corresponds to the annual output of iron and steel.

3.2.1 History of Wood Research

With his *"Discorsi e Dimostrazioni matematiche"* [Gal38] [Mathematical Discourses and Demonstrations], GALILEO GALILEI created the starting point of solidity theory. He used beams made of wood for his experiments on the fracture resistance of clamped bending girders.

The first scientific investigations of wood and wood use were performed already at the beginning of the 18th century by DU HAMEL DU MONCEAU [1700-1781) and LETERECE DE BUFFON (1707-1788) [DHDM55]. A series of additional studies on wood production and use were made starting in about 1750. JOHANN HEINRICH VON COTTA (1763-1844) and GEORG LUDWIG HARTIG (1764-1837) worked above all on the solidity of wood. In 1809, CARL FRIEDRICH WIEBEKING (1762-1842) [Wie09], in his capacity as the director of the Bavarian Water, Bridge, and Highway System, reported on the testing of wooden girders. Parallel to that, investigations were performed on other mechanical properties of wood so that in 1837, a first overview of the properties of wood was published by KARMASCH [Kar37].

A comprehensive scientific approach to the topic of wood was started at the beginning of the 20th century with the founding of the Forest Products Laboratory in Madison, Wisconsin, USA, in 1910. Shortly thereafter came institutes in India[5] (1912), Germany[6] and Canada[7] (1913). The first compilation of knowledge in the wood sciences was presented in 1936 by KOLLMANN [Kol36], 1939 by TRENDELENBURG [Tre39] and 1949 by VORREITER [Vor49]. Along with DINWOODIE [Din81], BODIG & JAYNE [BJ82] and NIEMZ [Nie93b], KOLLMANN's work [Kol36] is especially important among standard works on the mechanical properties of wood.

3.2.2 The Structure of Wood

The structure of wood can be subdivided into macro- (visible with the naked eye or the magnifying glass), micro- (visible with the microscope) and ultrastructure (visible with the electron microscope). Figure 3.4 shows the macroscopic structure of wood by way of a profile through the trunk. We refer to DINWOODIE [Din81], GIBSON & ASHBY [GA97], [WHB99] and especially to NIEMZ [Nie93a] [Nie93b] for a more in-depth view of the topic.

[5] Forest Products Laboratory Research Institute, Debra Dun.
[6] Institute for Wood and Cellulose Chemistry, Eberswalde (starting in 1934, Reich Institute for Wood Research).
[7] Forest Products Laboratory, Montreal.

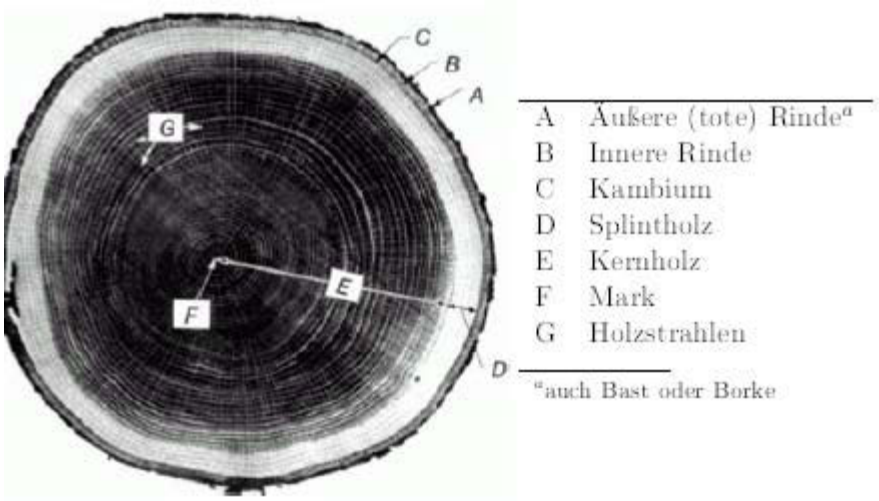

Figure 3.4: Profile Through a White Oak (Quercus alba) from [WHB99]

* also bast or bark

[Key: A) Outer (dead) bark*; B) Inner bark; C) Cambium; D) Sapwood; E) Heartwood; F) Pulp; G) Wood spots].

Macroscopic Structure

If we look at the profile through a trunk, then going from the outside to the inside, we can see the following areas (Figure 3.4): (A) outer bark whose thickness varies greatly, depending upon the type and age of the tree and (B) inner bark that takes care of the transport of the nutrition from the leaves to the growth areas of the tree. The cambium (C) is a very thin layer constituting the transition between the bark and the sapwood. This is the place where most of the lateral growth takes place. The wooden profile of the trunk can be subdivided into sapwood (D), which is responsible for nutrition transport from the roots to the leaves, and heartwood (E), whose cells no longer take care of the tasks of the sapwood. The ratio between sapwood and heartwood varies greatly, depending on the type, growth speed and age of the tree. With the exception of the very young trees, the share of the sapwood amounts to 10-60% of the radius. Sapwood and heartwood again can be subdivided into periodic structures, the annual rings. Annual rings result from differing growth conditions at the start and end of the growth season within a year. For example, in tropical forest species, one can generally find no growth rings due to the year-round growth. The inner, bright area of an annual ring is called early wood and usually has definitely larger cavities and rather small cell wall thicknesses when compared to the darker late wood that is found at the end of a growth season. The transition between early and late wood is normally relatively abrupt, but it depends on the species of the wood and the growth conditions. Figure 3.6 clearly shows the transition from early wood to late wood. Wood rays (G in Figure 3.4 and 2 in 3.6) are used for the transport and deposit of nutrients; in the horizontal plane, they point radially outward and connect several layers of pith up to the bark.

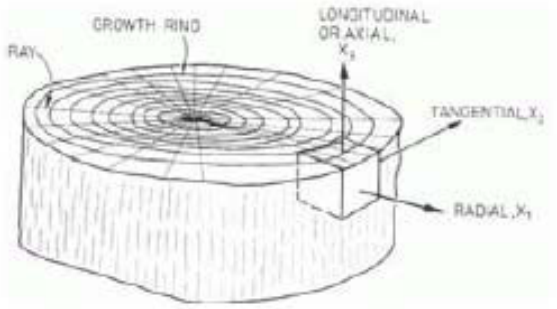

Figure 3.5: Profile Through a Wood Trunk with Axial, Tangential and Radial Direction According to GIBSON & ASHBY [GA97]

Three directions are usually employed for the description of the structure and properties of wood due to its approximately orthotropic structure: axial or longitudinal, radial and tangential (Figure 3.5).

Microscopic Structure

Wood is a cellular material on the microscopic level. The often hexagonally shaped prisms mostly have empty cavities or those that are partly filled with methyl cellulose or resin residues (see Figure 3.7). The ratio between wood wall thickness and cell wall thickness according to GIBSON & ASHBY [GA97] is between 0.05 (for Ochroma lapopus) and 0.80 (for Guaiacum Officinale). The mostly long cells, which at the ends are pointy, are called tracheids.

The structure of hardwood and softwood can be differentiated on the microstructural level. In the case of softwood, we speak of tracheids and wood rays; in the case of hardwoods, we distinguish between fibers, vessels and wood rays.

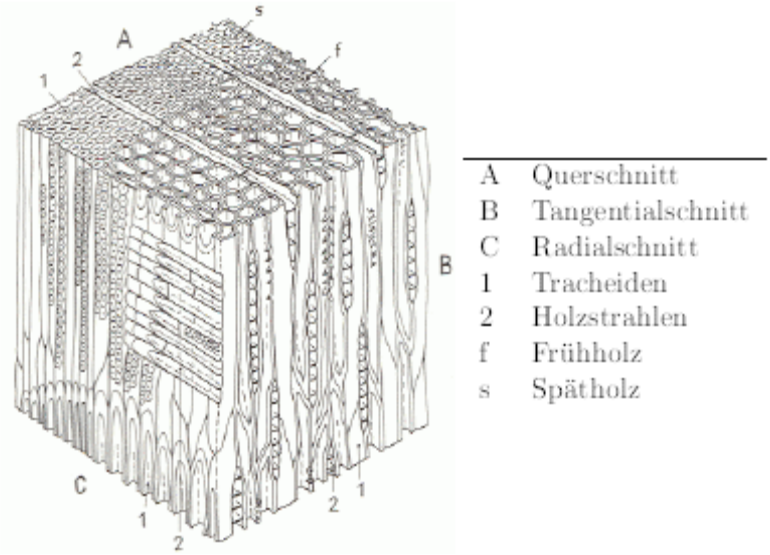

Figure 3.6: Microstructure of Wood from NIEMZ [Nie93b]

[Key: A) Profile; B) Tangential layer; C) Radial layer; 1) Tracheids; 2) Wood rays; f) Early wood; s) Late wood].

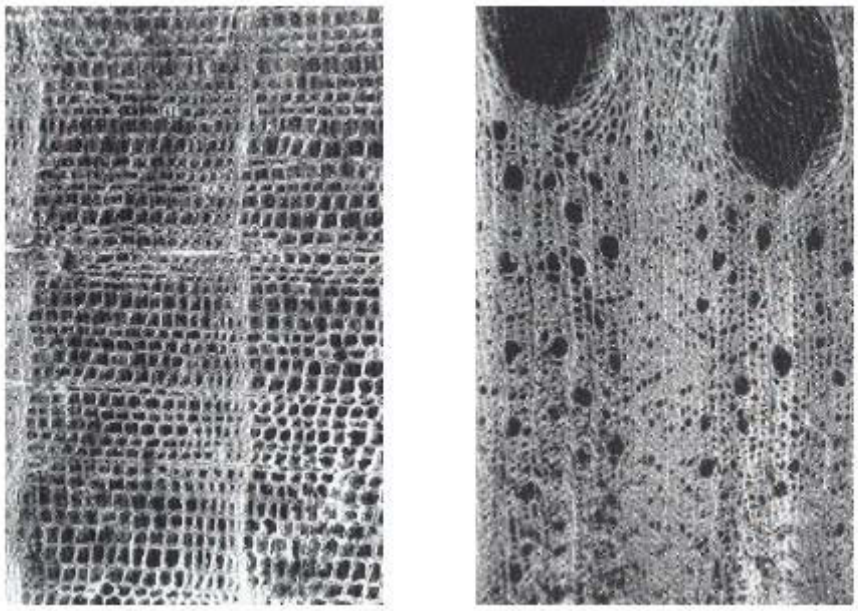

Figure 3.7: Hardwood (left) and Softwood (right) Profile on a Microscopic Level from GIBSON & ASHBY [GA97]

Table 3.1: Volumetric Fractions and Dimensions of Wood Cells According to BODIG & JAYNE [BJ82]

	Softwood		**Hardwood**		
	Tracheids	Rays	Fibers	Vessels	Rays
Vol. share [%}	85-95	5-12	37-70	6-55	10-32
Axial magnitude [mm]	2.5-7.0		0.6-2.3	0.2-1.3	
Tangential magnitude [µm]	25-80		10-30	20-500	
Radial magnitude [µm]	17-60		10-30	20-350	
Cell wall thickness [µm]	2-7		1-11	-	

Table 3.1 presents a tabular listing of characteristic features. The wood rays in the case of the softwoods are narrow and are only a few cell levels wide in the axial direction, whereas the wood rays in the hardwoods are definitely wider and cover larger areas in the axial direction. In the hardwoods, there are so-called vessel canals in which nutrients are transported in the axial direction. The share of the vessel canals in hardwoods can be as much as 55% (Figure 3.7, left), whereas the share of the wood rays in softwoods amounts to a maximum of 12%. The fibers of late woods (hardwood) compared to early woods have smaller diameters, whereas as tracheids of late wood (softwood) have the same diameter but greater cell wall thicknesses when compared to early wood.

Ultrastructure

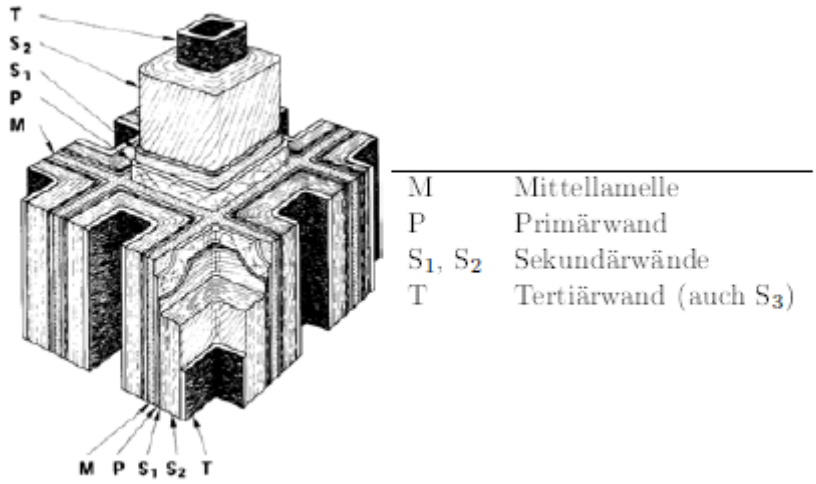

Figure 3.8: Ultrastructure of Wood According to KLEIN & SCHWAB [KS89]

[Key: M) Middle lamella; P) Primary wall; S_1, S_2) Secondary wall; T) Tertiary wall (also S_3)].

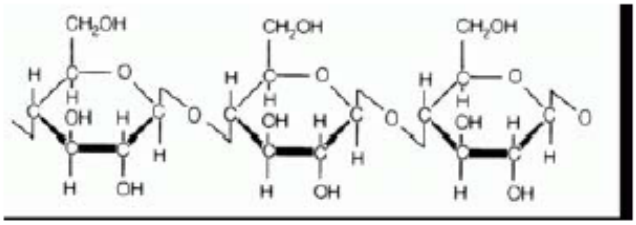

Abbildung 3.9: Ausschnitt aus einem Zellulosemolekül

Figure 3.9: Excerpt from a Cellulose Molecule

On the ultrastructural level, wood can be construed as a fiber-reinforced composite structure. The main components are cellulose, hemicellulose and lignin. With a weight of about 40-45%, cellulose $(C_6H_{10}O_5)_n$ constitutes the basic substance for the "fiber" (Figure 3.9). With a crystallitic structure, the cellulose molecule forms amorphous arrangements (microfibrils) that form the actual fibers in the various layers of the wood cell walls (see Figure 3.8). Hemicellulose, which together with lignin can be considered as a "matrix" just like cellulose, is made up of carbohydrates. In contrast to the cellulose polymerization level (about 8,000-10,000 units), the hemicellulose polymerization level is definitely less (< 200 units). Lignin consists of a complex, three-dimensional molecule with phenyl groups and in contrast to cellulose is not crystalline. For a more in-depth investigation, reference is made to NIEMZ [Nie93b] and BODIG & JAYNE [BJ82].

3.2.3. Compression Mechanisms

The function of shock absorbers for transport casks is important above all in terms of the properties of wood exposed to pressure stress. This is why we will not touch on the traction, thrust or bending area which, each by itself, would presume an intensive coverage of the entire topic.

In small expansions, there is basically a linear-elastic behavior in all three direction. The elasticity module in the axial direction is definitely greater than the modules in the radial and tangential direction. Pressure resistance or the crush limit is reached after the end of the elastic phase following a short transition area. In case of radial and tangential stress, we can observe a plateau that rises constantly all the way up to slightly until the start of a strong consolidation with a compression ratio of between 0.2 and 0.8. In contrast to radial/tangential stress, axial stress displays a differently intensive loss of cohesion after the attainment of pressure resistance. Then there are declining or constant force deformation developments until the onset of solidification in analogy to the stress in the radial/tangential direction (see Figure 3.10).

The mechanical properties of wood are anisotropic due to the prismatic structure of the cells. If we neglect the radius of the annual rings, then we can start with orthotropic material behavior (axial, radial and tangential direction). Because of the prismatic cell shape, the fiber position is of basic significance for the mechanical properties of wood. The greatest strength exists in the axial direction, whereas it definitely decreases with increasing angle between the stress direction and the fiber direction.

Axial compression. The cell walls begin to collapse at the tracheid ends at the end of elastic deformation. A macroscopic strain band or kink band is formed upon reaching pressure strength. In case of low density according to GIBSON & ASHBY [GA97], the cell walls are shifted into the cavities of opposite cells in the manner of a toothing (Figure 3.11). In the case of hardwoods, there is increased local kinking of the cell wall. Both forms of behavior are illustrated schematically in Figure 3.12. After that, there is a stationary fiber kinking, as described by POULSEN [Pou97], which, however, only in case of flawless wood, leads to macroscopically visible deformations. According to GROSS [Gro05], in case of small flaws, there are frequently oppositely extending strain or kink bands, which result in great lateral traction stresses. The wood is frequently split longitudinally as a result of this stress. At the start of consolidation, all wood cavities in the wood have collapsed, and the material behaves like a cell wall substance according to ADALIAN & MORLIER [AM02].

Radial/tangential compression. Failure laterally with respect to the fiber is characterized by the outward kinking of the cell walls parallel to the force. Lateral evasion results in a damage band of increasing size. In the radial direction, the wood rays result in a strengthening of the structure.

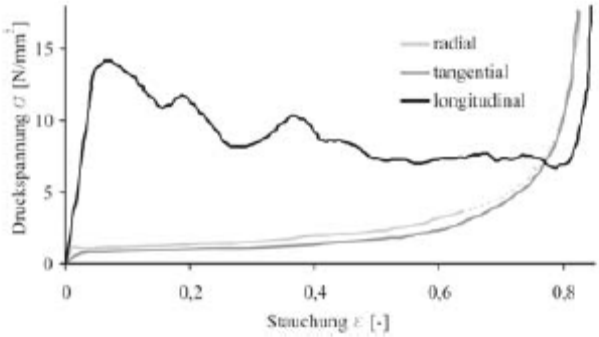

Figure 3.10: Basic Stress-Expansion Curve in Balsawood in Response to Pressure Stress According to GIBSON & ASHBY [GA97]

[Key: Druckspannung = Pressure of stress; Stauchung = Compression].

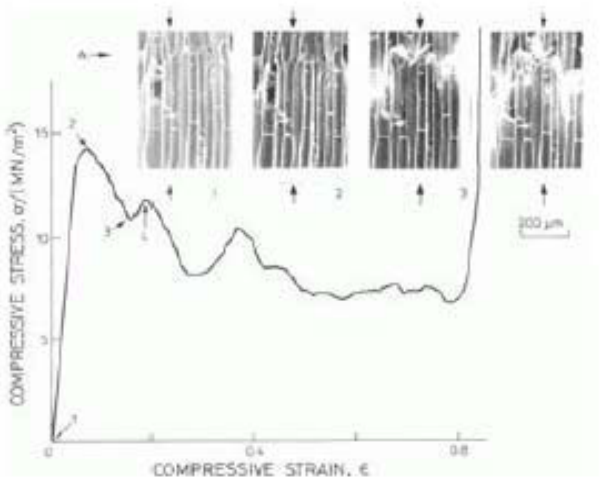

Figure 3.11: Pressure Stress Compression Curves in Response to Stress on Balsawood in the Axial Direction According to GIBSON & ASHBY [GA97]

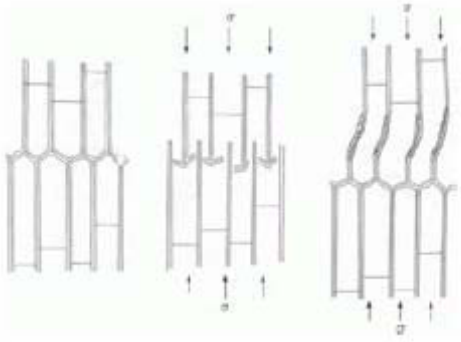

Figure 3.12: Schematic Failure Mechanisms According to GIBSON & ASHBY [GA97]; left: undeformed, center: deformed softwood, right: deformed hardwood

3.3 Factors Influencing the Mechanical Properties of Wood

The mechanical properties of wood are influenced by a large number of factors. Here we present an overview of the magnitude of the influence being exerted on the mechanical properties.

3.3.1 Fiber Position

As described in Section 3.2.3 in the case of an axial stress direction, we can see definitely greater average stresses and partly differing pressure stress compression curves when compared to the radial/tangential stress direction. The factor between average stress in the axial and transversal (radial and tangential) direction can, according to EASTERLING et al. [E+82] amount to as much as 10 (for example, for balsa). The magnitude of the difference between the radial and tangential directions depends greatly on the wood species. According to GIBSON & ASHBY [GA97], this influencing factor can be neglected for all and according to [WHB99] for some species; on the other hand, GOODMAN & BODIG [GB70] mention a significant difference in the behavior between the tangential and the radial directions. EASTERLING et al. [E+82] show that for both hardwood and softwood, the difference between the radial and tangential directions is statistically significant. KENNEDY [Ken68] traces this difference back to the different behavior of early wood and late wood and shows that a small portion of late wood will lead to greater pressure strength in the radial direction and a large portion of late wood will result in higher pressure strength in the tangential direction.

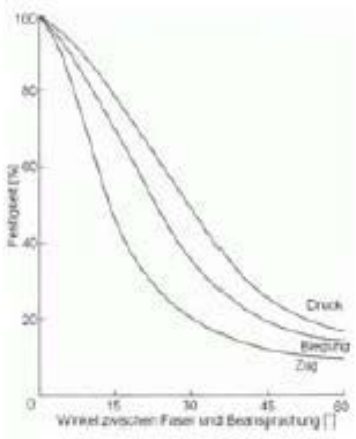

Figure 3.13: Influence of Fiber Position on Strength According to DINWOODIE [Din81]

[Key: Druck = Pressure; Faserlage = Fiber position; other entries illegible].

Equation 3.2 was derived by HANKINSON, 1921 [Han21] for the interpolation of the mechanical properties with relation to the fiber positions between 0º (axial) and 90º (transversal) (Figure 3.13). Later, KOLLMANN [Kol36] proposed an experiment of n = 2.5 to 3 for the pressure area. KEYLWERTH [Key51] confirmed equation 3.2 with n = 2 in terms of the theory of elasticity, and the equation was also validated experimentally by GEHRI & STEURER [GS79].

$$\sigma_{dB,\phi} = \frac{\sigma_{dB\parallel} \cdot \sigma_{dB\perp}}{\sigma_{dB\parallel} \cdot \sin^n \cdot \phi + \sigma_{dB\perp} \cdot \cos^n \cdot \phi}$$

ϕ	-	Last-Faser-Winkel
n	-	2...3
$\sigma_{dB\parallel}$	-	Druckfestigkeit parallel zur Faserrichtung
$\sigma_{dB\perp}$	-	Druckfestigkeit orthogonal zur Faserrichtung

(3.2)

φ	-	Load-fiber angle
n	-	2 ... 3
$\sigma_{AB\parallel}$	-	Pressure strength parallel to fiber position
$\sigma_{AB\perp}$	-	Pressure strength orthogonal to fiber position

3.3.2 Density

Density exerts essential influence on the mechanical properties of wood along with fiber position. GLOS [Glo78] investigated the influence of various active substance and action characteristics in detail (raw density, annual ring width, annual ring layout, branchiness, fiber deviation, pressure wood share, wood moisture, relative air humidity) on mechanical properties in case of small deformations. Density and moisture caused more than 90% of the variance in the results in case of monoaxial pressure tests. BUES [Bue86] confirmed this fact and emphasized that the variability above all can be traced to the raw density fluctuation. GIBSON & ASHBY [GA97], NIEMZ & SONDEREGGER [NS03] and DINWOODIE [Din00] assigned so much significance to it that an attempt was made to describe the properties, independently of the wood species, as a function of the density:

$$f = k \cdot \rho^n$$

f	-	Festigkeit
k	-	Proportionalitätskonstante
ρ	-	Dichte
n	-	Kurvenexponent

(3.3)

f	-	Strength
k	-	Proportionality constant
p	-	Density
n	-	Curve exponent

DINWOODIE [Din00] determined a correlation coefficient of 0.902 between strength and density [Din00] with the help of experiments on more than 200 samples. The densities varied between 150-1,000 kg/m^3. In areas of small density differences, VORREITER [Vor49] assumes

a linear connection between density and mechanical properties, such as elasticity modules and pressure strength. The density of the wood types to be used is therefore defined for the production of transport containers.

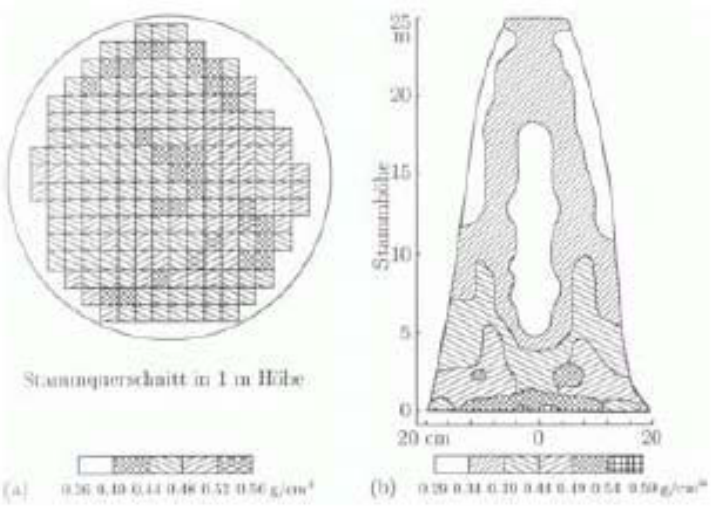

Figure 3.14: Density Distribution in a Pine Trunk According to GÖHRE [Göh58] (a) Trunk cross-section, (b) Longitudinal trunk profile

[Key: Stammdurchschnitt in 1 m Höhe = Trunk cross-section at a height of 1 m; Stammhöhe = Trunk height].

Considerable raw density differences developed within a trunk, as agreed upon by GÖHRE [Göh58] and GÖTTSCHE-KÜHN & FRÜHWALD [GKF86]. GÖHRE [Göh58] presents this situation on the basis of a lateral profile and longitudinal profile through a pine trunk (Figure 3.14).

3.3.3 Temperature

Basically, declining strengths can be expected in case of rising temperatures according to NIEMZ [Nie93b]. The magnitude of the influence exerted by the temperature on the elasticity module according to KOLLMANN [Kol82] amounts to as much as 40% between -20 and +60ºC. The drop in the pressure strength according to GLOS & HENRICI [GH90] amounts to about 55% between -20 and +150ºC. A cause is generally believed to be represented by the intermolecular attraction forces (hydrogen bridge bonds), which are weakened by the frequency of the atomic or molecular oscillations caused by the temperature. According to NIEMZ [Nie93b], the magnitude of the influence is additionally a function of the sample shape with which the characteristics are determined.

3.3.4 Moisture

Wood must be understood as a partly hygroscopic, capillary-porous substance. The share of cavities on the average amounts to 50-60% of the volume. Wood can take on and store water by way of absorption and capillary transport processes. The water contained in the wood

influences the mechanical properties. The wood moisture content is calculated according to equation 3.4.

$$u = \frac{m_u - m_{dtr}}{m_{dtr}} \cdot 100[\%]$$

u	-	Feuchtegehalt
m_u	-	Masse des feuchten Holzes
m_{dtr}	-	Masse des darrtrockenen Holzes

(3.4)

u	-	Moisture content
m_n	-	Moisture of moist wood
m_{dtr}	-	Mass of oven-dried wood

Basically, the type of water infiltration is a decisive factor in determining the magnitude of the influence exerted by the moisture on the mechanical properties. No water is present in the wood in the oven-dried state. Water is absorbed by absorption and capillary condensation in the wood moisture range of between 0 and about 22-35% until the fiber saturation point has been reached. Water occurs only in the "bound" form, it is stored between the microfibrils and, according to KOLLMANN [Kol82], changes the intervals[8] of the microfibrils among each other, depending on the moisture share. A change in the intervals results in a change in the attraction forces of the microfibrils (hydrogen bridge bonds) and thus has an effect on the cohesion of the wood. The fiber saturation area characterizes the maximum possible content of bound water. This area begins between about 22 and 35% moisture content and as a mean value at about 28%. From here on in, the water is freely deposited in the hollow spaces. According to KOLLMANN [Kol82], any further infiltration of water above and beyond the fiber saturation area does not have any meaning for the strength properties.

3.3.5 Stress Velocity

REID & PENG [RP97] investigated the influence of expansion rate on the strength properties for five different wood species with the help of a "Split-Hopkinson-Bar" experimental setup. At stress velocities of up to 360 m/sec, they showed that there is a partly linear and partly exponential dependence between the pressure strength and the stress velocity. In case of an axial stress direction, the dynamic factor is

$$S_d = \frac{\sigma_d}{\sigma_s}$$

S_d	-	Dynamischer Faktor
σ_d	-	Dynamische Spannung
σ_s	-	Statische Spannung

(3.5)

[8] Interfibrillary cavities.

S_d	-	Dynamic factor
σ_d	-	Dynamic stress
σ_s	-	Static stress

between 1 and 4.5 at a stress velocity of up to 360 m/sec. That corresponds to expansion rates of up to 18,000 s^{-1}.

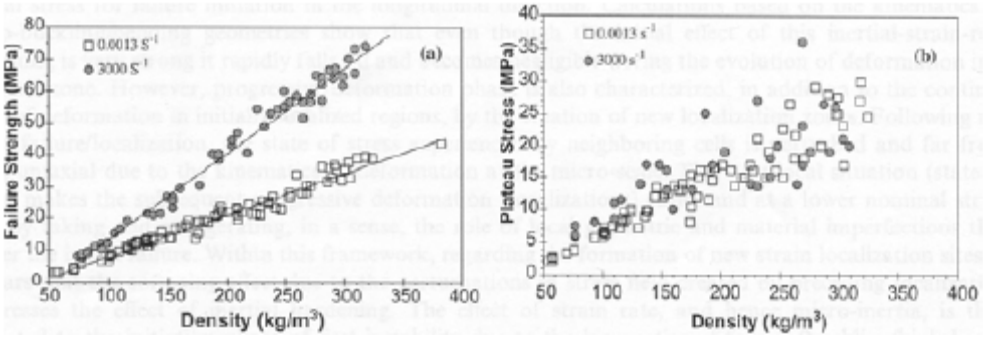

Figure 3.15: Expansion Rate as a Function of Plateau Stress and Pressure Strength in Balsawood According to VURAL & RAVICHANDRAN [VR03]

According to VURAL & RAVICHANDRAN [VR03], the pressure strength for balsawood increases with the expansion rate, whereas the average pressure stress compression plateau is almost not influenced at all by the expansion rate (Figure 3.15). Higher expansion rates also result in an earlier start of consolidation.

KOLLMANN & COTE [KCJ68] show a linear dependence of the pressure strength on the stress velocity. An increase in the pressure strength by a factor of 1.07 can be derived for pine, birch and oak for every 10-fold increase in the stress velocity.

Investigations on the expansion rate dependence in case of large deformations have so far not been published.

3.3.6 Attenuation

FOSTER [Fos92] determined that in case of periodic stress, attenuation factors [are significant] for axial stress regardless of the stress level, of the load history and of the frequency. In case of stress in the axial direction, attenuation factors between v = 0.002 - 0.009 and radial/tangential factors between v = 0.006 - 0.018 are given.

3.3.7 Transversal Strain

Due to the anisotropy of the wood, we must, according to NIEMZ [Nie93b], consider here six Poisson constants for the elastic area. According to NEUHAUS [Neu81], the usual reduction to three constants for wood is not possible because

$$s_{ij} \neq s_{ji} \tag{3.6}$$

s_{ij} - Querdehnzahl od. Poissonsche Konstante

s_{ij} - Poisson's constant

According to ZINK et al. [ZHS97], one can generally expect decreasing Poisson's ratios for poplar trees in case of greater stresses. SLIKER [Sli85] [Sli89] determines the Poisson constants for nine species of wood. While s_{ar}, s_{al}, s_{rt} and s_{tr}[9] are between 0.3 and 0.7, s_{ra} and s_{ta} amount to 0.03 and 0.043 (effective radial and tangential directions on axial direction).

Information for the plastic area is difficult to derive via the transversal stress because the plastic deformation of wood is characterized by failure.

3.3.8 Effective Magnitudes

DILL-LANGER et al. [DL+03] describe a decreasing strength with increasing sample size for the area of traction [stress]. According to WOLCOTT et al. [W+89], the elasticity module in the pressure area rises with increasing relative sample height, whereas the sample volume does not influence the strength. SCHNEEWEISS [Sch63] emphasizes that for the case of the ash tree, the strength in case of transversal stress is a function of the sample size. According to DOBBIN [Dob90], the strength data determined on small, flawless wood specimens are definitely higher than those determined on specific structural parts. ISSLER, ROUSS & HÄFELE [IRH03] present a general magnitude factor as a function of the related highly stressed volume. For a scale factor of 1:2.5, we get a strength decline for the 1:1 case to 0.84 ± 0.08. The reasons for this are given in the mentioned publications as influences deriving from volume and marginal layer along with nonhomogeneities and inherent stresses in the wood.

3.3.9 Influence of Structure

According to KENNEDY [Ken68] and MASCIA & CRAMER [MC00], changes in the density, the temperature and the moisture exert less influence on the mechanical properties of wood than does the volume ratio from early wood and late wood, and they thus emphasize the significance of this influencing factor.

Basically, deviations from the structural makeup (branches, cracks, etc.) exert very great local influence on the behavior of wood exposed to pressure stress. Branches represent a jump in the quasihomogeneous structure of the wood with different fiber positions and densities. Pressure wood (wood compressed by natural growth) has a definitely higher density than normally grown wood (according to [WHB99] 30-40%) and thus points up the dependences described in Section 3.3.2. Young wood (in the vicinity of the pith) has reduced density and displays definitely larger angles between microfibrils and axial direction. Both characteristics result in reduced strength.

[9] a = axial, r = radial, t = tangential

3.3.10 Conclusions Regarding Influencing Magnitudes

GIBSON & ASHBY [GA97] correctly stated: *"Wood is complicated stuff."* The mechanical properties and the factors changing them in various wood species are investigated in a series of studies; basic mechanisms are understood and documented in detail. A big handicap for the problem tackled in this study is the concentration of the past investigations upon the area of elastic deformations or small plastic deformations (for example, POULSEN [Pou97]. Most of the investigations on the mechanical properties of wood were initiated by questions from the construction industry, which naturally considers wood generally only in the elastic area. Very few publications address the behavior of wood in response to pressure stress in conjunction with large deformations. More investigations on the properties of wood in case of large deformations are necessary for shock-absorber design. Modeling should be done for the behavior of wood in response to axial pressure stress in conjunction with large deformations. Particular consideration should be given to the influence of temperature, moisture content and stress velocity.

3.4 Summary

The various construction principles for shock-absorbing parts combine the same functional principle: conversion of kinetic energy into form change energy. It is about wood-filled shock absorbers that prevailed along with foams and honeycomb structures, especially in Europe and Asia.

A bibliography search was performed on the mechanical properties of wood and their dependence on various influencing factors. The behavior of wood in case of small deformations was investigated adequately; on the other hand, so far very little has been published on the behavior of wood in response to pressure stress in conjunction with large deformations. It was proposed with the help of more extensive investigations to model the behavior of wood in response to pressure stress in conjunction with large deformations.

The influences deriving from various parameters upon the mechanical properties of wood were investigated above all for the elastic area. It is not clear to what extent the results - above all, regarding the dominating influencing factors represented by density, temperature, moisture, expansion rate and influence of magnitude - can be transposed to the area of large deformations. The influence of the parameter consisting of the structure of the wood usually is minimized by suitable sorting of the wood products.

4 Experimental Investigations

In this chapter, we will describe the experimental investigations on the behavior of wood with the help of small samples, parts experiments with shock-absorbing parts and drop tests with prototypes of shipping items for radioactive substances. In a first part, we present the basic concepts, the implementation and evaluation of cask and shock-absorber drop tests. The drop tests are used as verification base in order to investigate the applicability of various computation methods to actual transport casks holding radioactive substances. The deformed shock-absorbing parts are analyzed in order to determine the energy-absorption mechanisms responsible for the shock absorption. In another part, we will describe shock tests with wood samples to determine the pressure stress compression interrelationships under the effects of various influencing parameters.

4.1 Cask Drop Tests

The description of the drop tests is guided partly, for example, by [MNK08]. After a brief description of the drop test facility, we introduce the drop casks MHI MSF69BG® AND GNS CONSTOR® V/TC as well as the test object represented by shock- absorber testing in greater detail, and we present the pertinent test results. The tests were performed by the "Experimental Cask Investigations" team of BAM. The results are used with the permission of the GNS and the MHI.

4.1.1 Description of Drop Test System

The new drop test system of BAM in Horstwalde is the largest of this kind in the world and meets the IAEA requirements for drop tests using shipping items holding radioactive substances up to a total weight of 200 mg.

The BAM drop test system consists of three main components: the drop tower with the winch house and the hoisting winch, a light-metal shop with movable roof and the impact foundation, as described in greater detail in MÜLLER, MINACK & DROSTE [MMD04] and DROSTE, MÜLLER & MINACK [DMM05] and as shown in Figure 4.1. The drop tower, a 36-m-high steel pipe structure, stands over the shop on four separate piling foundations. At a height of 33 m, the carrier platform holds the hoisting winch, whose maximum permissible hoisting mass is 200 mg and whose maximum hoisting height is 30 m.

The nonresilient impact foundation for test objects of up to 200 mg, built according to the IAEA Regulations [TSR08], consists of a massive steel-reinforced concrete ashlar (concrete grade B25/B35) with dimensions of 14 m x 14 m x 5 m and a steel impact plate embedded in the middle, flush with the surface. This 220-m-thick impact plate (impact surface 4.5 m x 10 m) is connected via 40 pieces of M36 threaded spindles with the reinforced concrete ashlar in a form-locking and force-locking manner and constitutes a direct impact area for the test objects. The total mass of the impact foundation is 2600 mg.

The test object is dropped with a drop device that works in a moment-free manner. A hydraulically supplied force causes a tear bolt to be ripped off; nailed upon the latter is the test

object via a coupling piece (drop fork). This moment-free drop guarantees the exact maintenance of the adjusted drop orientation of the test object after the impact.

a Abwurfvorrichtung
b Messkabel
c Aufprallfundament[a]
d Abspannseile
e Messwarte
f Meßauslöser (Trigger)
g Schutzwand

[a]Stahlplatte, Stahlbeton

Figure 4.1: Structure of Experiments for Drop Test System as BAM

[Key: a) Drop device; b) Measurement cable; c) Impact foundation[a]; d) Tension release ropes; e) Measurement station; f) Measurement trigger (trigger); g) Protective wall].

[a] Steel plate, reinforced concrete.

4.1.2 MSF69BG® Fuel Element Transport and Storage Cask, Scale 1:1

The test cask is an original-scale model of the transport and storage casks (TLB) MSF69BG® by the manufacturer Mitsubishi Heavy Industries Ltd. To hold up to 69 fuel elements from boiling-water reactors (Figure 4.2).

Table 4.1: Main Dimensions and Masses of Selected Parts of the MSF69BG® Test Casks

MSF69BG®	**Dimensions and Masses**
Total length with shock absorbers	6900 mm
Outside diameter of cask body	2178 mm
Outside diameter of shock absorbers	3205 mm
Mass of loaded casks	113 mg
Mass of a shock absorber	7 mg
Total mass of test objects	127 mg

The monolithic, forged cask body consists of low-alloy steel. The outside of the cask body surrounds a neutron shielding layer consisting of epoxy resin, which is enveloped in a steel jacket. One pair each of supporting pegs is arranged to handle the cask on the lid and the bottom. A double-lid system consisting of a primary and secondary lid closes the cask. The lids are made of low-alloy, forged steel. The lid seal is provide by means of metal seals that are made in the form of aluminum-jacketed Doppel-Helicoflex® steel. The lids are screwed with an inside hexagonal slender-head screw, size M42. The carrying basket to hold the fuel elements consists of 69 individual aluminum hollow sections with a square cross-section that fill the cask's inside space in a form-locking manner. The test cask is charged with substitute fuel elements that are made as hollow section with a square cross-section. The geometric main dimensions and masses of selected cask parts can be seen in Table 4.1.

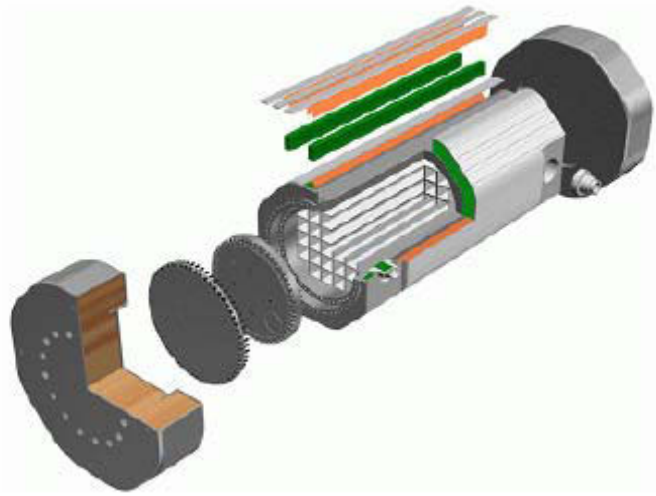

Figure 4.2: Schematic Illustration of Test Cask MSF69BG® with Carrying Basket Structure

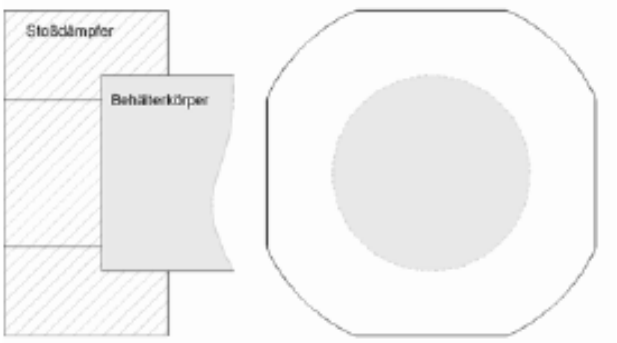

Figure 4.3: Schematic Profile Through MSF69BG® Shock Absorber

[Key: Stossdämpfer = Shock absorber; Behälterkörper = Cask body].

On the lid and the bottom, the test cask is equipped with one shock absorber each (lid and bottom shock absorbers). The shock absorbers have a 5-mm-thick jacket made of high-grade steel and are filled with balsawood, cedar wood and oak wood. A schematic sketch of the shock absorber can be seen in Figure 4.3.

4.1.3 CONSTOR® V/TC Fuel Element Transport and Storage Cask, Scale 1:1

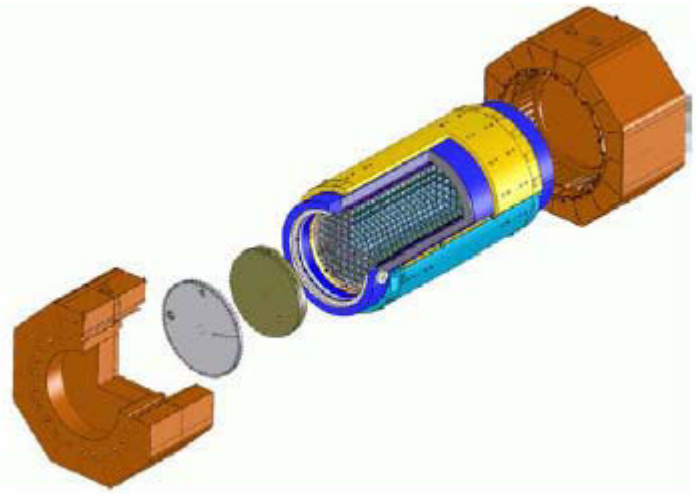

Figure 4.4: Schematic Illustration of the CONSTOR® V/TC Test Cask according to KÖNIG et al [K+05]

The CONSTOR® V/TC test cask of the Gesellschaft für Nuklearservice GmbH (GNS) [Company for Nuclear Service] is an original-sized model of the CONSTOR® V/69 transport and storage cask for spent fuel elements from light-water reactors with a total thermal output amounting to a maximum of 30 kW. This construction principle is currently employed as CONSTOR® RBMK 1500 for the intermediate storage of spent fuel elements from the Ignalina power plant in Lithuania. Figure 4.4 presents a schematic illustration of the CONSTOR® V/TC.

The cask body of the CONSTOR® V/TC consists of a steel and heavy concrete sandwich construction and is closed with a double-lid sealing system. Between an outer and an inner jacket made of steel (see Figure 4.5), there is a filling consisting of Constorit®, a special cement with iron added. The content is simulated by a substitute body. The flange area is welded upon the inner and outer jacket. Copper sheet metal pieces are attached between the inner and outer jackets to derive the decay heat. After two drop tests with 1:2 models, the construction was expanded by a wider outer subdivided jacket (Overpack - in Figure 4.4 yellow/bright blue) for protection against impacts upon a spike. The main geometric dimensions and masses of the CONSTOR® V/TC test cask can be seen in Table 4.2.

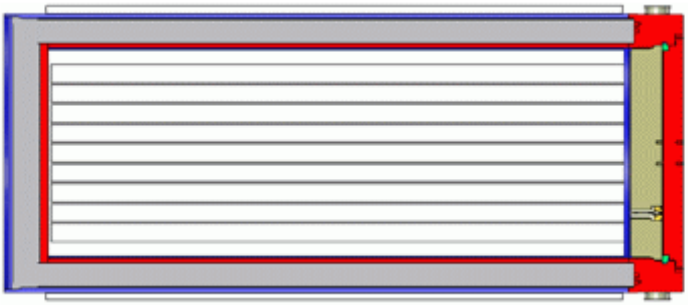

Figure 4.5: Schematic Profile Through a CONSTOR® V/TC Without Shock-Absorbing Parts According to CONSTOR® V/TC

Table 4.2: Main Dimensions and Masses of Selected Parts of the CONSTOR® V/TC Test Cask

CONSTOR® V/TC	**Dimensions and Masses**
Total length with shock absorbers	7445 mm
Outside diameter of cask body	2332 mm
Outside diameter of shock absorber	3510 mm
Outside diameter of protective plate in shock absorber	2700 mm
Mass of charged cask	
Mass of a shock absorber	110 mg
Mass of the Overpack	20 mg
Total mass	31 mg
	181 mg

The shock-absorbing parts consist of a wood-filled steel plate construction. The shock-absorber construction contains an internal 60-mm-thick divided impact plate to protect the lid system against point-like stress. The outer cladding consists of sheet metal pieces with a thickness of 5 mm. The filling of the cavities consists of fir wood with alternating fiber layers (stressed 50% axially, 50% transversally). The angle between the two side surfaces is 135º. The bottom and lid shock absorbers have the same structure. Basic dimensions of the shock-absorbing parts can be seen in Figure 4.6.

4.1.4 Shock-Absorber Testing

A shock-absorber test was conducted on a scale of 1:2 with the help of a substitute mass that was leaned against a CASTOR® transport cask; only the shock-absorber and shock-absorber attachment components were subjects of the investigations. All of the other components were used to ensure the necessary drop mass, or they were auxiliary components. The substitute mass consisted of a cylindrical base body and a screwed lid in the position of the primary lid. We decided to refrain from secondary lids, small lids, seals and content models as well as carrying baskets.

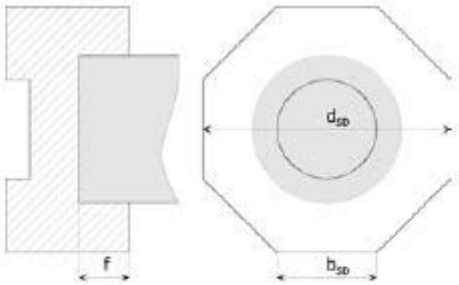

d_{SD} =3510 mm	Stoßdämpferdurchmesser
b_{SD} =1554 mm	Breite der Stoßdämpfergrundfläche
f =900 mm	Tiefe des Stoßdämpfers unter der projizierten Behälterfläche

Figure 4.6: Schematic Profile Through a CONSTOR® V/TC Shock Absorber

d_{SD}	Shock absorber diameter
b_{SD}	Width of shock-absorber base surface
f=900 mm	Depth of shock absorber below projected flask surface

The substituted mass was replicated after a cask in order realistically to acquire possible factors influencing the shock-absorber reaction. The main geometric dimensions and masses of the test object can be seen in Table 4.3. The test sample was provided by GNS.

Table 4.3: Main Dimensions and Masses of Selected Parts of the Shock-Absorber Test

Shock-Absorber Test	**Dimensions and Masses**
Total length including shock absorbers	3700 mm
Outside diameter, cask body, substitute mass	1225 mm
Outside diameter, shock absorber	
Outside diameter, protective plate in shock absorber	1500 mm
Mass of cask	1211 mm
Mass of a shock absorber	
Total mass	10.8 mg
	1.5 mg
	13.8 mg

The structure of the shock-absorbing parts is similar to that of the CONSTOR® V/TC. They consist of an interior steel plate on which stands the steel sheet structure. The cavities of this steel sheet structure are filled with fir wood.

4.1.5 Performance of Drop Tests

Test Specimen MSF69BG®, Scale 1:1 - Slap Down

This drop test was performed on September 24, 2004 before the eyes of the international technical experts, who happened to be in Berlin on the occasion of the 2004 "Packaging and

Transport of Radioactive Materials" (PATRAM) Fair. The test cask was dropped from a height of 9.3 m upon the nonresilient foundation. The drop position of the test cask was chosen with a 10º inclination of the longitudinal axis of the cask with respect to the horizontal that the first impact took place on the bottom shock absorber and the second impact occurred on the lid shock absorber. This drop position is called Slap Down and can be seen in Figure. 4.7.

Figure 4.7: Performance of the MSF69BG® Drop Test in the Slap Down Drop Position on 09/24/2004

Test Specimen MSF69BG®, Scale 1:1 - Vertical Drop

A drop test in the vertical drop position took place on November 16, 2004 at the BAM drop test facility in Horstwalde as part of an application for the licensing of a transport cask holding radioactive substances. The test cask dropped from a height of 9.3 m upon the nonresilient foundation. The impact took place on the lid side.

Test Specimen CONSTOR® V/TC, Scale 1:1 - Horizontal Drop

This drop test was performed on September 21, 2004, as in the case of the test on September 24, before the eyes of international technical experts, who happened to be in Berlin on the occasion of the 2004 "Packaging and Transport of Radioactive Materials" (PATRAM) Fair. The test cask fell from a height of 9.0 m with horizontally arranged longitudinal cask access (see Figure 4.8) upon the nonresilient foundation.

Shock-Absorber Testing

The drop test was performed on June 27, 2006 at the drop test stand of the BAM in Horstwalde. The test object fell from a height of 9.0 m with horizontally arranged longitudinal cask access upon the nonresilient foundation.

4.1.6 Results

Results of Drop Tests with MSF69BG®

Slap Down drop position. In case of the slap down drop, the center of gravity of the cask is not perpendicularly above the impact contact point, as in the case of the vertical or edge drop; therefore, the test cask is made to rotate after impact of the first cask end (primary impact). The subsequently second impact (secondary impact) with the opposite end takes place with

Figure 4.8: Performance of the CONSTOR® V/TC Drop Test in the Horizontal Drop Position on 09/21/2004

Figure 4.9: Performance of Shock Absorber Testing Drop Test in the Horizontal Drop Position on 069/271/2006

an impact velocity that is greater than the velocity resulting from a freefall (see also QUERCETTI, BALLHEIMER & WIESER [QBW02]. Here is the detail regarding the impact kinetics of the test cask: In the first 40 msec, as of the start of impact (t = 0), the bottom end of the cask is delayed by the initial impact velocity (13.5 m/sec) resulting from the free drop with a maximum rigid body play of 508 m/s^2 (52 g) to 0 m/sec. The bottom shock absorber in this process remains in contact with the impact plate, while the lid end of the test object is accelerated to an impact velocity of about 16 m/sec due to rotation. The second impact is definitely rougher with a maximum rigid body delay in the amount of 1088 m/sec than the first impact (508 m/s^2 OR 52 g). The impact duration is 42 msec for the first impact and 30 msec for the secondary impact. A visual examination after the drop test did not show any visual damage to the cask body. The way in which both the order of magnitude of the deformations of the shock-absorbing parts checked with the anticipated figures. The integrity of all screw connections was preserved. The tightness of the cask was ensured.

Vertical-drop drop position. As in the case of the slap down impact, a visual inspection after the drop test did not show any visible damage to the cask body or any other components of the tightly sealed enclosure. The integrity of the screw connections and the tightness of the casks were preserved.

Figure 4.10 shows the delay-time curve at measurement point A311z. The measurement is on the cask body on the lid side inside in the 0º position. The delay amounts to a maximum of about 380 m/s^2 (39 g). The decline in the delay between 20 msec and 30 msec results from an impact of the cask content upon the primary lid, Due to the impact kinetics and the gap between the content and the lid, there was a time delay in the impact. The deformations of the shock

absorber can be seen in Table in 4.4 The undeformed shock absorber at this point is about 610 mm. A deformation of 259 mm therefore corresponds to a deformation grade of 42.5%.

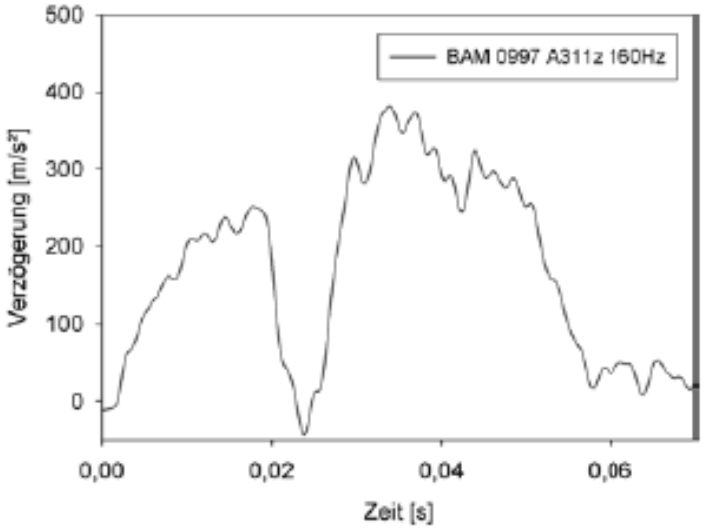

Figure 4.10: Experimentally Determined Deceleration-Time Curve for the 9.3-m Vertical Drop of the MSF69BG® (Low Pass Filter 1160 Hz)

[Key: Y-axis=Delay; X-axis=Time].

Table 4.4: Experimentally Determined Deformation from the 9.3-m Vertical Drop of the MSF69BG®

MSF69BG® Vertical Drop	**Test**
Maximum deformation	259 mm
Maximum deformation degree	42.5%

Results of Drop Test with CONSTOR® V/TC

A visual inspection after the drop test did not reveal any visible damage to the cask body or the outer jacket (Overpack). The integrity of all screw connections was preserved. The tightness of the cask was ensured.

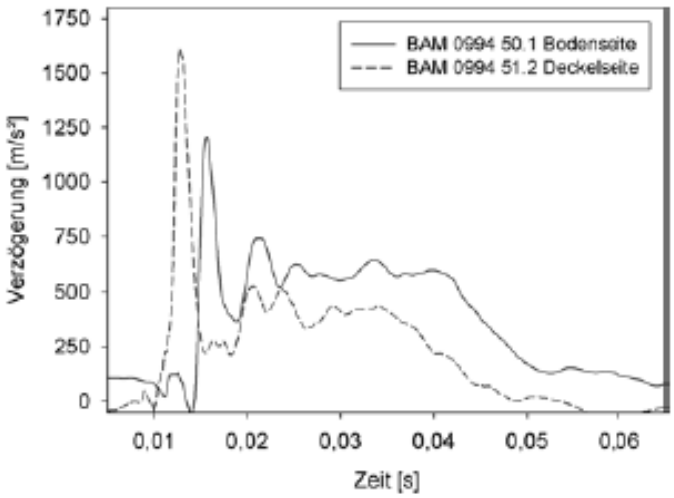

Figure 4.11: Experimentally Determined Deceleration-Time Curves for the 9-m Horizontal Drop of the CONSTOR® V/TC on the Lid and on the Bottom (150-Hz Low-Pass Filter)

[Key: Verzögerung = Delay; Zeit = Time; Bodenseite = Bottom; Deckelseite = Lid].

Table 4.5: Experimentally Determined Deformations from the 9-m Horizontal Drop, CONSTOR® V/TC

CONSTOR® V/TC	**Test**
Maximum deformation, lid,	150 mm
Maximum deformation, bottom	171 MM
Maximum deformation grade, lid	37.9%
Maximum deformation grade, bottom	42.2%

Figure 4.11 shows delay-time curves of two acceleration sensors (BA) processed with a 150-Hz low-pass filter. BA 51.2 is on the lid on the inside of the cask flange in the 180º position, that is to say, opposite the impact side. BA 50.2 is at the corresponding spot in the bottom area of the cask. In spite of the very low filter frequency of 150 Hz, we can see a pronounced peak in the delay-time curve at about 12 msec at measurement point 51,2 (lid). Using the low-pass filter with a boundary frequency of 150 Hz, the maximum delay was 1600 m/s^2 (163 g). A comparison of the curves of the measurement signals 50.2 (cask body, bottom) and 51.2 (cask body, lid) in Figure 4.11 shows a time shift of about 3-5 msec between the two signals. An analysis of the high-velocity video images[1], taken during the drop test, shows that the cask impacted with a small angle between the longitudinal cask axis and the foundation. The primary impact took place on the lid, whereas the secondary impact occurred on the bottom. The impact angle can be estimated according to equation 4.1 at 0.5-1º from the time difference between the acceleration signals (see Figure 4.11).

[1] We used a camera system by the KODAK Company with 4,500 images/second.

$$\alpha = \arcsin\left(\frac{v \cdot \delta t}{l_{Beh}}\right) \approx 0,5 - 1°$$

α	Slap Down Winkel
v	Fallgeschwindigkeit
δt	Zeitdifferenz der Beschleunigungssignale
l_{Beh}	Behälterlänge

(4.1)

α	Slap Down angle
v	Drop velocity
δt	Time difference between the acceleration signals
l_{cask}	Cask length

Table 4.5 shows the deformations measured on the shock-absorbing parts. The slight inclination of the longitudinal cask axis with respect to the foundation during the impact process can explain the deviation between the bottom and the lid.

Results of the Shock-Absorber Testing Drop Tests

An analysis of the cask impact using high-speed video images show that the test specimen at the moment of impact had a slight axial twist (Figure 4.12).

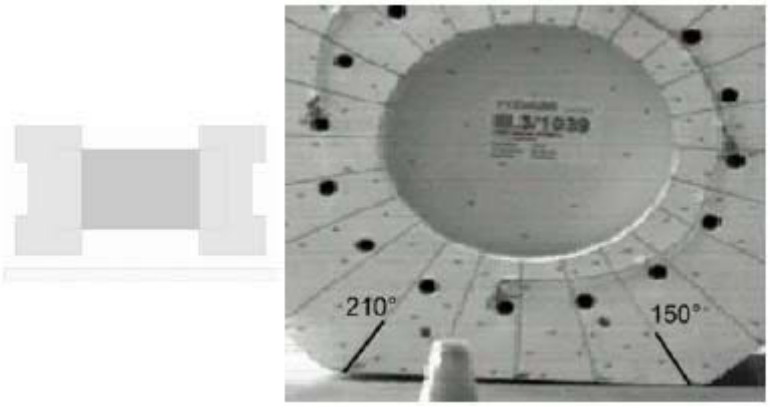

Figure 4.12: High-Speed Video Image at Moment of Impact Upon the Lid Shock Absorber

On the basis of the time difference between the impact against the bottom and the lid, we can draw conclusions to the effect that the test object impacted at an angle of about 0.2º between the longitudinal axis and the foundation. External deformations on the shock absorbers could be seen after the drop test, but no significant damage could be identified to the shock-absorber substitute mass. The greatest deformation on the shock-absorbing part could be seen at the impact level (150-200º). Here and there, welding seams were torn along the shock-absorber metal cladding. At a filter frequency of 2 kHz, the maximum delay in the middle of the cask amounted to about 2560 m/sec (260 g). Figure 4.13 shows the rigid body delay-time curves

(350-Hz filter frequency). The deformations of the cask substituted mass remain within the elastic range.

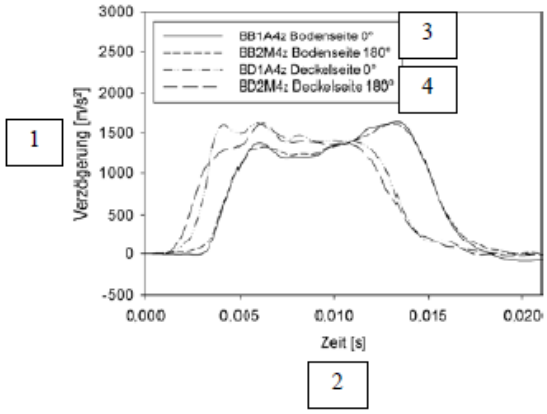

Figure 4.13: Acceleration-Time-Curves, Shock Absorber Testing, in the 0º and 180º Positions (impact at 180º on the bottom and lid, 9-m horizontal drop)

[Key: 1) Delay; 2) Time; 3) Bottom; 4) Lid].

4.1.7 Deformation Measurement Using the Strip Projection Method

An optical three-dimensional deformation measurement using the strip projection method was performed for the first time for the shock-absorbing parts during the shock-absorber test. A three-dimensional service model of the object to be measured is calculated on the basis of a point cloud determined with the help of a stereo camera. The measurement was performed by the "Measurement and Testing Technology, Sensors" team of the BAM.

Description of Method

The three-dimensional sensor consists of an LCD projector and two cameras arranged in a stereo pattern. The mutually firmly positioned camera arrangement are so calibrated with relation to a measurement volume using a local sensor coordinate system that from the image dots found in both cameras, which show the same object dot, one can determine that dot's three-dimensional coordinates in this sensor coordinate system.

In a time sequence, the projector casts parallel-oriented bright and dark light planes into the measurement volume. The light planes are detected on the surface of the shock absorber as a strip pattern. Each individual surface point in both camera images can be identified by of the sequence of these strip patterns. The position and orientation of both cameras in space is known from the above-described camera calibration; therefore, we can now determine the three-dimensional coordinates that belong these homologous dots.

For the time being, however, we only determined the three-dimensional dot cloud in an individual sensor picture. To measure a shock-absorber all around, we need to assemble numerous image parts next to each other. That was done with circular measurement markers applied additionally upon the shock absorber; the center coordinates of these markers in the

object coordinate system are known from a previously performed photometric measuring process. If the centers of the measurement markers are determined in the strip projection views, then the dot clouds from the local sensor coordinate system can be transformed into the superordinate object coordinate system from the photometric measurement process. The surface segments of the measurement markers used for assistance and on which no three-dimensional data are generated are subsequently interpolated. Further information can be found in [AT007].

Uncertainty of Results

The increased uncertainty of results deriving from the ATOS II measurement system used in combination with the pertinent photogrammetry determined on the basis of the VDI/VDE Guideline 2634 "Optical 3-D Measurement Systems" [VD106} is better than ±0.1 mm for a measurement volume on the order of magnitude of the shock absorbers. This means that the absolute distance values, determined for the shock absorbers that are measured all around in their own coordinate system, will be within the mentioned range of values with a probability of 95%.

Implementation

To determine the deformation, the shock-absorbing parts were mounted on the cask, separately and together, both before and after the drop test. Figure 4.14 shows the measurement setup.

Figure 4.14: Measurement Setup for Measuring the Shock-Absorbing Part During the Shock-Absorber Test Using the Strip Projection Method

Results

Figure 4.15 shows a shock absorber that is to be measured prior to the test. The different colors show the very minor deviations from the final product specifications.

Figure 4.16 shows a three-dimensional model of a shock-absorbing part as the result of measurement using the strip projection method after the drop test. Deviations from the state prior to the test are color coded. We can see definite deformations in the impact area.

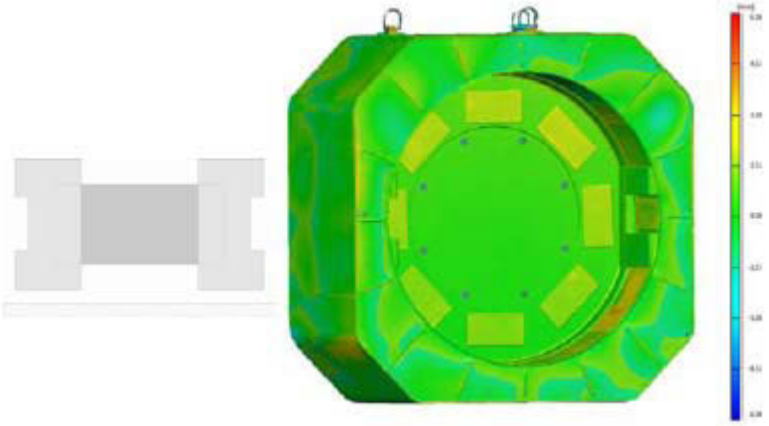

Figure 4.15: 3-D Model of a Shock-Absorbing Part as a Result of Measurement Using the Strip Projection Method Prior to Impact, Color Coding and Deviation from the Final Product Specifications

[Key: 1) View upon inside of shock absorber].

Form changes can be quantified with a high degree of accuracy by comparing the measurements before and after the drop test. The relative change in the distance dimension between the impact surface and the shock-absorber protection plate amounts to about 61 mm. Further details can be found in GRÜNDER et al. [GKMM07].

Conclusion

The optical measurement method was used for the first time for the purpose of digitalizing the three-dimensional surface arrangement. The strip projection method is very well suited when it comes to making a relative comparison of the models before and after the drop test, all with relation to an internal mathematical model, and thus precisely quantifying the deformation of the shock-absorbing parts.

4.2 Analysis of Shock-Absorbing Parts

The drop tests, shown in Subchapter 4.1, were analyzed in greater detail in the context of this study with regard to the behavior of shock-absorbing parts in connection with energy absorption.

4.2.1 Elastic Resiliency

An analysis, done with the help of carrying peg substitute models[2] on the MSF69BG® in the Slap Down drop, showed that the shock-absorbing part is again elastically extended backward after the end of the shock process by a significant amount. For this drop position and this shock-absorbing part, the elastic resiliency came to about 20-30 mm. The interval of the

[2] Substitute carrying pegs, made of thin sheet metal, were intended to clarify whether carrying pegs come into contact with the impact foundation during the drop test.

deformed carrying peg substitute models from the foundation was measured after the drop test. That corresponds to an elastic resiliency of about 5-7.5%.

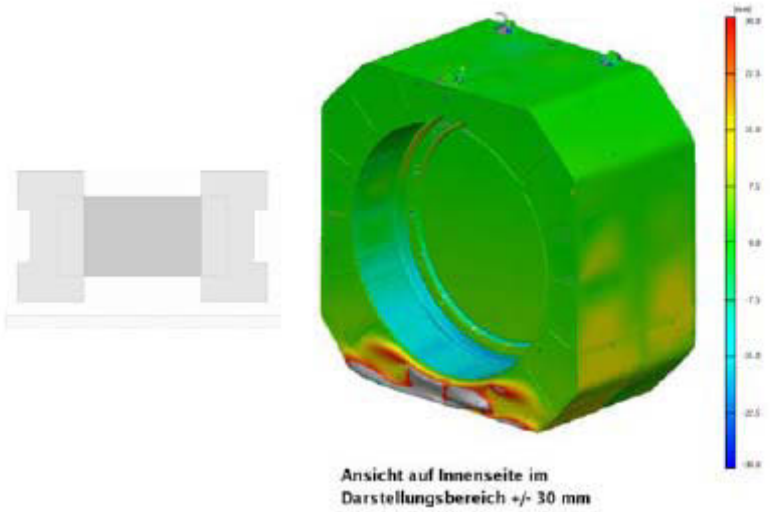

Figure 4.16: 3-D Model of a Shock-Absorbing Part as a Result of Measurement Using the Strip Projection Method Following the Impact, Color Coding of the Change with Respect to the Test Object Measured Prior to Impact

[Key: 1) View upon inside within imaging range of +/- 30 mm].

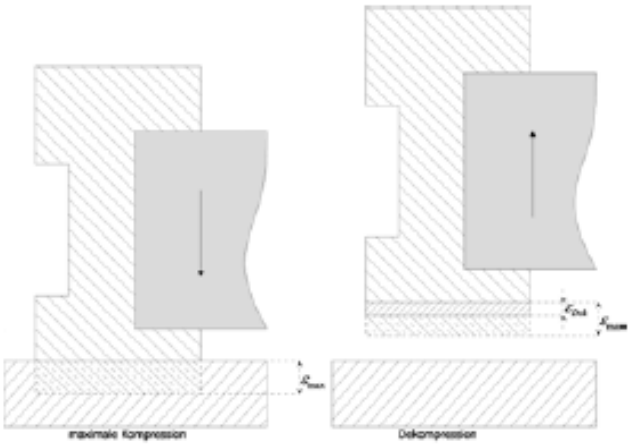

Figure 4.17: Schematic Illustration of the Elastic Resiliency, left: maximum compression, right: after elastic resiliency

[Key: Maximale compression = Maximum compression; Dekompression = Decompression].

A comparison of the experimentally and mathematically determined deformations of the shock-absorbing part is essential in evaluating the quality of a calculation. The maximum deformation during the test, however, does not correspond to the deformation after the drop test. After the end of the shock, the parts of the shock absorber again shrink elastically and thus bring

about a change in the form (Figure 4.17). The measured deformation is smaller than the maximum deformation that occurred. From the calculation, one usually takes the maximum deformation for the purpose of making a comparison. The maximum deformation determined in a calculation is this possibly not conservative when the calculation method is verified with the help of measured deformations. To compare measured and calculated deformation, one must therefore add the elastic resiliency to the measured deformation.

4.2.2 Energy Absorption

Figure 4.18: Shock-Absorber Filling of the MSF69BG® Bottom Shock Absorber after a 9-3-m Slap Down Drop, Viewed Diagonally from the Direction of the Foundation

[Key: Behälterseite = Cask; Aufprallfläche = Impact surface; Stossdämpfer Aussenseite = Outside of shock absorber].

Figure 4.18 show the bottom shock-absorbing part of the model, original size of the MSF69BG® (see Section 4.1.6), where, after a 9.3-m Slap Down drop, the outer sheet-metal cover of the bottom shock absorber was removed. The areas below the line marked A are deflected upward during the impact. There are only minor deformations of these wood areas. The different deformation of the shock-absorber areas could be observed in a similar manner on the similarly structured lid shock absorber. The area in which the largest part of the energy absorption was observed corresponds precisely to the wood packets that are located inside the shock-absorbing part precisely below the projected surface of the cask body. From this we can conclude that it is above all material under the projected surface of the cask body that contributes to energy conversion. Areas located further to the outside are deflected by the compression and contribute only little to the energy absorption.

It follows from this that in designing and making shock-absorbing parts, one must make sure that areas that are to contribute to energy absorption must be covered by rigid structures,

such as the cask body and stiff internal steel structures of the shock absorber in the direction of deformation.

4.2.3. Sheet Metal Behavior

The sheet metal structure performs a supporting function and takes care of the cohesion of the shock absorber; a precise knowledge of the behavior of the sheet-metal structures is therefore important. An analysis of the cracks in sheet-metal structures of CONSTOR® V/TC showed that local deformations in the heat influence zone or a welding seam frequently cause that area to fail. A part of the wood packets, lying under these sheet-metal pieces, can be deflected as a result of the lateral pressure and will thus not be available for providing lateral support for the wood in the main energy absorption zone. Kink phenomena are frequently decisive in terms of the stresses on the sheet-metal structure. The kinking of the sheet-metal structures is adequately described in the bibliography provided for this study (for example, by JONES [Jon03]).

4.2.4 Deformation Mechanisms

The analysis in Section 4.2.2 showed that wood in the shock absorber contributes to energy absorption to different degrees. So far, there has been no model that would describe energy absorption by wood in the shock absorber. This is why the shock-absorbing parts in this case were taken out after the drop test, the outer sheet-metal covers were removed and the existing wood packets and fiber bundles were analyzed and subdivided into classes in terms of their deformation.

Axial stress. In looking at the distribution of wood deformation over the circumference of the shock absorber (Figures 4.18 and 4.21), we can observe similar failure mechanisms at the beginning in each area of the shock absorber. The end of the elastic phase of the wood under the marginal conditions in the shock absorber is not initiated by flowing but rather by the outward kinking of entire wood fiber bundles due to lateral traction failure (Figure 4.19). The number of the kink points is not constant. As a result of the outward kinking of the fibers, one can observe an apparent transversal expansion, that is, with relation to the stress direction.

Figure 4.19: Kinked Wood Fiber Bundle Using the Example of a Piece of Fir Wood Compressed in the Axial Direction During a 9.0-m Drop in a Shock-Absorbing Part

Figure 4.20 shows that as fiber bundle, we must not consider the entire piece of wood but only the wood of one annual ring width. The piece of wood must then be construed as several parallel-connected wood fiber bundles. Figure 4.20 shows the shearing failure following up on the above-described lateral traction failure. Due to the shear stress, the composite structure fails along the early wood-late wood boundary, and both slide off against each other.

Figure 4.20: Kinked Wood Fiber Bundle Using the Example of Fir Wood Compressed in the Axial Direction (Experiment M. Neumann, BAM, 2007)

Failure due to sliding fiber levels along the early wood-late wood boundary is referred to here as "fiber delamination." A similar failure form can be observed in conjunction with delamination phenomena when working with glass-fiber and carbon-fiber reinforced synthetic substances (GFK & CFK) (HÖRMANN [Hör92]) and concrete (NEUBAUER [Neu00]. Due to the expansion of the wood fiber bundles initiated by the lateral traction failure in conjunction with a slight lateral expansion inhibition, the wood is increasingly compressed in the radial and tangential direction along with presumably definitely diminished energy absorption.

Figure 4.21: Shock-Absorber Filling of the MSF69BG® Bottom Shock Absorber after a 9.3-m Slap Down Drop, View from the Cask

The mechanisms involved in energy absorption will change along with increasing deformation as a function of the position in the shock absorber. In the main impact zone in the middle of the shock absorber, the wood is presumably strongly supported by wood located in the lateral environment and is thus prevented from being shifted naturally. Here we observe a large number of local kinking levels. This phenomenon will now be called cavity compression. In the case of cavity compression, presumably accompanied with high energy dissipation, the cell cavities are compressed up to the start of solidification (see Figure 3.2.3).

In areas further to the outside, the wood in the shock absorber is supported laterally to a definitely lesser extent. Following an initial lateral traction failure, the individual fibers can be deflected laterally and presumably will contribute only little to energy absorption.

The subdivision of the shock absorber into areas with fiber delamination and cavity compression must be adapted to the geometric conditions in the shock absorber and to the wood that is used on the basis of experimental results. Figure 4.22 shows the subdivision according to zones with cavity compression and zones with fiber delamination with radial/tangential compression using the example of the MSF69BG® bottom shock absorber. Looking at the red-marked surface, the cavity compression prevails, while in surrounding areas, fiber delamination prevails with subsequent radial/tangential compression. In the circumferential direction of the shock absorber (Figure 4.21), we can observe cavity compression in an area of about ±10-15º from the symmetry axis in the case of the shock absorber we are looking at here.

Figure 4.22: Shock-Absorber Filling of the MSF69BG® Bottom Shock Absorber after a 9.3-m Slap Down Drop After Removal of the Outer Sheet-Metal Pieces, Subdivision into Zones with Cavity Compression and Fiber Delamination

Figure 4.23 shows zones that, for example, deviate partly by way of fiber delamination of [sic; or] compression. No pure fiber delamination with radial/tangential compression can be observed in the marginal areas due to the metal cladding with sheet-metal pieces. The portion of cavity compression, of course, is minor and is confined to the kink zone. The wood area shown in Figure 4.23 thus presumably contribute only little to energy absorption.

Figure 4.23: Shock-Absorber Filling of the MSF69BG® Bottom Shock Absorber after a 9.3-m Slap Down Drop After Removal of the Outer Sheet-Metal Pieces, Zones of Fiber Delamination

In the direction of the longitudinal cask axis (Figure 4.22), the areas not covered by rigid cask or shock-absorber structures will be deflected (see Section 4.2.2). In a similar manner, areas located on the outside and thus supported by sheet metal only unilaterally (see Figure 4.23) will evade compression likewise and presumably contribute only little to energy absorption.

4.2.5 Conclusion

The analysis of the compression mechanisms of the deformed wood areas in shock absorbers in the preceding section showed that the behavior of wood in response to pressure stress in the axial direction and in case of great deformations must be considered as a function of the lateral expansion inhibition.

It is therefore proposed that the shock absorbers be subdivided into three zones that presumably contribute to energy absorption in differently intensive ways.

1. **Zone I**
   The wood in this zone evades compression without significant energy absorption or load increase. Figure 4.18 shows this area below the line labeled A.

2. **Zone II**
   The wood in Zone II cannot deviate without failure. The wood shows lateral traction failure, it kinks out and is then compressed mostly radially/tangentially.

3. **Zone III**
   In the case of the wood in Zone III, lateral traction behavior also takes place at the start, but the wood fibers are so strongly supported laterally that we can observe primarily cavity compression here. This area presumably contributes greatly to absorption of the impact energy.

We established the hypothesis now that a lateral expansion inhibition will result in higher pressure force and absorbed energy in case of large deformations in case of axially stressed wood. To test this hypothesis, compression tests on wood samples with large deformations are designed, performed and evaluated. These tests are described in the following subchapter.

4.3 Shock Tests on Wood Samples

In this subchapter, we describe tests on encased and unencased wood specimens. The following questions are to be answered with the help of the results derived from these tests.

4.3.1 Objective

The uncertainties regarding the magnitude of the influence exerted by various marginal conditions upon the behavior of wood are described in Section 3.3.10. Here, we identified, above all, density, temperature, moisture, expansion rate and magnitude factors as important factors influencing the mechanical properties of wood. The influence deriving from moisture and density can be minimized for shock-absorbing parts by sorting and corresponding marginal production conditions. In this case, the effects of temperature and magnitude cannot be examined due to the fact that experimental facilities are not available and because that would take too much time.

In Section 4.2.5, we established hypotheses on the behavior of the wood in response to pressure stress in the axial direction in the shock absorber on the basis of analysis of shock-absorbing parts. There we showed that in the impact area in the main energy-absorption zone, the wood is compressed along with definitely lateral expansion inhibition, whereas in the less well-supported areas, it evades the impact zones laterally. Experiments are to be performed with and without lateral expansion inhibition to clarify and quantify the influence exerted by lateral expansion inhibition upon the mechanical properties that are relative in terms of pressure stress.

Another object of the tests is to determine "pressure flow curves" in the area of large deformations with simultaneous investigation of the influence from multiaxial and monoaxial stresses and various constant stress velocities. The multiaxial stress is to be so adjusted that the multiaxiality conditions in shock-absorbing parts will be met. Flow curves determined in this fashion are to be used as basis for the calculation of the compression of shock-absorbing parts with simplified numerical methods and FEM. The influence deriving from the expansion rate and lateral expansion inhibition on the pressure flow curves will be tested for their statistical significance.

4.3.2 Test Objects

In the past, especially samples with a round cross-section such as, for example, the form used by DIERSCH et al. [D+94] with a diameter of 100 mm and a height of 50 mm were used for the pressure tests with wood. DIN 52185 [DIN76] (*Testing of Wood - Determination of Pressure Stress Parallel to Fiber)* - proposes an ashlar-shaped sample with, if at all possible, a quadratic cross-section whose edge length is to be a = 20 mm. In case the fibers or the wood run irregularly with wide, alternating rotary growth zones (annual rings), the sample dimension is to be so chosen that at least five annual rings or fresh growth zones will be covered. The height of the samples should be 1.5 to 3 times the width. TABARSA & CHUI [TC01a] [TC01b] propose chose samples with an edge length of 8 mm. The experimental setup used in this study necessitates a sample height of about 100 mm in order constantly to achieve the desired high stress velocity.

The long, slim sample shape, described in DIN 52185 [DIN76], results from the desire of setting an as-much-as- possible ideal-uniaxial stress state. As illustrated in Figure 4.24, the lateral expansion and thus a lateral evasion of the sample surfaces is prevented due to the friction in the contact surface between the underlying support and the sample or between the pressing stamp and the sample along with increasing compression.

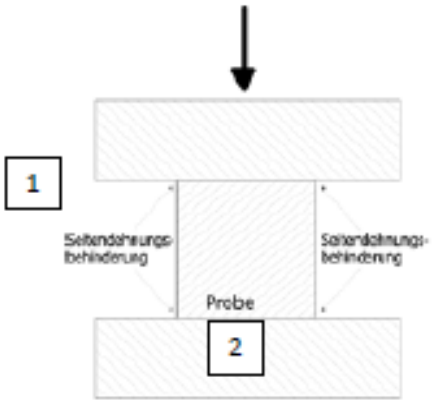

Figure 4.24: Schematic Illustration of the Lateral Expansion Inhibition at the Contact Surfaces in Case of Uniaxial Pressure Tests with Wood

[Key: 1) Lateral expansion inhibition; 2) Sample].

In tests where the samples are compressed with large deformations, the fiber structure and the resultant failure mechanisms of the wood must be given adequate consideration. To bring about a similar stress situation as in the case of the shock-absorbing parts, we propose here a cubic sample shape that can be seen in Figure 4.25 because it most likely corresponds to the geometric conditions prevailing in shock-absorbing parts.

Figure 4.25: Cubic Sample Made of Fir Wood with an Edge Length of 100 mm

Figure 4.26: Cubic Sample Made of Fir Wood with Lateral Expansion Inhibition Destroyed During Test Consisting of Glass-Fiber Reinforced Synthetic Substance

The test objects were made in Germany from fir wood (PICEA ABIES). The samples are made of whole construction wood, sorting class S10, according to DIN 4074-1 [DIN08a] with a moisture of 15±3%. That corresponds to a strength class of C24 according to DIN EN 338 [DIN08b]. To generate a lateral expansion inhibition, tests were performed with wood samples with cladding consisting of glass-fiber-reinforced and carbon-fiber-reinforced synthetic substances (GFK and CFK) and with sheet-metal pieces of various thicknesses. Cladding was to be so shaped that there would be no failure of the cladding and so that the compression could take place under effective lateral expansion inhibition. The high degree of brittleness of the fiber-reinforced synthetic substances cause cracks in the glass fibers or the carbon fibers in case of relatively small deformations and thus brought about a failure of the lateral expansion inhibition (see Figure 4.26). Sheet metal[3] as cladding was investigated with thicknesses of 0.5 mm and 1 mm. As shown in Subchapter 4.2, wood declines in case of axial compression toward lateral evasion after initial failure; therefore, in case of tests done in the axial direction, we need a more intensive sideward expansion inhibition. In this study, we use sheet metal with a thickness of 1 mm for tests in the axial direction and 0.5 mm for tests in the radial or tangential direction. The required sheet-metal thicknesses were determined with the help of preliminary experiments. Sheet-metal thicknesses of 0.5 mm were not adequate in tests with axial sample alignment. In this case, the sheet metal fails frequently. To be able to estimate the portion of form change energy, which is absorbed by the sheet metal, we perform pressure tests with sheet metal without wood filling (Table 4.8).

Sample Designation

The experimental parameters comprise lateral expansion inhibition, wood fiber direction and stress velocity. The samples are numbered with a system consisting of a V and a sequential, three-digit number. The test series were labeled with an abbreviation for lateral expansion inhibition (m for with, o for without lateral expansion inhibition), followed by an abbreviation for the fiber alignment (l for longitudinal-axial, q for lateral-transversal) and finally the tress velocity (1, 300, 3,000 mm/sec).

4.3.3. Experimental Setup and Implementation

[3] Steel JS235JRG2.

Figure 4.27: Servohydraulic Impulse Test Stand of BAM

The servohydraulic 1000-kN impulse test stand of BAM (Figure 4.27) was developed to investigate parts exposed to shock stress and equipped with electronic control instruments and powerful servovalves. Depending on the test cylinder, the test stand permitted a maximum testing force (traction/pressure) of 1000 kN or 630 kN at 600 mm work path. The maximum piston velocity is 4.5 m/sec or 8.5 m/sec. The machine can be operated statically with either path control or force control. The path-time curve can be programmed dynamically. The dimensions of the test stand are 8 m x 3 m x 2.6 m. The samples can be clamped firmly and positioned flexibly.

Figure 4.28 shows a diagram illustrating the servohydraulic impulse test stand of BAM. The settings for the functional generator to produce the stress can be seen in Table 4.6. Table 4.7 presents an overview of the measurement sensors used.

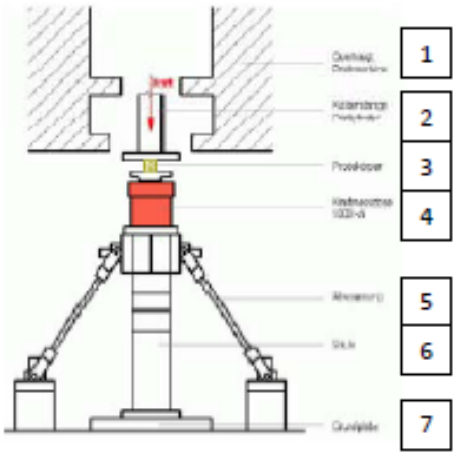

Figure 4.28: Schematic Illustration of the BAM Servohydraulic Impulse Test Stand

[Key: 1) Crosshead, test machine; 2) Piston rod, test cylinder; 3) Specimen body; 4) Force measurement can; 5) Rock; 6) Column; 7) Base plate; 8) Force].

Table 4.6: Settings of the Functional Generator in the BAM Impulse Test Stand

Signal Form	**Control Type**	**Velocity**
Ramp	Path	1 mm/sec
Ramp	Path	300 mm/sec
Ramp	Path	3,000 mm/sec

Table 4.7: Measurement Value Acquisition from Shock Tests on Wood on the BAM Impulse Test Stand

Name	**Measurement Magnitude**	**Measurement Range**	**Accuracy**
W125 (inductive half-bridge)	Path	±125 mm±	MK1
KMD1000 (DMS full bridge)	Force	±1000 kN	MK1
B25 (inductive half-bridge)	Acceleration	±100 g	±0.2%
PMIS3 (incremental)	Velocity	±3 m/sec	±40µm/m

Table 4.8: Listing of the Shock Tests Performed on Wood Samples

Number Samples/Test	**Wood Fiber Direction**	**Velocity [mm/sec]**	**Lateral Expansion Inhibition**	**Test Numbers**
10	axial	1	Sheet metal 1.0 mm	46-55
10	axial	300	Sheet metal 1.0 mm	61-70
10	axial	3,000	Sheet metal 1.0 mm	81-90
10	radial	1	Sheet metal 0.5 mm	31-35; 56-60
10	radial	300	Sheet metal 0.5 mm	71-80
10	radial	3,000	Sheet metal 0.5 mm	91-100
10	axial	1	-	1; 110-118
10	axial	300	-	3; 130-138
10	axial	3,000	-	5; 148-156
10	radial	1	-	2; 101-109
10	radial	300	-	4; 121-129
10	radial	3,000	-	6; 139-147
1	-	1	Sheet metal 1.0 mm, empty	119
1	-	1	Sheet metal 0.5 mm, empty	120
34	div.	div.	Preliminary experiments	

The tests were performed in a workshop with a temperature of 17-19ºC. The samples were photographed, they were inserted in the test stand and the test was performed. After the end of the test, the sample was taken out of the test stand, it was photographed, the experimental conditions were documented and the measurement data were stored. Table 4.8 presents an overview of the shock tests performed on wood.

Figure 4.29 shows the velocity-time curves that typically develop on the basis of the data given in Table 4.6 (300 mm/sec and 3,000 mm/sec).

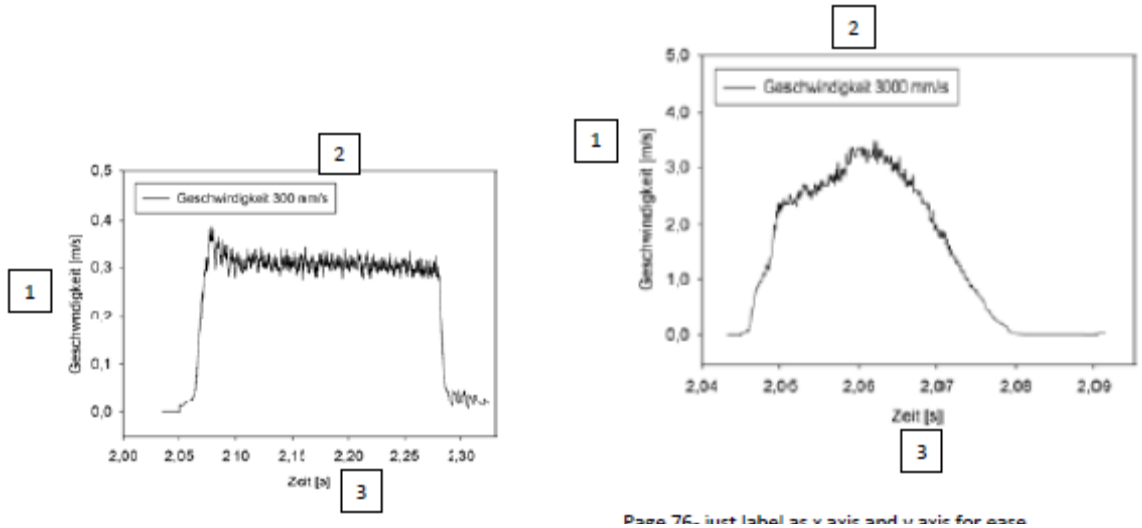

Figure 4.29: Piston Velocity of the Testing Machine at 0.3 m/sec (V71) and 3 m/sec (V91) on the BAM Impulse Test Stand

[Key: 1) Velocity; 2) Time].

4.3.4 Test Evaluation

The objective of the tests was to determine pressure flow curves for wood under various lateral expansion inhibitions and stress velocities. An evaluation was made with regard to the factors influencing the expansion rate and the lateral expansion inhibition upon the pressure strength or crush limit, the pressure force at 50% deformation and the energy dissipated up to 50% deformation. The latter energy is a measure of the energy absorption capacity of the wood sample.

Measurement data processing. To guarantee the comparability of the tests and to form a mean value, the tests were corrected to a common path channel. That was necessary because the start of the test featured differing decelerations in relation to the start of the measurement value acquisition. The following steps were taken for each test data item in order to process the measurement data.

1. Zero point shifting of the path-time function[4].

2. A nonparametric spline[5] is calculated for the supporting points of a newly defined time channel (T0) for the corrected path channel against the test-time channel.

3. Similar to Point 2, the force channel is newly calculated against the test-time channel.

[4] In such a way that the start of the force rise was assigned the moment t=0.
[5] Piece-by-piece interpolation function with the help of polynomials, constantly differentiable.

4. The relief part (part of the elastic resiliency and return of the piston) out of the force spline against the path spline is cut out. That is necessary to get a monotonously rising path channel.

5. A nonparametric spline is made from the force spline (see Point 3) against the path spline (see Point 2) for the support points of an equidistantly generated path channel (X0, 0 to 100 mm, 250 values).

6. Mean value formation of matching tests.

As a result of the measurement value processing done in this way, all experimental results will relate to the artificially generated path channel (see Point 5) and are thus directly comparable. We proceed according to equation 4.2 in order to determine the energy absorption capacity.

$$W_{\hat{s}} = \int_{s=0}^{\hat{s}} = Fds$$

$W_{\hat{s}}$	Energieabsorptionsvermögen bei Zieldeformation $\hat{s}$
s	Deformation
$\hat{s}$	Zieldeformation
F	Kraft

(4.2)

$W_{\hat{s}}$	Energy absorption capacity in case of target deformation
s	Deformation
$\hat{s}$	Target deformation
F	Force

The work, determined by integration in this fashion, was equated to the energy absorbed by the sample.

Statistical analysis. Pressure forces and absorbed energies are analyzed statistically in case of certain deformations. We consider here the pressure strength in case of tests in the axial direction or the crush limit in case of tests in the radial/tangential direction (in this case, approximately by the expansion at 3.2% deformation) as well as the absorbed energy and force at 50%. For that purpose, the corresponding experimental data are transferred to the statistical evaluation program SIGMAPLOT [SIG07] and are analyzed. Figures 4.33 to 4.35 show the box plots of the individual test series. In the case of tests in the axial direction with lateral expansion inhibition when it comes to evaluating the force and the energy absorbed at 50% deformation, only those tests are included in the evaluation where the sheet-metal jacket had not yet failed. In test group ml1, four tests failed (V48, V51, V53, V55), in ml300, two tests failed (V63, V65) and in ml3000, three tests failed (V84, V87, V88). A photo of specimen V63, whose lead jacket had failed before 50% deformation, can be seen in Figure 4.30. To evaluate the pressure strength, all

tests of the corresponding test groups are used because the failure of the sheet-metal structures took place only after pressure strength was attained.

Figure 4.30: Torn Sheet-Metal Jacket in a Sample with Axially Stressed Wood (V63, ml300)

To evaluate whether the difference between two test series is significance, we performed parametric t tests for unconnected basic totalities (see WERNECKE [Wer04]). In the process, we tried to examine with the help of two hypotheses[6] whether the random samples differ from each other. If the p-value[7] according to t-test magnitude

$$t = \frac{\bar{x} - \bar{y}}{s_u} \sqrt{\frac{n(x) \cdot n(y)}{n(x) + n(y)}}$$

$\bar{x} - \bar{y}$	Differenz der Mittelwerte
s_u	Variabilitätsmaß
$n(x), n(y)$	Stichprobenumfang

(4.3)

$\bar{x}$ - $\bar{y}$	Difference in mean value
s_u	Extent of variability
n(x), n(y)	Random sample volume

is smaller than a significance level α, which is to be defined, then the HO hypothesis is rejected and the HA hypothesis is accepted. If we start with a 95% confidence interval, then we have a = 0.05. In the case described here, a p-value of 0.04 tells us that a difference between the two random samples (for example, pressure strength as a function of the expansion rate) can be generalized to the basic totalities. The prerequisite for the use of parametric t-tests is the normal distribution of the magnitude to be examined, something that is given here by way of approximation.

4.3.5 Test Results

[6] H0 hypothesis: In case of variation of one parameter (for example, expansion rate), the considered property does not change (for example, pressure strength). HA hypothesis: The property changes.

[7] Also probability of exceeding the amount or probability of error.

Figures 4.31 to 4.32 show the pressure force-compression curves after mean value formation in case of axial and tangential or radial stress direction. Here we show the influence of the stress velocity and the lateral expansion inhibition upon the pressure flow curves.

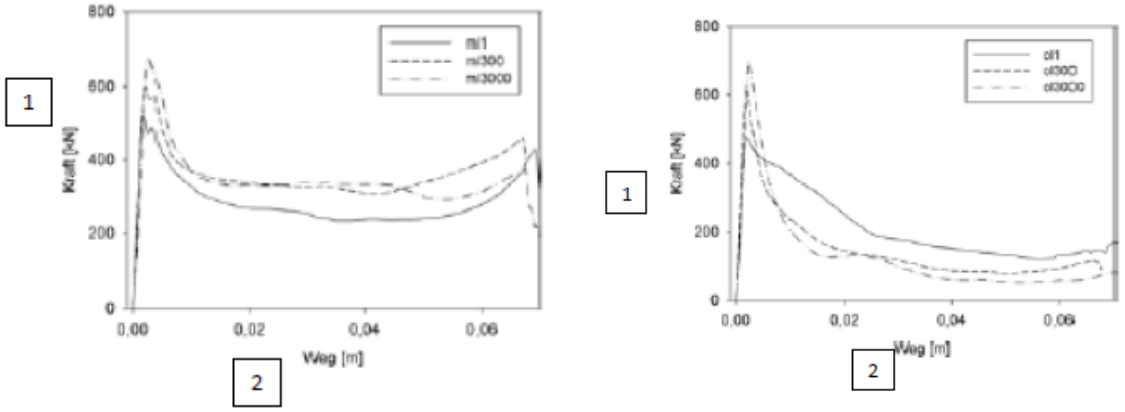

[1= y-axis, 2= x-axis]

Figure 4.31: Shock Tests Against Wood Samples: Force-Deformation Curves in Case of Axial Stress, Expansion Rate Influence With (left) and Without (right) Lateral Expansion Inhibition, In Each Case, Mean Values from 10 Tests

[Key: 1) Force; 2 Path].

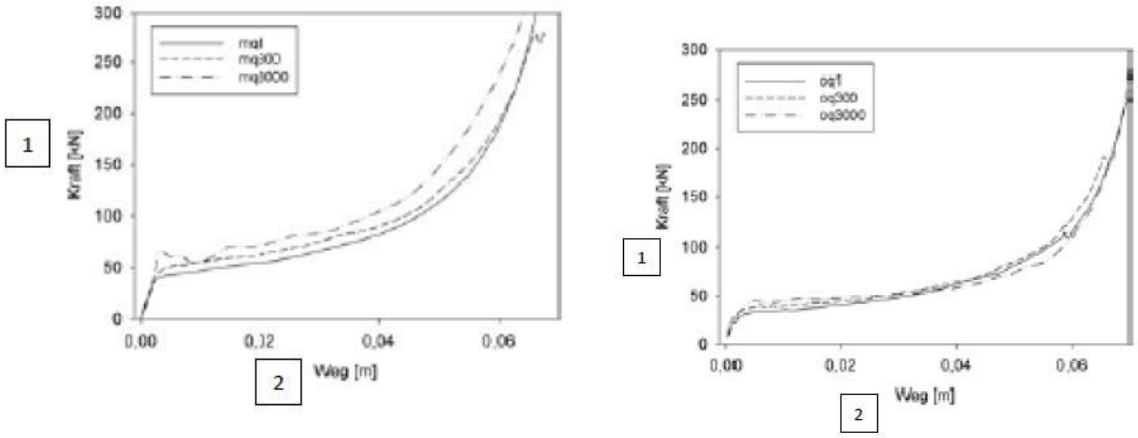

Figure 4.32: Shock Tests Against Wood Samples: Force-Deformation Curves in Case of Tangential/Radial Stress, Expansion Rate Influence With (left) and Without (right) Lateral Expansion Inhibition, In Each Case, Mean Values from 10 Tests

[Key: 1) Force; 2 Path].

Pressure Strength

Axial stress. Figure 4.33, left, and Table 4.9 show that the influence of the expansion rate on the pressure strength (concepts according to DIN 52185 [DIN76] and DIN 52192 [DIN79]) is significant with and without lateral expansion inhibition. A higher expansion rate results in greater pressure strength. Figure 4.33, left, and Table 4.9 furthermore show that the influence of the lateral expansion inhibition on the pressure strength is not significant at any stress velocity. But it should be noted that a significant lateral expansion inhibition takes effect only in the follow-up rupture area. From the influence of the lateral expansion inhibition on the pressure strength, we cannot draw any conclusions as to the influence of multiaxiality of the stress test upon the pressure strength.

Radial stress. In case of radial stress (Figure 4.33, right, and Table 4.10), the influence of the expansion rate on the compression limit is not clear. The differences between the stress velocities 1 mm/sec and 300 mm/sec are not significant; but the deviation between 300 mm/sec and 3,000 mm/sec is significant. At this point, we recommend that in any follow-up investigations, we increase the testing volume in order to create adequate back-up support for the statistical bases. In case of high stress velocity, a higher expansion rate in each case results in a greater compression boundary. Equally significant is the influence of the lateral expansion inhibition upon the compression boundary at high stress velocities. If we decide to do without a lateral expansion inhibition, then the compression limit compared to the tests with the lateral expansion inhibition definitely declines except for the test at 1 mm/sec. Due to the elastic area, which is definitely greater in case of radial stress, the expansion inhibition is presumably already more effective than in case of tests in the axial direction.

Pressure Force at 50% Deformation

Axial stress. Figure 4.34, left, shows the analysis of the pressure forces at 50% deformation for axial stress. A significant increase in the pressure force was determined here in conjunction with lateral expansion inhibition in comparison to unhindered lateral expansion possibilities (Table 4.11). In tests with lateral expansion inhibition, an increase in the expansion rate results in significantly higher pressure forces at 50% deformation. The decline in the pressure strength at higher expansion rates during tests without lateral expansion inhibition (test series ol1, ol300 and ol3000) can be explained by dynamic effects. As a result of the high stress velocity at 300 mm/sec and 3,000 mm/sec, less already-splintered sample parts remained in the experimental setup and contribute to increasing the sample resistance.

The statement by GROSSE [Gro05] to the effect that a top load in the radial or tangential direction will not lead to a stiffening in the axial direction must thus be further spelled out in the following manner: Only in case of small deformations before there are any macroscopic splits will transversal top loads not result in a stiffening in the axial direction. In the follow-up rupture area, assuming increasingly occurring splits in the a-t level, a lateral expansion inhibition will result in a higher resistance in the axial direction.

Radial stress. The expansion rate does not exert any significant influence on the pressure force at 50% deformation (Table 4.12). Without lateral expansion inhibition, we can again observe smaller forces at higher expansion rates due to the increasing ejection of little pieces of wood out of the experimental setup. Compression in the radial/tangential direction, of course, does not result in an expansion in the axial direction, but a stress in the radial direction will result in an expansion in the tangential direction and vice versa. Because of that, an increase in the resistance in tests with lateral expansion inhibition compared to tests without lateral expansion inhibition is significant also in case of compression in the radial/tangential direction (Table 4.12).

Form Change Energy at 50% Deformation

Axial stress. Figure 4.35, left, and Table 4.13 show the form change energy at 50% deformation for axial stresses. With lateral expansion inhibition, the form change energy rises with rising expansion rate, but, of course, the difference is significant only between 1 mm/sec and 300 mm/sec. The previously mentioned dynamic effects are responsible for the declining form change energies at higher expansion rates in tests without lateral expansion inhibition (ol11, ol300, ol3000). With the help of these dynamic effects, we can investigate the influence of multiaxiality on the form change energy at 50% deformation only in case of 1 mm/sec stress velocity. As the comparison between tests with and without lateral expansion inhibition (ml1 and ol1) shows in Table 4.13, the difference is significant. In tests with lateral expansion inhibition, in other words, significantly more energies are absorbed than in tests without lateral expansion inhibition.

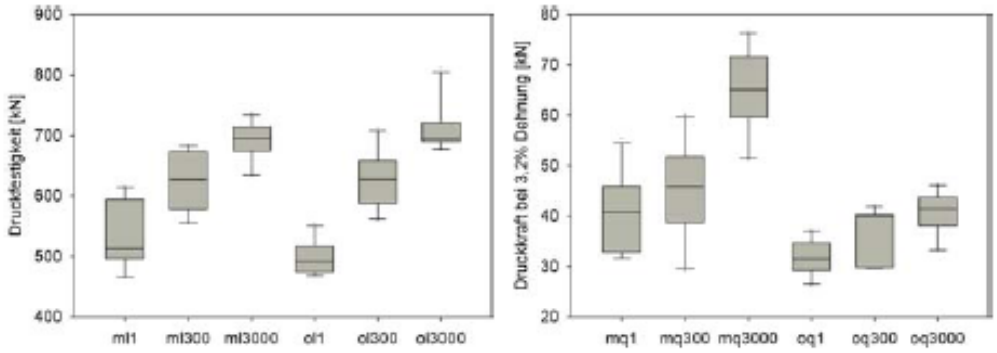

Figure 4.33: left: Boxplot Pressure Strength, Fail, Longitudinal; right: Boxplot Compression Boundary, Fail, Lateral, With and Without Lateral Expansion Inhibition, Expansion Rate Influence

[Key: X-axis= Pressure strength; 2) Y-axis=Pressure force at 3.2% expansion].

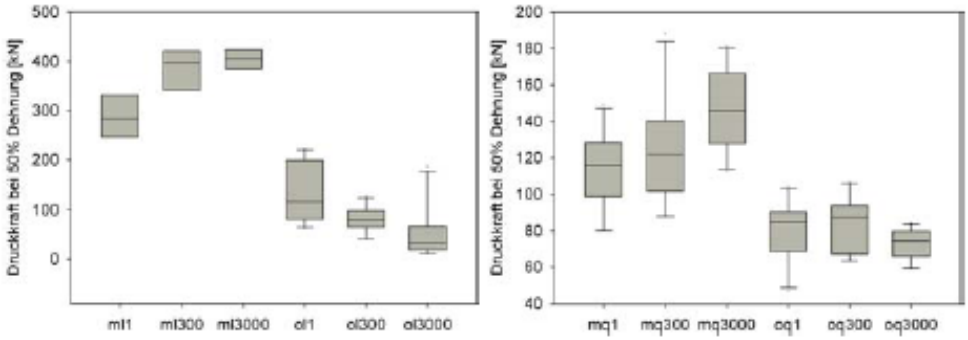

Figure 4.34: left: Boxplot Pressure Force at 50% Expansion, Fir, Longitudinal; right: Boxplot Pressure Force at 50% Expansion, Fir, Lateral, With and Without Lateral Expansion Inhibition, Expansion Rate Influence

[Key: Y-axis= Pressure force at 50% expansion].

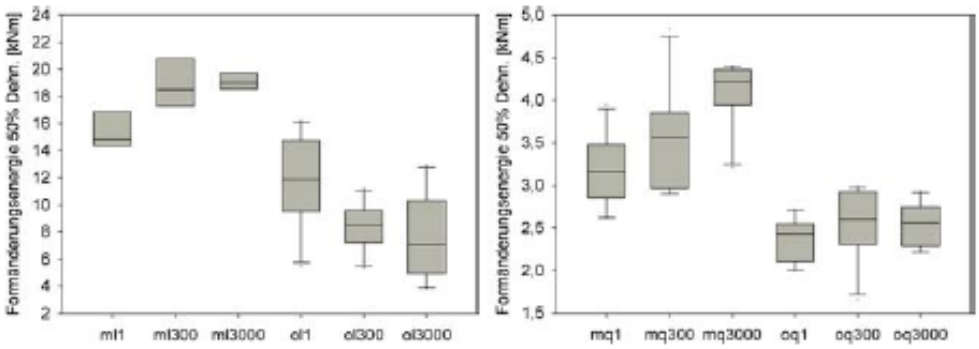

Figure 4.35: left: Boxplot Form Change Energy at 50% Expansion, Fir, Longitudinal; right: Boxplot Form Change Energy at 50% Expansion, Fir, Lateral, With and Without Lateral Expansion Inhibition, Expansion Rate Influence

[Key: Y-axis= Form change energy at 50% expansion].

		ml1	ml300	ml3000	ol1	ol300	ol3000
ml1	p	-	$7,5 \cdot 10^{-4}$	$1,3 \cdot 10^{-7}$	0,104		
ml300	p		-	$1,2 \cdot 10^{-3}$		0,85	
ml3000	p			-			0,25
ol1	p				-	$7,5 \cdot 10^{-7}$	$1,0 \cdot 10^{-10}$
ol300	p					-	$3,9 \cdot 10^{-4}$
ol3000	p						-

Table 4.9: Results of the t-Tests Regarding Pressure Strength in Case of Stress in Axial Direction in the Test Program for Shock Against Wood with Fir Wood Samples

		mq1	mq300	mq3000	oq1	oq300	oq3000
mq1	p	-	0,22	$1,8 \cdot 10^{-6}$	$2,5 \cdot 10^{-3}$		
mq300	p		-	$1,2 \cdot 10^{-4}$		0,014	
mq3000	p			-			$1,2 \cdot 10^{-7}$
oq1	p				-	0,025	$3,8 \cdot 10^{-5}$
oq300	p					-	0,050
oq3000	p						-

Table 4.10: Results of the t-Tests Regarding Compression Limit in Case of Stress in Radial/Tangential Direction in the Test Program for Shock Against Wood with Fir Wood Samples

		ml1	ml300	ml3000	ol1	ol300	ol3000
ml1	p	-	0,0249	$9,6 \cdot 10^{-3}$	$2,3 \cdot 10^{-4}$		
ml300	p		-	0,371		0,0	
ml3000	p			-			$3,3 \cdot 10^{-9}$
ol1	p				-	0,0185	$5,1 \cdot 10^{-3}$
ol300	p					-	0,159
ol3000	p						-

Table 4.11: Results of the t-Tests Regarding Pressure Strength at 50% Deformation in Case of Stress in Axial Direction in the Test Program for Shock Against Wood with Fir Wood Samples

		mq1	mq300	mq3000	oq1	oq300	oq3000
mq1	p	-	0,395	$2,5 \cdot 10^{-3}$	$1,2 \cdot 10^{-3}$		
mq300	p		-	0,0560		$1,5 \cdot 10^{-3}$	
mq3000	p			-			$7,1 \cdot 10^{-9}$
oq1	p				-	0,559	0,263
oq300	p					-	0,0519
oq3000	p						-

Table 4.12: Results of the t-Tests Regarding Pressure Strength at 50% Deformation in Case of Stress in Radial/Tangential Direction in the Test Program for Shock Against Wood with Fir Wood Samples

		ml1	ml300	ml3000	ol1	ol300	ol3000
ml1	p	-	$1,3 \cdot 10^{-3}$	$1,3 \cdot 10^{-3}$	0,037		
ml300	p		-	0,90		$4,0 \cdot 10^{-10}$	
ml3000	p			-			$3,1 \cdot 10^{-7}$
ol1	p				-	$8,2 \cdot 10^{-3}$	0,0101
ol300	p					-	0,57
ol3000	p						-

Table 4.13: Results of the t-Tests Regarding Form Change Energy at 50% Deformation in Case of Stress in Axial Direction in the Test Program for Shock Against Wood with Fir Wood Samples

		mq1	mq300	mq3000	oq1	oq300	oq3000
mq1	p	-	0,095	$7,8 \cdot 10^{-5}$	$4,3 \cdot 10^{-5}$		
mq300	p		-	0,034		$3,2 \cdot 10^{-4}$	
mq3000	p			-			$4,4 \cdot 10^{-9}$
oq1	p				-	0,25	0,13
oq300	p					-	0,96
oq3000	p						-

Table 4.14: Results of the t-Tests Regarding Form Change Energy at 50% Deformation in Case of Stress in Radial/Tangential Direction in the Test Program for Shock Against Wood with Fir Wood Samples

Radial stress. Figure 4.35, right, and Table 4.14 show the form change energies at 50% deformation in response to radial/tangential stress. Due to the wide scatter, the rise in form change energy is significant only in case of tests with lateral expansion inhibition between 300 mm/sec and 3,000 mm/sec. In this case, the number of tests should be increased. The influence of the lateral expansion inhibition on the form change energy is significant at 50% deformation. With lateral expansion inhibition and in response to radial stress, higher energies were absorbed than without lateral expansion inhibition.

Mean Values

Table 4.15 shows the mean values of the pressure strengths or compression boundaries and the pertinent standard deviations of all recorded test series. Table 4.16 shows the mean values of the form change energies at 50% deformation.

Influence of Sheet Metal

Figure 4.36 shows the force-deformation curves for compression tests with sheet-metal samples with a raw thickness of 1.0 mm and 0.5 mm. In experiments with axial stress direction, the energy, absorbed by the sheet metal, amounts to a maximum of 5% of the total energy and is thus negligible.

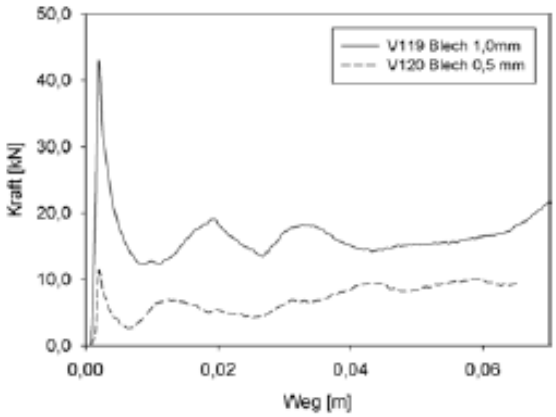

Figure 4.36: Force-Deformation Curve in Response to Pressure Stress on Sheet Metal Box Profiles with Wall Thicknesses of 1.0 mm (V119) and 0.5 mm (V120)

[Sheet Metal Key: Y-axis= Force; X-axis= Path].

Versuchsreihe	Mittelwert	Standardabweichung
ml1	530,7 kN	52,28 kN
ml300	622,0 kN	48,41 kN
ml3000	691,9 kN	31,22 kN
ol1	498,6 kN	27,67 kN
ol300	626,0 kN	46,98 kN
ol3000	711,4 kN	40,80 kN
mq1	40,75 kN	7,55 kN
mq300	45,67 kN	9,48 kN
mq3000	64,93 kN	8,05 kN
oq1	31,58 kN	3,36 kN
oq300	36,38 kN	5,22 kN
oq3000	40,80 kN	4,20 kN

Table 4.15: Mean Values and Standard Deviations of the Pressure Strength or Compression Boundaries in the Test Program for Shock Against Wood with Fir Wood Samples

[Key: 1) Test series; 2) Mean value; 3) Standard deviation].

Versuchsreihe	Mittelwert	Standardabweichung
ml1	15,34 kNm	1,40 kNm
ml300	18,90 kNm	1,69 kNm
ml3000	18,80 kNm	1,49 kNm
ol1	11,95 kNm	3,22 kNm
ol300	8,419 kNm	1,55 kNm
ol3000	7,049 kNm	2,97 kNm
mq1	3,175 kNm	0,389 kNm
mq300	3,576 kNm	0,560 kNm
mq3000	4,091 kNm	0,375 kNm
oq1	2,361 kNm	0,239 kNm
oq300	2,549 kNm	0,412 kNm
oq3000	2,540 kNm	0,238 kNm

Table 4.16: Mean Values and Standard Deviations of the Form Change Energies at 50% Deformation in the Test Program for Shock Against Wood with Fir Wood Samples

[Key: 1) Test series; 2) Mean value; 3) Standard deviation].

Determination of Average Stress-Expansion Curves

Technical stresses and expansions are determined by reference of the force-deformation curves with regard to the initial sample cross-section surface or the initial height of the sample.

A conversion of the technical stresses and expansions into two stresses and expansions according to LUDVIK [Lud09] (also called logarithmic stress and expansion measure, see also ISSLER, RUOSS & HÄFELE [IRH03]) does not lead anywhere when working with wood subjected to axial stress because this theory starts with volume constancy. As described in Section 2.2.3, the cavities in the wood collapse upon compression in the axial direction. This results in a volume that keeps shrinking in the course of compression.

The shock-absorbing parts that are used in the tests illustrated in Subchapter 4.1 partly have fir wood fillings with wood that is stressed 50% axially and 50% tangentially-radially. A characteristic is derived for this practical case by simple mean-value formation (in each case, 50% weighting) from pressure flow curves that are determined from the axial and tangential/radial direction.

$$\sigma_{50/50} = \frac{\sigma_a + \sigma_t}{2} \tag{4.4}$$

$\sigma_{50/50}$	Spannungs-Dehnungs-Verlauf bei 50% axial und 50% tangentialer Beanspruchung
σ_a	Spannungs-Dehnungs-Verlauf bei axialer Beanspruchung
σ_t	Spannungs-DehnungsVerlauf bei tangentialer Beanspruchung

$\sigma_{50/50}$	Stress-expansion curve at 50% axial stress and 50% tangential stress
σ_a	Stress-expansion curve in response to axial stress

σ_t Stress-expansion curve in response to tangential stress

4.3.6 Summary

The tests described in this subchapter made it possible to determine pressure flow curves for monoaxial and multiaxial stress of fir wood at varying stress velocities. The following results were achieved:

1. Lateral expansion inhibitions do not exert any significant influence on the pressure strength in response to axial stress. In case of radial stress, lateral expansion inhibitions resulted in significantly higher pressure strengths. The cause presumably is represented by the definite expansion in the tangential direction in response to radial stress in combination with a small elasticity module of wood in the radial/tangential direction.

2. In case of axial stress, the lateral expansion inhibition exerts significant influence on the pressure force and the absorbed energy at 50% deformation. More energy is absorbed with lateral expansion inhibition and the pressure force at 50% deformation is greater than in tests without lateral expansion inhibition.

3. Faster stress velocities have resulted in higher form change energies and forces, although not all differences were significant in the context of this study. In case of axial stress, the stress velocity exerts significant influence on the pressure strength.

4. The kink band development at an angle of about 65º with respect to the direction of stress described by DINWOODIE [Din00] and POULSEN [Pou97] in conjunction with the failure of undisturbed wood could be observed neither in the tests with wood nor in the analysis of the shock absorbers.

5. Flow curves were determined for the *"ImpactCalc"* method described in Chapter 5 and, on the average, that method corresponds to the lateral support in the shock absorber.

With the help of Point 1, one can confirm the hypothesis established in Section 4.2.5. The lateral expansion inhibition resulted in significantly higher pressure forces and absorbed energies in the case of axially stressed wood.

4.4. Conclusions

The behavior of wood in response to radial and tangential stress is less complex than the behavior of wood in response to axial stress on the basis of the determined nonsoftening behavior. At this point, we would like to note once again: The nonsoftening [desolidarizing] behavior of axially stressed wood is a matter of great interest when it comes to the simulation of accident situations involving transport casks with wood-filled shock absorbers. This study is therefore concentrated on axially stressed wood.

Model for the Behavior of Axially Stressed Wood

Building on the analysis of the shock-absorbing parts in Section 4.2.4, the conclusions arising therefrom (Section 4.2.5) as well as the results of the shock-on-wood test program in Section 4.3.5, we can for the first time propose here a model for the behavior of axially stressed wood in case of large deformations. The model considers the lateral expansion inhibition of the wood mixture that takes shape in the course of compression.

The behavior of wood can be characterized as follows in the context of the proposed model:

1. Upon attainment of the pressure strength, development of a kink plane in the wood with generally opposite surfaces. Due to the resultant lateral traction stresses, the wood is split longitudinally (lateral traction failure).

2. The further behavior must be considered as a function of the lateral expansion inhibition in the wood (see Subchapter 4.2):

   a) Lateral expansion inhibition "slight"

    The wood evades laterally unhindered; no further kink band levels or only a few additional ones are formed. By rotating wood fibers, wood is, above all, radially and tangentially compressed. In the course of greater deformation, more and more wood is radially/tangentially compressed and less and less wood is compressed axially. This results in a global force-deformation interrelationship, which declines up to the start of consolidation (see Figure 4.37 a).

   b) Lateral expansion inhibition "average"

    Here we generally observe formation of several kink levels because, after a brief deformation, any further lateral evasion is increasingly hindered and there again causes formation of new kink planes. Wood is compressed partly axially and partly radially/tangentially. The decline of the global force-deformation interrelationships turns out to be less than in case of slight lateral expansion inhibition (see Figure 4.37 b).

   c) Lateral expansion inhibition "high"

Here we generally observe formation of a very large number of local kink planes because lateral evasion is possible only to a minimal extent. In that way, wood is compressed axially almost exclusively. The force-deformation curve remains relatively constant over rather wide areas (see Figure 4.37 c).

3. Start of consolidation depending on the ratio between the density of the wood and the cell-wall density.

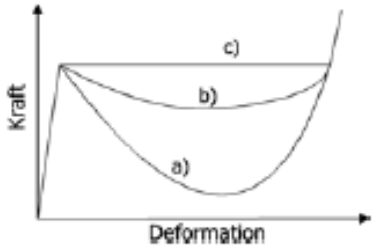

Figure 4.37: Diagram Illustrating Force-Deformation Curves for the Compression of Wood in the Axial Direction as a Function of the Lateral Expansion Inhibition

[Key: Y-axis= Force; X-axis=Deformation].

Concerning the zone subdivisions derived for the shock absorbers for the cask drop tests, it should be noted that the zone subdivision can change along with changes in geometry on the shock absorber. The underlying principle for energy absorption is identical, although the spatial extension of the zones may vary.

Model for the Behavior of Shock-Absorbing Parts

From the results of the analysis of the shock-absorbing parts as well as the wood tests, one can derive the statement to the effect that the softening material behavior of wood exerts important influence on the energy absorption capacity of shock-absorbing parts on transport casks holding radioactive substances. If wood is strongly supported laterally in the course of compression, then there will be a deformation of the wood along with great energy conversion of kinetic energy into form-changing energy. If the wood in the shock absorber can evade laterally, then we are dealing with a definitely reduced energy absorption capacity. In that way, with regard to shock-absorbing parts, the interaction of wood and surrounding steel and sheet-metal structure will be of decisive significance. The greater the cohesion of the shock absorber as a result of the externally located sheet metal structure, the more energy can the shock-absorbing part absorb.

4.5 Summary

Various tests were described in this chapter. Acceleration and deformation measurements during cask drop tests are used for the subsequent verification of calculation methods.

The behavior of wood in shock-absorbing parts in response to pressure stress in the axial direction was analyzed. The wood was separated into zones on the basis of the physical compression mechanism. The hypothesis was established to the effect that lateral expansion inhibitions in the case of axially stressed wood will lead to higher pressure forces and absorbed energies.

The hypothesis that was established was then confirmed with the help of the "shock-on-wood" testing program: In case of axially stressed wood and large deformations, lateral expansion inhibitions resulted in higher pressure forces and absorbed energies. On the basis of this conclusion as well as the analysis of the shock-absorbing parts, a model was proposed for the first time for the axial stress of wood in case of large deformations: For the compression of wood, the model considers the lateral expansion inhibition in relation to the continuing mechanics aspect that would be the multiaxiality of the stress state in the continuum. The energy that can be absorbed by the wood increases the greater is the lateral expansion inhibition. It follows from this that to provide a realistic simulation of the behavior of shock-absorbing parts in accident situations, a new approach should be used for modeling the wood: The softening of axially stressed would should be controlled by the lateral expansion inhibition. As far as the shock-absorbing part is concerned, this means that the energy absorption capacity of the shock absorber depends on the availability of the outer sheet metal structure to prevent a deviation of the heavily stressed wood packets.

To recalculate accident stresses on transport casks with wood-filled shock-absorbing parts, the elastic resilience must be added for a comparison of measured and calculated deformation with respect to the measured reshaping. That is the only way one can make a realistic comparison between measured and calculated deformation.

It follows from the analysis of the energy-absorbing areas of the shock absorber that when it comes to designing and building shock-absorbing parts, one must make sure that areas that are expected to contribute to energy absorption must be covered by rigid structures, such as the cask body and stiff internal steel construction of the shock absorber in the direction of deformation. Areas that are not covered will deviate without any noteworthy energy absorption.

Pressure flow curves for the compression of wood in case of large deformations were determined by means of the "shock-on-wood" testing program. The influence of the lateral expansion inhibition and the stress velocity upon various points on the pressure flow curves was investigated. In the process, higher stress velocities in general resulted in higher pressure forces and absorbed energies, although not all these interrelationships were significant in the context of this study. In the case of axially stressed wood, lateral expansion inhibitions result in higher pressure forces and absorbed energies.

The strip projection optical method was used for the first time in measuring the shock-absorbing parts. The method facilitates the recording of a precise reshaping contour before and

after the test and is thus very well suited for damage and reshaping documentation on the shock-absorbing parts. The method should be used for the documentation of results of drop tests. At this point, we want to develop a possibility for coupling finite element methods.

5 Modeling Using Simplified Numerical Methods

Initial attempts to calculate reshaping and delays of transport casks holding radioactive substances with shock-absorbing parts were documented by WILKINS [WG73]. A series of studies has since then addressed the calculation of the behavior of shock-absorbing parts of transport casks holding radioactive substances by way of drop tests. The goal of these studies mostly was the derivation of a maximum impact delay or the attendant maximum shock force as an initial magnitude for a quasistatic stress analysis on the components of the tightly sealed enclosure. Section 2.2.6 briefly presents the quasistatic analysis. The possibilities of using quasistatic analyses will not be discussed in the context of this study. Other potential possibilities of practical use are parameter studies dealing with minor variations in the geometries or the material properties as well as estimations of the occurring rigid body delay in the course of designing and evaluating shock-absorbing parts for transport casks holding radioactive substances. In this chapter, we want to explain the fundamentals in greater detail for the calculation of the shock forces and deformations of shock-absorbing parts with the help of simplified numerical methods, and we then want to present a new method.

5.1 Overview of Methods Used So Far

Spring-mass models constitute the basis for most of the programs to calculate the behavior of shock-absorbing parts of transport casks holding radioactive substances in the course of drop tests. The basic problem springs from the fact that there has been little public discussion on these computation methods. Companies that make transport casks for radioactive substances frequently develop or commission the development of analytical methods. In most cases, publications contain only very little information on specific marginal conditions involved in the methods and do not permit any reproduction of the computation results nor any comparison of the various methods among each other.

Codes with the names CRUSH and CASH were developed in Japan on the basis of spring-mass systems by ASADA et al. [A+88] and IKUSHIMA & HODE [IH89]. Compared to the experimental drop test, deviations were found in connection with determined delays of up to 120%. NOLAN, EGGERS & SHIH [NES89] describe a model that computes the time curves of acceleration and deformations, giving special consideration to various impact angles. The deviations from deformations and decelerations amount to as much as 15% in making a comparison of the computation with the experiment (TN Gemini Model) in the case of horizontal and vertical drops; on the other hand, in case of inclinations of 30º and 60º, there will be deviations of up to 100%. SHIRAI, ITO & FUNAHASHI [SIF92] describe an analytical computer model with up to 20 Kelvin elements[1]. Of course, in this study, we investigated, above all, the interaction among various cask components as well as the content. AMMERMAN [Amm92] uses the empirical function shown in equation 5.1 for the force-reshaping characteristic of the shock absorber. [Translator's note: Author makes a distinction between deformation and verformung = deformation, reshaping]. This study focuses on the impact upon real foundations and the modeling of the shock absorber is not discussed in any greater detail.

[1] Parallel circuit consisting of spring and attenuation element.

$$F_i = D\left[1 - e^{-Ex_i} + F\left(e^{G(x_i - H)} - e^{GH}\right)\right]$$

D, E, G, H	Konstanten
F_i	Federkraft
x_i	Federweg

D, E, G, H	Constants
F_i	Spring force
x_i	Spring travel

IKUSHIMA et al. [IIOA92] present a code by means of which one can calculate rigid body delays and deformations and compare them to the experiment. The deviations of delays and shock-absorber deformations amount to as much as 66% without going into any greater detail as to the possible causes of these deviations. DIERSCH et al. [D+94] present a method on the basis of a spring-mass system that determines only maximum reshapings and delays and no time curves. DUVALL [Duv02] proposes a program for the determination of time curves of delays and reshapings. Of course, the program is presented only in a rudimentary fashion and the determined results are not related to any drop tests.

Many of these approaches entail the disadvantage to the effect that they cannot be used to calculate any time curves of shock-absorber reshaping or cask acceleration. Nevertheless, if time curves are computed, then the shock-absorber geometry and the extension ratios in the shock absorber are modeled only inadequately. In the context of this work, we developed a tool by means of which one can calculate the time curves of the shock-absorber reshaping and cask acceleration with precise consideration given to the geometric conditions (see NEUMANN et al. [NWB07]). For instance, a precise comparison is made possible, among other things, using the methods shown in this study.

5.2 Fundamentals of Computation

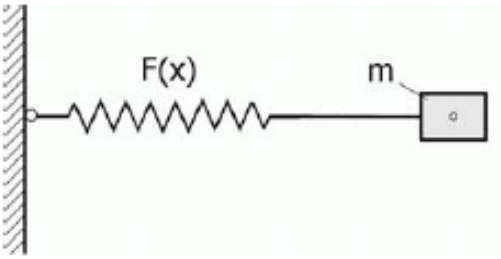

Figure 5.1: Single-Mass Oscillator

In using the computation method based on spring-mass models, the shock absorber is considered as a nonlinear spring system that is stressed by a mass (Figure 5.1). The differential equation of the free, unattenuated oscillation system is the basis of the computation:

$$m\ddot{x} + F(x) = 0$$

m	Masse
x	Wegvariable
$F(x)$	nichtlineare Federkraft

(5.2)

m	Mass
x	Path variable
$F(x)$	Nonlinear spring force

Here we consider only the oscillations up to the first maximum because, in this case, the maximum reshapings and forces of concern and the spring force is known only in the compression phase. No external forces are at work here; therefore, the particular situation of the differential equation is zero and the solution is described only by the homogeneous solution.

Here are the initial conditions for the recomputation of the differential equation: $t = 0;\ x = 0;\ \dot{x} = v_0$. No spring characteristics are generally known for the shock-absorbing parts; therefore, they must be replaced by suitable descriptions. The term $F(x)$ describes the spring force, which, converted into the interrelationship of an object that is to be compressed, can be substituted by $A(x)\cdot\sigma(x,y)$. Here, $A(x)$ describes the current contact surface with the foundation[2] and $\sigma(x,y)$ describes the normal stress working on the surface as a function of the spring travel and the position in the shock absorber (see Figure 5.2). The reshaping x is used as independent variable of the differential equation. The following differential equation results from that:

$$m\ddot{x} + A(x) \cdot \sigma(x, y) = 0$$

x	Verformung des Stoßdämpfers
y	Seitliche Position im Stoßdämpfer
$A(x)$	Schnittflächenfunktion
$\sigma(x, y)$	Spannung in Abhängigkeit von x und y

(5.3)

x	Reshaping of shock absorber
y	Lateral position in shock absorber
$A(x)$	Section plane function
$\sigma(x,y)$	Stress as a function of x and y

5.3 Development of a Separate Computation Program

In the following, we will present a new method that facilitates the computation of time curves of the rigid cask body delay, the shock-absorber deformation and the shock-absorber reaction forces of transport casks holding radioactive substances [NW07]. The basis for the *"ImpactCalc"* program is the solution of differential equation 5.3 whose individual terms will

[2] Red-marked intersection surface in Figure 5.4.

be explained in greater detail below. The term $m\ddot{x}$ describes the mass force of the system. The basic assumption here is the compression of the shock absorber, starting from the foundation in the positive x direction. In case of a horizontal drop (see Figure 2.7, right), a larger force is engaged in the course of higher reshaping. The surface is usually constant for a vertical drop.

Equation 5.3 indicates the mass and spring stiffness of the system. The shipping item mass is used as mass; but for the reaction force, there is proposed an integration of the stress $\sigma(x,y)$ prevailing for the current reshaping x in relation to the current theoretical boundary surface (see Figure 5.4) between the foundation and the shock absorber $A(x)$:

$$F = \int_{A(x)} \sigma(x,y)\, dA \tag{5.4}$$

$A(x)$ Flächenbegrenzungsfunktion

[2] rot markierte Schnittfläche in Abbildung 5.4

$A(x)$ Surface limitation function

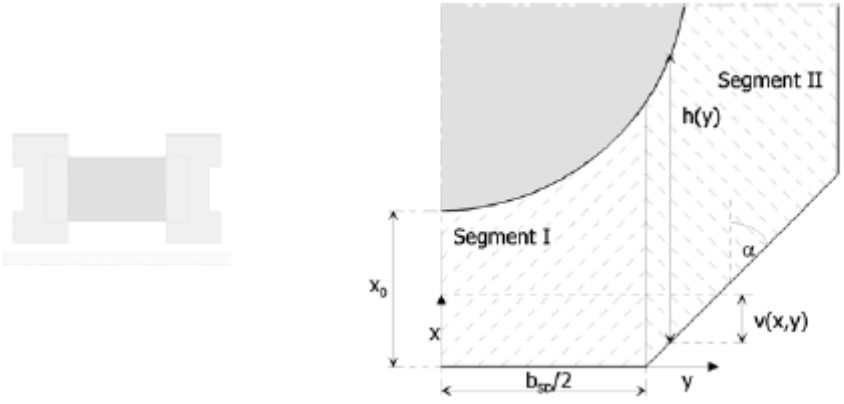

Figure 5.2: Schematic Illustration of a Partial Cross-Section Using the Example of an Octagonal Shock Absorber

The surface integral can be replaced by the following equation, assuming we perform an exact mean-value formation:

$$F(x) = \bar{\sigma}(x) \cdot A(x) \tag{5.5}$$

$\bar{\sigma}$ Spannungsfunktion - Exakte mittlere Spannung in der Stoßdämpferschnittfläche

(5.5)

$\bar{\sigma}$ Stress function - Exact mean stress in shock-absorber section plane

The determination of this stress function as well as of the shock-absorber section plane will be described in the next section.

5.3.1 Material Modeling

To determine the stress function $\bar{\sigma}$ used in equation 5.3, we must perform compression tests with wood samples. Compression tests using wood samples performed in this study are described in Subchapter 4.3. By means of compression tests with wood samples, one can determine wood-stress-expansion characteristics as basis for the computation of shock-absorber-stress-expansion characteristics. These characteristics are recorded as discrete force-shifting curves. After conversion into stress-expansion points, the point sequences can be interpolated to come up with constant functions. Here we use the wood characteristic at 300 mm/sec stress velocity and mean lateral expansion inhibition as determined in Subchapter 4.3. The lateral support roughly corresponds to the support in shock-absorbing parts in the main energy absorption zone. The expansion rate roughly corresponds to the expansion rate in the shock absorber. In the following, we will describe how such a specifically design-related stress function $\bar{\sigma}$ can be derived from wood characteristics.

Using the example of an octagonal shock absorber, Figure 5.2 shows the abstracted cross-section. Depending upon the position in the shock absorber, the wood is compressed in differently intensive ways. To take into account this differently intensive compression, the compression *σ(x,y)* is determined by referring the current deformation *v(x,y)* to the shortest distance *h(y)* between foundation and cask at point *y*:

$$\delta(x,y) = \frac{v(x,y)}{h(y)} \tag{5.6}$$

$\delta(x,y)$	Stauchung im Stoßdämpfer als Funktion von x und y
$v(x,y)$	Aktuelle Stoßdämpferverformung an der Position x,y
$h(y)$	Maximal mögliche Stoßdämpferverformung in y
x	Aktuelle Verformung im Stoßdämpfer in der Symmetrieebene
y	Laterale Position im Stoßdämpfer

δ(x,y)	Compression in shock absorber as function of *x* and *y*
v(x,y)	Current shock-absorber reshaping at position *x, y*
h(y)	Maximum possible shock-absorber reshaping at *y*
x	Current reshaping in shock absorber along symmetry plane
y	Lateral position in shock absorber

The stress for current reshaping x can be determined everywhere in the shock absorber with the help of the expansion *δ(x,y)* as a function of the current reshaping in the symmetry plane *x* and lateral position in the shock absorber *y* (see Figure 5.2) and the wood characteristic *σ(x)*:

$$\sigma\left(\delta(x,y)\right) = \sigma\left(\frac{v(x,y)}{h(y)}\right) \tag{5.7}$$

To eliminate the dependence of the lateral position in the shock-absorber y in equation 5.6, we propose here a mean-value formation of the function $\sigma(\delta(x,y))$ via y. The stress function of the shock absorber $\bar{\sigma}(x)$ now depends only on the deformation x in the symmetry plane of the shock absorber (see Figure 5.2):

$$\bar{\sigma}(x) = \left(\sum_{i=1}^{k} \int_{y_{min,i}(x)}^{y_{max,i}(x)} \sigma\left(\delta(x,y)\right)\, dy\right) \frac{1}{y_{max}(x)} \tag{5.8}$$

$\bar{\sigma}$	Mittlere Spannung in zur Verformung x gehörender Schnittfläche
k	Anzahl der Stoßdämpfersegmente (vgl. Abbildung 5.2
i	Segmentnummer

$\bar{\sigma}$	Average stress in section plane belonging to deformation x
k	Number of shock-absorber segments (see Figure 5.2)
I	Segment number

The dependence of the integration boundaries on x leads to the stress function $\bar{\sigma}(x)$ that describes the average stress level in the section plane belonging to x as a function of x. Various segments in the shock absorber can be considered by the summation of the integration area. For example, at least two segments are required for the case described in Figure 5.2: Segment 1 from $y = 0$ to $y = b_{SD}/2$ and Segment 2 for $y > b_{SD}/2$. For the example of an octagonal shock absorber during a horizontal drop (see Figures 5.2 and 5.4) when $\bar{\sigma}(x)$, it now follows:

$$\bar{\sigma}(x) = \left(\int_{0}^{\frac{b_{SD,1}}{2}} \sigma\left(\bar{\epsilon}_1(x,y)\right)\, dy + \int_{\frac{b_{SD,1}}{2}}^{\frac{b_{SD,1}}{2}+\tan(\beta)x_0 x} \sigma\left(\bar{\epsilon}_2(x,y)\right)\, dy\right) \frac{1}{y_{max}(x)} \tag{5.9}$$

$b_{SD,1}$	Breite der langen Kante des Stoßdämpfers (Abbildung 5.2)
β	Winkel der schrägen Kanten des Stoßdämpfers (Abbildung 5.2)
$\bar{\epsilon}_1$	Stauchung in Segment 1
$\bar{\epsilon}_2$	Stauchung in Segment 2

mit

$B_{SD,1}$	Width of long edge of shock absorber (Figure 5.2)

B	Angle of oblique edges of shock absorber (Figure 5.2)
$\bar{\varepsilon}_1$	Compression in Segment 1
$\bar{\varepsilon}_2$	Compression in Segment 2

when

$$\bar{\epsilon}_1(x,y) = \frac{x}{r_{Beh} - sign\left(r_{Beh}^2 - y^2\right)\sqrt{r_{Beh}^2 - y^2} + x_0}$$

r_{Beh}	Außendurchmesser des Behälters / der Stoßdämpferbasis
x_0	x bei maximaler möglicher Verformung (100% Deformation)

(5.10)

r_{cask}	Outside diameter of cask/of shock absorber base
x_0	x at maximum possible reshaping (100% deformation)

and

$$\bar{\epsilon}_2(x,y) = \frac{x - \left(\left(y - \frac{b_{SD,1}}{2}\right)\frac{1}{\tan(\beta)}\right)}{r_{Beh} - sign\left(r_{Beh}^2 - y^2\right)\sqrt{\left|r_{Beh}^2 - y^2\right|} + x_0 - \left(\left(y - \frac{b_{SD,1}}{2}\right)\frac{1}{\tan(\beta)}\right)}$$

(5.11)

and

$$y_{max} = \frac{b_{SD,1}}{2} + x\tan(\beta)$$

(5.12)

x is substituted with ε with the help of x_0 in order to get the stress function as a function of the expansion and not the deformation:

$$\epsilon = \frac{x}{x_0}$$

ϵ	Dehnung in der Symmetrieebene des Stoßdämpfers

(5.13)

ε	Expansion in symmetry plane of shock absorber

Figure 5.3 shows a comparison between the stress function of the shock absorber and the underlying wood characteristic (determined in Subchapter 4.3) using the example of octagonal shock absorbers in horizontal drop. At higher expansions, one can recognize that the stress function of the shock absorber has a lower stress level than the wood characteristic due to larger, still slightly compressed areas. The stress function, determined in this fashion, exactly takes into account the differing compression of various areas in the shock absorber as a function of the reshaping in the symmetry plane *x*. The multiplication of the stress function $\bar{\sigma}$ for each *x* or ε with the current surface *A(x)* provides precisely the same force as an integration of the really prevailing stress *σ(x,y)* via the surface *A*.

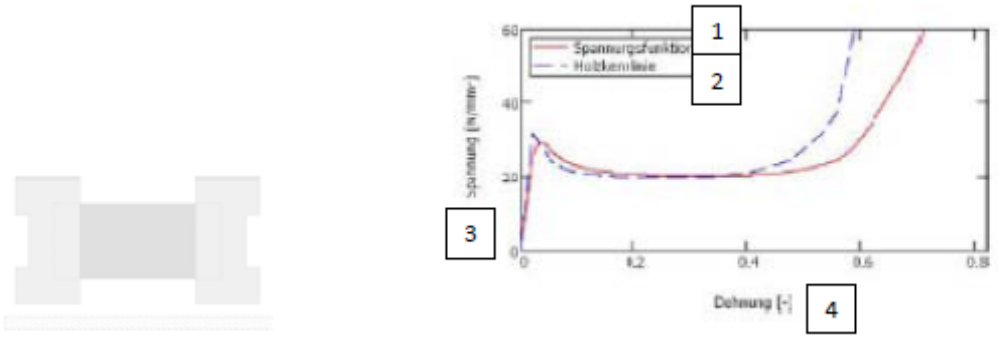

Figure 5.3: Comparison of Stress Function of Shock Absorber with the Underlying Wood Characteristic for the Horizontal-Drop Drop Position Using the Example of the CONSTOR® V/TC Shock Absorber

[Key: 1) Stress function; 2) Wood characteristic; 3) Stress; 4) Expansion].

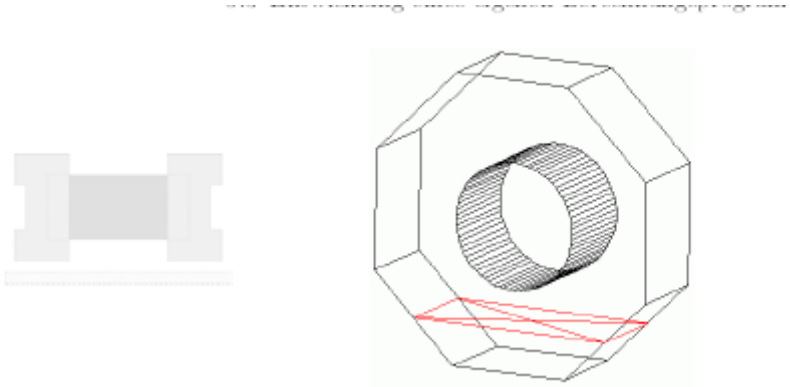

Figure 5.4: Section Plane Content Using the Example of an Octagonal Shock Absorber for the Horizontal-Drop Drop Position

5.3.2 Geometry Modeling

Along with the stress-expansion interrelationship, we must determine the interrelationship between the current section plane (see Figure 5.4) and the deformation *x*. We remember: The spring force term *F(x)* from equation 5.2 is replaced with the product of the

stress function $\bar{\sigma}$ and the section plane function *A(x)*. The average stress in the current shock-absorber section plane $\bar{\sigma}$, multiplied by the current section plane, will give us the momentarily prevailing pressure force in the shock absorber.

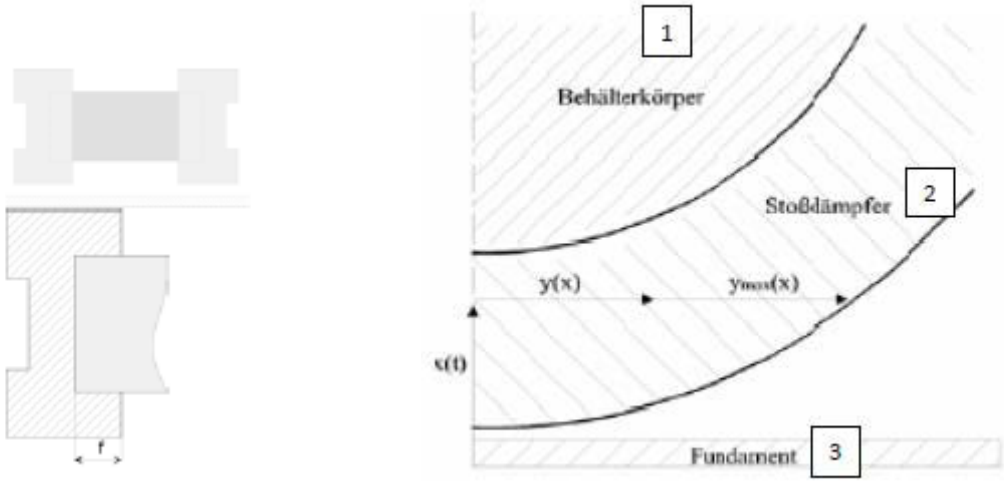

Figure 5.5: Schematic Illustration of a Partial Cross-Section for the Section Plane Calculation Using the Example of the Round Shock Absorber for the Horizontal Drop

[Key: 1) Cask body; 2) Shock absorber; 3) Foundation].

Basically, there are several possibilities for determining the section plane function. In simple geometries, working with a round shock absorber, one can determine the plane content, and one can describe all variables of the plane content function as a function of *x* (see Figure 5.5 for the horizontal-drop drop position)[3]:

$$A(x) = 2y_{max}(x)f_{SD}$$

$A(x)$	Schnittflächenfunktion (vgl. Abbildung 5.4)
$y_{max}(x)$	Stoßdämpferbegrenzungsfunktion (vgl. Abbildung 5.5)
f_{SD}	Tiefe des Stoßdämpfers (vgl. Abbildung 5.5)

(5.14)

$A(x)$	Section plane function (see Figure 5.4)
$y_{max}(x)$	Shock-absorber boundary function (see Figure 5.5)
f_{SD}	Depth of shock absorber (see Figure 5.5)

with the shock-absorber plane boundary function $y_{max}(x)$:

[3] The prerequisite here is a constant depth f_{SD} of the shock absorber.

$$y_{max}(x) = \sqrt{(2r_{SD} - x)x}$$

r_{SD} Radius des Stoßdämpfers

(5.15)

r_{SD} Radius of shock absorber

The plane function for a round shock absorber for the horizontal-drop drop position will then look like this:

$$A(x) = 2f_{SD}\sqrt{(2r_{SD} - x)x}$$

(5.16)

If the volume is known in case of complex geometries for the intersected geometry (for example, obliquely cut cylinder hoof [sic; zylinderhuf, cylinder stroke] in case of an edge drop of a cask with round shock absorbers - see Figure 5.6), then by substituting all of the variables of the volume function with x and formation of the differential quotient for x, one can determine the plane content of the section plane:

$$A(x) = \frac{dV(x)}{dx}$$

V Volumenfunktion

(5.17)

V Volume function

For the case of the cylinder hoof [sic] according to BRONSTEIN & SEMENDJAJEW [BS04], the volume under the marginal condition that b < R and $\phi < \pi$ would be as follows[4]:

$$V = \frac{h}{3b}\left[a\left(3R^2 - a^2\right) + 3R^2\left(b - R\right)\alpha\right]$$

(5.18)

[4] Variables according to Figure 5.6.

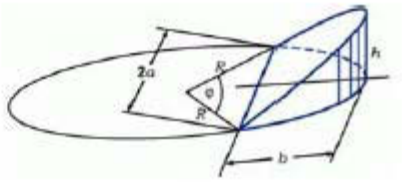

Figure 5.6: Cut Cylinder Hoof [sic} According to [BS04]

The section plane function resulting from equation 5.17 and equation 5.18 is not visible here due to its length.

5.3.3 Drop Positions Considered

Vertical Drop

For the vertical drop, we use only areas of the shock absorber under the cask body for the plane function. This assumption is justified in Section 4.2.2. The prerequisite is a cylindrical cask body with level alignment of the front surface. Two special cases exists here because this surface in the course of reshaping remains constant and because the expansion $\delta(x,y)$ is equal for all places in the shock absorber (see equation 5.7):

$$\bar{\sigma}(x) = \sigma(x) = const. \tag{5.19}$$

$\bar{\sigma}(x)$ Spannungsfunktion

$\bar{\sigma}(x)$ Stress function

$$A(x) = \pi r_{Beh}^2 = const. \tag{5.20}$$

$A(x)$ Schnittflächenfunktion

$A(x)$ Section plane function

For casks with an internal step in the outer contour (see Figure 5.6, left), the section plane function reads as follows, provided the internal area is not involved:

$$A(x) = \pi(r_{Beh}^2 - r_i^2) = const. \tag{5.21}$$

r_i Radius des inneren Absatzes

r_I	Radius of internal step

Horizontal Drop

The derivation of the stress function and the section plane function for octagonal and round shock absorbers was explained partly in earlier sections. The stress and section plane functions for an octagonal shock absorber look like this:

$$\bar{\sigma}(x) = \left(\int_0^{\frac{b_{SD,1}}{2}} \sigma\left(\bar{\epsilon}_1(x,y)\right)\, dy + \int_{\frac{b_{SD,1}}{2}}^{\frac{b_{SD,1}}{2}+\tan(\beta)x} \sigma\left(\bar{\epsilon}_2(x,y)\right)\, dy \right) \frac{1}{y_{max}(x)} \tag{5.22}$$

when $\bar{\varepsilon}_1$, $\bar{\varepsilon}_2$ and y_{max} according to equations 5.10 to 5.12 and

$$A(x) = n \cdot f_{SD}\left(b_{SD} + 2x\tan(\beta)\right) \tag{5.23}$$

n	Anzahl in Eingriff kommender Stoßdämpfer

n	Number of engaged shock absorbers

The stress and section plane functions for a round shock absorber look like this:

$$\bar{\sigma}(x) = \frac{\int_0^{\sqrt{(2r_{SD}-x)x}} \sigma\left(\frac{\sqrt{r_{SD}^2-y^2}-r_{SD}+x}{x_0-r_{SD}+\sqrt{r_{SD}^2-y^2}+r_{Beh}-sign\left(r_{Beh}^2-y^2\right)\sqrt{r_{Beh}^2-y^2}}\right) dy}{\sqrt{(2r_{SD}-x)x}} \tag{5.24}$$

r_{SD}	Radius des Stoßdämpfers
r_{Beh}	Außendurchmesser des Behälters / der Stoßdämpferbasis

r_{SD}	Radius of shock absorbers
r_{cask}	Outer diameter of cask/shock-absorber base

and

$$A(x) = 2f_{SD}\sqrt{(2r-x)x} \cdot n \tag{5.25}$$

5.3.4 Solution Algorithm and Results

Equation 5.3 can be solved with the stress and section plane functions determined on the preceding pages. The computation is performed in this study using the commercial computer algebra system MATHCAD, Version 13 [MCD06]. The solution algorithm is based on a Runge-Kutta method (see BUTCHER [But87]). As standard, 500 support points were used. Variation computations showed that a higher support point number did not improve the quality of the result.

Only the phase of shock-absorber compression is computed. Reliable setups are missing at this point for the phase of the relief following compression (also decompression or elastic resiliency). The relief phase is of little significance when it comes to the stress on the test specimen. This is why we refrain from a more precise modeling of this phase.

In the context of this study, the interrelationships were derived for vertical and horizontal drops for the usual cask and shock-absorber models (cylindrical cask, round and octagonal shock absorbers) and transferred to the *"ImpactCalc."*

Result Uncertainty

Along with geometry modeling, the stress function underlying this method exerts great influence on the computation result. The stress function of course was derived from experimental results with wood samples where the lateral expansion inhibition for the wood was adjusted in a specifically determined fashion as in the case of the shock-absorbing parts examined here. The energy absorption of the sheet metal construction of the shock absorber and its interrelationship with the wood is not considered here separately from the wood. Changes in the design can necessitate other stress functions. Analysis of the behavior of the shock-absorbing parts to be considered here in light of the drop tests thus is a prerequisite for the definition of a corresponding stress function.

5.4 Verification of the Analytical Setups

Verification is done on the basis of the experiments described in Chapter 4 with models of fuel-element transport casks/transport casks for radioactive waste. A description of the general marginal conditions is followed by considerations regarding verification for the individual drop positions.

5.4.1 General Aspects

Prerequisites

The prerequisite for the use of the program is represented by the fact that deformations on other parts of the shipping item rather than the shock-absorbing parts are negligible. That is the case when the resiliency of the shock-absorbing parts can be considered as being very high in comparison to the other parts of the shipping item. In this case, the cask bodies as well as the lid system can be considered as a rigid body. Multimass effects between content, lid system, shock-absorbing parts and other cask components must be ruled out, as was pointed out by BALLHEIMER, QUERCETTI & ZEISLER [BQZ02].

Comparison Criterion

The basis of verification is to be a comparison of the computed and experimentally determined force-time curves as well as the deformation of the shock-absorbing parts. One uses the deceleration, which can be converted into a force-time function via

$$F(t) = m \cdot a(t) \tag{5.26}$$

$F(t)$	Kraftfunktion
m	Masse
$a(t)$	Beschleunigungsfunktion

F(t)	Force function
m	Mass
a(t)	Acceleration function

because the force cannot be measured directly in the experiment. The prerequisite for this procedure is represented by the fact that the abovementioned conditions are maintained and that the cask can be conceived as a rigid body, excluding the shock absorber. The mass of the shock-absorbing parts must be small in comparison to the total shipping item because, in the course of the deformation of the shock-absorbing parts, the mass *m* in equation 5.26 is reduced by the mass of the already braked [sic] shock-absorber parts.

Another verification criterion is comparison between the computed and the experimentally determined shock-absorber deformation. Here it must be kept in mind that the measured shock-absorber deformations in general are smaller than those that occurred maximally in the drop test because the elastic resiliency was not considered. The computation determines the maximum deformation of the shock-absorbing parts. Controlling the reshaping is important in order to identify the penetration of the shock absorber (excessive compression, see Section 3.2.3) exactly as in the case of an impact of additional parts of the cask (for example, carrying pegs) and preventing it by means of corresponding design changes.

Filtration

Deceleration-time curves are measured with the help of locally applied acceleration sensors. To facilitate a comparison between experiment and computation, the effects of the local deformation effects that do not occur on shock-absorbing parts must be eliminated. These effects, for example, include the bending as well as ovalization oscillations of the cask body. These local processes and phenomena are not decisive for the basic shock-absorber behavior as long as the abovementioned marginal conditions (rigid body, no multimass effect) remain fulfilled. When these signals have small period durations in comparison to the shock duration, then by using a deep pass filter, one can turn off higher-frequency signals. The use of a low-pass filter is recommended in the Advisory Material of the IAEA § 701.9 [TSG08a]: *"When acceleration sensors are used to evaluate the impact behavior of the package, the cut-off*

frequency should be considered." Highly sensitive acceleration sensors measure a vast oscillation spectrum including high-frequency parts at the point at which the sensor is attached. That includes the shockwaves that run through the application site as well as all of the oscillations associated with the acoustic area. From the simple relationships for the single-mass oscillator:

$$x = a \sin \omega t \tag{5.27}$$

x	Schwingweg
$\hat{a}$	Amplitude
ω	Kreisfrequenz
t	Zeit

x	Oscillation path
$\hat{a}$	Amplitude
ω	Circuit frequency
t	Time

$$\ddot{x} = -\hat{a}\omega^2 \sin \omega t \tag{5.28}$$

one can compute the relationship of the path amplitudes of two differently frequent oscillation parts:

$$\frac{\hat{a}_1}{\hat{a}_2} = \frac{\omega_2^2 \ddot{x}_1}{\omega_1^2 \ddot{x}_2} \tag{5.29}$$

Equation 5.29 shows that an acceleration peak $\ddot{x}_2$, whose underlying frequency ω_2 amounts to ten times the frequency ω_1, is to be equated only with a stress of the model amounting to one-one-hundredth of the stress a_1. This means that the more high frequency a signal is, the less will be the underlying model stress, assuming the same amplitude. This is why the Advisory Material of IAEA § 701.9 [TSG08a] proposes the use of a filter frequency for shipping items with a mass of up to 100 mg:

$$f = [100 - 200\text{Hz}] \sqrt[3]{\frac{100}{m}} \tag{5.30}$$

f	Filterfrequenz [Hz]
m	Versandstückmasse [Mg]

f	Filter frequency [Hz]
m	Shipping item mass [mg]

5.4.2 Horizontal Drop

CONSTOR® V/TC

Figures 5.7 to 5.9 show the path, deceleration and force-time curves calculated with *"ImpactCalc"* for the horizontal drop of the CONSTOR® V/TC from a height of 9 m. After a strong rise that can be traced back to a broad shock-absorber surface that is immediately engaged, there follows a constant energy conversion with a slightly changing deceleration level. A summary of the computation results, including the shock-absorber deformation, will be found in Table 5.1.

Table 5.1: Results of the *"ImpactCalc"* Computation, 9-m Horizontal Drop, CONSTOR® V/TC

CONSTOR® V/TC	*"ImpactCalc"* **Lid**	*"ImpactCalc"* **Bottom**
Shock time compression phase	29.2 msec	29.4 msec
Maximum reshaping	209 mm	207 mm
Maximum reshaping degree	51.6%	51.1%
Maximum deceleration	519 m/s^2 (53 g)	519 m/s^2 (53 g)
Maximum reaction force	94 MN	94 MN

Figure 4.11 shows the deceleration-time curves from acceleration sensors in the lid and the bottom areas of the cask body during the 9-m horizontal drop of the CONSTOR® V/TC. A comparison of the experimentally determined deceleration curve on the lid with the computed curve (Figure 5.10) shows relatively good agreement regarding the computed and experimentally determined shock time and the average force level in the shock-absorber compression phase. The peak in the deceleration-time curve, which can be seen in Figure 5.10 at 3 msec is not reproduced by the computation. The wood characteristics underlying this program do not show this peak, and it cannot be derived either from the geometrical marginal conditions; the program therefore cannot determine this peak either.

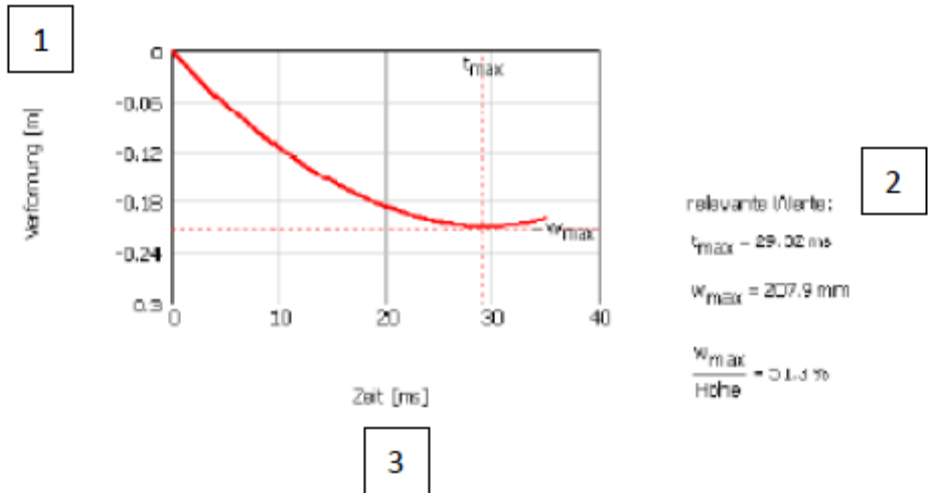

Figure 5.7: Deformation-Time Curve for 9-m Horizontal Drop of the CONSTOR® V/TC Computed by *"ImpactCalc"*

[Key: 1) Deceleration; 2) Relevant value; 3) Time; 4) Height].

Deceleration-Time Curve

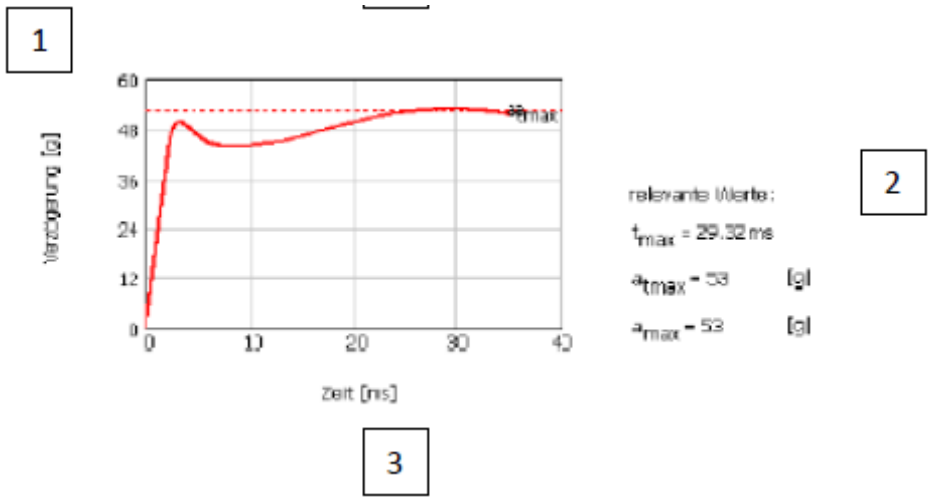

Figure 5.8: Deceleration-Time Curve for 9-m Horizontal Drop of the CONSTOR® V/TC Computed by *"ImpactCalc"*

[Key: 1) Deceleration; 2) Relevant value; 3) Time].

Shock Force Curve

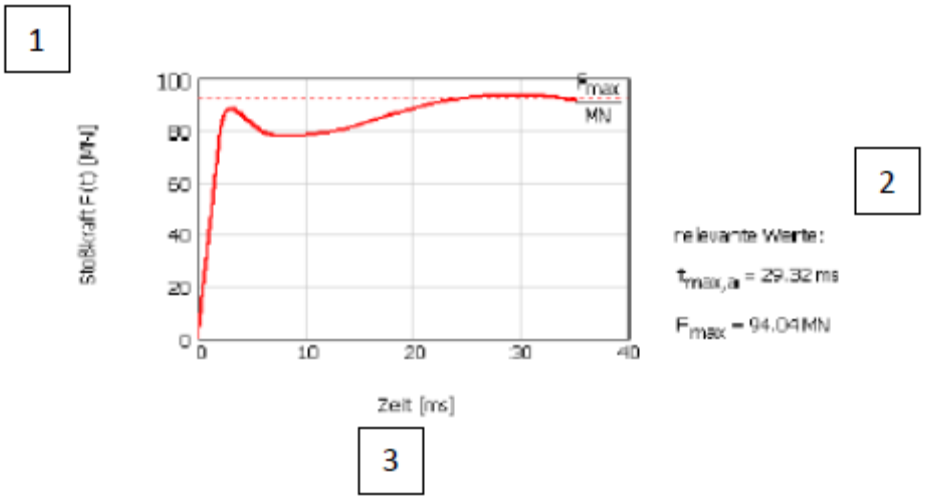

Figure 5.9: Force-Time Curve for 9-m Horizontal Drop of the CONSTOR® V/TC Computed with *"ImpactCalc"*

[Key: 1) Shock force; 2) Relevant value; 3) Time].

CONSTOR® V/TC, 9-m Horizontal Drop

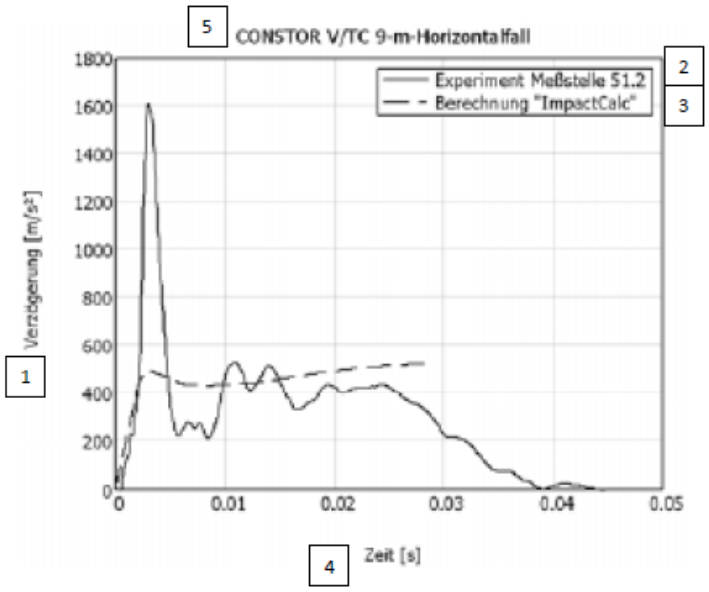

Figure 5.10: Comparison of the Experimentally Determined (Low-Pass Filter with 150 Hz) with the Deceleration-Time Curve for the 9-m Horizontal Drop of the CONSTOR® V/TC on the Lid Computed with *"ImpactCalc"*

[Key: 1) Rate deceleration; 2) Experiment measurement point; 3) *"ImpactCalc"* computation; 4) Time].

Table 5.2: Comparison of the Deformations Determined in the Drop Test with the Results of the *"ImpactCalc"* Computation of the 9-m Horizontal Drop of the CONSTOR® V/TC. The values in parentheses are based on an estimated elastic resiliency of 30 mm.

CONSTOR® V/TC	**Test**	*"ImpactCalc"*
Maximum reshaping, lid	150 mm (180 mm)	209 mm
Maximum reshaping bottom	171 mm (201 mm)	207 mm
Maximum reshaping degree, lid	37.0% (44.4%)	51.6%
Maximum reshaping degree, bottom	42.2% (49.6%)	51.1%

An analysis of the CONSTOR® V/TC experimental cask showed that the phenomenon of the high acceleration peak is explained by the special structure of the test casks. The great deadweights of the individual cask components that are not rigidly connected with each other, such as the outside and inside liners, the Constorit filling, Overpack and shock absorber result in a complex multimass dynamic during the impact process. This is why only a comparison of the shock-absorber deformations and the shock time during the shock-absorber compression phase is done on the CONSTOR® V/TC. A comparison of the computed and experimentally determined deformations shows that *"ImpactCalc"* overestimates the deformations conservatively by about 27% on the lid or 17% on the bottom.

The deformations shown in Table 5.2 are corrected by the elastic resiliency (see Section 4.2.1). When we consider an elastic resiliency of about 30 mm or 7.5% (according to Section 4.1), then we get deviations amounting to about 13% for the lid and about 3% for the bottom.

Shock-Absorber Testing

Table 5.3 presents a summary of the computation results, including the shock-absorber deformation.

Table 5.3: Results of the *"ImpactCalc"* Computation, 9-m Horizontal Drop, Shock-Absorber Test

Shock-Absorber Test	*"ImpactCalc"*
Shock time, compression phase	10.1 msec
Maximum reshaping	67.2 mm
Maximum reshaping degree	37.2%
Maximum deceleration	1660 m/s^2
Maximum reaction force	11.47 MN

Shock absorber test, 9-m horizontal drop

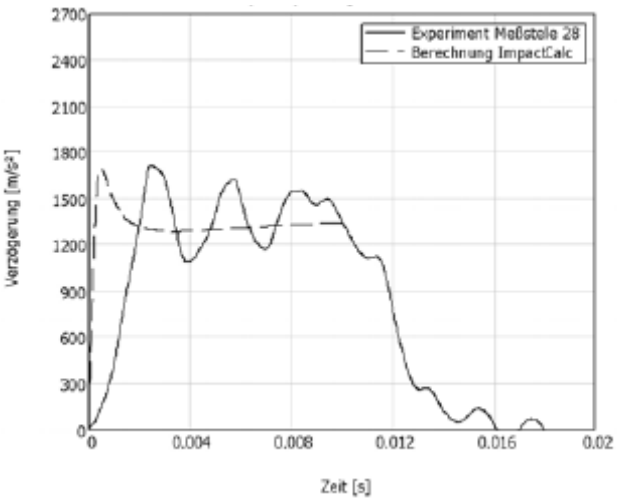

Figure 5.11: Comparison of the Experimentally Determined (Low-Pass Filter with 350 Hz) [Curve] with the Deceleration-Time Curve Computed with *"ImpactCalc"* for the 9-m Horizontal Drop, Shock Absorber Test

[Key: 1) Deceleration; 2) Experiment measurement point; 3) Computation *"ImpactCalc"*; 4) Time].

A comparison of the experimentally determined deceleration-time curve on the lid with the computed curve shows relatively good agreement regarding the computed and experimentally determined shock time and the basic curves in the shock-absorber compression phase (Figure 5.11). The difference between computation and experiment at the start of the shock process (steeper rise) can be explained by the gap closing effects and by the slight axial turning upon impact (see Figure 4.12).

Table 5.4: Comparison of the Decelerations and Deformations Determined in the Drop Test with the Results of the *"ImpactCalc"* Computation of the 9-m Horizontal Drop for Shock-Absorber Testing

Shock-Absorber Testing	**Test**	*"ImpactCalc"*	**Deviation**
Maximum deceleration			
Lid	1622 m/s^2	1660 m/s^2	2.3%
Bottom	1634 m/s^2	1660 m/s^2	1.6%
Maximum reshaping			
Lid	59.2 mm	67.2 mm	13.5%
Bottom	65.0 mm	67.2 mm	3.4%
Maximum reshaping including elastic resiliency (5%)			
Lid	62.2 mm	67.2 mm	8.0%
Bottom	68.3 mm	67.2 mm	-1.6%
Reshaping degree			
Lid	34.5%	37.4%	
Bottom	37.9%	37.4%	
Shock time	10-12 msec	10.2 msec	

A comparison of computed and experimentally determined deformations shows that *"ImpactCalc"* overestimated deformations conservatively by about 4% for the lid or 1% for the bottom. The deformations, shown in Table 5.4, are corrected by the elastic resiliency (see Section 4.2.1). If an elastic resiliency of about 5% is considered (according to Section 4.2.1), then we get deviations of about 8% for the lid and about 2% for the bottom.

5.4.3 Vertical Drop

Table 5.5 shows a compilation of the computation results including the shock-absorber deformation.

Table 5.5: Results of the *"ImpactCalc"* Computation, 9-m Vertical Drop, MSF69BG® on the Lid

MSF69BG®	*"ImpactCalc"* **Lid**
Shock time compression phase	43.1 msec
Maximum reshaping	317 mm
Maximum reshaping degree	52.2%
Maximum deceleration	371 m/s^2
Maximum reaction force	47.12 MN

A comparison of the experimentally determined deceleration- time curve and the computed curve displays relatively good agreement regarding the computed and experimentally determined shock time and the basic curves in the shock-absorber compression phase (Figure 5.12). The decline of cask body deceleration between 20 and 25 msec is not illustrated here. An analysis of other acceleration sensors showed that the content substitute masses at that point in time hit the primary lid and thus results in a brief decline of the deceleration. At the start of the shock process, the developing rigid body deceleration is conservatively overestimated.

MHI MSF69BG, 9.3-m Vertical Drop

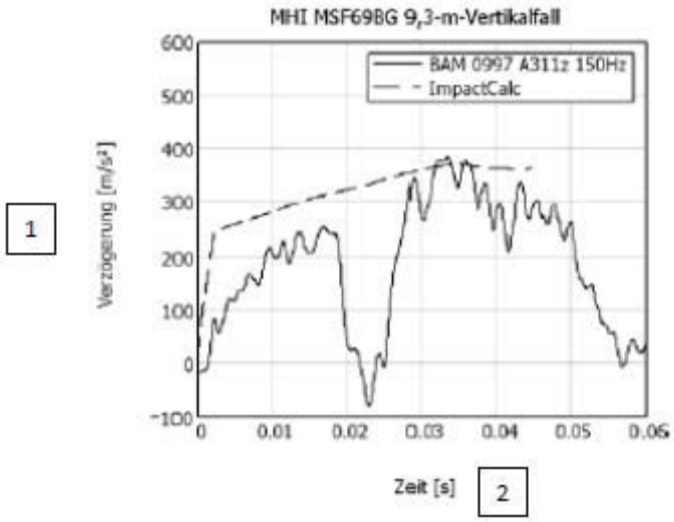

Figure 5.12: Comparison of Experimentally Determined (Low-Pass Filter with 150 Hz) [Curve] with the Computed Deceleration-Time Curve for the 9-m Vertical Drop, MSF69BG®, on the Lid

[Key: 1) Deceleration; 2) Time].

Table 5.6: Comparison of the Decelerations and Deformations Determined During the Drop Test with the Results of the *"ImpactCalc"* Computation, 9-m Vertical Drop, MSF69BG®, on the Lid

MSF69BG®	**Test**	*"ImpactCalc"*	**Deviation**
Deceleration	383 m/s^2	371 m/s^2	-3.1%
Reshaping	261 mm	317 mm	21.5%
Maximum reshaping including the elastic resiliency (5%)			
Reshaping	276 mm	317 mm	14.8%
Shock time	48-55 msec	43.1 msec	

A comparison of computed and experimentally determined deformations shows that *"ImpactCalc"* overestimated deformations conservatively by about 22%.

The deformations, shown in Table 5.6, are corrected by the elastic resiliency (see Section 4.2.1). If one considers an elastic resiliency of about 6% (according to Subchapter 4.1), then we get deviations between the computed and measured deformation amounting to about 15%.

5.5 Conclusions and Summary

In this chapter, we showed that the simplified numerical method *"ImpactCalc"* presented in this study is suitable for determining estimations for global kinetic parameters, such as cask rigid-body decelerations or shock-absorber deformations. With minor deviations, this method

can determine the curves of rigid-body decelerations and shock-absorber deformations for transport casks holding radioactive substances with wood-filled shock-absorbing parts.

Of course, the limitations of this method were also pointed up quite clearly. Using the example of CONSTOR® V/TC and MHI MSF69BG®, it was shown that it is a fundamental marginal condition of this method that the entire cask system, excluding the shock-absorbing parts, can be construed approximately as a uniform, continuous rigid body. This simplification can be made only if the resiliency of the container compared to the resiliency of the shock-absorbing parts is negligible and if no significant relative motion is possible between individual parts of the cask. From the result of the CONSTOR® V/TC computation, it must be concluded that the interaction between shock absorber and cask body must be subjected to further scrutiny, particularly for casks such as the CONSTOR® V/TC with large, heavy shock-absorbing parts (weight accounting for about 22% of the packaging) and mobile parts, such as the Overpack (mass accounting for about 16%).

Simplified numerical methods require precise verification. The estimating character of the method includes predictability of failure on the basis of the simplified assumptions in conjunction with the lateral expansion inhibitions in the shock-absorbing part that cannot be fixed a priori. The wood characteristics, determined in Subchapter 4.3, turned out to be parts characteristics that are suitable in the context of this method for the practical application cases considered here.

On the basis of the computation results for the CONSTOR® V/TC, it must be concluded that the widespread basic principle of evaluation of the maximum rigid body deceleration for model stress can no longer be meaningfully applied for casks such as the CONSTOR® V/TC. In the context of cask evaluation, we must therefore investigate, for example, by means of a dynamic comparison computation, whether the setup of a rigid body deceleration covers the cask stress.

In model testing, the method, assuming verification, can be specifically employed, for example, for parameter studies or as estimations of the rigid-body deceleration and shock-absorber deformation in the course of test planning. If certainties occurring in connection with a safety data determination are large enough to compensate for the uncertainties connected with the use of simplified numerical methods (property change of the shock absorber by change in friction, of the sheet metal behavior, etc.), then this method can also be used for safety data recording. The required safety factors should be determined on the basis of the possible property changes of the component of the shock-absorbing part. Assuming a verification with the results of drop tests of a similar model, we propose here the use of a sufficiently conservative safety factor of two for the results for computations with *"ImpactCalc"* in order to provide further evidence.

For risk analysis, one can estimate many different accident situations, for example, impact against real foundations, in a simple and reasonably priced manner and can be compared with the impact upon the nonresilient test stand foundation. The prerequisite is a verification by a comparison with the drop test results on the model to be considered.

6 Modeling with FEM

At the beginning of this chapter, we presented a brief overview of the fundamentals of FEM and of material theory, which is important in this connection. FEM is a numerical simulation method that is widely used in science and technology in order to determine approximation solutions for physical problems. The method is employed in model testing of transport casks holding radioactive substances in combination with drop tests for stress determination.

After an introduction into the continuum-mechanics fundamentals that are important for this study, this chapter presents various modeling forms for the simulation of wood exposed to pressure stress in conjunction with large deformations. Their applicability is tested with the help of various material formulations in the commercial FE program LS-DYNA [Hal97] [LSD08]. In a first step, the shock tests, described in Subchapter 4.3, are recomputed in order to evaluate the applicability of the modeling forms using simple geometries. The conclusions obtained in this way can be applied to the particular practical case and can be conclusively evaluated with the help of results deriving from drop tests with transport casks holding radioactive substances.

As unit system, we basically employ *g, mm, ms, N, MPa*.

6.1 Introduction and Fundamentals

In this subchapter, we will first of all take up the fundamentals of continuum mechanics that will be important in this connection. Based on a series of balance setups, we will describe the marginal conditions in which the FEM is embedded as well as the fundamental equations of the FEM because these underlying interrelationships cannot be found in such a summarized fashion in other studies.

6.1.1 Continuum Mechanics Fundamentals

The fundamentals of continuum mechanics will be presented in a brief form and only to the extent that they are important for an understanding of the following parts of the study. We will dispense with a description of the kinematic fundamentals, referring to the corresponding bibliography (for example, BETTEN [Bet93]). The basis is to be the Euclidean space R^3. A delimited quantity of particles[1] is to be labeled as a body or continuum B, and in that body, each particle can be associated with a point in space and the body remains continuous in case of deformation.

Stress and Distortion Tensor

The general stress state in a body is described by the stress tensor σ or, with another symbol, the components of the stress tensor σ_{ij}. The description of the form change state is presented for small deformations by the distortion tensor ε or the components of the distortion tensor ε_{ij}. The stress tensor σ can be broken down into a volume-changing (hydro- or isostatic) and a shape-changing (deviatory) par:

[1] Material points

$$\sigma_{ij} = \sigma_{ij}^0 + s_{ij}$$

σ_{ij}	Komponenten des Spannungstensors
σ_{ij}^0	Komponenten des Kugeltensors (hydrostatischer Anteil)
s_{ij}	Komponenten des Spannungsdeviators (deviatorischer Anteil)

(6.1)

σ_{ij}	Components of the stress tensor
σ_{ij}^0	Components of the ball tensor (hydrostatic part)
s_{ij}	Components of the stress deviator (deviatory part)

We proceed in a similar manner for the distortion tensor. Using the KRONECKER symbol:

$$\delta_{ij} = \begin{cases} 1 & \text{für } i = j \\ 0 & \text{für } i \neq j \end{cases} \qquad (6.2)$$

[Key: für = for].

and EINSTEIN's summation convention, it now follows that:

$$\sigma_{ij} = \frac{\sigma_{kk}}{3}\delta_{ij} + s_{ij} = \sigma_m \delta_{ij} + s_{ij}$$

δ_{ij}	KRONECKER Symbol
σ_m	Mittelspannung (mittlere Spannung, isostatische Spannung)

(6.3)

δ_{ij}	KRONECKER symbol
σ_m	Average stress (average stress, isostatic stress)

$$\epsilon_{ij} = \epsilon_{ij}^0 + e_{ij} = \frac{\epsilon_{kk}}{3}\delta_{ij} + e_{ij} = \epsilon_m \delta_{ij} + e_{ij}$$

ϵ_{ij}	Komponenten des Verzerrungstensors
ϵ_{ij}^0	Komponenten des Verzerrungskugeltensors (hydrostatischer Anteil)
e_{ij}	Komponenten des deviatorischen Anteils des Verzerrungstensors
ϵ_m	mittlere Dehnung, volumetrische Dehnung

(6.4)

ε_{ij}	Components of distortion tensor
ε_{ij}^0	Components of the distortion ball tensor (hydrostatic part)
e_{ij}	Components of the deviatory part of the distortion tensor
ε_m	Average expansion, volumetric expansion

In the following, we will take a closer look at the stress tensor. In analogy, all operations can also be transferred to I distortion tensor because both tensors involve symmetrical tensors of the second stage ($\sigma_{ij} = \sigma_{ji}$ or $\varepsilon_{ij} = \varepsilon_{ji}$).

A Cartesian axis system can always be defined for the stress tensor (main axis transformation) in that all secondary diagonal elements of the stress tensor are turned into zero ($\sigma_{ij} = 0$ for $I \neq j$). The following must therefore be fulfilled for equation 6.5:

$$(\sigma_{ij} - \delta_{ij}\sigma_\lambda)\, a_j = 0 \qquad (6.5)$$

σ_λ Eigenwerte, Hauptspannungen
a_j Komponenten der Eigenvektoren zum Eigenwert λ

σ_λ Eigenvalue, principal stresses
a_j Components of the eigenvectors for the eigenvalue λ

For nontrivial solutions of equation 6.5, the determinant of the coefficient matrix must disappear:

$$\det(\sigma_{ij} - \delta_{ij}\sigma_\lambda) = 0 \qquad (6.6)$$

In the Euclidean space R^3, the solution of equation 6.6 supplies the following characteristic polynomial or characteristic equation:

$$\sigma_\lambda^3 - I_1\sigma_\lambda^2 + I_2\sigma_\lambda - I_3 = 0 \qquad (6.7)$$

I_1, I_2, I_3 1., 2. und 3. Invariante des Spannungstensors

I_1, I_2, I_3 1st, 2nd and 3rd invariant of the stress tensor

The invariants of tensors depend on the stress state at the considered point but not on the chosen coordinate system. For σ_{ij}, they are as follows:

$$I_1 = \text{Spur}(\sigma_{ij}) = \sigma_{ii} \qquad (6.8)$$

$$I_2 = +\frac{1}{2}(\sigma_{ii}\sigma_{jj} - \sigma_{ij}\sigma_{ji}) \qquad (6.9)$$

$$I_3 = \det(\sigma_{ij}) \qquad (6.10)$$

[Key: spur = trace].

Similarly, eigenvalues and invariants can be given for the stress deviator:

$$\det\left(s_{ij} - \delta_{ij} s_\lambda\right) = 0 \tag{6.11}$$

$$s_\lambda^3 - J_1 s_\lambda^2 + J_2 s_\lambda - J_3 = 0 \tag{6.12}$$

$$J_1 = \text{Spur}\left(s_{ij}\right) = s_{ii} = 0 \tag{6.13}$$

$$J_2 = -\frac{1}{2}\left(s_{ij} s_{ji}\right) \tag{6.14}$$

$$J_3 = \det\left(s_{ij}\right) \tag{6.15}$$

J_1, J_2, J_3 1., 2. und 3. Invariante des Spannungsdeviators

J_1, J_2, J_3 1st, 2nd and 3rd invariant of the stress deviator

We will not further touch here upon the invariants of the ball tensor because it is not relevant due to the identity between the first invariant of the stress tensor and the first invariant of the ball tensor for the following material models.

The stress state can be described objectively[2] with the help of three independent invariants. Usually, the first invariant of the stress tensor I_1 and the second and third invariants of the stress deviators J_2, J_3 are used for this purpose because, with the help of the first invariant of the stress tensor, one can fully describe the hydrostatic stress part, and with the help of the second and third invariants of the stress deviator, one can fully describe the deviatory stress part.

6.1.2 Material Theory

Independently of each other, the basic laws of continuum mechanics describe the kinematic, kinetic and energetic magnitudes that must basically apply to every system. In addition, however, we need information on the material behavior. Material laws describe the specific peculiarities of the macroscopic behavior with phenomenological variables. The following axioms should apply for material theory:

Causality principle. By way of independent variables, we only have the displacements u_i and the temperature Θ. All other variables of a thermomechanical material can be derived from that.

Principle of determinism. All dependent variables[3] in a material point in space are definitely determined by the history of the independent variables u_i, Θ in the entire body B.

Principle of local effect. The condition at a material point depends only on the values of the independent variables in its immediate vicinity[4].

[2] Independently of the observer.
[3] Stress and distortion measures, heat flows, etc.
[4] Also principle of near action.

Objectivity. The material laws are independent of the station of the observer and of any rigid body motion.

In the following, we will briefly touch on the areas of material theory that are most important in this connection. For intensive coverage, we would recommend reading MARSDEN & HUGHES [MH82], NOLL [Nol74], PIPKIN & RIVLIN [PR59] [PR60] and TRUESDELL [Tru85] as well as the works of general continuum mechanics (BETTEN [Bet01], WILLNER [Wil03]).

Elasticity

A material is called elastic when all dependent constitutive variables are definite functions of the independent constitutive variables of the current point in time, that is to say, if they do not depend on the stress history. This means that elastic processes are not dissipative. An elastic material returns to its initial state after complete relief. In the case of linear elasticity, we start with a linear connection between stress and distortion.

In case of isothermal limitation, the specific free energy consists only of form-changing energy:

$$\Phi = \frac{1}{2}\epsilon_{ij} C_{ijkl} \epsilon_{kl}.$$

Φ	Spezifische freie Energie
C_{ijkl}	Materialtensor

(6.16)

Φ	Specific free energy
C_{ijkl}	Material tensor

The generalized HOOK's law can be derived only by derivation of Φ for the distortions ε_{ij}:

$$\sigma_{ij} = \frac{\partial \Phi}{\partial \epsilon_{ij}} = C_{ijkl}\epsilon_{kl}$$

(6.17)

The material tensor C_{ijkl} has 81 entries for general anisotropy. Depending on the symmetry type (monoclinic, orthotropic, transversal-isotropic, isotropic, etc.), one can reduce the number of constants. There are two elastic constants for the special case of isotropy. For a more in-depth understanding, we would recommend reading the pertinent literature (for example, BETTEN [Bet01]).

Plasticity

With the help of

- flow condition,
- flow rule,
- consolidation law,

one can constitutively describe plastic material behavior. In the multiaxial stress space, the flow condition defines a surface that separates the stress states into areas of elastic and elastic deformation. The flow rule defines the direction of the plastic deformation and the consolidation law describes the evolution of the flow surface in the course of plastic deformation.

The characteristic feature of plastic material behavior is represented by the fact that lasting distortions occur after complete relief. Assuming small deformations, the distortion is additively split into a part of elastic ε^e and a part of plastic ε^p distortion. The elastic distortions can be determined with HOOK's law, derived in the preceding subsection. There is no clear connection anymore between a stress and distortion tensor; therefore, we need incremental formulations that must then be integrated over the entire stress history.

Flow condition. The flow condition F can be subdivided into a pure stress part $f(\sigma_{ij})$ (the flow criterion) and a material parameter k that is to be determined experimentally:

$$F(\sigma_{ij}) = f(\sigma_{ij}) - k = f(I_1, J_2, J_3) - k = 0 \tag{6.18}$$

In the n-dimensional stress space (here $n = 6$), the flow condition represents a closed surface. Direct visualization is not possible due to its dimensionality. If we look at the stresses, of course, in the principal axis representation (see Section 6.1.1), then the flow conditions can be illustrated graphically in the three-dimensional principal axis space. A classification can be made with the help of the type of dependence of the flow condition on the invariance. Flow surfaces are frequently illustrated with the section surface of the flow surface in the principle stress space with the octahedron plane[5] (Figure 6.1). These surfaces characterize the material behavior in case of purely shape-changing stress.

The flow condition according to VON MISES [vM28] starts with the assumption that in the case of crystalline materials, the flow depends only on the deviatory part of the stress state. This setup results from investigations on the start of flow of crystals.

$$F(J_2, k) = \sqrt{3J_2} - k \tag{6.19}$$

In the principal stress space, this flow condition defines a circular cylinder located along the hydrostatic axis, unlimited downward and upward (Figure 6.1, left).

[5] Also deviator plane.

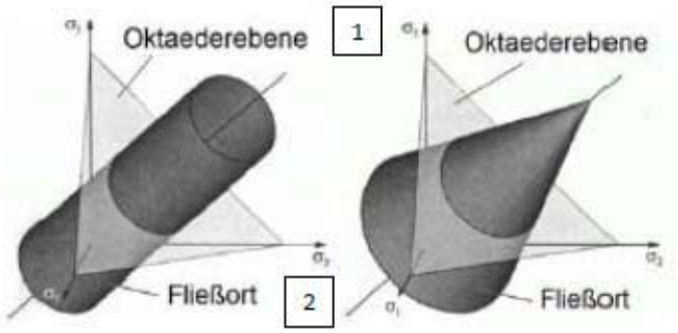

Figure 6.1: Flow Conditions According to VON MISES [vM28] and DRUCKER & PRAGER [DP52] in the Principal Axial Space

[Key: 1) Octahedron plane; 2) Flow side].

The flow condition according to DRUCKER & PRAGER [DP52] is often used for materials subjected to friction, such as floors and concrete. The flow condition looks like this:

$$F(I_1, J_2) = \alpha I_1 + \sqrt{J_2} - k \quad (6.20)$$

A dependence on the hydrostatic stress state is defined by means of the first invariant of the stress tensor (Figure 6.1, right).

According to BETTEN [Bet01], the flow condition must basically have a convex surface, something that can be derived from DRUCKER's stability postulate (see HOFSTETTER & MANG [HM95]). As for a number of other isotropic flow conditions, such as those of MOHR COULOMB or TRESCA, as well as anisotropic flow conditions, such as those of HILL or according to TSAI & WU, we would like to refer to the pertinent literature (for example, BETTEN [Bet01]), or they are presented in the context of the discussion of the material laws that are implemented in LS-DYNA [Hal97] [LSD08].

Flow rule. The direction of the plastic flow is defined with the help of the flow rule:

$$d\varepsilon^{p} = d\lambda \left(\frac{\partial Q}{\partial \sigma} \right) \quad (6.21)$$

Here, $d\lambda$ is the plastic multiplier that in the current iteration step determines the amount of plastic expansion and Q is the plastic potential that provides the direction of the plastic expansion. An associated flow rule is obtained if the flow condition $Q = F$ is used for the plastic potential. Plastic flow in conjunction with associated flow rules thus always takes place in a direction perpendicular to the flow surface, whereas in nonassociated flow rules, plastic flows are also possible in directions other than the perpendicular direction.

Consolidation law. In the course of increasing plastic expansion, materials frequently display increasing flow strength, something that can be interpreted as a translation of or a change in the magnitude of the flow surface. Isotropic consolidation is a boundary case; here, the flow surface remains fixed in the principal stress area, where it becomes slowly larger. In a second borderline case, in other words, kinematic consolidation, the position of the flow surface in the principal stress area is changed, but the magnitude remains constant.

Consideration of Attenuation

In mechanics, attenuation effects are frequently considered as attenuation in proportion to the velocity. In FEM for reasons of numerical efficiency, one frequently uses RALEIGH's attenuation (see BATHE [Bat02]), which is split up into a mass-dependent and a stiffness-dependent part:

$$\mathbf{C} = \alpha\mathbf{M} + \beta\mathbf{K} \tag{6.22}$$

$\mathbf{C}$	Dämpfungsmatrix
$\mathbf{M}$	Massenmatrix
$\mathbf{K}$	Steifigkeitsmatrix
α, β	durch zwei Dämpfungsmaße gegebene Konstanten

$\mathbf{C}$	Attenuation matrix
$\mathbf{M}$	Mass matrix
$\mathbf{K}$	Stiffness matrix
α, β	Constants given by two measures of attenuation

6.2 Possibilities of Modeling Wood

6.2.1 Problem Description

In many fields of practical application, wood constructions are considered only up to the point of failure (attainment of strengths, etc.). That is not sufficient in the sense of this study because wood is very severely deformed as shock-absorbing material and continues to absorb energy in spite of large-volume failure in conjunction with large deformations.

The macrostructural behavior of wood must be inspected more closely in the post-rupture area so that one may identify possible setups for material laws by means of which one can adequately describe the behavior of wood in the case of large deformations in the post-rupture area in response to axial stress. In Subchapter 4.4, we derive the fact that the energy absorption of the wood fiber mixture, which is formed in the course of compression, depends on the lateral expansion inhibition of the mixture. Although the failure starts on the microscopic magnitude level, the effects and thus also the visible order of magnitude of the failure are definitely macroscopic and are no longer negligible in relation to the system dimensions (see also GROSSE [Gro05]). A phenomenon, which is so fashioned by microscopic and macroscopic effects, is

difficult to acquire in terms of continuum mechanics because continuum mechanics starts with a continuously coherent medium.

6.2.2 Continuum Mechanics Substitute Model with Multiaxiality

A physical model for the behavior of wood in response to axial stress and large deformations is derived in Subchapter 4.4. This model is translated for the first time into the continuum-mechanics interrelationship where, in this particular case, a continuum mechanics substitute model is proposed which - in spite of macroscopic cracks and large-area failure in the wood - is supposed to be capable of describing the behavior of wood in response to pressure stress and large deformation. The fiber mixture, which takes shape in the course of deformation, is simulated here as a continuous system. This procedure requires adaptations of various material law parameters.

On the basis of the derivations from the experimental results described in Section 4.2.5, the flow surface of the "substitute continuum" should be dependent not only on the deviatory stress state but also on the hydrostatic stress state and thus on the 1st invariant of the stress tensor. The multiaxiality of the stress state is taken into consideration due to the dependence of the flow surface evolution on the hydrostatic and deviatory stress state. When we use a monotonously rising hydrostatic flow curve and a softening deviatory flow curve, then in combination with significant lateral expansion and corresponding expansion inhibition, one can possibly simulate the behavior of wood also under large deformations. The model can be in a position to control the stress prepositioning in conjunction with the outward kinking of the wood fiber bundles in accordance with lateral expansion inhibition. If the lateral expansion inhibition was small, then the stress was controlled above all by the deviatory part that is modeled in a softening [desolidarizing] manner. During the test, the wood fiber bundles kink out at this point and evade the stress laterally. If the lateral expansion inhibition is high, then the multiaxiality of the stress state and the hydroscopic flow curve that keeps rising or is not modeled in a softening fashion takes over the control of the flow surface. The outkinking wood is prevented from a lateral expansion and is compressed by cavity compression.

The numerical instabilities connected with the use of a softening flow curve may possibly turn into a problem.

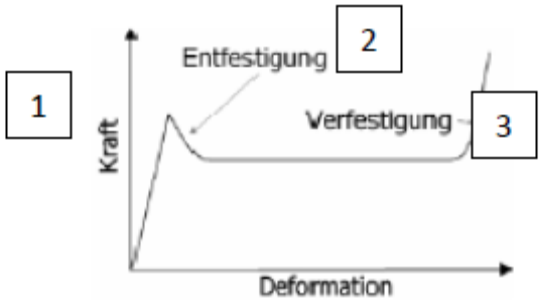

Figure 6.2: Principal Force-Deformation Curve with Softening and Hardening

[Key: 1) Force; 2) Softening; 3) Hardening].

6.2.3. Other Modeling Setups

At this point, we want to derive and present other possibilities for the modeling of axially stressed wood in case of large deformations. That the wood is described as a locally coherent system in spite of macroscopic cracks and large-area failure also applies to these setups. That requires adaptation for various material law parameters. Particular emphasis is placed here on the modeling of softening (see Figure 6.2) because, while the pressure strength in the wood generally determines the stress for the cask, a deformation of the wood into the area of hardening (see Fig. 6.2) for the practical case of a *shock-absorbing part* must be capable of being ruled out or estimated. The softening is a function of the lateral expansion inhibition; therefore, depending on the construction of the shock absorbers, we can find differently intensive softenings. The level of softening influences the energy absorption of the shock absorber.

The behavior of wood can basically be described only to a limited extent by way of the deterministic approach due to the statistical fluctuations of the material properties and the complexity of the compression mechanisms in response to axial stress. In the following, we will present or develop various other modeling setups and we will evaluate their applicability to the case at hand.

Softening flow curve. One possibility has to do with the modeling of the wood as continuum when one uses a softening flow curve. Here, the damage is "smeared" over the computation object in a continuum-mechanics fashion (see, for example, failure of composite fiber structures in HÖRMANN [Hör02]). It is thus treated just like materials that are simpler in terms of structural mechanics without softening. In that way, a large number of material models can be applied to the case of wood. The possible numerical instabilities or localization phenomena have a negative effect. By localization phenomenon, we mean the development of narrow failure zones in which the deformations are concentrated, whereas other areas are relieved.

When it comes to localization, a problem is created by the attendant discretization dependence of the results when one uses the classical continuum theory in combination with a local material formulation (HÖRMANN [Hör02], BAŽANT [BO76]). In physical terms, this means that the type of the partial differential equation in connection with dynamic problems changes from hyperbolic to elliptical and the good setup of the initial marginal value problem is lost (HILL [Hil62]) and the results therefore become network dependent. For the tension area, that means that in case of infinite refinement, the phenomenon of the dissipated energy tending toward zero will appear according to BAŽANT & OH [BO76], CRISFIELD [Cri79] or DE BORST [dB86]. For the pressure area, this results in the pathological network dependence of the softening, as can be seen in Figure 6.7, or to global network dependence (material models 24, 26 and 63 in LS-DYNA).

The problems described in conjunction with the modeling of softening material behavior can be tackled by means of regularization strategies. These strategies are so named because the

underlying mathematical equations are regularized and the good setup of the initial marginal value problem is thus assured.

Regularization strategies are theories, such as the theory of nonlocal integral continua according to BAŽANT [Baz84] and PIJAUDIER-CABOT & BAŽANT [PCB84] on the basis of COSSERAT & COSSERAT [CC09] or the theory of gradient widening of continuum models according to PERZYNA [Per66] or MÜHLHAUS & AIFANTIS [MA91] and AIFANTIS [Aif92]. An overview of the different nonlocal formulations can be found in BAŽANT & JIRÁSEK [BJ02]. As a caveat, one must note that nonlocal theories according to LEUKART [Leu05] can be converted in the context of the FEM only in a very complex numerical fashion because the local character of the FEM is violated by the three-dimensional mean value formation.

As described in Section 6.2.5 using the example of material law 26, only pronounced viscous effects have a regularizing influence (see also HAUFE [Hau01]). Evidently, viscous effects occur either in connection with very high stress velocities or in the case of pronounced viscous material properties. Both prerequisites are not met in the context of this study.

Structural discretization. One possibility of modeling the compression of wood in the axial direction consists in discretizing the smallest decisive structural magnitude. In this connection, that will be the tracheids (see Section 3.2.2) and their cell walls. The macroscopic part is not possible due to the resultant discretization; therefore, the annual rings that predominate during the failure of wood can also be considered as the smallest structural magnitude (see Section 4.2.4). In that way, one neglects microstructural effects and one "smears" them macroscopically. Local microscopic effects are of significance only in an integral fashion for global behavior in conjunction with large deformations. Many studies address the underlying failure types, for example, BODIG [Bod66], DEBAISE, PORTER & PENTONEY [DPP66], EASTERLING et al. [E+82], BARISKA & KUČERA [BK85], GONG & SMITH [GS00a], MÜLLER [Mül03], SMITH & VASIC [SV03], also at various angles (REITERER & STANZL-TSCHEGG [RST01]). Fundamentals are also described in standard works on wood.

The underlying crack criteria are also covered, among other things, by DAUDEVILLE [Dau99], EBERHARDSTEINER [Ebe02] and MACKENZIE-HELNWEIN et al. [MHEM03].

The basis for structural discretization is the determination of local failure with fracture-mechanics methods; and for that, according to the current state of science, one must a priori know the crack curves. According to the current state of technology and science, modeling these curves is very laborious in view of the large number of cracks that develop during the axial compression of wood. Also problematical in the case of this method is the extremely fine discretization of the wood in the shock absorber in view of the orders of magnitude of the shock absorber. The number of required elements would result in disproportionately laborious computations.

Substitute structure discretization. The procedure described in the section entitled *Structural Discretization* can also be simplified in that one abstracts the described discretization of the annual ring zones to one kink element per wood block in the shock absorber. Along with a

wood matrix, we also model a stiffening that fails under load and thus models the softening. In that way, we can get around the problem of expansion localization. The lateral expansion inhibition and thus the level of softening, however, is not considered in this way. This variant therefore also demands a precise knowledge of the average softening in the wood.

Material softening controlled by fracture mechanics. For example, BAŽANT & OH [BO83], LOURENÇO & ROTS [LR97] and WEIHE [Wei95] addressed the objective control of material softening with the help of fracture mechanics criteria. In the process, the softening process is described with the help of the energy dissipation triggered by the crack formation (see also SCHLEGEL & RAUTENSTRAUCH [SR02]). It must be emphasized here that for this variant likewise in analog to the variant of *structural discretization*, the course of each individual crack must already be known and must be modeled accordingly. Modeling a large number of possible crack fronts would be too expensive and thus impractical for the cohesiveness of this study.

Damaging models. Damaging mechanics considers degradation of the mechanical properties caused by microstructural failure by applying a microscopic damage parameter that successively reduces the mechanical properties in the material law. Using damaging mechanics cannot lead anywhere in view of the macroscopic damage and the subsequent hardening.

"Min-max consideration" without softening. Transport casks holding radioactive substances must reliably withstand accident events under various potential conditions. According to IAEA [TSR08], [TSG08a], that includes fluctuations in the temperature from -40ºC all the way to operating temperature. These temperature fluctuations of up to 150K for shock-absorbing parts must be included in the evaluation of the mechanical properties. The state of science concerning the dependence of the mechanical wood properties on the temperature was described in Section 3.3.3.

Due to fluctuations of the mechanical properties, one must basically use an upper and a lower covering curve; therefore, the mechanical properties in case of softening behavior can also be estimated with a covering upper and lower curve. If no possibly truly realistic but conservatively covering computation results are acceptable, this variant can be right on target when it comes to the evaluation of safety test data. The resultantly growing conservativities can be problematic when it comes to verification.

Energy equivalence setup without softening. A curve can be derived on the basis of the energy equivalence criterion if, in contrast to "min-max consideration," no covering but rather an as accurate as possible computation is to be made. In that way, the energy absorbed by the shock absorber is correctly modeled with a target deformation.

Part characteristic with FE substitute model. Basically, the reaction force of the shock-absorbing part can also be applied as force-time curve upon the components of the tightly sealed enclosure. To do that, we must know the precise force-time curve as well as the distribution of the reaction force over the circumferential direction of the cask body. The average mechanical properties of the shock absorber are transferred to a simple model. That can be done by the definition of a geometric substitute model or by definition of an adequate nonlinear

spring characteristic. This form of modeling severely restricts the predictability for shock-absorber constructions that are not secured by a large number of drop tests.

6.2.4 Discussion

The variant *continuum mechanics substitute model with multiaxiality* is given further consideration because it, for the first time, considers the multiaxiality of the stress state in the substitute continuum. It can be in a position to describe the behavior of wood in response to axial compression in a generally valid manner, although only approximately because of continuum-mechanics smearing.

A caveat must be stated for the other modeling variants to the effect that the general behavior of wood in response to pressure stress cannot be described independently of the lateral expansion inhibition or in accordance with the multiaxiality of the stress state in the continuum-mechanics substitute model for the wood fiber mixture. An adaptation to the particular lateral expansion inhibitions prevailing in the shock absorber is necessary for each individual case. This means that the derivation of the global model for the wood fiber mixture is not possible.

If one knows the lateral expansion inhibition in the shock absorber, then a computation with *softening flow curve* can possibly be on target provided the numerical problems connected with the use of softening flow curves are not dominant.

The variant *structural discretization* is impractical due to the required large element number and the modeling effort and is not further pursued here.

For the variant *substitute structural discretization*, the kink element must be modeled for each wood layer. This modeling form does not lead anywhere for the shock-absorbing parts of transport casks holding radioactive substances that consist of a large number of wood layers and is not further pursued here.

The variant *fracture-mechanically controlled material softening* constitutes a promising research area that should be pursued further. Any further dealing with this topic in the context of this work is forbidden by the implementation that so far has not been done in commercial FE systems as well as the necessity of the manual selection of fracture surfaces in the wood.

The last-mentioned three variants *min-mix consideration without softening, energy equivalence setup without softening* and *parts characteristic with FE substitute model* to estimate the shock force of a shock-absorbing part presuppose a precise analysis of the processes taking place in each individual shock absorber in response to accident stress. A recomputation of the wood tests does not lead anywhere with these variants. Nevertheless, this variant [sic] can supply practical estimates for the determination of the stresses to which the cask is exposed. At this point, a test should, if at all possible, be recomputed; therefore, the variant *energy equivalence setup without softening* should be examined in further detail on the basis of the recomputation of a cask drop test.

The discussion of the variants shows that only modeling with the variant *continuum-mechanics substitute model with multiaxiality* can be in a position to describe the behavior of the shock absorber in response to pressure stress with the help of the multiaxiality of the stress state in the substituted continuum. The lateral expansion inhibition and thus the anticipated softening must be known a priori for the other variants. The variants *continuum-mechanics substitute model with multiaxiality* and *softening flow curve* should be further investigated on the basis of the recomputation of compression tests on wood samples. To recomputed drop tests with transport casks holding radioactive substances, it would, in addition, be necessary to investigate more in detail the variant *energy equivalence setup without softening*, above all because the necessary accuracy of the knowledge on the behavior of shock-absorbing parts depends directly on the safety margin of the cask model considered under test requirements.

6.3 Recomputation of Shock Tests on Wood Samples

When simulating the wood tests presented in Subchapter 4.3, one can review and evaluate the applicability of the various modeling forms by means of simple geometries. The principal energy absorption connected with drop tests occurs in zones with a medium or high lateral expansion inhibition (Subchapter 4.4). This is why tests with a high lateral expansion inhibition are simulated in this study. The results can then also be transferred to average lateral expansion inhibitions. The effect of softening can be observed here even more pronouncedly. The nonlinear, explicit, commercial FE program LS-DYNA [LSD08] is used here.

6.3.1 Objective

The objective of recomputation should be an evaluation of the applicability of various material laws and modeling forms for the simulation of the behavior of wood under pressure stress. For this purpose, all possible material formulations should be identified, discussed and evaluated by a comparison with the experimental results. Through parameter studies on important additional possible influencing factors, the latter should then be evaluated.

6.3.2 FEM Models, Investigation Matrix

With the help of a quarter model (two symmetry planes) of the sample with which the tests were performed (Section 4.3.2), a comparison is made of the results of the various modelings (Figure 6.3). The model has 706 nodes and 532 elements.

The wood is modeled by three-dimensional solid elements[6] with eight nodes, linear displacement setup and reduced integration. To model the sheet metal, one sues shell elements with four nodes according to a setup by BELYTSHKO & TSAI [BT84]. The force introduction plates are modeled by means of two rigid planes (rigidwall). One velocity is given for the rigid plane that is in motion and thus simulates the stress created by the piston of the test unit.

Comparison Criterion

[6] Hexahedron

Agreement of the pressure force compression curves is used as comparison criterion. The change in the interval between the rigid planes related to the initial height of the sample corresponds to the pressure on the sample. Forces are given as reaction forces of the rigid planes.

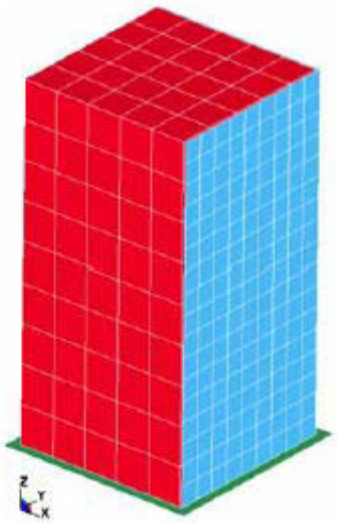

Figure 6.3: FEM Quarter Model of the Wood Sample with Sheet Metal

6.3.3 Material Models

In Section A.1, we derive that to solve the underlying marginal-value problem of the FEM after using all of the balance equations for assistance, there are still no equations (Table A.1). These equations are provided by the material models and describe the specific material behavior. The FE program LS-DYNA has a large number of possibilities when it comes to modeling material behavior. The VON MISES flow condition [vM28] is applied in many of the material models that contain plasticity. Accordingly, flowing is possible only in a shape-changing but not in a volume-changing fashion. Flow laws for foams and honeycombs in general permit the modeling of the plastic volume compression that is to be observed in wood. Therefore, when it comes to wood, one can use, above all, material models that were developed for honeycomb structures and foams. Table 6.1 shows a selection of the suitable material model. Here, we dispensed with models that cannot be applied to hexahedron-shaped elements. We selected material models that might possibly be useful for the *continuum-mechanics substitute model with multiaxiality* (75), *softening flow curve* and *energy equivalence setup without softening* (24, 26, 63, 103, 126, 142, 143) modeling foam.

Discussion of Material Models

Mat24. Material model 24 (*mat_piecewise_linear_plasticity*) is widely used in the simulation of shock-like events[7] as a generally isotropic material model with VON MISES flow

[7] Crash events

criterion. The softening is isotropic, the expansion rate effects can be applied via a COWPER-SYMONDS model or vial a scaling of the flow surface. The model is used primarily for metals.

Mat26. Material models 26 (*mat_honeycomb*) and 126 (*mat_modified_honeycomb*) are orthotropic material models with three basic areas developed for aluminum honeycomb structures. The material is linear elastic in the first area. The elastic and the anisotropic plastic areas are separated by multiplanar flow condition according to JOHANSON [Joh64] with fixed flow surfaces for standard and thrust stresses. In that way, one can graphically illustrate the material model only in the hexadimensional stress area. In the case of the anisotropically plastic area (area 2), all three directions *x, y, z* are completely uncoupled, that is to say, a load in the plastic area in one direction does not produce any plastic effect in the other two directions. As of a relative volumetric expansion to be defined, both models become isotropically elastically plastic material models. Material models 26 and 126 differ from each other by the use of differing expansion dimensions. Technical tensions and expansions for the function of the flow surface evolution must be used for material model 126, while volumetric expansions must be used for material model 26. In addition, material model 126 makes it possible to include expansion rate effects.

Table 6.1: Direction of Material Models in LS-DYNA That May Possibly Be Suitable for the Simulation of the Wood Under Pressure Stress

Material Model		**Anisotropy**	**Flow Condition**
24	linear plasticity	no	VON MISES
26	honeycomb	yes	JOHANSON
63	crushable foam	no	JOHANSON
75	bilkhu-dubois	no	Ellipsoid
103	aniso. viscoplastic	yes	VON MISES
126	modified honeycomb	yes	JOHANSON
142	trans. aniso. Honeycomb	yes	JOHANSON
143	wood	yes	not documented

Mat63. Material model 63 (*mat_crushable_foam*) is an isotropic material model that was developed for foams. Similar to material model 26, this material has a multiplanar flow condition according to JOHANSON [Joh64], which, in the case of material model 26, however, is set up in the principal stress area. Here, flowing occurs only as a function of the maximum amount of the principal stress. The material model must not be confused with material model **crushablefoam* of the FE program ABAQUS [ABA06]. The ABAQUS model corresponds to the material model 75 described below in many parts.

Mat75. Material model 75 (*mat_bilkhu_dubois*) can be traced back to FAUNAS & DUBOIS [FDB97]. This material has an ellipsoid flow surface in the principal stress area. The section plane with the octahedron plane (see Figure 6.1.2) is circular. The evolution of the flow surface can be controlled as a function of the hydrostatic and uniaxial stress state by putting in two independent flow curves for uniaxial pressure via expansion and hydrostatic pressure via expansion. In contrast to the *crushable-foam* material model of ABAQUS [ABA06], the shape of the flow surface can change in the course of evolution. The material model can possibly be used

with the help of the combination of plastic compressibility in conjunction with simultaneous form-change possibilities of the ellipsoid flow surface for the described *continuum-mechanics substitute model with multiaxiality*.

Mat103. Material model 103 (*mat_anisotropic_viscoplastic*) is the anisotropic broadening of material model 24. The isotropic material model 24 is sufficient for a first evaluation because, in this investigation, only uniaxial stress tests in the axial stress direction are recomputed in the beginning.

Mat142. Material model 142 (*mat_transversely_isotropic_crushable_foam*) is a transversal-anisotropic modification of material model 26. It goes back to HIRTH, DUBOIS & WEIMAR [HDBW02]. Particular emphasis was placed on the realistic imaging of the behavior in response to stress between the principal material directions[8]. Here, we will consider only material model 26 due to the similarity between material models 26 and 142 and the stability problems connected with the use of material model 142, as described by SCHLEGEL & RAUTENSTRAUCH [SR02].

Mat143. (*mat_wood*) Material model 143 (*mat_wood*) was developed for impact situations against wood in the highway transportation system of the USA. This material model will not be considered any further here because it is documented to a very minor extent and, besides, it is a function of units.

Overview of plasticity modeling. Equations 6.23 to 6.27 show the flow conditions of the described material models to the extent that they are documented. The stress is elastic for values of $f < 0$, while values of $f > 0$ are not permitted. The flowing action begins when the function is $f = 0$. All variants of Y here designate isotropic or anisotropic flow boundaries.

LSDYNA #24
$$f = |I_2| - \sqrt{\frac{2}{3}}Y \tag{6.23}$$

LSDYNA #26
$$f_{ij} = |\sigma_{ij}| - Y_{ij} = 0 \tag{6.24}$$

LSDYNA #63
$$f_i = |\sigma_{ij}| - Y = 0 \tag{6.25}$$

LSDYNA #75
$$f = \left(\frac{p - \frac{1}{2}(p_c - p_t)}{a}\right) + \left(\frac{\sigma_v}{b}\right)^2 - 1 = 0 \tag{6.26}$$

LSDYNA #126
$$f_{ij} = |\sigma_{ij}| - Y_{ij} = 0 \tag{6.27}$$

Y	Isotrope Fließgrenze
Y_{ij}	Anisotrope Fließgrenze
p	Hydrostatischer Anteil der Fließgrenze
p_c	Hydrostatischer Anteil der Fließgrenze - Druck
p_t	Hydrostatischer Anteil der Fließgrenze - Zug
σ_v	VON MISES Vergleichsspannung
a	1. Halbachsenlänge der elliptischen Fließfläche
b	2. Halbachsenlänge der elliptischen Fließfläche

[8] Usually referred to as off-axis loading

Y	Isotropic flow boundary
Y_{ij}	Anisotropic flow boundary
p	Hydrostatic part of flow boundary
p_c	Hydrostatic part of flow boundary - pressure
p_t	Hydrostatic part of flow boundary - tension
σ_v	VON MISES comparison stress
a	1st hemiaxis length of elliptical flow surface
b	2nd hemiaxis length of elliptical flow surface

The equations that control the evolution of the flow surfaces of the individual material models can be seen in 6.28 to 6.32.

LSDYNA #24	$Y = E_{pl}\epsilon_{pl}$	(6.28)
LSDYNA #26	$Y_{ij} = Y_{ij}^0 + H_{ij}\left(\epsilon_v^{tng}\right)$	(6.29)
LSDYNA #63	$Y = Y^0 + H\left(\epsilon_v^{tng}\right)$	(6.30)
LSDYNA #75	$Y = Y^0 + H(\epsilon_{pl})$	(6.31)
LSDYNA #126	$Y_{ij} = Y_{ij}^0 + H_{ij}\left(\epsilon_{ij}^{tng}\right)$	(6.32)

E_{pl}	Plastischer Tangentenmodul
H	Isotrope Verfestigungskurve
H_{ij}	Anisotrope Verfestigungskurve

E_{pl}	Plastic tangent module
H	Isotropic hardening curve
H_{ij}	Anisotropic hardening curve

Only associated flow rules are used here except for material model 75; therefore, the flow of the plastic expansions for all material models up to material model 75 is controlled by the flow condition $F_{ij} = f_{ij}$:

$$\dot{\epsilon}_{ij}^p = \dot{\lambda}\frac{\delta F}{\delta \sigma_{ij}} \qquad (6.33)$$

The flowing of the plastic expansions in the case of material model 75 is define by

$$F = \sqrt{\frac{3}{2}\sigma_{ij}\sigma_{ij}} \qquad (6.34)$$

Density, elastic properties and flow curves must be given for all material models. For some models, we need additional material parameters that were estimated by values from the pertinent literature or whose influence on the computation results was evaluated by parameter studies. The definition of Poisson's ratio is very important along with the flow curves. In case of stress in the axial direction in the elastic area, wood, according to NIEMZ [Nie93b], has a Poisson's ratio of between 0.43 and 0.46. But in the post-fracture area, the wood is no longer as exactly describable as a continuum; therefore, one must use a substitute Poisson's ratio. Plastic volume constancy prevails in material models with VON MISES flow conditions, that is to say, one automatically presumes a plastic Poisson's ratio of $v_{pl} = 0.5$ Material models with JOHANSON flow conditions, such as material 26 and 63, generally are uncoupled, that is to say, we use a plastic Poisson ratio of $v_{pl} = 0$. Material model 75 puts the Poisson ratio, which must be supplied, over the entire elastic and plastic areas.

Conclusion

The use of material model 85 is recommended for the *continuum-mechanics substitute model* described in Section 6.2.2. Controlling the form of the flow surface by means of the multiaxiality of the stress state in the substitute continuum is possibly an option for simulating the softening occurring in the wood as a function of the lateral expansion inhibition.

Investigating materials 24, 26 and 63 is recommended for the modeling variant *softening flow curve*. In that way, a material model with VON MISES flow condition and two material models with multiplanar flow condition according to JOHANSON [Joh64] can be compared.

6.3.4 Influencing Parameters

Below, we find a selection of additional parameters that can decisively influence simulation. The selection is based on lessons learned in model testing.

- Contact definitions
- Network fineness/error estimation
- Friction
- Attenuation

Parameter studies will be performed in the following to evaluate the sensitivity of the recomputation results on the parameters.

Contact Definitions

Contact definitions represent contact conditions, that is to say, they prevent one contact partner from beginning to penetrate a second contact partner. They differ from each other by the manner and way in which the penetration is prevented. Some contact definitions presuppose nodular velocities upon the start of penetration to zero or prescribe velocities for them by means

of which they are again precisely on the contact surface during the next time step (*constraint* method). Others presuppose the so-called *penalty* method where internal force pairs are applied at the penetration points. The amounts can be calculated from the penetration depth and the contact stiffness. This means that the method is theoretically energy-neutral. Contact stiffness is usually determined by the program from material properties and element dimensions. Possible contact types will be described below in LS-DYNA [LSD08].

Parts of the model are generally defined as contact partners so that contact forces can be given specifically and so that it will not be necessary to check the contact conditions for all nodes of the model with every computation step. The efficiency of computer technology has resulted in a neglect of these contact types in favor of global contacts where the penetration of each node into each free surface is checked out[9]. The model parts that are in contact with each other must be described for first-named contacts. In the simplest case, the two models, which are in contact with each other, are described as "master" or "slave" sides. The penetration of slave nodes into segments of the master side is examined. This type of contacts is therefore referred to as unilateral contacts[10]. If the penetration of two contact partners into each other is examined, then we speak of symmetrical contacts[11]. In large deformations, instabilities frequently occur due to theoretically negative volumes[12]; therefore, the inner contact[13] was developed. Here we check whether nodes of a tetrahedron element penetrate the outer surface of that same element and hinders this movement.

Other differences are brought out in LS-DYNA for the treatment of contacts with shell elements. Shell elements are treated like tetrahedron elements in case of contacts with the option *automatic*. This means that the orientation of the element perpendiculars is meaningless. By using real shell thicknesses, however, in the course of big time steps, it is possible that contact violations might not be recognized or the nodes are steered out to the false side.

Error Estimation

According to KOCH [Koc03], one must in error estimation during FE analyses distinguish between:

1. Idealization error (physical model formation),
2. Discretization errors (geometry and material imaging) and
3. Numerical errors.

The error that occurs during the transfer of the real structure into a physical model is referred to as idealization error. Its magnitude depends as to whether and, if yes, in what way various influencing factors are considered.

---

[9] In -LS-DYNA *single_surface* or *general_contact*
[10] For example, *nodes_to_surface* contacts
[11] For example, *surface_to_surface* contacts
[12] Often referred to as the turning up of the elements
[13] *contact_interior*

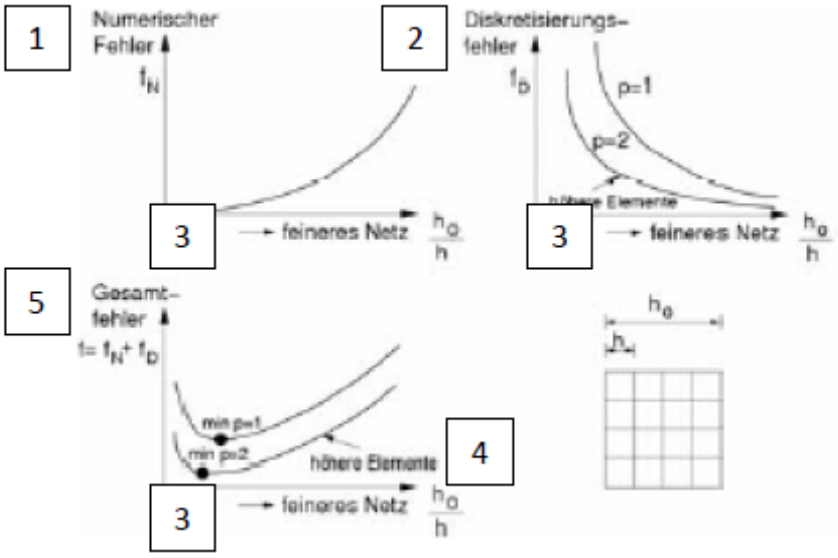

Figure 6.4: Errors Influencing the FEM Analysis According to KOCH [Koc03]

[Key: 1) Numerical error; 2) Discretization error; 3) Finer network; 4) Higher elements; 5) Total error].

The discretization error designates the error that occurs during the transfer of the geometry and the solution variables to the FE net. The numerical error is generated during the solution of the equation system, for example, by numerical integrations, rounding errors or iteration methods. ARGYRIS & MLEJNEK [AM86] try to describe the discretization errors and the numerical errors in qualitative terms. Figure 6.4 shows the curves for the discretization and numerical errors according to KOCH [Koc03], going back to ARGYRIS & MLEJNEK [AM86]. The total error is minimized at a certain net fineness, which is a function of the problem, the order of the displacement setup and the storage processing in the computer system. It follows from this that finer nets do not automatically result in better results.

Friction

COULOMB's friction is considered as dissipative energy part in contact definition. Friction coefficients[14] are between 0.5 (adhesion friction) and 0.15 (sliding friction) for the pairs of wood-wood and wood-steel according to DUBBEL [GF04]. The friction coefficient can also be smaller due to moisture or resin deposits on the contact surfaces.

Attenuation

Attenuation can be considered as a dissipative energy part over the material model; this is because, in case of harmonic excitation of resonance cells, theoretically infinitely large deflections can occur. Excessive attenuation coefficients, of course, result in unrealistic computation results so that special attention can be paid to the determination of realistic

[14] Also friction coefficients or friction numbers

attenuation coefficients. It is usually recommended that one completely dispense with attenuation in computations. Attenuation factors between ν = 0.002-0.009, and in case of radial/tangential stress between ν = 0.006-0.018, apply to wood in case of axial stress according to FOSTER [Fos92].

6.3.5 Results

Material Models

Material model 24. The global pressure force-compression curve of the test can be reproduced acceptably when making a computation with material model 24. Figure 6.5 shows the experimentally determined curve and the calculated curves for two parameter variants. The flow curve in the area of large expansions must be lowered due to plastic incompressibility because the surface that is perpendicular to the force introduction rises more than in the test. The deformation picture developing during the computation is physically unrealistic. The big deviatory distortions of the elements, which cause numerical instabilities and net dependences (Figure 6.6) are a problem.

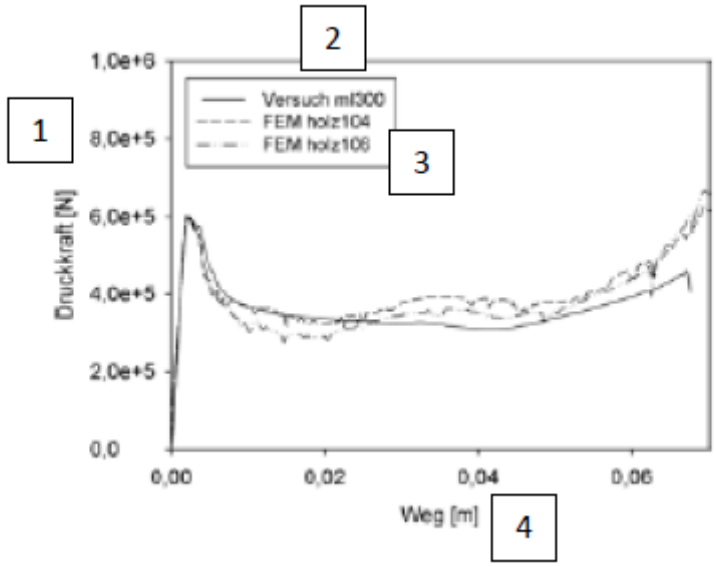

Figure 6.5: Comparison Experiment ml300 (compression, fir, axial 300 mm/sec) with the Computation Using Material Model 24 and Softening Flow Curve (wood104 and wood106)

[Key: 1) Pressure force; 2) Test; 3) Wood; 4) Path].

Material model 26. Due to the uncoupling of the plastic expansions in the orthogonal directions, the combination of material model 26 and a softening flow curve will lead to the pronounced net dependence shown in Figure 6.7. Of course, the global deformations can be localized in individual element levels and thus generate the curve shown in Figure 6.7, but above and beyond this effect, there are no pronounced distortions in the elements. The uniaxial compression behavior can be recomputed in a stable manner with material model 26. If no

softening were to be introduced, then the pressure force-compression curves determined in case of uniaxial compression tests could be satisfactorily recomputed. Material model 26 offers an orthotropic formulation of the material behavior; therefore, wood, with is orthotropic structure, can be modeled well if one neglects the effect of the lateral expansion dependent softening.

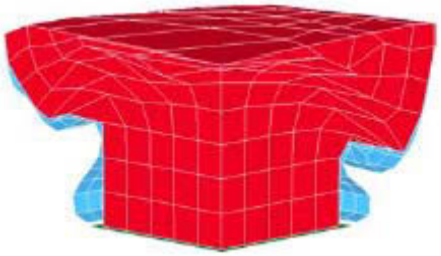

Figure 6.6: Net Deformation in Computations with Material Model 24

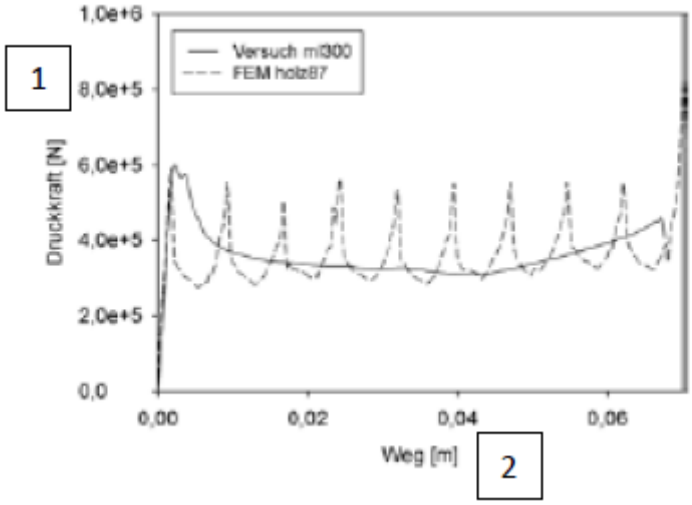

Figure 6.7: Comparison Experiment ml300 (compression, fir, axial, 300 mm/sec) with the Computation and Softening Flow Curve (wood87)

[Key: 1) 1) Pressure force; 2) Test; 3) Wood; 4) Path].

Material model 63. Figure 6.8 shows the pressure force-compression curve of the recomputation with the isotropic material model 63. Localization effects (Figure 6.8) can be seen in analogy to the results of the recomputation with material model 26. Marginal influences (Figure 6.9) can be observed in the further outlying areas due to the automatic alignment of the flow surface in the principal stress area. In analogy to material model 26, the behavior of wood in response to uniaxial compression can be simulated with adequate accuracy provided we dispense with the modeling of the softening. Only isotropic material properties can be defined; therefore, the orthotropic behavior of wood cannot be modeled. Computation variants with minor changes in the computation parameters showed that even minor changes in the initial parameters of the material model will not allow the computation to converge. These instabilities can be traced back to the effects of the automatic alignment of the flow surface in the principal stress area in combination with softening flow curve.

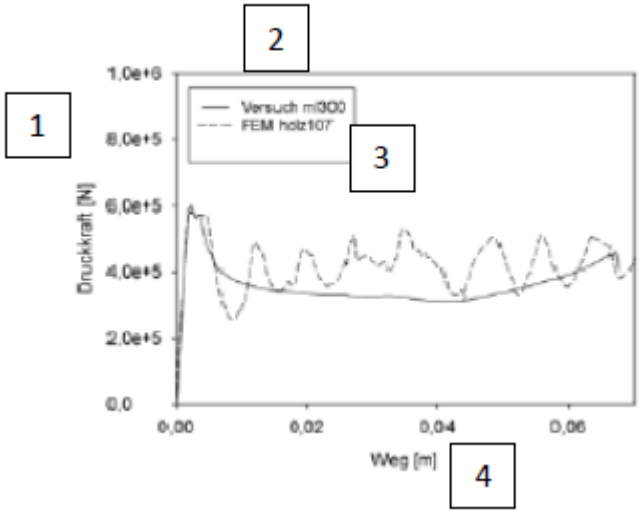

Figure 6.8: Comparison of Experiment m1300 (compression, fir, axial, 300 mm/sec) with the Computation Using Material Model 63 and Softening Flow Curve (wood107)

[Key: 1) Pressure force; 2) Test; 3) Wood; 4) Path].

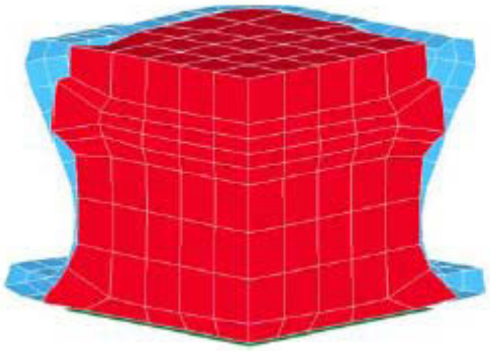

Figure 6.9: Marginal Layer Influences in Computation with Material Model 63 (wood100)

Material model 75. The adaptation of the material parameters to the test is relatively complex because six different material parameters control the evolution of the flow surface. Figure 6.10 shows another graphic illustration of the flow surface. Plotted on the abscissa is the hydrostatic pressure, described by the ball tensor of the stress tensor, while plotted on the ordinate is the VON MISES comparison stress that depends only on the deviatory stress state:

$$\sigma_v = \sqrt{\frac{3}{2} s_{ij} s_{ij}}$$

s^{ij} Spannungsdeviator (deviatorischer Anteil des Spannungstensors) (6.35)

$\overline{s^{ij}}$ Stress deviator (deviatory part of the stress tensor)

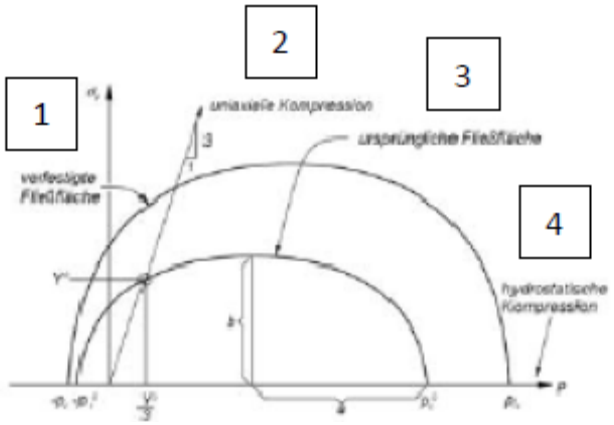

Figure 6.10: Evolution of the Flow Surface of Material Model 75

[Key: 1) Hardened flow surface; 2) Uniaxial compression; 3) Original flow surface; 4) Hydrostatic compression].

As we can see in Figure 6.10, the shape of the flow ellipse is defined by the points of the uniaxial and hydrostatic flow boundary. Both are given as functions of volumetric expansion.

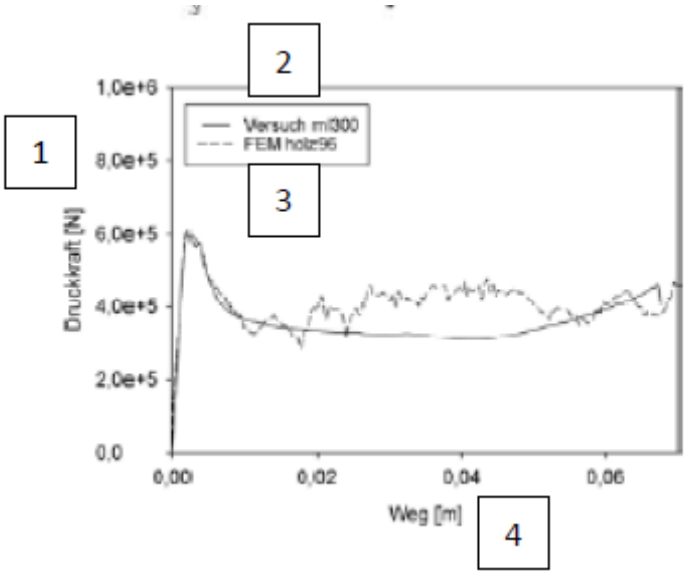

Figure 6.11: Comparison, Pressure Force Plotted Against Path of Experiment m1300 (compression, fir, axial, 300 mm/sec) with the Computation Using Material Model 75 and Softening Flow Curve (wood 96)

[Key: 1) Pressure force; 2) Test; 3) Wood; 4) Path].

Using the *continuum-mechanics substitute model with multiaxiality* (Section 6.2.4), the separation between hydrostatic and deviatory and not uniaxial stress states is a prerequisite as shown by computations using various parameter variations with material model 75. Let us once again describe the foundation of the *continuum-mechanics substitute model with multiaxiality* in order further to explain the basis of this conclusion: By combining significant lateral expansion with corresponding lateral expansion inhibition, we want to control the evolution of the flow surface with the help of the ratio derived from deviatory and hydrostatic part [sic] in light of the stress state. If the continuum-mechanics substitute model does not have any lateral expansion inhibition, then plastic expansions will be controlled exclusively by the deviatory stress part due to the plastic lateral expansion factor ν_{pl} close to 0.5. The deviatory part of the plastic flow of the volumetric expansion is influenced here because the uniaxial flow curve is defined as a function of the volumetric expansion, something that does not lead anywhere in the context of this study. The motivation of the setup of material model 75 presumably springs from the fact that in the case of foams, uniaxial stresses result in negligible expansions in the transversal directions (ABAQUS [ABA06], SCHREYER, ZUO & MAJI [SZM94]).

Additional Parameters

Material model 26 was used without attenuation and the contact definition *surface_to_surface* was used with a friction coefficient of 0.1 in order to investigate additional parameters. Material model 26 was chosen because, in this case, there are no large deviatory distortions and the computation therefore is relatively stable.

Contact definitions. The choice of contact definition does not decisively influence the computation results when it comes to recomputing the tests with wood samples if one uses physically meaningful parameters. Figure 6.12 shows a comparison of the support forces for various contact definitions using the computation example ml300 with material model 26; they differ from each other only slightly.

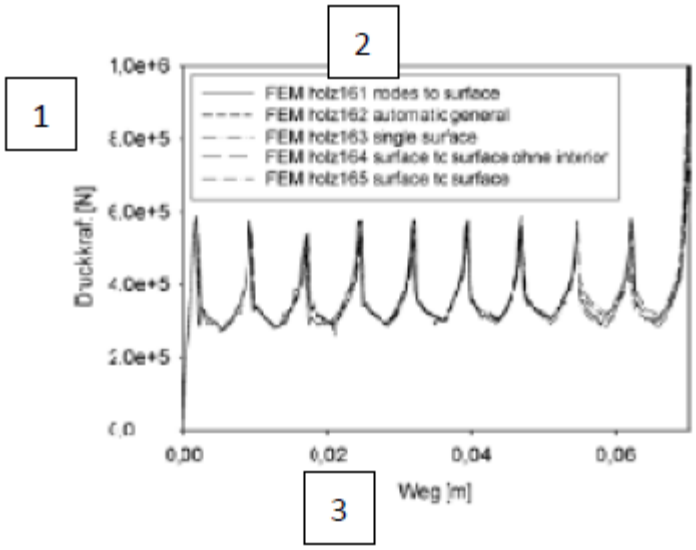

Figure 6.12: Comparison of the Pressure Force-Deformation Curves Obtained with the Help of Differing Contact Definitions Using Computation Example ml300 (compression, fir, axial, 300 mm/sec) with Material Model 26

[Key: 1) Pressure force; 2) Wood; 3) Path].

Error estimation/discretization. The main cause of idealization errors that are made when one uses the continuum-mechanics substitute model is the neglect of the fracture behavior and the attendant cracks resulting from smearing upon a continual model. This is why the behavior of wood in response to pressure stress can be described only approximately in case of large deformations.

The role of discretization assumes special importance because all of the compared variants are discretization dependent. It is therefore basically not possible to achieve an error minimum according to ARGYRIS & MLEJNEK [AM86]. The pronounced net dependence can be seen in Figure 6.13 in the computation with material model 24. The discretization, which is about 2.5 times finer, results in a basically different deformation image. A different modeling form must be chosen when encountering such dependences, as we can see in Figure 6.13.

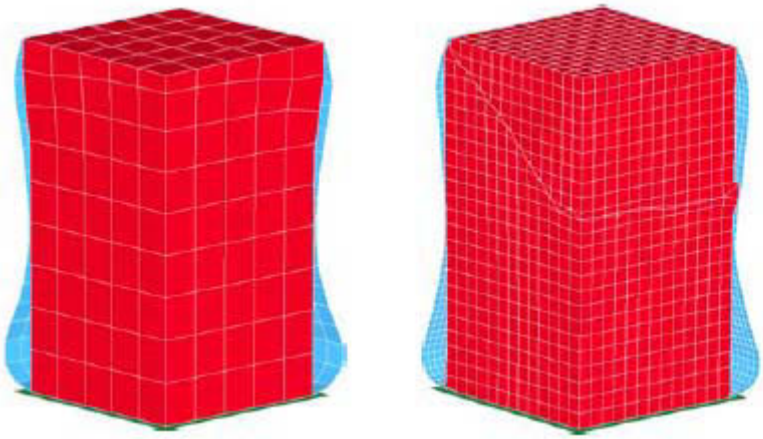

Figure 6.13: Pathological Dependence of the Malposition of the Marginal Value Problems on the Discretization When One Uses Softening Flow Curves on Computation Example ml300 (compression, fir, axial, 300 mm/sec) with Material Model 24 at 35 msec, left: rough discretization, computation stable up to the end (270 msec), right: fine discretization, discontinuation at 35 msec

Friction. Figure 6.14 shows the pressure force-deformation curves on the basis of differing friction coefficients. The values vary between 0.1 and 1.0. The influence of the friction on the pressure force-deformation curves is minor. In the context of the simulation of a cask impact, we want to determine once again what influence the friction exerts.

Attenuation. Figure 6.15 shows the influence of various attenuation factors (RALEIGH attenuation in proportion to the stiffness[15]) using the example of the pressure force-deformation curves obtained with material model 26. The attenuation values vary between 0.00 and 1.00. The implementation of attenuation in the computation takes place via the material model; therefore, the influence must be determined more exactly for each material model. For material model 26, considering the parameter set used here, the influence is significant only for unrealistic attenuation values, something that might possibly be due to the use of stiffness-dependent attenuation. Figure 6.15 clearly shows the regularizing effect of attenuation in case of high attenuation factors.

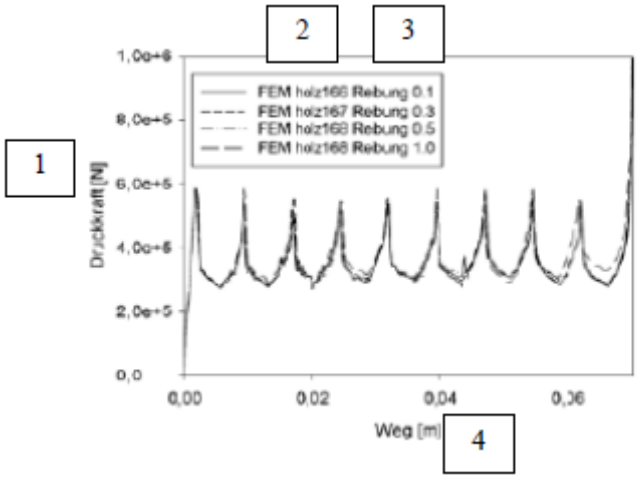

Figure 6.14: Comparison of the Pressure Force-Deformation Curves Obtained with the Help of Differing Friction Coefficients Using the Computation Example ml300 (compression, fir, axial, 300 mm/sec) with Material Model 26

[Key: 1) Pressure force; 2) Wood; 3) Friction; 4) Path].

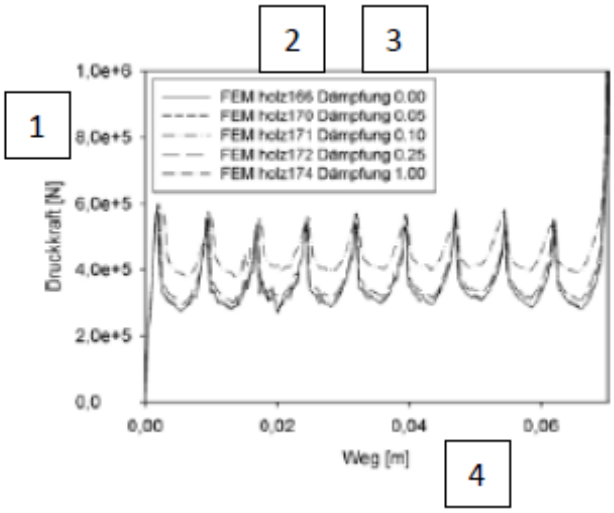

[15] Implemented via the material model definition of wood

Figure 6.15: Comparison of the Pressure Force-Deformation Curves Obtained with the Help of Differing Attenuation Factors Using the Computation Example ml300 (compression, fir, axial, 300 mm/sec) with Material Model 26

[Key: 1) Pressure force; 2) Wood; 3) Friction; 4) Path].

Sheet Metal Modeling

To estimate the forces necessary for the deformation of the sheet metal in response to lateral expansion inhibition, two tests were performed in the course of which only the sheet metal jacket with a sheet metal thickness of 0.5 mm and 1.0 mm was compressed. Figure 6.16, by way of comparison, shows pressure force-compression curves of experiment and recomputation in case of a sheet metal thickness of 1.0 mm. The stress level for initial failure (kinkout) is slightly underestimated; nevertheless, the curve, the order of magnitude and the developing kink forms are well reproduced.

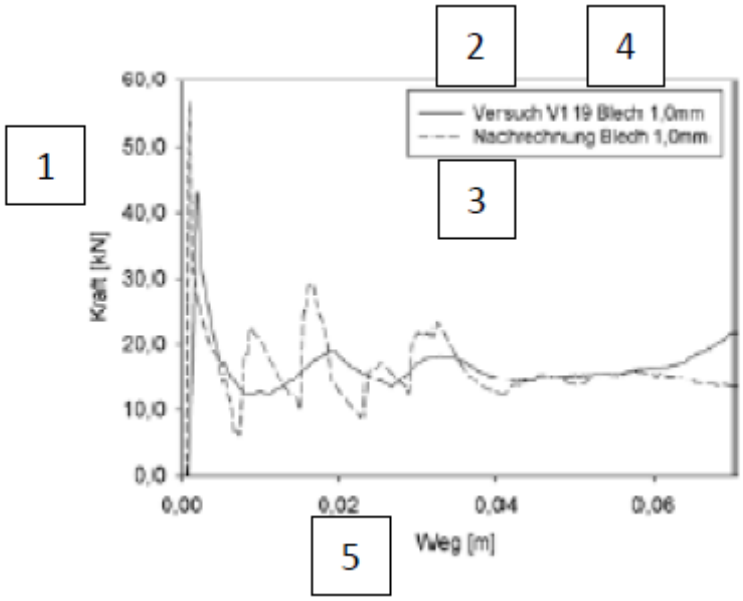

Figure 6.16: Pressure Force-Compression Curves, Comparison Experiment and Simulation for a Sheet Metal Sample Without Wood Filling, 1.0 mm Thickness

[Key: 1) Force; 2) Test; 3) Recomputation; 4) Sheet metal; 5) Path].

Compared to the value of the energy absorbed by the wood, the sheet metal in tests with wood-sheet metal samples in the axial wood direction (sheet metal thickness 1.0 mm) absorbs about 5%, and in tests with transversal wood direction (sheet metal thickness 0.5 mm), it absorbs about 9% of the total energy.

6.3.6 Summary

None of the variants discussed here was able satisfactorily to describe the behavior of wood in response to axial pressure stress in case of large deformations. The experimental results

could be retraced in a global fashion with the help of the pressure force-deformation curves determined with material model 24. Large deviatory dispersions on individual elements, resulting from localization influences, show that the initial marginal value problem is badly posed. The solution is unstable.

The pressure force-deformation curves obtained with the help of material model 26 do not describe the experiment satisfactorily because we can see a global discretization dependence due to the collapse of individual element levels. But the solution is relatively stable. This material model should be investigated with nonsoftening flow curve in the context of the simulation of a cask impact. The experiment could not satisfactorily be retraced globally with the help of material model 63; in addition, there were influences from the margin that influenced the stability of the numerical computation.

Material model 75 was selected for the modeling variant *continuum-mechanics substitute model with multiaxiality*. An investigation showed that the dependence of the uniaxial flow behavior on the volumetric expansion does not permit any separation between deviatory and hydrostatic stress state and that material model 75 is thus unsuitable for the proposed continuum mechanical substitute model. In the context of further investigations, we want to program a material model that under orthotropic marginal conditions will control the evolution of the flow surface on the basis of the hydrostatic and deviatory stress state. That could be done on the basis of existing setups, such as those of the group around EBERHARDSTEINER [MHEM03] [MMHE04] with a flow surface according to TSAI & WU [TW70], GROSS [Gro05], SCHMIDT & KALISKE [SK06], SCHREYER, ZUO & MAJI [SZM94] or MILLER [Mmil00], broadening to include large deformations and coupling to the continuum-mechanics substitute model with flow surface form that would be changeable in the course of evolution. The flow surface is defined in the hexadimensional stress state, something that cannot be illustrated graphically; therefore, Figure 6.17 shows a flow surface according to TSAI & WU [TW70] for the level case.

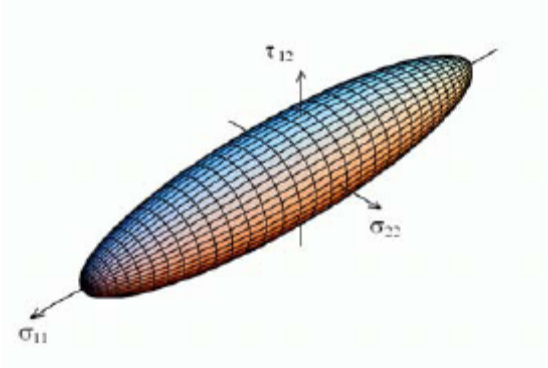

Figure 6.17: Illustration of the Anisotropic Flow Surface According to TSAI & WU for the Level Case

The use of RALEIGH attenuation that is adequately proportional to the stiffness is justifiable for the simulation of the behavior of shock-absorbing parts.

Contact definitions did not decisively influence the results that were obtained.

The proposed variant of the *continuum-mechanics substitute model with multiaxiality* can be construed in this context as regularization strategy for the pressure area in case of large deformations. Figure 6.11 shows that the globally softening material behavior can be modeled over a vast area. Assuming appropriate material formulation, this setup could bring results.

6.4 Recomputation, Drop Test, Shock-Absorber Testing

In this subchapter, we describe recomputations of a drop test of a substitute cask mass with shock-absorbing parts. A description of the drop test is given in Section 4.1.4. This involves a test with shock-absorbing parts that are dynamically loaded with a test mass replicated by a cask. The objective of the test was not to determine the stress upon the substitute mass but rather to investigate the behavior of shock-absorbing parts under realistic stress conditions.

In the earlier subchapters, we proposed different variants for the modeling of wood in response to axial pressure stress and we took a closer look at their applicability on the basis of the simulation of shock tests against wood. The conclusion was that none of the modeling forms investigated with the help of the shock test results could be recommended for any further investigations. It was proposed to take a closer look at the applicability of the modeling *energy equivalence setup on the basis of a simulation of a cask drop test.*

6.4.1 Objective

In this subchapter, we want to see to what extent the proposed modeling form is capable of determining a realistic simulation of the behavior of shock-absorbing parts in response to accident stress.

The investigation was to be performed with the help of two models, a "simplified" and a "detailed" model to investigate whether the degree of detailing of the shock-absorbing parts exerts any influence of the quality of the computation results using the example of the local cask deceleration.

The influence of the friction, of the attenuation and the foundation modeling upon the computation results in the form of local cask decelerations should be investigated and evaluated.

In conclusion, we want to derive recommendations for the modeling of shock-absorbing parts using the FE method.

6.4.2 Models and Investigation Matrix

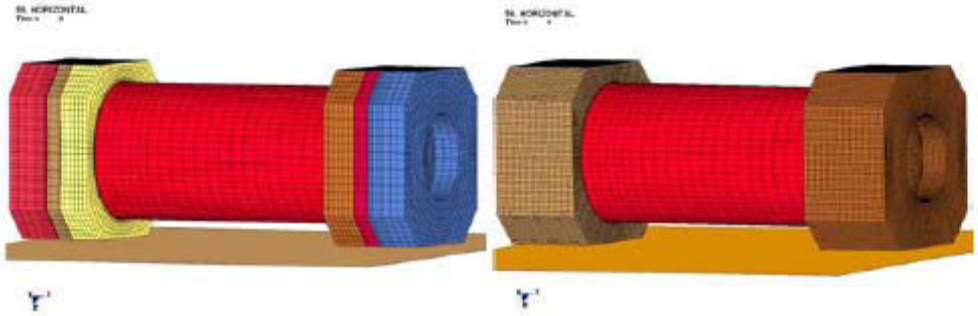

Figure 6.18: FE Models of the Shock-Absorber Testing Experiment Series with Simplified (left) and Detailed Shock-Absorber Model (right) at Computation Moment t=0 msec

Figure 6.18 shows the FE model with simplified (left) and detailed shock-absorber model (right).

Cask and lid modeling. The substitute cask body and primary lid masses are modeled equally in both variants (Figure 6.19). Moderator borehole zones present on the cask body are considered by a hollow cylinder with diminished stiffness and density. The primary lid and the cask body are connected with each other by *truss* elements[16] that simulate the screwing arrangement. Table 6.2 summarizes the basic model data. Elastic material models are used because of the experimentally determined purely elastic stress of the cask and the primary lid. Cross-linkage is done with 8-node hexahedron elements with reduced integration because the stiffness is partly definitely overestimated [LSD08] when one employs fully integrated elements and larger element-length/width conditions.

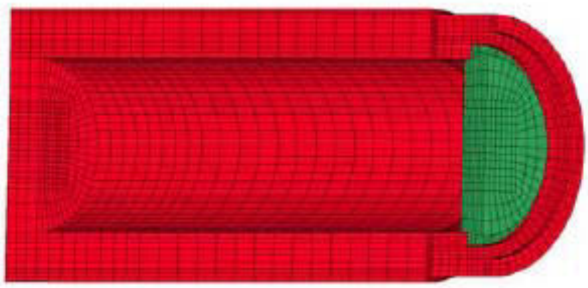

Figure 6.19: FE Models of the Shock-Absorber Testing Experiment Series, Cask and Primary Lid Mass at Computation Moment t=0 msec

Impact foundation modeling. The impact foundation is modeled by a rigid plane[17], which does not permit any entry or penetration of nodes and no absorption of energy. This modeling therefore extensively corresponds to the situation on the nonresilient impact foundation of BAM in Horstwalde, which has more than 200 times the mass of the test object and a massive impact plate.

[16] 1-d rod elements with tension-pressure stressability

[17] *rigidwall_planar_id*

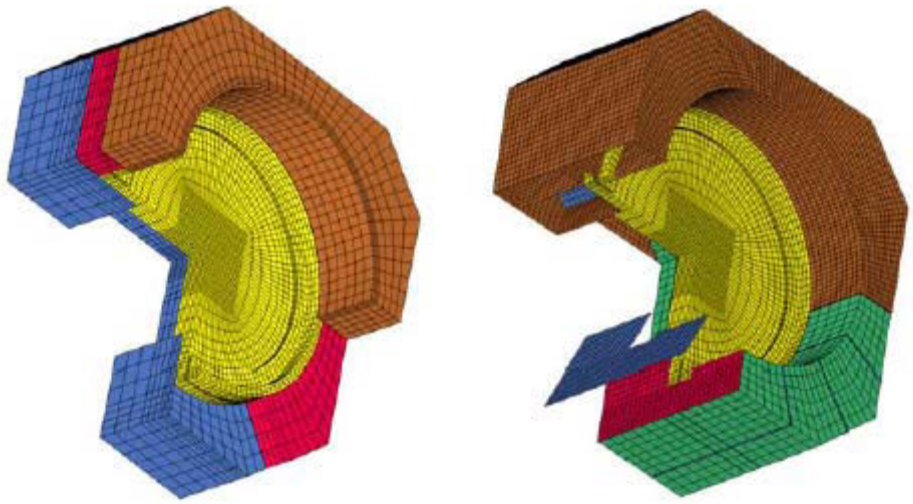

Figure 6.20: FE Model of the Shock-Absorbing Testing Experiment Series, Simplified (left) and Detailed FE Model of the Shock-Absorber Model (right) as Computation Moment t=0 msec

Shock-absorber modeling simplified model. The shock absorber is modeled as an interconnected continuum without inner and outer sheet-metal structures (Figure 6.20, left). The tripartite division of the shock absorber is introduced for reasons of stability for the FE computation. In an interconnected due to sharp transitions, one finds intensive expansion localizations that can cause numerical instabilities. As material model, we use *mat_honeycomb* (material model 26) [LSD08].

Shock-absorber modeling detailed model. Figure 6.20, right, shows the detailed shock-absorber model. All sheet-metal structures are modeled with the help of shell elements. For the shell elements, we use a setup according to BELYTSCHKO-TSAI [BT84] with two integration points against the thickness and Gaussian integration algorithm. The sheet-metal pieces are connected with each other by common nodes on all coinciding positions. Sheet-metal pieces were defined with their nominal thicknesses. As material model for the sheet metal, we use *mat_piecewise_linear_plasticity* (material model 24). The chambers separated by the sheet-metal pieces are filled by 8-node tetrahedron elements that simulate the wood filling. We use *mat_honeycomb* as material model.

Table 6.2: Basic FE Model Data from the Shock-Absorber Testing Experiment Series

Model Part	Nodes	Elements	Material Model
Total model detailed	153046	136922	
Total model simplified	128452	104330	
Cask	32830	25104	*elastic*
Cask body	29124	22080	*elastic*
Primary lid	3706	3024	*elastic*
Screws	0	24	*elastic*
Shock-absorber simplified	62232	49692	*honeycomb*
Steel structure	36974	29520	*elastic*

Wood/sheet metal	25258	20172	*elastic*
Shock-absorber detailed	127368	111794	
Steel structure	36974	29520	*elastic*
Intermediate sheet metal	14064	18768	*piecewise_linear_plasticity*
Outer sheet metal	44804	44994	*piecewise_linear_plasticity*
Wood	31526	18512	*honeycomb*

6.4.3 Results - Simplified Shock-Absorber Model

The quality of recomputation is evaluated by a comparison of the deceleration-time curves measured locally during the test. (At this point, we would like to note once again that the drop test does not involve a "real" path. The mass and the basic geometry, however, on a scale of 1:2 correspond to the structure of a cask of current design). The decelerations are filtered in order to mask the oscillation effects of the substitute cask mass. Up to what degree this filtering is permissible will depend on the objective of the comparison. If we want to compare the rigid body deceleration in order to evaluate the shock-absorbing parts, then one can employ filtering. The important thing is that test and computation results are processed with the same filter and the same filter frequency. In this case, that would be the SAE-SCS filter [Gre02] with a low-pass boundary frequency of 180 Hz. The pertinent components are not modeled in sufficient detail for a stress determination on the cask and the lid system.

Figure 6.21 shows local decelerations on the bottom and the lid based on experiments and recomputation. Good agreements can be seen especially for the bottom decelerations. The lid deceleration is overestimated to a minor extent and the curve is well reproduced. To generate this curve, friction and flow curves have to be adapted in a physically meaningful framework. The flow curves can and under certain circumstances must be adapted in the case we are dealing with here if the experiments did not precisely cover the deformation mechanisms of the shock-absorbing parts during tests for the purpose of determining pressure flow curves. Flow curves had to be lowered in this connection (Figure 6.22). The lowering of the flow curve can be interpreted in physical terms as follows:

1. The global anisotropy of material model 26 must be adapted to the local modeling conditions. The anisotropy is aligned by the global coordinate system, while the anisotropy on the shock-absorbing part is best described in a cylinder coordinate system. Due to the interconnected areas in the substituted model, the outer shock-absorber areas contribute an excessive portion.

2. The stratification of the wood in the shock absorber must be taken into consideration. Interconnected samples were tested in response to purely axial and radial/tangential stress in the course of the test program given in Subchapter 4.3; on the other hand, the shock-absorber filling consists of about 20-30-mm thick layers of wood that are not connected with each other and whose alignment changes. The separations in the wood mixture must be interpreted already as wood layers that have already failed. The lateral tension behavior (see Section 3.2.3), which is frequently observed on cohesive wood exposed to axial stress occurs to a lesser extent. The energy necessary for rupture is no longer available for energy absorption.

Table 6.3 shows a comparison of the deformations occurring in the experiment and the recomputation. The deviations are relatively small. Even if we assume an elastic resiliency of 5%, the maximum deviation amounts to about 11%. In view of the simplifications that must be accepted during wood modeling, this deviation must be evaluated as being acceptable.

Table 6.3: Comparison Between Measured and Computed Deformations with Simplified Shock-Absorber Model Variant 91

Shock-Absorber Testing	**Test**	**FEM Computation**	**Deviation**
Bottom side	65.0 mm	70.5 mm	8.5%
Lid side	59.2 mm	55.3 mm	-6.6%
with elastic resiliency of 5%:			
Bottom side	68.3 mm	70.5 mm	3.2%
Lid side	62.2 mm	55.3 mm	-11.1%

The friction coefficient (Table 6.4) must be selected relatively high to prevent an evasion of the shock-absorber elements. In the real part, this function is assumed by the outer sheet-metal structure, which holds the wood packets in the principal energy absorption zone under the cask body.

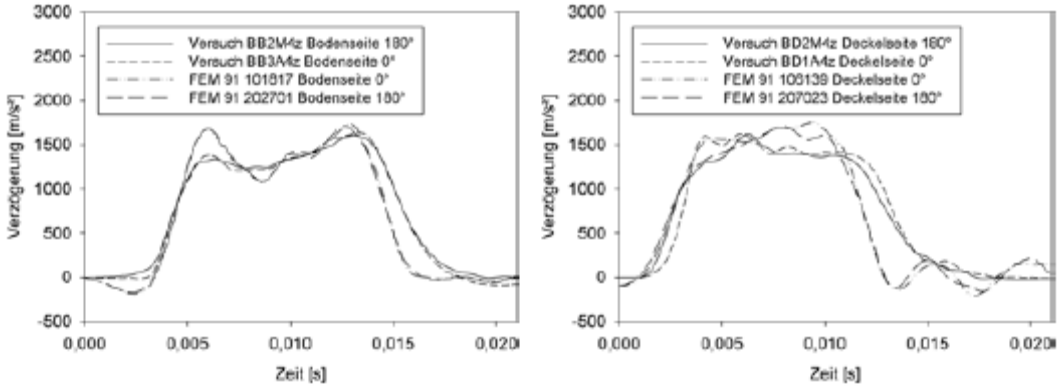

Figure 6.21: Comparison of Results of Shock-Absorber Test Experiment, Measurement Points on the Bottom (left) and on the Lid (right) at 0 and 180º and FEM Computation with Substitute Shock-Absorber Model Variant 91

[Key: 1) Deceleration; 2) Test; 3) Bottom; 4) Lid; 5) Time].

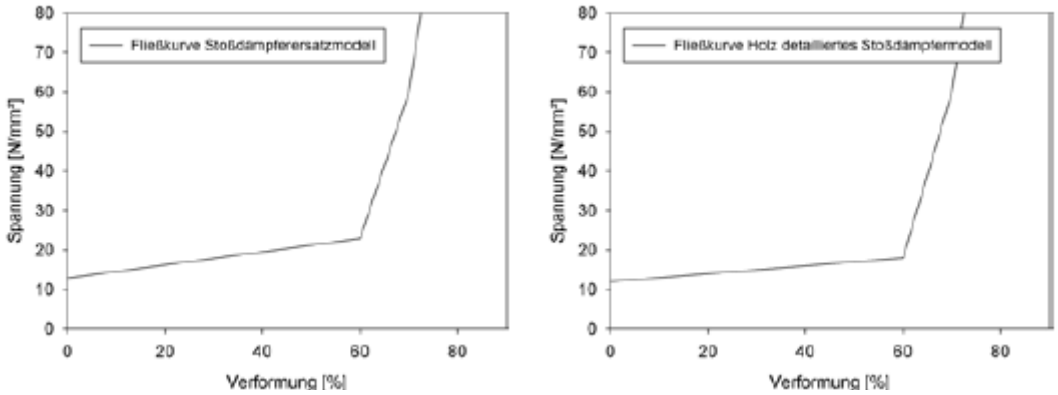

Figure 6.22: Flow Curve for the Substitute Shock-Absorber Model (left) and for the Wood

[Key: 1) Stress; 2) Flow curve substitute shock-absorber model; 3) Flow curve, wood, detailed shock-absorber model; 4) Distortion].

Parameter law. Table 6.4 shows the standard parameter law with which computation results shown in Figure 6.21 were determined. Annex B presents other settings of the material models.

Table 6.4: Standard Settings of the FE Model with Simplified Shock Absorber

Parameter	**Value**
Time step control	
Scaling factor	0.66
Contact definition	automatic general
Friction	0.3
Attenuation	none
Foundation modeling	rigidwall
Friction	0.3
Primary lid connection	*truss* elements
Shock absorber connection	*truss* elements
Material models	honeycomb
Flow curve	Fig. 6.22

Variations. Figure 6.23 shows the curves of lid and bottom decelerations for four different friction factors. The dependence of the computation results indicates the great influence exerted by friction. When the friction coefficients are reduced, we can see increased deviation by the shock-absorbing part (see Fig. 6.26). At the same time, the shock-absorber deformation is increased by about 60%. The shock absorber punches through, something that is indicated by the sudden rise in the deceleration in Fig. 6.23, left, for variant 93 or 132 at about 20 msec. In the real shock absorber, sheet-metal pieces prevent the wood areas from slipping apart, and this holding function is provided in the substitute model by friction.

The influence of RALEIGH attenuation, which is proportional to the stiffness (see BATHE [Bat02] and equation 6.22) can be seen in Figure 6.24. The stiffness proportional term

of the RALEIGH attenuation has an effect above all on the high-frequency oscillations. The influence naturally can be recognized only indirectly because filtered results are compared here. The effects on the filtered local decelerations are minor, whereas the influence on the unfiltered local deceleration is quite clear. The influence of mass proportional RALEIGH attenuation can be seen in Figure 6.25. The mass proportional attenuation has an effect, above all, at low frequencies; therefore, the rigid-body motion is also attenuated in this way. Even small attenuation factors exert significant influence.

Contacts, where differently elemented areas of the FEM "are glued together" (*tied* contacts), must basically be employed with a certain amount of caution. Figure 6.26 shows expansions on the cask body that result from an identification of the contact areas that was erroneously obtained from algorithms. Expansions in the vicinity of the glued contact areas are partly definitely falsified.

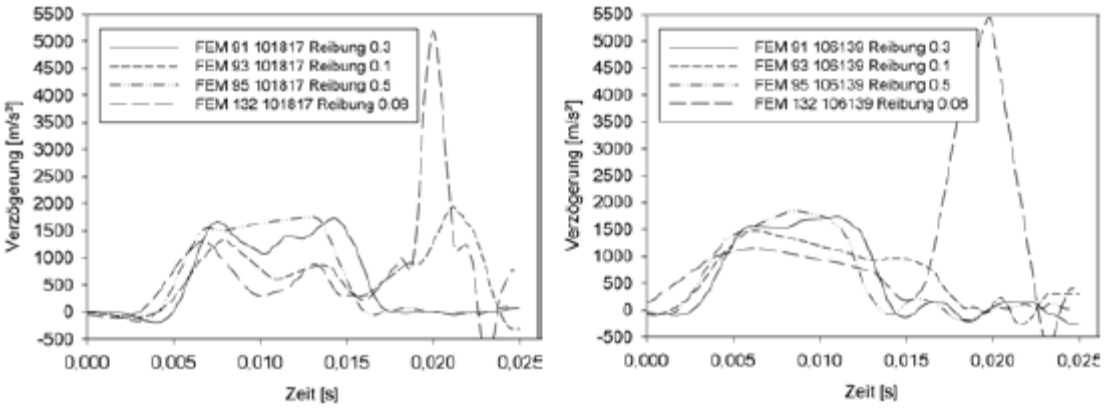

Figure 6.23: Mathematically Determined Decelerations Under Variation of the Parameter Flexion Bottom (left) and Lid (right) at 0º When Using the Simplified Shock-Absorber Model Variants 91, 93, 95, 132

[Key: 1) Deceleration; 2) Friction; 3) Time].

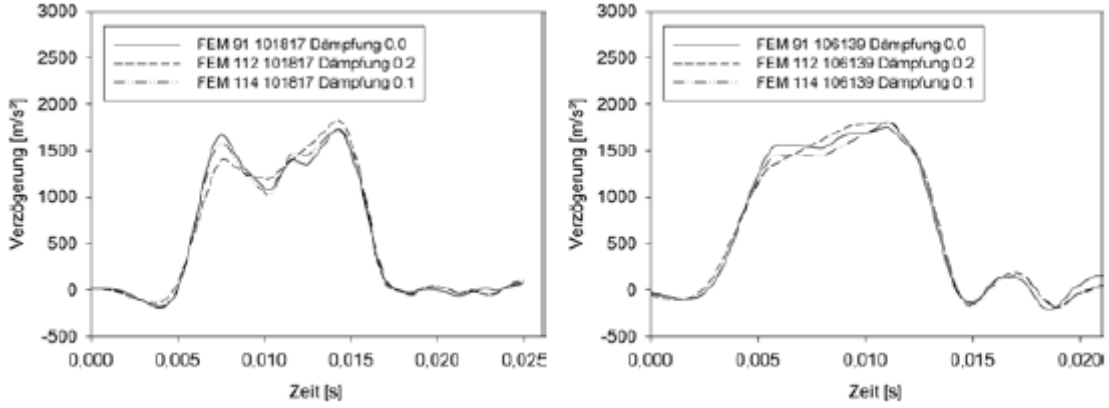

Figure 6.24: Mathematically Determined Decelerations Under Variation of the Parameter Stiffness Proportional RALEIGH Attenuation Bottom (left) and Lid (right)

at 0º When Using the Simplified Shock-Absorber Model Variants 91, 112, 114

[Key: 1) Deceleration; 2) Attenuation; 3) Time].

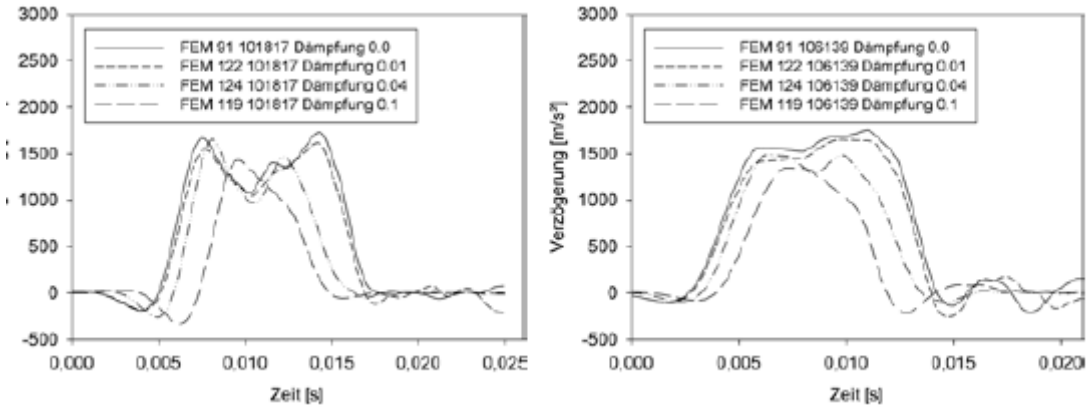

Figure 6.25: Mathematically Determined Decelerations Under Variation of the Parameter Mass Proportional RALEIGH Attenuation Bottom (left) and Lid (right) at 0º When Using the Simplified Shock-Absorber Model Variants 91, 122, 124, 119

[Key: 1) Deceleration; 2) Attenuation; 3) Time].

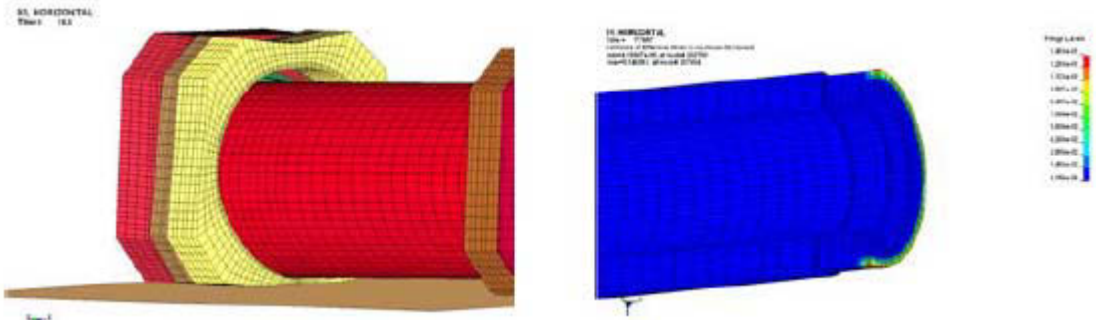

Figure 6.26: Bottom Shock-Absorber Penetration in FE Computation with Simplified Shock-Absorber Model Variant 93 with Reduced Friction Coefficient (left) and Influence of Expansions Due to the Erroneously Recognized *tied-C*ontact on the Lid (right)

[Key: Illegible].

6.4.4 Results - Detailed Shock-Absorber Model

Figure 6.27 shows local bottom and lid deceleration-time curves from experiment and recomputation. One can see a basic similarity along the curves, although there are minor deviations for the deceleration and the shock time.

Table 6.5 presents a comparison of the deformations occurring in the experiment and the recomputation. While the bottom deviation is minor, the lid deformation is overestimated by

about 15%. If one considers the elastic resiliency of about 5%, then the deviations are definitely diminished.

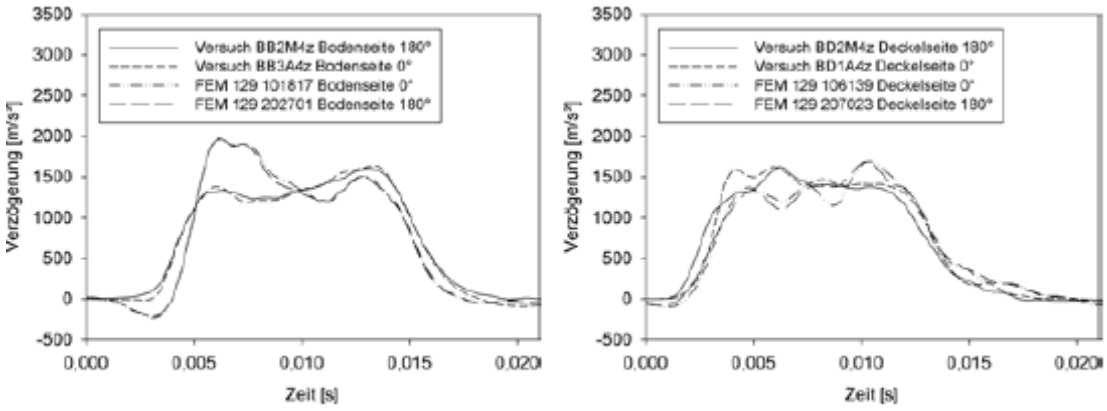

Figure 6.27: Comparison of Local Deceleration-Time Curves in the Shock-Absorber Testing Experiment with FEM Computation Using Detailed Shock-Absorber Model Variant 129, Measurements bottom (left) and lid (right) at 0 and 180º

[Key: 1) Deceleration; 2) Bottom; 3) Lid; 4) Time].

Standard settings. The settings shown in Table 6.6 were used as the standard when they deviated from the LS-DYNA standard settings [LSD08].

Figure 6.22 shows the flow curve used for wood. The flow curve was lowered when compared to the test results (as can be seen in Subchapter 4.3).

Variations. In contrast to impacts without shock-absorber parts, the difference in the local decelerations between modeling of the impact surface with a rigid wall (rigidwall) and a modeling of the impact plate made of steel used at the test stand foundation of the BAM in Horstwalde (see Section 4.1.1) is minor. Figure 6.28 shows a comparison of the local bottom and lid decelerations at 0º. The foundation is stressed elastically only to a minor extent due to the shock-absorbing part that is very resilient when compared to the foundation.

Table 6.5: Comparison Between Measured and Computed Values of the Deformation with Detailed Shock-Absorber Model Variant 129

Shock-Absorber Testing	**Test**	**FEM Computation**	**Deviation**
Bottom side	65.0 mm	69.8 mm	7.4%
Lid side	59.2 mm	67.9 mm	14.7%
with elastic resiliency of 5%:			
Bottom side	68.3 mm	69.8 mm	2.2%
Lid side	62.2 mm	67.9 mm	9.2%

Table 6.6: Standard Settings of the FE Model with Detailed Shock Absorber

Parameter	Value
Time step control	
Scaling factor	0.66
Contact definition	automatic general
Shell thickness is used	2
Friction	0.1
Attenuation	none
Foundation modeling	rigidwall
Friction	0.2
Primary lid connection	*truss* elements
Shock absorber connection	*truss* elements
Material models	
Wood	honeycomb
Sheet metal	*piecewise_linear_plasticity*
Screws	*elastic*

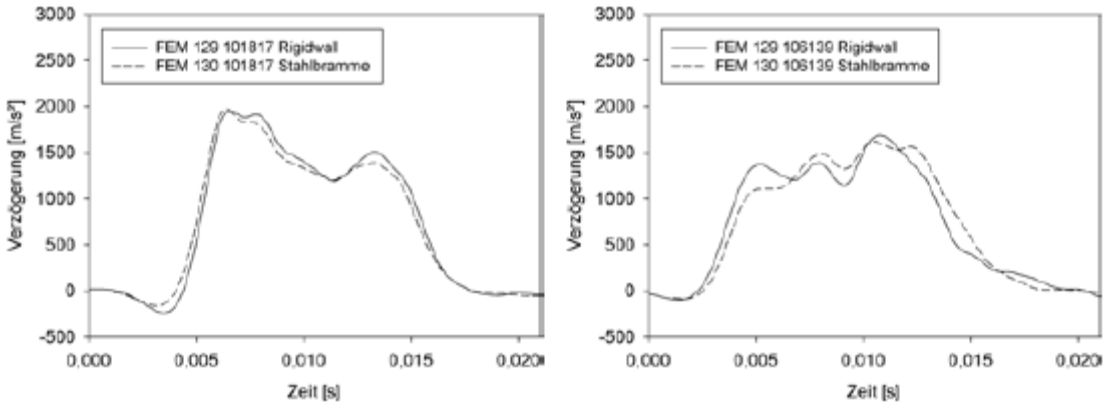

Figure 6.28: Deceleration-Time Curves Under Variation of the Foundation Modeling (Rigidwall or Modeling of the Impact Plate), Bottom (left) and Lid (right) at 0º When Using the Detailed FEM Shock-Absorber Model Variants 129, 130

[Key: 1) Deceleration; 2) Steel slab; 3) Time].

Computations with detailed model while varying the friction factors showed that the magnitude of the influence of the friction factor is less than in case of simplified modeling. The influence on the computation results is slight in case of variation within the usual values for friction factors between wood and steel (0.1-0.5).

6.4.5 Conclusions Concerning the Recomputation of Shock-Absorber Testing

The recomputation of the shock-absorber testing drop tests show that the behavior of the shock-absorbing parts in response to pressure stress can be nicely replicated with a nonsoftening flow curve on the basis of the modeling variant *energy equivalence setup*. The prerequisite for a recomputation is a corresponding consideration of the compression mechanisms of the wood in the shock absorber. For that purpose, the flow curves must be adapted as a function of the lateral

expansion inhibitions in the shock-absorber and test results [sic]. The methods should be used only with a verification by means of drop tests using similar drop test objects (particularly, similar shock-absorbing parts).

We investigated two detailing degrees for shock-absorbing parts, a simplified model and a detailed model. Using the simplified model, it was possible satisfactorily to reproduce local bottom and lid deceleration-time curves. That necessitated adaptations of material parameters to the test results. A variation of the magnitudes of the friction coefficients exerted significant influence on the computation results. If the friction coefficient is chosen too small, then the material will evade laterally under the cask body and will no longer be available for energy absorption. In the case of real shock-absorbing parts, the sheet-metal structure - not modeled in the simplified model - performs this holding function. The evasion behavior of the wood could be simulated realistically only with an empirically determined friction coefficient of 0.3. The simplified model can basically be used for a simulation of the compression of shock-absorbing parts if the force introduction of the shock-absorbing part is known a priori. The prerequisite for this is a verification [of] drop tests with identical models. Special attention must be devoted to the friction coefficients that must be set. The basic predictability of the results determined with this modeling form must thus be evaluated as being rather minor. An evaluation of the influence of changing marginal conditions, such as, for example, changes in the temperature, is impossible due to the dependence of the computation results on the friction coefficients.

Local bottom and lid deceleration-time curves could be replicated satisfactorily with the detailed shock-absorber model. Here again, an adaptation of the material parameters to the experimental results was necessary. Except for the use of unrealistically small values, the friction, however, does not exert any decisive influence on the developing force-time curves. When realistically modeling the sheet-metal behavior, this variant, assuming a verification with the help of drop test results, can be used in order effectively to simulate the behavior of shock-absorbing parts in drop tests with transport casks holding radioactive substances. The influence of changing marginal conditions, such as changes in the temperature, can now be evaluated.

The LS-DYNA material model 26 *mat_honeycomb* proved to be a suitable material description due to its structure, which is well suited for wood, except for the modeling of the softening (anisotropic, uncoupled flow conditions, hardening of relative volume change) for the investigated modeling form *energy equivalence setup* and both investigated modeling grades. The use of adequately stiffness-proportional RALEIGH friction is justifiable for the simulation of the behavior of shock-absorbing parts. The influence on the expansions occurring on the cask body, however, should be investigated. The vaporization of the rigid-body motion must be observed carefully when using mass proportional RALEIGH attenuation. Friction exerts significant influence, especially on the substitute shock-absorber models because it decides on the possibility of a lateral evasion of the shock-absorber areas that are earmarked for energy absorption. A detailed modeling of the impact foundation was not necessary in the combination investigated here; in case of deviations of the elasticity ratio between shock absorber and foundation, a modeling of the foundation, however, can be helpful when it comes to recomputing the performed drop tests.

If one may assume extensive verification with experimental methods, then the FEM can be used for model testing and risk analysis for stress determination in a very practical manner. By means of an experimental verification, the simulation model must be adapted to the marginal conditions prevailing during the test by means of physically acceptable corrections regarding the multiaxiality of the tension state. For model testing, the modeling setup can be used most effectively for data on the components of the shipping items that constitute the tightly sealed enclosure. The prerequisite is the verification with the help of drop test results on a sufficiently similar test specimen.

A stress determination for various accident situations, considering the real packaging behavior, which would be more realistic in comparison to analyses conducted so far, can be performed in the course of a risk analysis with the help of the FEM.

As a function of the deviatory and hydrostatic stress state, one should define a material model that is capable of describing the behavior of a substitute continuum-mechanics model for the wood mixture in the post-rupture area under the influence of multiaxiality. The status of simulation described here could be improved considerably with the described material model, as implemented in a computation model with detailed shock-absorber modeling.

6.5 Summary

In this chapter, we presented a substitute continuum-mechanics model for the simulation of the behavior of axially pressure-stressed wood at large deformations. Then the wood fiber mixture that forms as a result of axial stress along with large deformations is modeled in a "smeared" manner by way of continuum mechanics. The multiaxiality of the triaxial stress state in the model should control the evolution of the flow surface. If the lateral expansion inhibition and thus the multiaxiality are minor, then the flow surface - modeling softening - should become smaller. If the lateral expansion inhibition and thus the multiaxiality are high, then the flow surface should become larger with increasing stress. Various modeling setups were proposed for the conversion of the substitute model in the FEM. The *softening flow curve, substitute continuum-mechanics model with multiaxiality* and *energy equivalence setup* variants were recommended for further work. Material models of the LS-DYNA FE program, which potentially can be applied to the proposed modeling setups, were presented and evaluated. Material models 24, 26, 63 and 75 of the LS-DYNA FE program were selected for an additional investigation.

The applicability of the material models and modeling forms was evaluated with the help of a recomputation of the shock tests against wood samples presented in Subchapter 4.3. None of the investigated combinations was able globally to simulate the behavior of wood in the post-rupture area with large deformations. The results, determined with the *softening flow curve* modeling variant were basically a function of discretization and, except for one case, were not numerically stable and therefore could not be recommended for any further use. The applicability of the LS-DYNA material model 75 was investigated for the modeling variant *substitute continuum-mechanics model with multiaxiality*. The material model does not separate deviatory from hydrostatic stress conditions; therefore, the material model was not suitable for the proposed modeling variants.

Using the results from a drop test, the modeling variant *energy equivalence setup* was transferred to the specific application case, in other words, the simulation of a drop test with a cask-like substitute mass and shock-absorbing part. Cask kinematics (filtered lid and bottom deceleration) could be simulated satisfactorily with simplified and detailed shock-absorber models. Friction coefficients decisively influenced the determined curves in the case of simplified modeling. The extrapolability of the simplified modeling for parameter investigations should be evaluated as being very poor due to the dependence of the computation results on the friction coefficients.

The influence of the friction coefficient on the lid and bottom decelerations was minor when the detailed shock-absorber model was used. This modeling form can be used to evaluate the influence of changing marginal conditions, such as changes of the temperature or the geometry.

The LS-DYNA material model 26 *mat_honeycomb* proved to be a suitable material description for the investigated modeling form *energy equivalence setup* and both investigated modeling grades. The use of adequate stiffness proportional RALEIGH attenuation can be justified for the simulation of the behavior of shock-absorbing parts. We advise against using mass proportional RALEIGH attenuation. Friction exerts significant influence, especially for the substitute shock-absorber models. A detailed modeling of the impact foundation was not necessary in the combination investigated here. The type of contact definition exerted little influence on the computation results.

If one may assume extensive verification with experimental methods, then the FEM can be used for model testing and risk analysis for stress determination in a very practical manner. By means of an experimental verification, the simulation model must be adapted to the marginal conditions prevailing during the test by means of physically acceptable corrections regarding the multiaxiality of the tension state. For model testing, the modeling setup can be used most effectively for data on the components of the shipping items that constitute the tightly sealed enclosure. The prerequisite is the verification with the help of drop test results on a sufficiently similar test specimen.

A stress determination for various accident situations, considering the real packaging behavior, which would be more realistic in comparison to analyses conducted so far, can be performed in the course of a risk analysis with the help of the FEM.

7 Summary

The goal of this study was to develop a model for the behavior of wood-filled shock-absorbing parts of transport casks holding radioactive substances. This model was used in order to derive and evaluate modeling strategies for shock-absorbing parts in the course of mathematical determination of the release risk during the shipment of radioactive substances and for the evaluation of safety characteristics in the context of model testing of transport casks holding radioactive substances. The results of this study represent progress for the investigation of the shipment risk as well as for model testing because the safety behavior of transport casks holding radioactive substances can, with the results of this study, be better modeled and quantified as part of the safety engineering accident chain.

Shock-absorbing parts, tested in the course of drop experiments, were broken down and analyzed to shape the model for the behavior of shock-absorbing parts. To absorb significant energy, the wood must be covered by rigid container or shock-absorber structures in a position-stabilizing manner. To make a realistic comparison between measured and computed shock-absorber deformation, we must also add an elastic resiliency of the shock-absorbing part after the impact to the measured deformation, amounting to between 5% and 7.5%. The optical measurement method of strip projection, which was developed for the purpose of measuring three-dimensional objects, was employed for the first time for measuring shock-absorbing parts of shipment casks for radioactive substances and is very well suited for damage and deformation documentation. The method was to be employed to document deformations on shock-absorbing parts in drop tests.

Differing failure and compression mechanisms could be seen for wood, depending on the position in the shock-absorbing part. With the help of experiments on wood samples, it was possible to confirm the hypothesis derived therefrom: After attaining pressure strength, the energy-absorption capacity of the wood in the shock-absorbing part depends on the lateral expansion inhibitions. The more intensively the wood is supported laterally, the greater will be the energy absorption. Faster stress velocities in general resulted in stronger pressure forces and absorbed energies, although not all of the interrelationships examined in this study were significant. The dependence of the pressure strength on the expansion rate was determined. Increasing pressure rates resulted in higher pressure strength. On the basis of the experimental investigations, a model was developed for the behavior of axially stressed wood in conjunction with large deformations. The model considers the lateral expansion inhibition for the compression of wood - and in the continuum-mechanics context, that would be the multiaxiality of the stress state in the continuum. The energy that can be absorbed by wood grows the greater is the lateral expansion inhibition. That results in a model for the behavior of wood-filled shock-absorbing parts: The energy-absorption capacity of the shock absorber depends on the ability of the outer sheet-metal structure to assure the cohesion of the shock absorber and to prevent a primarily axial stress of the wood as well as an evasion of an entire wood packet. To build shock-absorbing parts, it is necessary to ensure the lateral support of the wood and the cohesiveness of the shock absorber by means of adequately dimensioned sheet-metal structures.

The simplified numerical method *"ImpactCalc,"* as developed in this study, is suitable for determining estimates for global kinematic parameters, such as rigid cask body decelerations or

shock-absorber deformations. With slight deviations, the method is capable of determining curves of rigid-body decelerations and shock-absorber deformations in shipment casks for radioactive substances with wood-filled shock-absorber parts. For this purpose, we must construe the entire cask system, excluding the shock-absorbing parts approximately as a uniform, cohesive, rigid body. This simplification can be made only if the resiliency of the cask when compared to the resiliency of the shock-absorbing parts is negligible and if no significant relative motion is possible between the individual parts of the cask.

It follows from the experimental and computational results on the CONSTOR® V/TC that the widely used principle of evaluation of maximum rigid-body deceleration as model stress for casks, such as CONSTOR® V/TC, can no longer be meaningfully employed. As part of cask evaluation, one must, for example, investigate by means of a dynamic comparison computation whether the setup of a rigid-body deceleration covers the cask stress. Assuming verification, the method can be used appropriately in model testing to determine rigid-body decelerations and shock-absorber deformations. Assuming a verification with the results of drop tests involving a similar model, we propose the use of a sufficiently conservative safety factor of two for the results of computations using *"ImpactCalc"* for further evidence. For risk analysis, one can, in a simple and cost effective manner, estimate many different accident situations, for example, an impact against real foundations, and they can be compared with the impact upon the nonresilient test stand foundation.

A continuum-mechanics substitute model was proposed for modeling with the Finite Elements Methods, which the proposed physical model on the behavior of the wood ties in with the continuum-mechanics interrelationship. In the model, the multiaxiality of the triaxial stress state controls the evolution of the flow surface. In that way, the degree of lateral expansion inhibition decides the softening or hardening material behavior. Other simplified modeling forms were derived and evaluated.

Using a simulation of the compression experiments with wood, it was determined that none of the proposed modeling strategy was in a position to model the behavior of wood in response to pressure stress and in the presence of large deformations, including softening. The investigated variants "*softening flow curve"* resulted in pronounced network dependences and numerical instabilities. No suitable material model is available for the modeling variant *"substitute continuum-mechanics model with multiaxiality."*

By simulation of a drop test with a cask body and shock-absorbing parts, it was shown that the modeling form *"energy equivalence setup,"* while lowering the flow curve, was suitable for computing a cask kinematic as determined in the experiments. The LS-DYNA material model 26 *mat_honeycomb* proved to be a suitable material description for the investigated modeling form *energy equivalence setup* and both investigated modeling degrees. The use of adequate stiffness proportional RALEIGH attenuation is justifiable to simulate the behavior of shock-absorbing parts. We advise against using mass proportional RALEIGH attenuation. Friction exerts significant influence on the determined shock force curves, especially with respect to the substitute shock-absorber models. A detailed modeling of the impact foundation was not necessary for the combination investigated here. The contact definition exerted little influence on the computation results.

If one may assume far-reaching verification with experimental methods, then the FEM can be used effectively in model testing and risk analysis for stress determination. By means of experimental verification, the simulation model must be adapted to the marginal conditions prevailing in the experiment by means of physically justifiable corrections regarding the multiaxiality of the stress state. When it comes to model testing, the modeling setup can be used effectively for test data on the components of the shipping items that constitute the tightly sealed enclosure. The prerequisite here is verification with the help of drop test results using an adequately similar test specimen. In the course of a risk analysis using the FEM, one can make a comparison with the previously performed analyses of more realistic stress determination for various accident situations, considering the real packaging behavior.

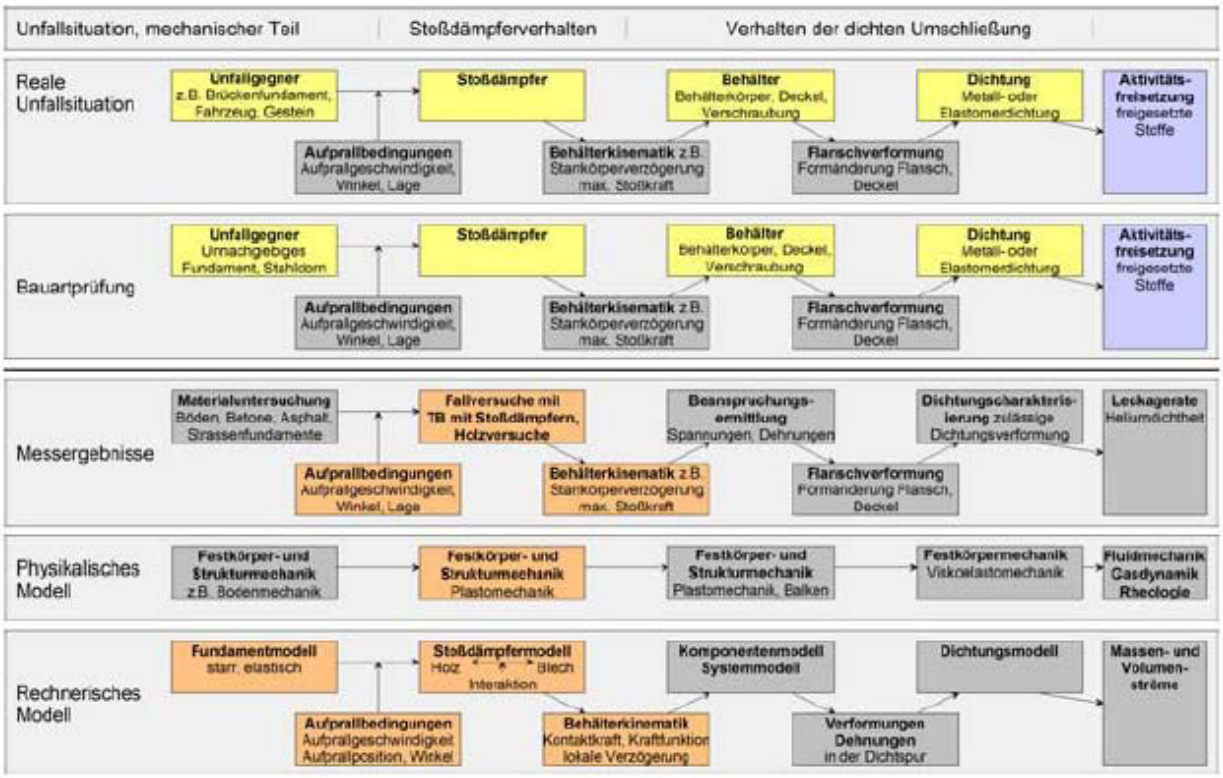

Figure 7.1: Excerpt from the Scheme Showing the Safety Engineering Chain with Progress Achieved by This Study

[Key: 1) Accident situation, mechanical part; 2) Shock-absorber behavior; 3) Behavior of tightly sealed enclosure; 4) Real accident situation; 5) Accident body, for example, bridge foundation, vehicle, rocks; 6) Shock absorber; 7) Cask, cask body, lid, screw locks; 8) Seal, metal or elastomer seal; 9) Activity release, released substances; 10) Impact conditions, impact velocity, angle, position; 11) Cask kinematic, for example, rigid-body deceleration, maximum shock force; 12) Flange deformation, form change, flange, lid; 13) Model testing; 14) Accident body, nonresilient foundation, steel dome; 15) Measurement results; 16) Material investigation, floors, concrete, asphalt, highway foundations; 17) Drop tests with transportation cask containing shock absorbers, wood experiments; 18) Stress determination, stresses, expansions; 19) Seal characterization, permissible seal deformation; 20) Leakage rate, helium tightness; 21) Physical

model; 22) Solid body and structural mechanics, for example, flow mechanics; 23) Solid body and structural mechanics, plastic mechanics; 24) Solid body and structural mechanics, plastic mechanics, beams; 25) Solid body mechanics, viscosity mechanics; 26) Fluid mechanics, gas dynamics, rheology; 27) Mechanical model; 28) Foundation model, rigid, elastic; 29) Shock-absorber model, wood-sheet metal, interaction, 30) Component model, system model; 31) Seal model; 32) Mass and volume flows; 33) Impact conditions, impact velocity, impact position, angle; 34) Cask kinematic, contact force, force function, local deceleration; 35) Deformations, expansions in the sealed track].

Figure 7.1 shows the excerpt, already presented in Chapter 1, from the safety-engineering action chain, this time supplemented by the action that was "operationalized" with measurements as well as physical and computer models; the sections marked with orange color indicate that this study determined essential results and produced progress. The results of the performed drop tests and the wood experiments can be integrated into the measurement results. Various impact conditions were investigated and the cask kinematics were determined experimentally. Using experimental results, we determined a typical model of the behavior of wood in response to axial pressure stress, and that resulted in a model for the behavior of shock-absorbing parts. For simplified numerical and FEM methods, we supplied mathematical models of shock-absorbing parts, and we evaluated their applicability and, in one case, the influence of foundation modeling. Various impact positions were investigated mathematically and cask kinematics were determined. The physical models were arranged according to GUMMERT & RECKLING [GR94].

Figure 7.2 is a summary showing the possible routes as determined and evaluated in this study for the computation of the load introduction into the cask body for mathematical data evidencing the accident safety of the transport cask holding radioactive substances or for studies to determine the hazard potentials connected with the shipment of radioactive substances. Dynamic FE methods or the simplified numerical method *"ImpactCalc"* can be used.

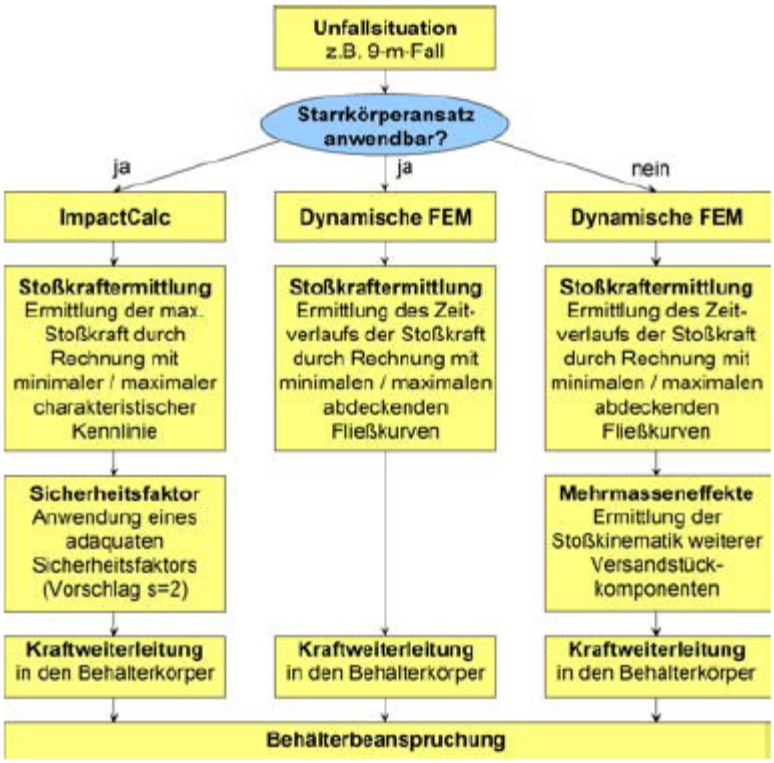

Figure 7.2: Scheme Showing Possible Procedures To Be Used for Mathematical Data Evidencing the Accident Safety of Transport Casks Holding Radioactive Substances

[Key: 1) Accident situation, for example, 9-m drop; 2) Rigid-body setup applicable?; 3) Yes; 4) No; 5) Dynamic FEM; 6) Shock force determination, determination of maximum shock force by computation with minimal/maximal characteristic curves; 7) Shock force determination, determination of the time curve of shock force by computation with minimal/maximal covering flow curves; 8) Shock force determination, determination of time curve of shock force by computation with minimal/maximal covering flow curves; 9) Safety factor, use of an adequate safety factor (proposal s=2); 10) Multimass effects, determination of shock kinematic of other shipping item components; 11) Force propagation into the cask body; 12) Cask stress].

In conclusion, we might keep in mind that this study and the method developments presented herein make a decisive contribution to an understanding of the behavior and the simulation possibilities of shock-absorbing parts and can be a basis for further design developments and continued research activity in this field.

8 Outlook

The behavior of shock-absorbing parts as well as the possibilities of modeling it and computation with various methods as characterized in this study constitute but one part of the mechanical safety evaluation in the course of model testing and risk analysis.

In any risk analysis, a mathematical computation of the cask stresses in accident situations would be possible on the basis of this study. Further investigations would be necessary regarding the behavior of the sealing systems in response to accident stresses and the modeling of the "real" obstacles, such as vehicles or bridge foundations.

More extensive concretizing materials or parts investigations for various design forms of shock-absorbing parts are necessary when it comes to model testing, for example, in the course of a specific licensing procedure. That includes further experiments on wood samples with which one could determine the influence of temperature, moisture and sample size on the energy-absorption capacity of wood in case of large deformations.

The transferability of experimental results on wood samples, for example, under various temperature conditions upon real shock-absorber designs, could be examined in the course of experiments with prototypes or models on a suitable scale using transport and storage containers under operational, space and low-temperature conditions.

The considerations can be expanded to other impact positions and more complex geometries for simplified numerical methods.

Depending on the deviatory and hydrostatic stress state, by defining a material model that is capable of describing the behavior of a substitute continuum-mechanics model for the wood mixture in the post-fracture area under the influence of multiaxiality, the status of simulation described here can be improved considerably.

Basically, the investigations and computation methods used in this study can be used also for other shock-absorbing materials, although that would require appropriate materials investigations.

A Fundamentals of the Finite Elements Method

Let us agree that the marginal conditions, as described in Subchapter 6.1, apply to the interrelationships described below.

A.1 Balanced Equations

Balanced equations describe generally valid principles or laws that are independent of special continuum properties. They describe the change in terms of time of a physical magnitude Φ (random tensor) that will describe the state of the body during a process. If the change in terms of time is Φ = 0, then we are dealing with a special case of a preservation principle.

Mass balance. The prerequisite to the effect that the mass of a body is constant at all times with the help of Euler's divergence formula leads to the local mass continuity equation:

$$\dot{\rho} + \rho \operatorname{div}(\mathbf{v}) = 0 \tag{A.1}$$

m	Masse
ρ	Dichte
$\operatorname{div}(\mathbf{v})$	Divergenz des Geschwindigkeitsvektors

m	Mass
ρ	Density
$div(\mathbf{v})$	Divergence of velocity vector

or the global mass continuity equation in the momentary configuration:

$$\int_v \dot{\rho} + \rho \operatorname{div}(\mathbf{v})\, dv = 0 \tag{A.2}$$

Impulse balance. The change of the impulse in terms of time must be equal to the action of all surface and volume forces:

$$\dot{I} = \int_v \rho \dot{v}_i dv = \int_v \rho f_i dv + \int_a t_i da \tag{A 3}$$

I	Impuls
v_i	Geschwindigkeitsvektor
a	Fläche
v	Volumen
f_i	Kraft pro Volumen
t_i	Kraft pro Fläche

I	Impulse
v_i	Velocity vector
a	Surface
v	Volume
f_i	Force per volume
t_i	Force per surface

With the help of the GAUSSIAN principle that describes the interrelationship between an area integral via the volume V and the integral via the pertinent surface A

$$\int_v \nabla \cdot \phi \, dv = \oint_a n \cdot \phi \, da$$

∇	Nabla Operator
$\nabla \cdot \phi$	Divergenz von Φ
n	Normalenvektor auf der Oberfläche

(A.4)

∇	Nabla operator
$\nabla \cdot \phi$	Divergence of Φ
n	Perpendicular vector on the surface

and the interrelationship between Cauchy's stress tensor σ_{ij} and Cauchy's stress vector t_i

$$t_i = \sigma_{ij} \cdot n_j \qquad \text{(A.5)}$$

one can describe the local form of the impulse balance in the momentary configuration:

$$\sigma_{ij,j} + \rho f_i = \rho \dot{v}_i \qquad \text{(A.6)}$$

$\sigma_{ij,j}$	div(σ) Divergence of σ

Rotary impulse balance. The change in terms of time of the total rotary impulse $\dot{D}_i$ is equal to the resultant rotary moment of all external forces M_{Ri}.

$$\dot{D}_i = \int \epsilon_{ijk} x_j \ddot{x}_k \rho dv = M_{Ri} = \int_v \epsilon_{ijk} x_j \rho f_k \, dv + \int_a \epsilon_{ijk} x_j \rho t_k da$$

ϵ_{ijk}	LEVI-CEVITA Permutationstensor dritter Stufe

(A.7)

ε_{ijk}	LEVI-CEVITA permutation tensor, third stage

With the help of the Gaussian principle (equation A.4), one can substitute the surface integral, and equation A.7 then gives us

$$\epsilon_{ijk}\left(\sigma_{kj}\sigma_{jk}\right) = 0 \tag{A.8}$$

It follows from this that Cauchy's stress tensor σ_{ij} must be symmetrical.

Energy balance. The global form of the energy balance is known as thermomechanical energy preservation principle or 1st principal theorem of thermodynamics. The time change of the internal energy and of the kinetic energy of the continuum corresponds to the output of the external volume and surface forces as well as of the supplied or evacuated heat quantity in the volume or via the surface per [unit of] time. The local evaluation [interpretation] in the momentary configuration gives us:

$$\rho U = \sigma_{ki} d_{ki} \rho - q_{i,i} \tag{A.9}$$

U	Innere Energie
d_{ki}	Deformationsgeschwindigkeitstensor

U	Internal energy
d_{ki}	Deformation velocity tensor

Here, the term $\sigma_{ki}d_{ki}$ describes the mechanical form change energy density per [unit of] time.

Entropy balance. The entropy balance equation is called the 2nd principal theorem of thermodynamics: In case of irreversible processes. The entropy always increases for closed systems, whereas the entropy remains constant for reversible processes.

$$T_{ki} d_{ki} - \rho\left(\dot{\Phi} + \dot{\Theta} S\right) - \frac{q_i}{\Theta} Q_i \geq 0 \tag{A.10}$$

T_{ki}	2. PIOLA KIRCHHOFFscher Spannungstensor
Φ	Spezifische freie Energie
Θ	Absolute Temperatur
S	Spezifische Entropie
q_i	Temperaturgradient
Q_i	Wärmestrom

T_{ki}	2nd PIOLA KIRCHOFF's stress tensor
Φ	Specific free energy
Θ	Absolute temperature
S	Specific entropy
q_i	Temperature gradient
Q_i	Heat flow

Equation A.10 is referred to as the Clausius-Duhem inequality.

Marginal value problem. In the preceding sections, we derived the local form of the impulse balance (equation A.6). The balance is fulfilled therein, point by point; therefore, equation A.6 is also referred to as a strong form of the balance. The margin of the continuum is now subdivided into a part Γ_D on which the displacements $\bar{u}$ (DIRICHLET marginal condition) and a part Γ_N on which are prescribed the stresses $\bar{t}$ (NEUMANN marginal condition). The local impulse balance thus leads to a marginal value problem for whose solution the supplied balance theorems are available.

Table A.1: Variables and Equations in Continuum Mechanics

Number of Field Magnitudes		**Number of Equations**	
Displacements u	3	Mass balance	1
Stresses σ_{kl}	9	Impulse balance	3
Density ρ	1	Rotary impulse theorem	3
Special internal energy $\bar{u}$	1	1st principal theorem of thermodynamics	1
Temperature Θ	1	2nd principal theorem of thermodynamics	(1)
Heat flow q	3		
Specific entropy S	1		
Total	19		8

The balance between existing equations and unknowns for the Euclidean space $\mathbb{R}^3$ in Table A.1 shows that other equations are needed on top of those already supplied. The missing equations for the unequivocal solution of the marginal-value problem are supplied by constitutive equations.

A.2 Finite Elements Method

The boundary value problem from Chapter 6.1.1 consists of coupled partial differential equations that can be solved only in the rarest of cases. This is why one generally employs numerical solution methods. The Finite Elements Method is a procedure that is in wide use to solve these marginal-value problems. In the process, the body is subdivided into finitely many subareas on which all structural magnitudes are discretized. At this point, we want to show only a small introduction for an understanding of the fundamental equations; for any further work, we would like to refer to the standard works on continuum mechanics, such as BETTEN [Bet01],

WILLNER [Wil03] and, on the Finite Elements Methods, BATHE [Bat02], WRIGGERS [Wri01] and ZIENKIEWICZ & TAYLOR [ZT05].

A.2.1 Principle of Virtual Work

The strong form of the impulse theorem is converted into the so-called weak form to solve the marginal-value problem (see Chapter 6.1.1). For example, the balance is no longer fulfilled locally, but rather only integrally over the entire system. The unknowns of the system are not calculated by balance conditions but are derived from energy considerations. The principle of virtual work states that for a statically possible deformation, the virtual work δW_a of the external forces and moments must be equal to the virtual internal work δW_i:

$$\delta W_i = \delta W_a \tag{A.11}$$

The possible deformations are referred to here as virtual jigglings[1]. The matrix notation customary in FEM is used for further work. With the help of the impulse balance (equation A.6), we get:

$$\int_V (\operatorname{div}(\boldsymbol{\sigma}) + \mathbf{f})\, \delta\mathbf{u}\, dV = 0$$

$\delta\mathbf{u}$	virtuelle Verschiebung
u	Verschiebung
$\mathbf{f}$	Vektor aller äußeren Kräfte (inkl. Massenkräfte)

(A.12)

$\delta_{\mathbf{u}}$	Virtual displacement
u	Displacement
$\mathbf{f}$	Vector of all external forces (including mass forces)

With the help of

$$\operatorname{div}(\boldsymbol{\sigma} \cdot \delta\mathbf{u}) = \operatorname{div}\boldsymbol{\sigma} \cdot \delta\mathbf{u} + \boldsymbol{\sigma} : \frac{\partial \delta\mathbf{u}}{\partial \mathbf{x}} \tag{A.13}$$

and the GAUSSIAN theorem

$$\int_{\mathcal{B}} \operatorname{div}(\boldsymbol{\sigma} \cdot \delta\mathbf{u})\, dV = \int_{\Gamma_N} \mathbf{t} \cdot \delta\mathbf{u}\, dA - \int_{\mathcal{B}} \boldsymbol{\sigma} : \frac{\partial \delta\mathbf{u}}{\partial \mathbf{x}}\, dV$$

$\mathbf{t}$	Oberflächenkräfte

(A.14)

[1] A fictitious, infinitesimal, geometrically possible and timeless displacement or twisting.

t Surface forces

we get:

$$\int_{\mathcal{B}} \boldsymbol{\sigma} : \frac{\partial \delta \mathbf{u}}{\partial \mathbf{x}} \, dV = \int_{\Gamma_N} \mathbf{t} \cdot \delta \mathbf{u} \, dA + \int_{\mathcal{B}} \mathbf{f} \cdot \delta \mathbf{u} \, dV. \tag{A.15}$$

With the help of the virtual velocity gradients:

$$\delta \mathbf{L} = \frac{\partial \delta \mathbf{u}}{\partial \mathbf{x}} \tag{A.16}$$

which can be split up into a symmetrical δ**D** and an antimetric δ**W** part

$$\delta \mathbf{L} = \delta \mathbf{D} + \delta \mathbf{W} = \frac{1}{2} \left(\delta \mathbf{L} + \delta \mathbf{L}^T \right) + \frac{1}{2} \left(\delta \mathbf{L} - \delta \mathbf{L}^T \right) \tag{A.17}$$

one can write the principle of virtual work[2] in its classical form:

$$\int_{\mathcal{B}} \boldsymbol{\sigma} : \delta \mathbf{D} \, dV = \int_{\Gamma_N} \mathbf{t} \cdot \delta \mathbf{u} \, dA + \int_{\mathcal{B}} \mathbf{f} \cdot \delta \mathbf{u} \, dV. \tag{A.18}$$

A.2.2 Discretization

The body B is now broken down into n_{ele} finite elements:

$$\mathcal{B} = \bigcup_{e=1}^{n_{ele}} \mathcal{B}^e \tag{A.19}$$

The weak form of the balance e(A.18) with extraction of the mass inertial term out of the vector of the external volume forces now becomes a sum via the elements:

$$\sum_{e=1}^{n_{ele}} \int_{v_e} \hat{\boldsymbol{\sigma}} : \delta \hat{\mathbf{D}} \, dv + \sum_{e=1}^{n_{ele}} \int_{v_e} \rho \ddot{\hat{\mathbf{u}}} \cdot \delta \hat{\mathbf{u}} \, dv - \sum_{e=1}^{n_{ele}} \int_{v_e} \rho \hat{\mathbf{f}} \cdot \delta \hat{\mathbf{u}} \, dv - \sum_{e=1}^{n_{ele}} \int_{s_e} \hat{\mathbf{t}} \cdot \delta \hat{\mathbf{u}} \, da = 0 \tag{A.20}$$

[2] Principle of virtual jiggling or displacement for static cases.

One usually selects set-up functions for the elements by means of which one can separate the local and time dependences:

$$\hat{\mathbf{u}}(\mathbf{x},t) = \mathbf{H}_u(\xi_i)\,\mathbf{u}_e(t)$$

$\mathbf{H}_u(\xi_i)$	Matrix der Formfunktionen
ξ_i	Orts- Elementparameter
$\mathbf{u}_e$	unbekannte Knotengrößen im Element

(A.21)

$\mathbf{H}_u(\xi_i)$	Matrix of form functions
ξ_i	Local element parameters
$\mathbf{u}_e$	Unknown node magnitudes in element

Due to the separation, the derivation operations for the formation of the distortions act only on the form functions $\mathbf{H}_u(\xi_i)$:

$$\boldsymbol{\epsilon} = D_{\epsilon u}\mathbf{H}_u\mathbf{u}_e$$

$D_{\epsilon u}$	Differenzialoperator

(A.22)

$D_{\varepsilon u}$	Differential operator

We proceed similarly with the virtual magnitudes, which, however, according to definition, are not a function of the time. The nodular magnitudes are not a function of the location; therefore, they can be factored out of the integral. Equation A.20, used for a single element, gives us the following:

$$\delta\hat{\mathbf{u}}_e\left\{\int_{v_e} D_{\epsilon u}\mathbf{H}_u^T\hat{\boldsymbol{\sigma}}\,dv + \int_{v_e}\mathbf{H}_u^T\rho\mathbf{H}_u\,dv\,\ddot{\hat{u}}_e - \int_{v_e}\mathbf{H}_u^T\rho\hat{\mathbf{f}}\,dv - \int_{s_e}\mathbf{H}_u^T\hat{\mathbf{t}}\,da\right\} = 0 \qquad \text{(A.23)}$$

By interpreting the integrals, one gets the element vector of the internal forces:

$$\mathbf{r}_e = \int_{v_e} D_{\epsilon u}\mathbf{H}_u^T\hat{\boldsymbol{\sigma}}\,dv \qquad \text{(A.24)}$$

the element mass matrix

$$\mathbf{M}_e = \int_{v_e}\mathbf{H}_u^T\rho\mathbf{H}_u\,dv\,\ddot{\hat{u}}_e \qquad \text{(A.25)}$$

the element load vector from volume loads

$$\mathbf{f}_{f,e} = \int_{v_e} \mathbf{H}_u^T \rho \hat{\mathbf{f}} \, dv \tag{A.26}$$

and the element load vector from marginal loads

$$\mathbf{f}_{t,e} = \int_{s_e} \mathbf{H}_u^T \hat{\mathbf{t}} \, da \tag{A.27}$$

which now, with the help of the assembling operator A according to HUGHES [Hug87], are incorporated in the system matrices:

$$[\mathbf{r}, \mathbf{M}, \mathbf{f_f}, \mathbf{f_t}] = \mathop{\mathrm{A}}_{e=1}^{E} [\mathbf{r_e}, \mathbf{M_e}, \mathbf{f_{f,e}}, \mathbf{f_{t,e}}] \tag{A.28}$$

Here are the resultant system balance equations:

$$\mathbf{M}\ddot{\mathbf{u}} + \mathbf{r} = \mathbf{f}_u \tag{A.29}$$

whereby the system load vectors were combined for volume and marginal loads.

A.2.3 Linearization in Case of Nonlinear Problems

Equation A.29 is a linear equation system only for linear problems, as in the case of linear elastic material behavior. We have a high-grade nonlinear equation system here due to the nonlinear material laws employed here. Iterative methods must be used for the solution. The NEWTON RAPHSON method is frequently employed for this purpose. We will not present it here; instead, we would like to refer to DEUFLHARD [Deu04].

A.2.4 Time Integration for Dynamic Problems

The idea underlying all time integration methods is the discretization of the time axis into discrete time steps τ. The objective is the deterministic determination of subsequent states $t+\tau$ of a system by means of the initial conditions given at moment t. The various methods for time integration can be subdivided into explicit and implicit methods. In the case of explicit methods, the differential equations are evaluated at moment t, while in the case of implicit methods, this is done at moment $t+\tau$. For the explicit case, there now follows a linear equation system, and in the case of implicit nonintegration, there will be nonlinear equation systems that must be solved

iteratively. Explicit methods are only conditionally stable, while implicit methods are very laborious in terms of mathematics. There are many methods for time integration and the best-known implicit method is the generalized method according to NEWMARK [New59]. The method of central differences is frequently used for explicit integration. The EULER forward method is another option. A discussion of other time integration methods can be found in HUGHES [Hug87].

A.2.5 Solution of the Linear Equation System

All of the mentioned methods for the solution of nonlinear or time-dependent problems will lead to a linear equation system:

$$\mathbf{K}\,\mathbf{u} = \mathbf{f} \tag{A.30}$$

K	Systemmatrix
u	unbekannte Knotengrößen
f	gegebene rechte Seite

K	System matrix
u	Unknown node magnitudes
f	Right side given

This equation system can be solved with the help of standard methods (for example, GAUSSIAN elimination). The coefficient matrix, however, is mostly only lightly occupied, and it is also symmetrical; therefore, one can use more effective methods. We differentiate between direct and iterative solution methods. Direct methods for small problems are based on a matrix breakdown (mostly CHOLESKY method of $\mathbf{LDL}^T$ factorization); iterative methods, such as the JACOBI or the LANCZOS method, are often used for working on major problems (see also BATHE [Bat02]).

B FE Model Settings

In this chapter, we present the FE material law parameters that are used in the FEM computation for wood.

Table B.1: Material Model 24 Settings for Fir Wood in Response to Axial Stress

Item	Symbol	Value
Density	RO	$4.5 \cdot 10^{-4}$ g/mm^3
Elasticity module	E	$3.0 \cdot 10^{3}$ MPa
Poisson's ratio	PR	0.45
Elongation limit	SIGY	50 MPa
Attenuation	DAMP	0.0

Table B.2: Material Model 26 Settings for Fir Wood in Response to Axial Stress

Item	Symbol	Value
Density	RO	$1.5 \cdot 10^{-3}$ g/mm^3
Elasticity module	E	$3.5 \cdot 10^{4}$ MPa
Poisson's ratio	PR	0.35
Elongation limit of compacted material	SIGY	70 MPa
Volume ratio, start of hardening	VF	0.3
Elasticity module, uncompacted axial	EAAU	$3.0 \cdot 10^{3}$ MPa
Elasticity module, uncompacted radial	EBBU	700 MPa
Elasticity module, uncompacted tangential	ECCU	400 MPa
Transversal elasticity module, uncompacted, t-r direction	GABU	700 MPa
Transversal elasticity module, uncompacted, r-a direction		
Transversal elasticity module, uncompacted, a-t direction	GBCU	40 MPa
	GCAU	700 MPa

Table B.3: Material Model 63 Settings for Fir Wood in Response to Axial Stress

Item	Symbol	Value
Density	RO	$4.5 \cdot 10^{-4}$ g/mm^3
Elasticity module	E	$3.0 \cdot 10^{3}$ MPa
Poisson's ratio	PR	0.45
Tensile strength	SIGY	50 MPa
Attenuation	DAMP	0.0

Table B.4: Material Model 75 Settings for Fir Wood in Response to Axial Stress

Item	Symbol	Value
Density	RO	$4.5 \cdot 10^{-4}$ g/mm^3
Elasticity module	E	$3.0 \cdot 10^{3}$ MPa
Poisson's ratio	PR	0.25

Tensile strength	SIGY	50 MPa
Viscous attenuation	V	0.0

Table B.5: Material Model 75 Settings, Sheet Metal

Item	**Symbol**	**Value**
Density	RO	$7.85 \cdot 10^{-3}$ g/mm^3
Elasticity module	E	$2.1 \cdot 10^5$ MPa
Poisson's ratio	PR	0.3
Elongation limit	SIGY	-0 MPa
Attenuation	DAMP	0.0
Expansion at which element erodes	FAIL	0.3

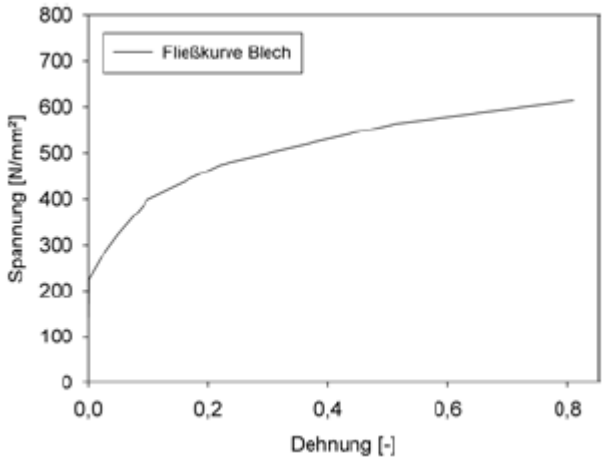

Figure B.1: Flow Curve for Sheet Metal Used for All Variants

[Key: Y-axis= Sheet-metal flow curve; X-axis= Stress; Fliesskurve Blech = Expansion].

List of Abbreviations

A_2	Activitätsgrenzwert [Radioactivity boundary value]
ADNR	Europäisches Übereinkommen über die Beförderung gefährlicherGüter auf Binnenwasserstrassen (ADN) in Verbindung mit der Verordnung über die Beförderung gefährlicher Güter auf dem Rhein (und Mosel) [European Agreement on the Transportation of Hazardous Goods on Inland Waterways (ADN) in Conjunction with the Decree on the Transportation of Hazardous Goods on the Rhine (and Moselle)
ADR	Europäisches Übereinkommen über die internationale Beförderung gefährlicher Güter auf der Strasse [European Agreement on the International Transportation of Hazardous Goods by Highway]
BA	Beschleunigungsaufnehmer [Acceleration sensor]
BAM	Bundesanstalt für Materialforschung und -prüfung [Federal Institute for Materials Research and Testing]
BfS	Bundesamt für Strahlenschutz [Federal Bureau for Radiation Protection]
BMBF	Bundesministerium für Bildung und Forschung [Federal Ministry for Education and Research]
CFK	Kohlefaserverstärkter Kunststoff [Carbon-Fiber Reinforced Synthetic Substance]
DMS	Dehnungsmessstreifen [Expansion measurement strip]
FEM	Finite Elements Method
GFK	Glasfaserverstärkter Kunststoff [Glass-fiber reinforced synthetic substance]
GGBefG	Gesetz über die Beförderung gefährlicher Güter [Law on the Transportation of Hazardous Goods]
GGG	Grauguss mit globularem Kugelgraphit [Gray cast iron with globular ball graphite]
GGVBinSch	Gefahrgutverordnung Binnenschifffahrt [Hazardous Goods Decree Inland Navigation]
GGVSE	Verordnung über die innerstaatliche und grenzüberschreitende Beförderung gefährlicher Güter auf der Strasse und mit der Eisenbahn [Decree on the Domestic and Border-Crossing Transportation of Hazardous Goods by Road and Rail]
GGVSee	Verordnung über die Beförderung gefährlicher Güter mit Seeschiffen [Decree on the Transportation of Hazardous Goods on Oceangoing Vessels]
GNS	Gesellschaft für Nuklearsysteme GmbH [Nuclear Systems Company, GmbH]
HAW	High-Active Waste
IAEA	International Atomic Energy Agency

IATA	International Air Transport Association
ICAO	International Civil Aviation Organization
IMDG	International Maritime Dangerous Goods Code
INF	International Code for the Safe Carriage of Packaged Irradiated Nuclear Fuel, Plutonium and High-Level Radioactive Wastes on Board Ships
KKW	Kernkraftwerk [Nuclear power plant]
MHI	Mitsubishi Heavy Industries Ltd.
LSA	Low Specific Activity
PSE	Projekt Sicherheitsstudien Entsorgung [Waste Disposal Safety Studies Project]
PSA	Probabilistische Sicherheitsanalyse [Probabilistic Safety Analysis]
PU	Polyurethan [Polyurethane]
RAM	Radioactive Material
RID	Ordnung über die internationale Eisenbahnbeförderung gefährlicher Güter [Directive on International Rail Shipment of Hazardous Goods]
TLB	Transport- und Lagerbehälter [Transport and Storage Cask]
TB	Transportbehälter [Transport cask]
IAEATRANSSC	Transport Safety Committee of the IAEA
USDOE	United States Department of Energy
SCO	Surface-Contaminated Object
UHMW	Ultra-High Molecular Weight
UNO	United Nations Organization
UN-ECOSOC	United Nations Economic and Social Council
USICC	United States Interstate Commerce Commission
UDM	Uniaxial Displacement Method
USNRC	United States Nuclear Regulatory Commission

Bibliography

[A+78] J.A. Andersen et al. PARC (Plutonium Accident Resistant Container), Program Research Design and Development. Technical Report SAND76-0587/NUREG/CR-0030, Sandia Laboratories, Albuquerque, NM, 1978.

[A+88] K. Asada et al. Development of simplified analysis codes for 9-m drop and 1-m puncture tests for a radioactive material transport cask. *Waste Management*, 88:135-144, 1988.

[ABA06] Abaqus Explicit Users Manual. Volume I, Version 6.6, 2006. Hibbit, Karlson & Sorensen, Inc.

[ADN06] ADNR - Verordnung zur Neufassung der Verordnung über die Beförderung gefährlicher Güter auf dem Rhein (ADNR) und zur Neufassung der Verordnung die Beförderung gefährlicher Güter auf der Mosel vom 21 Dezember 2006 [ADNR - Decree on the New Version of the Decree on the Transportation of Hazardous Goods on the Rhine (ADNR) and on the New Version of the Decree on the Transportation of Hazardous Goods on the Moselle, dated December 21, 2006 (BGBL [Federal Legal Gazette], II, p. 1378), 2006.

[ADN07] ADN - Gesetz zu dem Europäischen Übereinkommen vom 26 Mai 2000 über die internationale Beförderung gefährlicher Gütern auf Binnenwasserstraßen (ADN) vom 123 [sic] November 2007 [ADN - Law on the European Agreement of May 26, 2000 on the International Transportation of Hazardous Goods on Inland Waterways (ADNN), dated November 123 [sic] 2007] (BGBl. Federal Legal Gazette] II, p. 1906), 2007.

[ADR07] ADR - Agreement for the Transport of Dangerous Goods by Road, 2007. Europäisches Übereinkommen vom 30 September 1957 über die internationale Beförderung gefährlicher Güter auf der Strasse [ADR - European Agreement of September 30, 1957 on the International Transportation of Hazardous Goods by Road] (BGBl. [Federal Legal Gazette] 1969, II, p. 1489), neu gefasst am 28 August 2007 [new version, August 28, 2007] (BGBl. [Federal Legal Gazette], 2007, II, p. 1399), Appendices A and B.

[Aif92]E.C. Aifantis. On the role of gradients in the localization of deformation and fracture. *Journal of Engineering Science*, 30"1279-1299, 1992.

[Alg01] A.A.A. Alghamdi. Collapsible impact energy absorbers: on overview. *Thin-Walled Structures*, 39:189-213,2001.

[AM86] J. Argyris and H.P. Mlejnek. *Die Methode der Finiten Elemente in der elementaren Strukturmechanik. Bd. 1. Verschiebungsmethode in der Statik.* [*The Method of the Finite Elements in Elementary Structural Mechanics. Volume 1. Displacement Method in Statics]*, Vieweg, Braunschweig, 1986.

[AM02] C. Adalian and P. Morlier. Wood model for the dynamic behavior of wood in multiaxial compression. *Holz als Roh- und Werkstoff [Wood as Raw Material and Construction Material]*, 60:433-439, 2002.

[Amm92] D.J. Ammerman. A method for comparing impacts with real targets to impacts onto the IAEA unyielding target. In *Proceedings of 10th PATRAM*, Volume 2, pages 893-900, Yokohama, Japan, 1992.

[AS65] G.J. Appleton and J.Y. Servant. Packaging standards. IAEA 64-6413, Vienna, 1965.

[AtG08] AtG - Atomgesetz, 2008. Gesetz über die friedliche Verwendung der Kernenergie und den Schutz gegen Ihre Gefahren, in der Bekanntmachung vom 23 Dezember 1959 [AtG - Atomic Law, 2008. Law on the Peaceful Use of Nuclear Energy and Protection Against Its Hazards in the Announcement of December 23, 1959] [BGBl. [Federal Legal Gazette] I, p. 814), Neugefasst durch Bekanntmachung vom 15 Juli 2002, zuletzt geändert am 29 August 2008 [New Version, Announcement of July 15, 2002, last amended on August 29, 2008] (BGBl. [Federal Legal Gazette], I, p. 1793).

[AT007] Gesellschaft für optische Messtechnik (GOM) mbH, Braunschweig. *ATOS V6 Benutzerhandbuch* [Optical Measurement Technique Company (GOM) mbH, Braunschweig. *ATOS V6 User Handbook*], 2007.

[B$^+$83] R.A. Blythe et al. A study on the influence of target material on impact damage. In PATRAM 83 (*Proc. Symp. New Orleans), Oak Ridge National Laboratory, Oak Ridge, TN,* 1983.

[B$^+$86] K. Brehm et al. Permeation Through Elastomeric O-Ring Seals. In *Proceedings of 8th PATRAM*, Volume II, pages 359-367, Davos, Switzerland, 1986.

[B$^+$04] V. Ballheimer et al. Spent fuel transport associated with other dangerous goods in regular train units - assessment of hypothetical explosion impacts. RAMTRANS, 15(3-4):239-245, 2004.

[Bad63] B.E. Bader. Energy transfer in liquid hydrocarbon fires. SC-R-1366A (Sandia Corporation, Albuquerque), NM, 1963.

[BAM82] Beurteilung behälterspezifischer Fragen der trockenen Zwischenlagerung abgebrannter Brennelemente in einem Transportbehälterlager bei Gorleben, 1982. BAM-Gutachten [Evaluation of Specifically Cask-Related Questions of Dry Intermediate Storage of Spent Fuel Elements in a Transport Cask Depository at Gorleben, 1982. BAM Expert Report], File No. 102/3022.

[BAM08] http://www.tes.bam.de, 2008. BAM-Technisch Öffentliche Sicherheit - Gefahrstoffe/Gefahrgüter [BAM-Technical Public Safety - Hazardous Substances/Hazardous Goods].

[Bat02] K.J. Bathe. *Finite Element Methods*. Springer, Berlin, 2nd edition, 2002.

[Baz84] Z.P. Bažant. Imbricate continuum and its variational derivation. *Journal of Engineering Mechanics*, 110:1693-1712, 1984.

[Ber95] H.P. Berg. On the potential of probabilistic safety assessment. *Kerntechnik*, 60:71, 1995.

[Bet93] J. Betten. *Kontinuumsmechanik, Elasto-, Plasto- und Kriechmechanik* [Continuum Mechanics, Elasto, Plasto- and Creep Mechanics], Springer, Berlin, 1993.

[Bet01] J. Betten. *Kontinuumsmechanik* [Continuum Mechanics], Springer, Berlin, 2001.

[BFS03] Dezentrale Standort-Zwischenlagerung für abgebrannte Brennelemente, 2003. Broschüre des Bundesamtes für Strahlenschutz vom 1 September 2000, zuletzt geändert am 29 Mai 2003 [Decentralized Intermediate Site Storage for Spent Fuel Elements, 2003. Brochure issued by the Federal Bureau of Radiation Protection, September 1, 2000, last amended on May 29, 2003].

[BJ82] J. Bodig and B.A. Jayne. *Mechanics of Wood and Composites.* Van Nostrand Reinhold, New York, 1982.

[BJ02] Z.P. Bažant and M. Jirasek. Nonlocal integral formulations of plasticity and damage: survey and progress. *Journal of Engineering and Mechanics*, 128:1119-1149, 2002.

[BK85] M. Bariska and L.J. Kučera. On the fracture morphology in wood. Part 2: Macroscopical deformations upon ultimate axial compression in wood. *Wood Sci. Technol.,* 19:19-34, 1985.

[BMV04] Richtlinie für das Verfahren bei der Bauartzulassung von Versandstücken zur Beförderung radioaktiver Stoffe, von radioaktiven Stoffen in besonderer Form und gering dispergierbaren radioaktiven Stoffen (R003). Bundesministerium für Verkehr, Bau und Wohnungswesen, Verkehrsblatt Heft 23 [Guideline for the Procedure Governing Model Licensing of Shipping Items for the Transportation of Radioactive Substances, of Radioactive Substances in a Special Form, and Slightly Dispergatable Radioactive Substances (R003). Federal Ministry of Transportation, Construction and Housing, Traffic Gazette, No. 23, pp. 594-599, 2004.

[BO76] Z.P. Bažant and B.H. Oh. Instability, ductility and size effect in strain softening concrete. *Journal of Engineering Mechanics*, 102(2):331-344, 1976.

[BO83] Z.P. Bažant and B.H. Oh. Crack band theory for fracture of concrete. *Materials and Structures*, 16(93):155-177,1983.

[Bod66] J. Bodig. Stress-strain relationship for wood in transverse compression. *Journal of Materials*, 1(3):645-666, 1966.

[BPD00] V. Ballheimer, A. Probst, and B. Droste. Numerical assessment of spent fuel casks impacting on real targets. *RAMTRANS*, 11(1-2):45-51, 2000.

[BQZ02] V. Ballheimer, T. Quercetti, and P. Zeisler. Effects and consequences of interactions between containment components and context of type B packages during 9-m drop tests. *RAMSTRANS*, 130(3-4):305-312, 2002.

[BS04] I.N. Bronstein and K.A. Semendjajew. *Handbook of Mathematics*, Springer, Berlin, 2004.

[BT84] T.B. Belytschko and S.W. Tsai. Explicit algorithms for nonlinear dynamics of shells. *Comp. Meth. Appl. Mech. Eng.*, 43:251-276, 1984.

[Bue86] C. Bues. Untersuchung einiger Eigenschaften von Tannen- und Fichtenholz nach 17jähriger Wasserlagerung. *Holz als Roh- und Werkstoff* [Investigation of Some Properties of Spruce Wood and Fir Wood After 17 Years of Storage in Water. *Wood as Raw Material and Construction Material*], 1(44):7-15, 1986.

[But87] J.C. Butcher. *The Numerical Analysis of Ordinary Differential Equations: Runge-Kutta and General Linear Methods.* John Wiley and Sons Ltd., New York City, 1987.

[C+76] R.K. Clarke et al. Severities of transportation accidents. Technical Report SLA-74-0001, Sandia National Laboratories, Albuquerque, NM, 1976.

[C+83] G. Chevalier et al. Justification and advantages of crushing tests compared with fall tests and the modification of existing regulations. In *PATRAM 83 (Proc. Symp. New Orleans), Oak Ridge National Laboratory, Oak Ridge, TN,* 1983.

[CC09] E. Cosserat and F. Cosserat. *Théorie des Corps déformables* [Theory of Deformable Bodies]. Herrmann, Paris, 1909.

[Cla83] L.A. Clarenburg. Über die Entwicklung einer Sicherheitspolitik unter Berücksichtigung der Interessen der Bevölkerung [On the Development of a Safety Policy Considering the Interests of the Population]. In S. Hartwig, editor, *Große technische Gefahrenpotentiale, Risikoanalysen und Sicherheitsfragen*

[*Major Technical Hazard Potentials. Risk Analyses and Safety Questions*], pages 16-21, Springer, Berlin, 1983.

[CR80] J.D. Colton and C.M. Romander. Potential Crush Loading of Radioactive Material Packages in Highway, Rail and Marine Accidents. Technical Report NUREG/CR-1588, SRI International, Menlo Park, CA, 1980.

[Cri79] M.A. Crisfield. Local instabilities in the nonlinear analysis of reinforced concrete beams and slabs. *Proc. Inst. Civil Engrs.,* 732:55-62, 1979.

[D+83] J.M. Diggs et al. Testing to define the sensitivity of small type B packagings to the proposed IAEA crush test requirement. In *PATRAM 83 (Proc. Symp. New Orleans), Oak Ridge National Laboratory, Oak Ridge, TN,* 1983.

[D+94] R. Diersch et al. Investigation of the impact behavior of wooden impact limiters. *Nuclear Engineering and Design,* 150:341-348, 1994.

[D+95] B. Droste et al. Extended drop tests of DCI casks with artificial flaws demonstrating the existing safety margins. *RAMTRANS,* 6(2-3):177-182, 1995.

[D+98] B. Droste et al. Evaluation of safety casks impacting different kinds of targets. In *PATRAM 98 (Proc. Symp. Paris), Institute of Protection and Nuclear Security (IPSN), Paris,* 1998.

[Dau99] L. Daudeville. Fracture in spruce: experiment and numerical analysis by linear and nonlinear fracture mechanics. *Holz als Roh- und Werkstoff [Wood as Raw Material and Construction Material]*, 57:425-432, 1999.

[dB86] R. de Borst. *Non-linear analysis of frictional materials.* Dissertation, Technische Universiteit [Technical University], Delft, 1986.

[Den78] A.W. Dennis. Predicted occurrence rate of severe transportation accidents involving large casks. In *Proceedings of 5th PATRAM,* Volume II, pages 909-916, Las Vegas, USA, 1978.

[Deu04] P. Deuflhard. *Newton Methods for Nonlinear Problems.* Springer, Berlin, 2004.

[DFW05] Daten, Fakten und Hintergründe zum Wald und der Forstwirtschaft in Deutschland, 2005 [Data, Facts and Background Concerning the Forest and the Forestry Industry in Germany, 2005].
http://www.waldgipfel.de/download/dat-fakt-fw.pdf.

[DHDM55] H.L. Du Hamel Du Monceau. *Traité des arbres et arbustes, qui se cultivent en France en pleine terre [Treaties on Trees and Shrubs Cultivated in France in Open Terrain]*. Guérin et Delatour, Paris, 1755.

[DIN76] Fachnormenausschuß Materialprüfung im Deutschen Institut für Normung e.V., Berlin. *DIN - 52185: Prüfung von Holz - Bestimmung der Druckfestigkeit parallel zur Faser* [Technical Standards Committee Material Testing in the German Institute for Standardization, e.V., Berlin. *DIN - 52185: Testing of Wood - Determination of the Crush Strength Parallel to the Fiber]*, 1976.

[DIN79] Fachnormenausschuß Materialprüfung im Deutschen Institut für Normung e.V., Berlin. *DIN - 52192: Prüfung von Holz - Druckversuch quer zur Faserrichtung* [Technical Standards Committee Material Testing in the German Institute for Standardization, e.V., Berlin. *DIN - 52192: Testing of Wood - Crush Test Laterally with Respect to the Fiber Direction]*, 1979.

[Din81] J.M. Dinwoodie. *Timber - its nature and behavior.* Van Nostrand Reinhold, New York, 1981.

[DIN87] Deutsches Institut für Normung e.V., Berlin. *DIN - 31000 Teil 2: Allgemeine Leitsätze für das sicherheitsgerechte Gestalten technischer Erzeugnisse - Begriffe der Sicherheitstechnik - Grundbegriffe* [German Institute for Standardization, e.V., Berlin. *DIN - 31000 Part 2: General Principles for Safety-Oriented Development of Technical Products - Concepts of Safety Engineering - Basic Terminology]*, 1987.

[Din00] J.M. Dinwoodie. *Timber - its nature and behavior.* E and FN Spon, London, 2nd edition, 2000.

[DIN08a] Deutsches Institut für Normung e.V., Berlin. *DIN - 4074 Sortierung von Holz nach der Tragfähigkeit* [German Institute for Standardization, e.V., Berlin. *DIN - 4074 Sorting of Wood According to Load-Bearing Capacity]*, 2008.

[DIN08b] Deutsches Institut für Normung e.V., Berlin. *DIN EN - 338 Bauholz für tragende Zwecke - Festigkeitsklassen* [German Institute for Standardization, e.V., Berlin. *DIN EN - 338 Structural Wood for Supporting Purposes - Strength Classes]*, 2008.

[DL$^+$03] G. Dill-Langer et al. Size dependency of tension strength in natural fiber composites. *Physica A,* 325:547-560, 2003.

[DMM05] B. Droste, K. Müller, and M. Minack. The new BAM 200-ton drop test facility - construction and operation experiences. In *7th Int. Conference on Radioactive Materials Transport (RAMTRANS 2005)*, Cambridge, UK, 2005.

[Dob90] I. Dobbin. Relationship between small specimen and large panel bending test for on [sic] structural wood based panel. *Forest Products Journal*, 9:10-14, 1990.

[DP52]D.C. Drucker and W. Prager. Soil mechanics and plastic analysis or limit design. *Quarterly of Applied Mathematics,* 10(2):157-165, 1952.

[DP01]B. Droste and U. Probst. CASTOR-Behälter im Explosionbereich eines Propan-Kesselwagens [CASTOR Cask Within Explosion Range of a Propane Tank Car]. Technical University, 42(11-12):15-17, 2001.

[DPH99] B. Droste, U. Probst, and W. Heller. Impact on an exploding LPG rail tank car onto a CASTOR spent fuel cask. *RAMTRANS*, 10(4):231-240, 1999.

[DPP66] G.R. Debaise, A.W. Porter, and R.E. Pentoney. Morphology and mechanics of wood fracture. *Materials Research and Standards*, 6(10):493-499, 1966.

[Dro01] B. Droste. Bauartprüfung, Qualitätssicherung und Sonderversuche mit CASTOR-Behältern. Fachtagung Standortnahe Zwischenlager [Model Testing, Quality Assurance and Special Test with CASTOR Casks. Technical Conference on Intermediate Storage Dumps in the Vicinity of Nuclear Sites]. Bonn, 2001.

[Duv02] A.S. Duvall. The developments of simplistic code to determine the impact response of transport flasks. In *International Conference on Radioactive Materials Transport,* Edinburgh, GB, November 2002. Session 4, Paper 3.

[DVWQ02] B. Droste, H. Völzke, G. Wieser, and L. Qiao. Safety margins of spent fuel transport and storage casks considering aircraft crash impacts. *RAMTRANS*, 13(3-4):313-316, 2002.

[E+82] K.E. Easterling et al. On the mechanics of balsa and other woods. *Proceedings of Royal Society*. A383:31-41, 1982.

[Ebe02] J. Eberhardsteiner. *Mechanisches Verhalten von Fichtenholz, Experimentelle Bestimmung der biaxialen Festigkeitseigenschaften [Mechanical Behavior of Fir Wood, Experimental Determination of Biaxial Strength Properties]*, Springer, Vienna, 2002.

[F+93] H.J. Fett et al. Abfalltransporte zum Endlager für radioactive Abfälle Morsleben (ERAM): Bewertung der Transportsicherheit. [Waste Shipments to the Final Dump for Radioactive Waste, Morsleben (ERAM): Evaluation of Transport Safety]. Technical Report GRS-A-2025, GRS - Gesellschaft für Anlagen- und Reaktorsicherheit [GRS - Company for Plant and Reactor Safety], 1993.

[F+97] H.J. Fett et al. Transport risk assessment study for reprocessing waste materials to be returned from France to Germany. Technical Report GRS-141, GRS - Gesellschaft für Anlagen- und Reaktorsicherheit [GRS - Company for Plant and Reactor Safety], 1997.

[Far83]F.R. Farmer. Über die Notwendigkeit einer ausgewogenen Risikobeurteilung in der Industriegesellschaft. [On the Necessity of a Well-Balanced Risk Evaluation in Industrial Society]. In S. Hartwig, editor, *Große technische Gefahrenpotentiale.*

Risikoanalysen und Sicherheitsfragen [Major Technical Hazard Potential. Risk Analyses and Safety Questions], pages 22-28, Springer, Berlin, 1983.

[FDB97] B. Faunas and N. Du Bois. A simple elastoplastic model for foam materials. In *STAP Conference, Albuquerque*, 1997.

[FG66] A. Fairbairn and T.C. George. Tests for Type A and Type B packagings and capsules. Pergamon Press, London, 1966.

[Fis87] L.E. Fischer. Shipping Container Response to Severe Highway and railway Accident Condition. Technical Report NUREG/CR-4829, Lawrence Livermore National Laboratory, USA, 1987.

[Fos92] C.G. Foster. Damping and poisson factor behavior in timber considered as an orthotropic material, part 1, the loss factor. *Journal of Sound and Vibration*, 158(3):405-425, 1992.

[G+01] V.D. Guskov et al. Test facility of transport packagings for radioactive materials in the St. Petersburg region (Russia). *RAMTRANS*, 12(2-3):135-138, 2001.

[GA97] L.J. Gibson and M.F. Ashby. *Cellular solids*. Cambridge University Press, 2nd edition edition [sic], 1997.

[Gal38] Galileo Galilei. *Discorsi e Dimostrazioni matematiche [Mathematical Discourses and Demonstrations]*, Leyden, 1638.

[GB70] J.R. Goodman and J. Bodig. Orthotropic elastic properties of wood. *Journal of the Structural Division*, ASCE96(ST11):2301-2319, 1970.

[GDM92] R.E. Glass, T.A. Duffey, and P. McConell. Impact-limiting materials characterization. In *Proceedings of 10th PATRAM*, volume 2, pages 945-952, Yokohama, Japan, 1992.

[Gei99] Rudolph Geipel. Von Becquerel, Antoine-Henri zum Becquerel (Bq, SI Einheit). Radioaktivität in Geschichte, Natur und Technik. [From Becquerel, Antoine-Henri to Becquerel (Bq, SI Unit). Radioactivity in History, Nature and Technology. Technical report, Fachbereich Physik, Universität Erlangen [Physics Division, University of Erlangen], 1999.

[GF04] K.H. Grothe and J. Feldhusen. *Dubbel Taschenbuch für den Maschinenbau [Dubbel Pocketbook for Machine Building]*. Springer, Berlin, 21st edition, 2004.

[GGB06] GGBefG - Gefahrgutbeförderungsgesetz, 2006. Gesetz über die Beförderung gefährlicher Güter, in der Bekanntmachung von 29 September 1998 (BGBl. I S. 3114), zuletz geändert am 31 Oktober 2006 (BGBl. I S. 2407) [GGBefG - Hazardous Goods Transportation Law, 2006. Law on the Transportation of Hazardous Goods in the Announcement of September 29, 1998 (BGBl. [Federal

Legal Gazette] I, p. 3114), last amended on October 31, 2006 (BGBl. [Federal Legal Gazette] I, p. 2407].

[GGR03] BAM GGR 008 - Richtlinie für numerisch geführte Sicherheitsnachweise im Rahmen der Bauartprüfung von Transport- und Lagerbehältern für radioactive Stoffe. Amts- und Mitteilungsblatt/Bundesanstalt für Materialforschung und-prüfung (BAM) BAM GGR 008 - Guideline for Numerically Controlled Safety Data Records in the Context of Model Testing of Shipment and Storage Casks for Radioactive Substances. Official Gazette and Bulletin/Federal Institute of Materials Research and Testing (BAM)], 2003.

[GGV06] GGVSE - Gefahrgutverordnung Strasse und Eisenbahn, 2006. Verordnung über die innerstaatliche und grenzüberschreitende Beförderung gefährlicher Güter auf der Strasse und mit der Eisenbahn vom 11 Dezember 2001 (BGBl. I S. 3529), in der Fassung der Bekanntmachung vom 10 September 2003 (BGBl. I S. 1913), neu bekannt gemacht am 24 November 2006 (BGBl. I S. 2683) [GGVSE - Highway and Railroads Hazardous Goods Decree, 2006. Decree on Domestic and Border Crossing Transportation of Hazardous Goods by Road and Rail, dated December 11, 2001 (BGBl. [Federal Legal Gazette] I, p. 3529) in the Version of the Announcement of September 10 2003 (BGBl. [Federal Legal Gazette] I, p. 1913), newly promulgated on November 24, 2006 (BGBl. [Federal Legal Gazette] I, p. 2683).

[GGV07a] GGVSee - Gefahrgutverordnung See, 2007. Verordnung über die Beförderung gefährlicher Güter mit Seeschiffen vom 04 Dezember 2007 (BGBl. I S. 2815) [GGVSee - Maritime Navigation Hazardous Goods Degree, 2007. Decree on the Transportation of Hazardous Goods by Oceangoing Vessels, dated December 4 2007 (BGBl. [Federal Legal Gazette] I, p. 2815].

[GGV07b] GGVBinSch - Gefahrgutverordnung Binnenschifffahrt, 2007, zuletzt geändert am 26 Juni 2007 (BGBl. I S. 1222) [GGVBinSch - Inland Navigation Hazardous Goods Decree, 20070, last amended on June 26, 2007 (BGBl. [Federal Legal Gazette] I, p. 1222].

[Göh58] K. Göhre. Über die Verteilung der Rohdichte im Stamm und ihre Beeinflussung durch Wuchsgebiet und Standort. *Holz als Roh- und Werkstoff* [On the Distribution of Raw Density in the Trunk and the Way It Is Influenced by the Growth Area and Location. *Wood as Raw Material and Construction Material]*, 44:313-318, 1986.

[GH90] P. Glos and D. Henrici. Festigkeitsverhalten von Bauholz bei hohen Temperaturen. Technical report, Forschungsbericht, Institut für Holzforschung der Universität München [Shrink Behavior of Structural Wood at High Temperatures. Technical Report, Research Report, Institute of Wood Research, Munich University], 1990.

[GKF86] H. Göttsche-Kühn and A. Frühwald. Holzeigenschaften von Fichten aus Waldschadengebieten; Untersuchungen an gelagertem Holz. *Holz als Roh- und Werkstoff* [Wood Properties of Fir Trees from Damaged Wood Areas; Investigations on Stored Wood. *Wood as Raw Material and Construction Material]*, 44:313-318, 1986.

[GKMM07] K.P. Gründer, D. Kadoke, K. Müller, and A. Musolff. Characterization of shock absorber deformation by optical surface digitization. In *Proceednigs of PATRAM 2007*, Miami, USA, 2007.

[Gla80] F. Glaser. Simulation of Aircraft Crashes on Spent Fuel Transport and Storage Casks. In *Proceedings of 6th PATRAM*, Volume II, pages 1338-1346, Berlin, Germany, 1980.

[Glo78] P. Glos. *Zur Bestimmung des Festigkeitsverhaltens von Brettschichtholz bei Druckbeanspruchung aus Werkstoff- und Einwirkungskenngrößen [On the Determination of Strength Behavior of Stacked Plank Timber in Response to Pressure Stress on the Basis of Material and Action Characteristics]*, Dissertation, Munich Technical University, 1978.

[GR94] P. Gummert and K.A. Reckling. *Mechanics.* Vieweg & Sohn Publishers, Braunschweig/Wiesbaden, 1994.

[Gre02] B.D. Grenke. Digital filtering for J211 requirements using a fast fourier transform-based filter. *SAE TRANSACTIONS*, 111(7):359-401, 2002,

[Gro05] M. Grosse. *Zur numerischen Simulation des physikalisch nichtlinearen Kurzzeittragverhaltens von Nadelholz am Beispiel von Holz-Beton-Verbundkonstruktionen [On the Numerical Simulation of the Physically Nonlinear Short-Time Support Behavior of Coniferous Wood Using the Example of Wood-Concrete Composite Structures]*. Dissertation, Bauhaus-University, Weimar, 2005.

[GRS98] GRS Jahresbericht 1998. Gesellschaft für Anlagen- und Reaktorsicherheit mbH, Köln [1998 Annual GRS Report. Company for Power Plant and Reactor Safety, mbH, Cologne], 1998.

[GS79]E. Gehri and T. Steurer. Holzfestigkeit bei Beanspruchung schräg zur Faser [Wood Strength in Response to Stress]. Technical Report Bulletin 7/2, Schweizerische Arbeitsgemeinschaft für Holzforschung (SAH), 1979.

[GS00a] M. Gong and I. Smith. Failure of softwood under static compression parallel to grain. *Journal of the Institute of Wood Science*, 15(4):204-210, 2000.

[GS00b] Gefährliche Stoffe. Vorlesungsmitschrift Gefährliche Stoffe SS 99/00 [Hazardous Substances. Hazardous Substances Lecture Material SS 99/00, Bergische Universität Gesamthochschule Wuppertal, Prof. Dr. S. Hartwig, 2000.

[H+77a] S.W. Haeberlin et al. Consequences of Postulated Losses of LWR Spent Fuel and Plutonium Shipping Packages at Sea. Technical Report BNWL-2093, Batelle, Pacific Northwest Laboratories, Richland, WA, USA, 1977.

[H+77b] R.J. Hall et al. An Assessment of the Risk of Transporting Plutonium Dioxide and Liquid Plutonium Nitrate by Train. Technical Report BNWL-1996, Batelle, Pacific Northwest Laboratories, Richland, WA, USA, 1977.

[H+01] F.P. Henry et al. A comparison of requirements and test methodologies for a variety of impact absorbing materials. In *Proceedings of 13th PATRAM*, Chicago, IL, USA, 2001.

[H+02] A.G. Hanssen et al. Validation of constitutive models applicable to aluminum foams. *International Journal of Mechanical Sciences*, 44:359-406, 2002.

[Hal97] J.O. Hallquist. *Theoretical manual.* Livermore Software Technology Corporation, 1997.

[Han21] R. Hankinson. Investigation of crushing strength of spruce at varying angles to the grain. Technical Report 259, US Air Service Information Circular III, 1921.

[Har99] S. Hartwig. *Die Riskoanalyse als Hilfe für Sicherheitsentscheidungen [Risk Analysis as an Aid in Safety Decisions]*. Rich Schmidt Publishers, Berlin, 1999.

[Hau01] A. Haufe. *Dreidimensionale Simulation bewehrter Flächentragwerke aus Beton mit der Plastizitätstheorie [Three-Dimensional Simulation of Reinforced Surface Support Structures Consisting of Concrete with Plasticity Theory]*. Dissertation, Institut für Baustatik der Universität Stuttgart [Institute of Structural Statics of the Stuttgart University], 2001.

[HDBW02] A. Hirth, P. Du Bois, and K. Weimar. A material model for transversely anisotropic crushable foams in LS DYNA. In *7th International LS-DYNA Users Conference*, Dearborn, USA, 2002.

[Hil62] R. Hill. Acceleration waves in solids. *Journal of the Mechanics and the Physics of Solids*. 10:1-16, 1962.

[HM83] H.W. Huebner and J.P. Masslowski. Interactions between crush conditions and fire resistance for Type B packages less than 500 kg. In *PATRAM 83 (Proc. Symp. New Orleans), Oak Ridge National Laboratory, Oak Ridge, TN,* 1983.

[HM95] G. Hofstetter and H.A. Mang. *Computational Mechanics of Reinforced Concrete Structures.* Vieweg & Sohn Publishers, Braunschweig/Wiesbaden, 1995.

[Hör02] M. Hörmann. *Nichtlinear Versagensanalyse von Faserverbundstrukturen [Nonlinear Failure Analysis of Composite Fiber Structures]*, Dissertation, Stuttgart University, 2002.

[Hug87] T.J. Hughes. *The Finite Element Method*. Prentice Hall, Englewood Cliffs, 1987.

[IAE61] Regulations for the safe transport of radioactive materials. 1961 edition. IAEA, Safety series No. 6, Vienna, 1961.

[IAE64] Regulations for the safe transport of radioactive materials. 1965 edition. IAEA, Safety series No. 6, Vienna, 1964.

[IAE94a] IAEA - International Atomic Energy Agency, Vienna. *Compliance Assurance for the Safe Transport of Radioactive Material*. Safety Standard Series No. 112 edition, 1994.

[IAE94b] IAEA - International Atomic Energy Agency, Vienna. *Quality Assurance for the Safe Transport of Radioactive Material*. Safety Standard Series No. 113 edition, 1994.

[IAE96] IAEA - International Atomic Energy Agency, Vienna. *Radiation Protection and the Safety of Radiation Sources*. Safety Standard Series No. 120 edition, 1996.

[IAE03] IAEA - International Atomic Energy Agency, Vienna. *International Basic Safety Standards for Protection Against Ionizing Radiation and for the Safety of Radiation Sources*. Safety Standard Series No. 115 edition, 2003.

[IAE06] IAEA - International Atomic Energy Agency, Vienna. *Chernobyl's Legacy: Health, Environmental and Socioeconomic Impacts,* 2006.

[IAT08] International Air Transport Association - Dangerous Goods Regulations IATA-DGR 2008. 49th edition, Dössel & Rademacher Publishers, Hamburg.

[ICA07] Technical Instructions for the Safe Transport of Dangerous Goods by Air (ICAO), 2007. International Civil Aviation Organization - ICAO.

[IH89] T. Ikushima and S. Hode. Simplified analysis computer programs and their adequacy for radioactive materials shipping casks. In *Proceedings of 9th PATRAM*, Volume 3, pages 1202-1209, Washington, D.C. USA, 1989.

[IIOA92] T. Ikushima, T. Ishiwata, J. Oshika, and K. Asada. Simplified computer codes for cask impact analysis. In *Proceedings of 10th PATRAM*, Volume 3, pages 1419-1426, Yokohama, Japan, 1992.

[IMD06] IMDG Code - International Maritime Dangerous Goods Code, 2006. Amendment 33-06, Beilage zum Verkehrsblatt [Supplement for Verkehrsblatt], 2006, p. 844.

[INE01] International Nuclear Events Scale (INES), 2001.

[INF06] INf Code - International Code for the Safe Carriage of Packaged Irradiated Nuclear Fuel, Plutonium and High-Level Radioactive Wastes on Board Ships, 2006. International Maritime Organization, London.

[IRH03] L. Issler, H. Ruoss, and P. Häfele. *Festigkeitslehre - Grundlagen [Strength Theory - Fundamentals]*, Springer, Berlin, 2nd edition, 2003.

[ISO04] General terms and their definitions concerning standardization and related activities, 2004. ISO/IEC Guide 2.

[Jan91] K. Janberg. Ductile Iron Cast Development in Germany. Summary of the International Ductile Iron Progress Meeting, Appendix S, US Department of Energy, Arlington, Virginia, USA, 1991.

[JM83] R.M. Jefferson and J.D. McClure. Regulation versus Reality. In *PATRAM 83 (Proc. Symp. New Orleans), Oak Ridge National Laboratory, Oak Ridge, TN*, 1983.

[Joh64] J.R. Johanson. *J. Appl. Mech.,* 31:499-506, 1964.

[Jon03] N. Jones. *Structural Impact.* Cambridge University Press, Cambridge, 2nd edition, 2003.

[K$^+$05] S. König et al. Full-scale drop testing of the CONSTOR V/TC package program and preliminary results. *JNMM*, 33(1):4-10, 2005.

[Kar37] K. Karmasch. *Handbuch der mechanischen Technologie [Handbook of Mechanical Technology]*. Hellwingsche Hofbuchhandlung, Hanover, 1837.

[KCJ68] F.F.P. Kollmann and W.A. Cote Jr. *Principles of Wood Science and Technology, I Solid Wood.* Springer, Berlin, 1968.

[Ken68] R.W. Kennedy. Wood in transverse compression. *Forest Products Journal*, 18(3):36-40, 1968.

[Key51] R. Keylwerth. Die anisotrope Elastizität des Holzes und der Lagerhölzer [The Anisotropic Elasticity of Wood and of Stored Woods], Technical Report VDI-Forschungsheft 430, Deutscher Ingenieursverlag, Duesseldorf, 1951.

[Koc03] F. Koch. *Elementauswahl bei Finite-Elemente-Analysen [Selection of Elements for Finite Element Analyses]*. Shaker Publishers, Aachen, 2003.

[Kol36] F. Kollmann. *Technologie des Holzes und der Holzwerkstoffe [Technology of Wood and of Wood Materials]*. Springer, Berlin, 1st edition, 1936.

[Kol82] F. Kollmann. *Technologie des Holzes und der Holzwerkstoffe [Technology of Wood and of Wood Materials]*. Springer, Berlin, 2nd edition, 1982, reprint.

[Kos98] H. Koschick. Brunnen der Jungsteinzeit. Internationales Symposium Erkelenz vom 27 bis 29 Oktober 1997. *Materialien zur Boden- und Denkmalpflege im Rheinland* [Fountains of the Early Stone Age. Erkelenz International Symposium, October 27-29, 1997. *Materials on Soil and Monument Care in the Rhineland]*, 11, 1998.

[Kot04] L. Kotchetkov. Obninsk: number one. *Nuclear Engineering International*, 6:14-17, 2004.

[KS89]P. Klein and E. Schwab. Zum Verständnis des Quell- und Schwindverhaltens von Holz und Holzwerkstoffen. *Restauratorenblätter* [Understanding the Swelling and Shrinkage Behavior of Wood and Wood Materials. *Restorer Bulletins]*, 19:15-28, 1989.

[L$^+$91] F. Lange et al. Transportstudie Konrad: Sicherheitsanalyse des Transportes radioaktiver Abfäller zum Endlager Konrad [Konrad Transport Study: Safety Analysis for the Shipment of Radioactive Waste to the Konrad Final Dump], Technical Report GRS-84, GRS - Gesellschaft für Anlagen- und Reaktorsicherheit [Company for Plant and Reactor Safety], 1991.

[L$^+$07] F. Lange et al. Assessment, evaluation and further development of the safe transport of radioactive material. Final report of the research project SR 2479. Technical Report GRS-A-3378, GRS - Gesellschaft für Anlagen- und Reaktorsicherheit [Company for Plant and Reactor Safety], Cologne, 2007.

[Lah87] W.R. Lahs. Transporting spent fuel/Protection Provided Against Severe Highway and Railroad Accidents. Technical Report NUREG/BR-0111, U.S. Nuclear Regulatory Commission, March 1987.

[Leu05] M. Leukart. *Kombinierte anisotrope Schädigung und Plastizität bei kohäsiven Reibungsmaterialien [Combined Anisotropic Damage and Plasticity in the Case of Cohesive Friction Materials]*, Dissertation, Institut für Baustatik der Universität Stuttgart [Institute of Structural Statics of the Stuttgart University], 2001.

[LMB00] Q.M. Li, R.A.W. Mines, and R.S. Birch. The crush behavior of Rohacell-51WF structural foam. *International Journal of Solids and Structures,* 37:6321-6341, 2000.

[LR97]P.B. Lourenço and J.G. Rots. Multisurface interface model for analysis of masonry structures. *Journal of Engineering Mechanics*, 123:660-668, 1997.

[LSD08] Livermore Software Technology Corporation. *LS-DYNA Keyword Users Manual V.971*, 2008.

[Lud09] P. Ludvik. *Elemente der technologischen Mechanik [Elements of Technological Mechanics]*, Berlin, 1909.

[LVZ08] Luftverkehr-Zulassungs-Ordnung, 2008 in der Fassung der Bekanntmachung vom 10 Juli 2008 (BGBl. I, S. 1229) [Air Traffic Licensing Regulation, 2008, in the Version of the Announcement of July 10, 2008 (BGBl. [Federal Legal Gazette] I, p. 1229).

[M+75]T.I. McSweeney et al. An Assessment of the Risk of Transporting Plutonium Dioxide and Liquid Plutonium Nitrate by Truck. Technical Report BNWL-1846, Batelle, Pacific Northwest Laboratories, Richland, WA, USA, 1975.

[M+80]J.D. McClure et al. Relative response of type B packagings to regulatory and other impact test environments. In *Proceednigs of 6th PATRAM*, Volume II, pages 1247-1253, Berlin, Germany, 1980.

[MA91] H.B. Mülhaus and E.C. Aifantis. A variational principle for gradient plasticity. *Journal for Solids and Structures,* 28:845-857, 1991.

[MAG85] The resistance to impact of spent magnox fuel transport flasks. The Institution of Mechanical Engineers, Project Smash Hit, 224 London, England, 1985.

[MaN03] R.P. Mourão and M.M. Neto. The use of castor oil polyurethane foam in impact limiters for radioactive materials packages. *RAMTRANS*, 14(1):49-61, 2003.

[MC00] N.T. Mascia and S.M. Cramer. Effect of moisture content, specific gravity, temperature and number of annual growth rings on redwood elastic constants. *World Conference of Timber Engineering*, 1:1-6, 2000.

[McC77] J.D. McClure. An analysis of the qualification criteria for small radioactive material shipping packages. Technical Report SAND-76-0708, Sandia National Laboratories, Albuquerque, NM, 1977.

[MCD06] MATHCAD Engineering and Education, Inc., Cambridge, USA. *Benutzerhandbuch MATHCAD 13*, 2006.

[MD04] D. Mohr and M. Doyoyo. Large plastic deformation of metallic honeycomb - orthotropic rate-independent constitutive model. *International Journal of Solids and Structures*, 41:4435-4456, 2004.

[MF63] W. de L.M. Messenger and A. Fairbairn. The transport of radioactive materials. Interim Recommendations for the Application of Environmental Tests to the Approval of Packaging, United Kingdom Atomic Energy Authority AHSB SR 19, Risley, Warrington: UKAEA, 1963.

[MH82] J.E. Marsden and T.J.R. Hughes. *Mathematical Foundations of Elasticity*. Prentice Hall, Englewood Cliffs, New Jersey, 1982.

[MH95] W.M. McMurtry and G.F. Hohnstreiter. Impact limiter tests of four commonly used materials and establishment of an impact limiter data base. *PATRAM '95 (11th International Conference on the Packaging and Transportation of Radioactive Materials, December 3-8, 1995, Las Vegas, Nevada, USA)*, pages 883-890, 1995.

[MHEM03] P. Mackenzie-Helnwein, J. Eberhardsteiner, and H.A. Mang. A multisurface plasticity model for clear wood and its application to the finite element analysis of structural details. *Computational Mechanics*, 31:204-218, 2003.

[Mil00] R.E. Miller. A continuum plasticity model for the constitutive and indentation behavior of foamed metals. *International Journal of Mechanical Sciences*, 42(4):729-754, 2000.

[MJ77]T.I. McSweeney and J.F. Johnson. An Assessment of the Risk of Transporting Plutonium Dioxide by Cargo Aircraft. Technical Report BNWL-2030, Batelle, Pacific Northwest Laboratories, Richland, WA, USA, 1977.

[Mül03] U. Müller. *Analyse der mechanischen Eigenschaften von Massivholz unter Berücksichtigung der Zellstruktur [Analysis of Mechanical Properties of Massive Wood Considering the Cell Structure]*, Dissertation, Soil Science University, Vienna, 2003.

[MMD04] K. Müller, M. Minack and B. Droste. The new drop test facility for big full-scale casks. In *14th Int. Symposium on the Packaging and Transportation of Radioactive Materials (PATRAM 2004)*, Berlin, 2004. Paper 124.

[MMHE04] H.W. Müllner, P. Mackenzie-Helnwein, and J. Eberhardsteiner. Constitutive modeling of clear spruce wood under biaxial loading by means of an orthotropic single-surface model under consideration of hardening and softening mechanisms. In *Proceedings of the 2nd International Symposium on Wood Machining*, Vienna, 2004.

[MNK08] K. Müller, M. Neumann, and A. Kadji. Abschlussbericht zum Vorhaben "Fallversuche mit Brennelement-/HAW-Transport- und lagerbehältern in Originalgröße," 2008, gefördert vom Bundesministerium für Bildung und Forschung 9BMBF) unter Förderkennzeichen 02S8274 [Final Report on the Project "Drop Tests with Fuel Element/Highly Active Waste Shipment and

Storage Casks in the Original Size," 2008, promoted by the Federal Ministry of Education and Research (BMBF) under the Promotion Project 02S8274.

[MSD92] A.K. Maji, D. Satpathi, and S. Donald. Mechanical properties of aluminum honeycomb impact limiters. *RAMTRANS,* 3(2-3):109-199, 1992.

[Mur03] R.L. Murray. *Understanding Radioactive Waste*. Batelle Press, Columbus, Ohio, USA, 2003.

[NES89] D.J. Nolan, A.G. Eggers, and P. Shih. Design, analysis and testing of wood filled impact limiters. In *Proceedings of 9th PATRAM*, Volume 1, pages 44-54, Washington, D.C., USA, 1989.

[Neu81] H.F. Neuhaus. Elastizitätszahlen von Fichtenholz in Abhängigkeit von der Holzfeuchtigkeit. Technical Report Techn. Wiss. Mitteilungen des Instituts für Ingenieurbau [Elasticity Factors of Fir Wood as a Function of the Wood Moisture. Technical Report, Technical Scientific Communications of the Institute of Engineering Construction], Ruhruniversität Bochum, 1981.

[Neu00] U. Neubauer. *Verbungtragverhalten geklebter Lamellen aus Kohlenstoffaser-Verbund-Werkstoff zur Verstärkung von Betonbauteilen [Composite Support Behavior of Glued Lamellae Consisting of Carbon Fiber Composite Material to Strength Concrete Parts],* PhD thesis, Braunschweig Technical University, 2000.

[New59] N.M. Newmark. A method of computation for structural dynamics. *Journal of the Engineering Mechanics Division*, 85:67-94, 1959.

[Nie93a] P. Niemz. *Chemie des Holzes und der Holzwerkstoffe [Chemistry of Woods and Wood Materials]*, DRW-Verlag Weinbrenner GmbH & Co., Leinfelden Echterdingen, Germany, 1993.

[Nie93b] P. Niemz. *Physics des Holzes und der Holzwerkstoffe [Chemistry of Woods and Wood Materials]*, DRW-Verlag Weinbrenner GmbH & Co., Leinfelden Echterdingen, Germany, 1993.

[NIO07] Mining Disaster, 2007. National Institute for Occupational Safety and Health.

[Nol74] W. Noll. *The Foundations of Mechanics and Thermodynamics.* Springer, Berlin, 1974.

[NS03]P. Niemz and W. Sonderegger. Untersuchungen zur Korrelation ausgewählter Holzeigenschaften untereinander un mit der Rohdichte unter verwendung vom 103 Holzarten. *Schweiz. Z. Forstwes* [Investigations on the Correlation of Selected Wood Properties Among Each Other and with the Raw Density Using 103 Wood Species. *Swiss Forestry Journal]*, 154:489-493, 2003.

[NUR77] Final environmental statement on the transportation of radioactive material by air and other modes. NUREG-0170, U.S. Nuclear Regulatory Commission, Washington, D.C., 1977.

[NW07] M. Neumann and F. Wille. ImpactCalc, Beschreibung und Verifikation [ImpactCalc, Description and Verification], 2007. Interne Unterlage BAM Berlin.

[NWB07] M. Neumann, F. Wille, and V. Ballheimer. Estimation of cask deceleration and impact limiter deformation under 9-m drop test conditions using the calculation tool ImpactCalc. In *Proceedings of PATRAM 2007,* Miami, USA, 2007.

[NWD07] M. Neumann, F. Wille, and B. Droste. Using scale model impact limiter in the type assessment of transport casks for radioactive material. In *Proceedings of PATRAM 2007,* Miami, USA, 2007.

[P+80] R.B. Pope et al. An Assessment of Accident Thermal Testing and Analysis Procedures for a RAM Shipping Package. Technical Report ASME Paper 80-HT38, American Society for Testing and Materials, Philadelphia, PA, 1980.

[PCB84] G. Pijaudier-Cabot and Z.P. Bažant. Nonlocal damage theory. *Journal of Engineering Mechanics*. 113:1512-1533, 1984.

[Per66]P. Percyna. Fundamental problems in viscoplasticity. *Recent Advances in Applied Mechanics*, 9:243-377, 1966.

[PL64] G. Pretzch and F. Lange. Radiologische Auswirkungen der Freisetzungen von Radioaktivität aus einem Transportbehälter für abgebrannte Brennelemente nach Hohlladungsbeschuss [Radiological Effects of Releases of Radioactivity from a Transport Cask Holding Spent Fuel Elements After Exposure to Fire with Hollow Charges], Technical Report GRS-A-2168, GRS - Gesellschaft für Anlagen- und Reaktorsicherheit [GRS - Company for Plant and Reactor Safety], Cologne, 1994.

[Pop04] R.B. Pope. Historical background to the development of various requirements in the international regulations for the safe packaging and transport of radioactive material. *RAMTRANS*, 15(1):5-13, 2004.

[Pou97] J.S. Poulsen. *Compression in clear wood.* Dissertation, Lyngby University, Denmark, 1997.

[PR59] A.C. Pipkin and R.S. Rivlin. The formulation of constitutive equations in continuum physics. Part I. *Archive for Rational Mechanics and Analysis*, 4:129-144, 1959.

[PR60] A.C. Pipkin and R.S. Rivlin. The formulation of constitutive equations in continuum physics. Part II. *Archive for Rational Mechanics and Analysis*, 4(1):262-272, 1960.

[QBW02] T. Quercetti, V. Ballheimer, and G. Wieser. Analytical, numerical, and experimental investigations on the impact behavior of packaging for the transport of radioactive material under slap down conditions. *JNMM*, 30(3):18 ff, 2002.

[R+75] N. Rasmussen et al. Reactor Safety Study. Technical Report WASH-1400, U.S. Nuclear Regulatory Commission, Washington, D.C., USA, 1975.

[RID06] RID - Ordnung über die internationale Eisenbahnbeförderung gefährlicher Güter - Anlage I zu Anhang B des Übereinkommens über den internationalen Eisenbahnverkehr vom 09 Mai 1980 (COTIF-Ü bereinkommen) [BGBl. 1985, II S. 130), neu gefasst am 24 November 2006, [RID - Order on the International Rail Transport of Hazardous Goods - Appendix I to Appendix B of the Agreement on International Rail Traffic, May 9, 1980 (COTIF Agreement) (BGBl. [Federal Legal Gazette] 1985, II, p. 130), new version on November 2006], 2006.

[RP97] S.R. Reid and C. Peng. Dynamic uniaxial crushing of wood. *International Journal of Impact Engineering*, 19(5-6):531-570, 1997.

[RST01] A. Reiterer and S.E. Stanzl-Tschegg. Compressive behavior of softwood under uniaxial loading at different orientations to the grain. *Mechanics of Materials,* 33:705-715, 2001.

[S+00] J.L. Sprung et al. Reexamination of spent fuel shipment risk estimates. Technical Report NUREG/CR-6672, Sandia National Laboratories, USA, March 2000.

[Sch63] G. Schneeweiss. Der Großeneininfluss im Druckversuch quer zur Faser. *Holzforschung und Holzverwertung* [The Influence of Magnitude in the Compression Tests Laterally with Respect to the Fiber. *Wood Research and Wood Utilization]*, 15:125-130, 1963.

[Sch93] G. Schön. Grundkonzept der Sicherheitstechnik [Basic Concept of Safety Engineering]. *Safety Science,* 16:343-358, 1993.

[SFH00] B. Schulz Forberg and H.W. Hübner. Klassifizierung und Sicherheitsreserven von Transportbehältern für radioactive Stoffe. BAM-Forschungsbericht 230, 2. aktualisierte Auflage [Classification and Safety Reserves of Transport Casks Holding Radioactive Substances. BAM Research Report 230, 2nd updated edition], Wirtschaftsverlag NW, Bremerhaven, April 2000.

[SIF92] K. Shirai, C. Ito, and M. Funahashi. Evaluation of the impact behavior of the contents of reprocessing radioactive waste shipping cask subjected to drop impact. In *Proceedings of 10th PATRAM*, Volume 3, pages 1130-1137, Yokohama, Japan, 1992.

[SIG07] Scientific Solutions SA, Pully-Lausanne, Swizerland. *SIGMAPLOT 10*, 2007.

[SJ85] K. Schneider and C. Jobst. Sicherheitsanalyse der Transporte von radioaktiven Materialien für den Verkehrsträger Schiene. Technical Report Fachband 7, Projekt Sicherheitsstudien Entsorgung (PSE) [Safety Analysis of Shipments of Radioactive Materials with Regard to Rail Transport. Technical Report, Technical Volume 7, Waste Disposal Safety Studies Project (PSE)], Berlin, 1985.

[SK06] J. Schmidt and M. Kaliske. Zur dreidimensionalen Materialmodellierung von Fichtenholz mittels eines Mehrflächen-Plastizitätsmodells. *Holz als Roh- und Werkstoff* [On Three-Dimensional Material Modeling of Fir Wood by Means of a Multisurface Plasticity Model. *Wood as Raw Material and Construction Material*, 64:393-402, 2006.

[Sli85] A. Sliker. Orthotropic strains in compression parallel to grain tests. *Forest Products Journal*, 35(11/12):19-26, 1985.

[Sli89] A. Sliker. Measurement of the smaller poisson ratios and related compliances for wood. *Wood and Fiber Science*, 21(3):252-262, 1989.

[SR02] R. Schlegel and K. Rautenstrauch. Konsistente numerische Umsetzung anisotroper Ver- und Entfestigungsmodelle bei Verwendung mehrflächiger Fliessfunktionen [Consistent Numerical Conversion of Anisotropic Hardening and Softening Models in Conjunction with the Use of Multisurface Flow Functions]. In *20th CADFEM Users Meeting*, Friedrichshafen, Germany, 2002.

[SSB04] K.P. Singh, A.I. Soler, and C.W. Bullard. Validation of an impact limiter crush prediction model with test data: the case of the HI-STAR 100 package. In *14th PATRAM*, Berlin, 2004.

[SV03] I. Smith and S. Vasic. Fracture behavior of softwood. *Mechanics of Materials*, 35:803-815, 2003.

[SVA07] Kernkraftwerke der Welt, Les centrales nucleaires dans le monde - 2007. Schweizerische Vereinigung für Atomenergie (SVA), [Nuclear Power Plants of the World, The Nuclear Power Plants in the World - 2007. Swiss Atomic Energy Association (SVA), Postfach 5032, Bern, 2007.

[SVA08] Kernkraftwerke der Welt, Les centrales nucleaires dans le monde - 2008. Schweizerische Vereinigung für Atomenergie (SVA), [Nuclear Power Plants of the World, The Nuclear Power Plants in the World - 2008. Swiss Atomic Energy Association (SVA), Postfach 5032, Bern, 2008.

[SZM94] H.L. Schreyer, Q.H. Zuo, and A.K. Maji. Anisotropic plasticity model for foams and honeycombs. *Journal of Engineering Mechanics,* 1120(9):1913-1930, 1994.

[T+85] A. Tully et al. Sicherheitsanalyse der Transporte von radioaktiven Materialien für den Verkehrsträger Strasse [Safety Analysis of Shipments of Radioactive Materials with Regard to Road Transport]. Technical Report, Technical Volume 8, Waste Disposal Safety Studies Project (PSE), Berlin, 1985.

[TC01a] T. Tabarsa and Y.H. Chui. Characterizing microscopic behavior of wood under transverse compression. Part II. Effect of species and loading direction. *Wood and Fiber Science*, 33(2):223-232, 2001.

[TC01b] T. Tabarsa and Y.H. Chui. Stress strain response of wood under radial compression. Part I. Test method and influences of cellular properties. *Wood and Fiber Science*, 33(2):223-232, 2001.

[Thi99] H. Thieme. Altpaläolithische Holzgeräte aus Schöningen. Lkr. Helmstedt. Bedeutsame Funde zur Kulturentwicklug des frühen Menschen [Old Paleolithic Wood Implements from Shöningen, Rural District of Helmstedt. Significant Finds on the Cultural Development of Early Humans], *Germania*, 77:451-487, 1999.

[Tre39] R. Trendelenburg. *Das Holz als Rohstoff [Wood as Raw Material*], Hanser, Munich, 1939.

[Tru85] C. Truesdell. *The Elements of Continuum Mechanics.* Springer, New York, 1985.

[TSG08a] IAEA - International Atomic Energy Agency, Vienna. *Advisory Material for the IAEA Regulations for the Safe Transport of Radioactive Material, 1996 Edition (Revised),* TS-G-1.1, ST-2 Revised edition, 2008.

[TSG08b] IAEA - International Atomic Energy Agency, Vienna. *Planning and Preparing for Emergency Response to Transport Accidents Involving Radioactive Material,* TS-G-1.2, ST-3 Revised edition, 2008.

[TSR85] Regulations for the safe transport of radioactive materials, 1985 edition. IAEA, Safety Standard Series, No. TS-R-1 (ST-1), Vienna, 1985.

[TSR96] Regulations for the safe transport of radioactive materials, 1996 edition. IAEA, Safety Standard Series, No. TS-R-1 (ST-1), Vienna, 1996.

[TSR08] IAEA - International Atomic Energy Agency, Vienna. *Regulations for the Safe Transport of Radioactive Material, 2005 Edition (Revised)*, Safety Standard Series No. 113 edition, 2008.

[TW70] S.W. Tsai and E.M. Wu. A general theory of strength for anisotropic materials. *Journal of Composite Materials*, 5:58-80, 1970.

[UN57] Preparatory Commission of the International Atomic Energy Agency. United Nations, IAEA/PC/WG.4(S), New York, April 1957.

[UN59] Economic and Social Council resolution 724 of the twenty-eight session. United Nations, E/32990, Geneva, 1959.

[VDI06] Verein Deutschter Ingenieure. *VDI 2634 Blatt 1: Optische 3-D-Messsysteme, Bildgebende Systeme mit punktförmiger Antastung, und hier bezeichnet als dreidimensionale Längenmessabweichung* [Association of German Engineers. *VDI 2634, Bulletin 1: Optical 3-D Measurement Systems, Imaging Systems with Point Scanning Designated Here as Three-Dimensional Length Measurement Deviation]*, 2006.

[vM28] R. von Mises. Mechanik der plastischen Formänderung von Kristallen. *Zeitschrift für angewandte Mathematik und Mechanik* [Mechanics of Plastic Form Change in Crystals. *Bulletin of Applied Mathematics and Mechanics]*, 3(8):161-185, 1928.

[Vol03] M. Volkmer. *Basiswissen zum Thema Kernenergie.* Informationskreis Kern-Energie [Basic Knowledge on the Subject of Nuclear Energy. Nuclear Energy Information Group], Berlin, 2003.

[Vor49] L. Vorreiter. *Holztechnologisches Handbuch [Wood Technology Handbook]*, Fromme, Vienna, 1949.

[VR03] M. Vural and G. Ravichandran. Dynamic response and energy dissipation characteristics of balsa wood experiment and analysis. *International Journal of Solids and Structures*, 40:2147-2170, 2003.

[W+89]Wolcott et al. Testing small wood specimens in transverse compression. *Wood and Fiber Science*, 21(3):320-329, 1989.

[W+04]G. Wieser et al. Safety analysis of casks under extreme impact conditions. In *14th PATRAM*, Berlin, 2004.

[WAS75] Der Rasmussen-Bericht (WASH-1400): "Übersetzung der Kurzfassung" [Rasmussen Report (WASH-1400): "Translation of the Abstract." Springer, Berlin, 1975.

[Wei95] S. Weihe. *Modelle der fiktiven Rißbildung zur Berechnung der Initiierung und Ausbreitung von Rissen - Ein Ansatz zur Klassifizierung [Model of Fictitious Crack Formation to Calculate the Initiation and Propagation of Cracks - An Approach to Classification]*, Dissertation, Stuttgart University, 1995.

[Wer04] K.D. Wernecke. Medizinische Biometrie - Planung und Auswertung medizinischer Studien. Technical report, Institut für Medizinische Biometrie [Medical Biometrics - Planning and Use of Mechanical Studies. Technical report, Institute of Medical Biometrics], Charite - Berlin Medical University, 2004.

[WG73] M. Wilkins and M. Guinan. Impact of cylinders on a rigid boundary. *Journal of Applied Physics*, 44(3), 1973.

[WHB99] Wood handbook. Forest Products Laboratory. General Technical Report FPL-GTR-113, 1999.

[Wie09] C.F. Wiebeking. *Beyträge zur Brückenbaukunde [Contributions to Bridge Construction]*. Tübingen, 1809.

[Wie82] K.E. Wieser. Quetschtest für Transportverpackungen hochradioaktiver Stoffe. In *Amts- und Mitteilungsblatt der BAM 12, No. 3* [Crush Test for Transport Packages Containing Highly Radioactive Substances. In *Official Gazette and Bulletin, BAM 12, No. 3]*, pages 268-273, Berlin, Germany, 1982.

[Wil03] K. Willner. *Kontinuums- und Kontaktmechanik [Continuum and Contact Mechanics]*, Springer, Berlin, 2003.

[WJH83] K.E. Wieser, M. Jais, and U. Holzlöhner. Drop from the reactor building crane - an event covered by the 9-m drop test requirement? In *PATRAM 83 (Proc. Symp. New Orleans), Oak Ridge Laboratory, Oak Ridge, TN*, pages 879-885, 1983.

[WQ06] G. Wieser and L. Qiao. FEM - simulation of extreme thermal and mechanical accident loads on screwed spent fuel cask lid structures. In *Proceedings of PVP2006-ICPVT-11,* Vancouver, BC, Canada, 2006.

[Wri01] P. Wriggers. *Nichtlineare Finite-Elemente-Methoden [Nonlinear Finite Elements Methods]*, Springer, Berlin, 2001.

[Yos78] H.R. Yoshimura. Full Scale Simulations of Accidents on Spent Nuclear Fuel Shipping Systems. In *Proceedings of 5th PATRAM*, Volume 1, pages 463-476, Las Vegas, USA, 1978.

[ZHS97] A.G. Zink, R.B. Hanna, and J.W. Stelmokas. Measurement of poisson's ratios for yellow polar. *Forest Products Journal*, 47(3):78-80, 1997.

[ZT05] O.C. Zienkiewicz and R.L. Taylor. *The Finite Element Method for Solid and Structural Mechanics*. Elsevier Butterworth Heinemann, Burlington, 6th edition, 2005.